Increasing the Sensitivity of Optical Nanobiosensors for Neurotransmitter Detection

Von der Fakultät für Ingenieurwissenschaften
Abteilung Elektrotechnik und Informationstechnik
der Universität Duisburg-Essen

zur Erlangung des akademischen Grades

Doktor der Naturwissenschaften

genehmigte Dissertation

von

Julia Ackermann
aus
Miltenberg

Gutachter: Prof. Dr.-Ing. Karsten Seidl
Gutachter: Prof. Dr. rer. nat. Sebastian Schlücker
Gutachter: Prof. Dr. rer. nat. Sebastian Kruss
Tag der mündlichen Prüfung: 25.07.2024

Know what's weird?

Day by day

nothing seems to change,

but pretty soon,

everything is different.

Calvin and Hobbes, 1995
by Bill Watterson

Abstract - English

Cells release biomolecules that provide information about cell physiology and diseases. Detection of these molecules is difficult due to their complex release patterns and chemical diversity. Optical sensors made of single-wall carbon nanotubes (SWCNTs) offer high precision in imaging these dynamics. Depending on their chirality, they fluoresce in the near-infrared (NIR, $850 - 1700$ nm) biological transparency window and through a surface modification they detect target molecules by altering their fluorescence. Few scientists outside the 'SWCNT community' have yet exploited the potential of SWCNT sensors. This is due to the requirement of expensive NIR cameras and the lack of integration in materials/devices. In this Ph.D. thesis, an efficient phase separation process for the isolation of monochiral (6,4)-SWCNTs (880 nm emission) from mixed SWCNT samples is developed. It enables the detection of SWCNTs using high-resolution silicon (Si) cameras, which are broadly accessible to biologists and neuroscientists. A simulation also confirms that (6,4)-SWCNTs are ideal for biological imaging with Si cameras. Functionalization of (6,4)-SWCNTs with $(GT)_{10}$ single-stranded DNA (ssDNA) renders them sensitive to dopamine, an important neurotransmitter. These new SWCNT sensors exhibit 1.7x brighter fluorescence and 7.5x higher sensitivity compared to sensors based on mixed SWCNT samples. Fast (< 50 ms) and high-resolution imaging (> 50x more pixels) as well as imaging of cellular dopamine release with Si cameras are achieved. Furthermore, SWCNT coatings on glass are optimized. Homogeneous coatings are obtained by spin coating and varied in sensor density to maximize sensitivity. The resulting 'Smart Slides' can be sterilized with UV light and remain functional for at least 6 weeks, both in dry conditions or buffer. Finally, measurements of altered dopaminergic cell responses in response to various psychotropic substances are demonstrated. In summary, this work demonstrates SWCNT-based sensing to monitor cellular release events. Advances in (6,4)-SWCNT separation, sensitivity improvement, and integration into common laboratory instruments provide an easy accessible tool with high-resolution imaging capability for optical monitoring of biochemical processes in cells.

Abstract - Deutsch

Zellen setzen Biomoleküle frei, die Informationen über Zellphysiologie und Krankheiten liefern. Der Nachweis dieser Moleküle ist aufgrund ihrer komplexen Freisetzungsmuster und chemischen Vielfalt schwierig. Optische Sensoren aus einwandigen Kohlenstoff-nanoröhren (SWCNTs) bieten eine hohe Präzision zur Abbildung dieser Dynamik. Je nach Chiralität fluoreszieren sie im nahinfraroten (NIR, 850 – 1700 nm) biologischen Transparenzfenster und durch eine Oberflächenmodifikation erkennen sie Zielmoleküle, indem sie ihre Fluoreszenz verändern. Nur wenige Wissenschaftler außerhalb der 'SWCNT-Gemeinschaft' haben bisher das Potenzial von SWCNT-Sensoren genutzt. Dies ist bedingt durch die Erforderlichkeit teurer NIR-Kameras und die mangelnde Integration in Materialien/Geräte. In dieser Dissertation wird ein effizienter Separationsprozess zur Isolierung monochiraler (6,4)-SWCNTs (880 nm Emission) aus SWCNT-Mischproben entwickelt. Es ermöglicht den Nachweis von SWCNTs mit hochauflösenden Silizium (Si)-Kameras, die für Biologen und Neurowissenschaftler allgemein zugänglich sind. Eine Simulation bestätigt zudem, dass (6,4)-SWCNTs ideal für die biologische Bildgebung mit Si-Kameras sind. Die Funktionalisierung von (6,4)-SWCNTs mit $(GT)_{10}$-Einzelstrang DNA (ssDNA) macht sie empfindlich für Dopamin, einen wichtigen Neurotransmitter. Diese neuen SWCNT-Sensoren zeigen eine 1,7x hellere Fluoreszenz und 7,5x höhere Empfindlichkeit im Vergleich zu Sensoren, die auf SWCNT-Mischproben basieren. Es werden eine schnelle (< 50 ms) und hochauflösende Bildgebung (> 50x mehr Pixel) sowie die Bildgebung zellulärer Dopaminfreisetzung mit Si-Kameras erreicht. Außerdem werden SWCNT-Beschichtungen auf Glas optimiert. Es werden homogene Beschichtungen durch Spin Coating erzielt und in ihrer Sensordichte variiert, um die Sensitivität zu maximieren. Die resultierenden 'Smart Slides' können mit UV-Licht sterilisiert werden und bleiben mindestens 6 Wochen sowohl unter trockenen als auch Puffer-Bedingungen funktionsfähig. Schließlich werden Messungen veränderter dopaminerger Zellreaktionen als Reaktion auf verschiedene psychotrope Substanzen durchgeführt. Zusammenfassend demonstriert diese Arbeit die SWCNT-basierte Sensorik zur Überwachung zellulärer Freisetzungsereignisse. Fortschritte bei der (6,4)-SWCNT-Separation, der Verbesserung der Sensitivität und der Integration in gängige Laborgeräte bieten ein einfach zugängliches Werkzeug mit hochauflösender Bildgebungsfähigkeit zur optischen Beobachtung biochemischer Prozesse in Zellen.

Contents

List of Abbreviations

AA	ascorbic acid
AADC	aromatic amino acid decarboxylase
ADH	aldehyde dehydrogenase
APTES	(3-Aminopropyl)triethoxysilane
ATPE	aqueous two-phase extraction
Ca^{2+}	calcium ion
CaCl$_2$	calcium chloride
CL	chemiluminescence
Cl$^-$	chloride ion
CMOS	complementary metal–oxide–semiconductor
CNT	carbon nanotube
CT	computed tomography
DA	dopamine
DAT	dopamine transporter
DGU	density gradient ultracentrifugation
DOC	sodium deoxycholate
DOPAC	3,4-dihydroxy-phenylacetic acid
DOPAL	3,4-dihydroxy-phenylacetaldehyde
EP	epinephrine
EPA	Environmental Protection Agency
FRET	fluorescence resonance energy transfer
FSCV	fast-scan cyclic voltammetry
H$_2$O$_2$	hydrogen peroxide
HPLC	high-performance liquid chromatography
InGaAs	indium gallium arsenide
K$^+$	potassium ion
KCl	potassium chloride
L-DOPA	levodopa
LED	light-emitting diode
LNA	locked nucleic acid

MAO	monoamine oxidase
Na$^+$	sodium ion
NaBH$_4$	sodium borohydride
NaClO	sodium hypochlorite
NE	norepinephrine
NIR	near-infrared
OSHA	Occupational Safety and Health Administration
PBS	phosphate-buffered saline
PEG	polyethylene glycol
PET	positron emission tomography
SBR	signal-to-background ratio
SELEX	systematic evolution of ligands by exponential enrichment
SERS	surface-enhanced Raman spectroscopy
Si	silicon
SNR	signal-to-noise ratio
SPECT	single photon emission computed tomography
ssDNA	single-stranded DNA
SWCNT	single-wall carbon nanotube
TH	tyrosine hydroxylase
VMAT2	vesicular monoamine transporter
5-HT	5-hydroxytryptamine

List of Figures

List of Tables

Chapter 1

Introduction

1.1 Motivation

Neurological and mental health disorders impose a significant burden on global society, affecting hundreds of millions of people worldwide [WHO22]. The prevalence of these disorders is expected to rise even further due to population growth and aging [Fei20]. Despite their substantial impact, many of these disorders lack well-defined diagnostic protocols and available medications often only alleviate symptoms or proof ineffective, leaving many disorders incurable [Ou 19, Dal20, Gan23].

Neurotransmitters play a critical role in the proper functioning of the brain, and their dysfunction can thus lead to various neurological diseases, including Huntington's [Tye17], Parkinson's [Per16], Alzheimer's disease [Che21], as well as serious mental health diseases such as depression [Pan18] or schizophrenia [Ben15]. However, detecting neurotransmitters poses a challenge due to their presence in very low concentrations within the nervous system and other biological samples, along with a mix of numerous other biochemical molecules and minerals [Niy19]. In addition, their release processes in response to specific stimuli occur fast and highly localized, further complicating precise detection [Ou 19].

To date, several methods for neurotransmitter detection exist, ranging from *in vivo* techniques such as tomographic imaging [Gho22], microdialysis [Zes17], and electrochemical methods [Buc15], to *in vitro* optical methods based on fluorescence [Gub09], chemiluminescence (CL) [Ma 20], or colorimetry [Jaf17]. To achieve higher resolution, a combination of methods is often used, which already indicates that each detection method has its strengths and weaknesses [Niy19]. Consequently, in order to develop more effective treatment options for neurotransmitter-related disorders the development of more accurate detection methods in neuroscience are necessary.

In recent years, biosensors based on nanomaterials have seen vast improvements [Swa18]. They appear in various forms, such as nanoparticles, nanorods, nanowires, and nanotubes, and the material systems range from gold nanoparticles over transition metal dichalcogenides to carbon-based nanomaterials such as graphene, graphene quantum dots, and carbon nanotubes (CNTs) [Bau02, How14, Che17, Yoo20].

In particular, single-wall carbon nanotubes (SWCNTs) have emerged as versatile and promising building blocks for SWCNT-based sensing [Far17, Sch19]. These are 1D hollow tubes consisting of atomically thick graphene-like structures with typical diameters below one nanometer and lengths in the 1 µm range [Bau02, Yan20a]. Their nanoscale size combined with a large surface-to-volume ratio allows them to penetrate and interact with the biological environment. SWCNTs possess exceptional electrical and optical properties, making them suitable for use as both electrical and optical sensors [Sch19, Far17]. While electrical sensors are mainly suitable for easier on-chip integration, optical SWCNT sensors offer the advantage of non-contact and spatially resolved detection.

SWCNTs fluoresce in the near-infrared (NIR, 850 nm – 1700 nm), a region known as the tissue transparency window [O'C02]. Their fluorescence is stable and shows no blinking or bleaching, which sets them apart from many other fluorophores [Hon15]. SWCNTs can be functionalized with a wide range of typically amphiphilic molecules [Zhe03, Wan03, Fuj15, Ant17], allowing them to specifically detect various targets ranging from small molecules [Kru14, Har19, Won17], proteins [Bis16, Ehr21, Wil18a], sugars [Yum12, Zub22] and enzymes [Aga22] to bacteria [Nis20] and viruses [Met23]. At the single SWCNT level, they exhibit single molecule sensitivity [Jin10, Zha11, Kru17], making them versatile candidates for various biomedical sensor applications.

In 2014, a screening method known as corona phase molecular recognition identified specific single-stranded DNA (ssDNA) sequences for neurotransmitter detection [Kru14]. These sequences do not intrinsically have an affinity for neurotransmitters, but their adsorption to the SWCNT surface results in a conformational structure with specific binding sites. Since then, SWCNT-based sensors have demonstrated their remarkable ability for high-resolution detection of the essential neurotransmitters dopamine [Kru17, Bey19, Eli22] and serotonin [Din19] in cellular release processes. It has been shown that dopamine release can be detected with 100 ms time resolution while maintaining high spatial resolution in the nanomolar regime, exceeding 20,000 sensors per cell [Kru17]. The potential of SWCNT-based sensors for detecting dynamic biological processes with high spatiotemporal resolution is therefore unprecedented compared to current state-of-the-art methods [Eli22].

However, despite these impressive achievements, SWCNT-based sensing has remained relatively confined within the 'SWCNT community', most likely due to the requirement of specialized equipment (laser and NIR camera for fluorescence excitation and detection) and necessary sample preparation, which hinder easy experimentation [Yan21]. To fully exploit the power of this technology and expand its accessibility, it is necessary to simplify the experimental setup and facilitate integration with standard laboratory equipment.

1.2 Research Aim and Objectives

The overall research goal of this work is to enhance the accessibility and sensitivity of SWCNT sensing for the detection of dynamic processes such as neurotransmitter release.

One specific research objective to reach this goal is to increase the detection sensitivity of fluorescent SWCNT sensors using conventional microscopes. Standard microscope equipment relies on light-emitting diodes (LEDs), which are not as powerful as lasers, and Silicon (Si) cameras, which have a reduced quantum efficiency for detection in the NIR (max. 1000 nm). The aim is to find an optimal balance for the detection of fluorescence emission between the quantum efficiency of Si cameras and the advantages of NIR (e.g., reduced scattering and autofluorescence of biological samples). This investigation seeks to determine if the sensitivity achieved is sufficient for imaging dynamic biological processes, such as neurotransmitter release from cells.

Another research objective is to further increase the sensitivity of fluorescent SWCNT sensors for high-resolution detection of dynamic release processes by optimizing the sensor coating. Given their nanoscale dimensions, SWCNTs possess the ability to build highly functional dense surfaces, at which each sensor can effectively act as a 'pixel' to report the dynamic processes. To ensure sensitivity over a wide area, a uniform surface coating is essential. The goal is to explore the optimal coating density that enables highly sensitive measurements and assess its robustness for standard integration in materials.

1.3 Outline

The dissertation follows a cumulative structure, building on the manuscripts published as part of the doctoral thesis. The organization is as follows:

- Chapter 2 presents an overview of the scientific fundamentals of neurotransmitters and current approaches used for their detection. It provides a comprehensive understanding of SWCNTs from photophysical principles to SWCNT sensing (mech-

anisms) and measurement methods in the form of a review manuscript. The advantages and challenges of using optical SWCNT sensors for neurotransmitter detection are highlighted in detail.

- In Chapter 3 the most important results obtained during the doctoral thesis are presented. It comprises two research manuscripts that focus on different aspects of increasing the sensitivity and addressing the accessibility of SWCNT-based sensing for neurotransmitter detection. The manuscripts are embedded between an introduction that defines the underlying research questions that motivated each work, and a publication synopsis that summarizes the key findings and implications of each work.

- Chapter 4 follows with a more detailed discussion of the main findings with a comparison to the literature. It offers potential solutions to overcome existing challenges and suggests possible future research directions.

- Chapter 5 concludes with a summary of the major findings of the thesis.

Chapter 2

Neurotransmitters

This chapter provides an overview of the scientific fundamentals of neurotransmitters as well as current approaches used for their detection. The first section begins by discussing neurotransmitters as chemical messengers and their role in neural communication. The second section highlights the importance of detecting neurotransmitters for accurate diagnoses and effective treatment of associated disorders. The third section continues with a short review of the state-of-the-art in neurotransmitter detection techniques, highlighting the challenges and limitations associated with current methods. In the final section, the potential of SWCNTs as a novel approach for the optical detection of a variety of biomolecules, including neurotransmitters, is addressed.

2.1 Chemical Messengers of the Nervous System: An Introduction to Neurotransmitters

Since the discovery of the first known neurotransmitter - acetylcholine - by German pharmacologist Otto Loewi and British physiologist/biochemist Henry Dale in 1921, the understanding of neurotransmitters has expanded significantly [Loe21, Si 18]. To date, over 100 neurotransmitters have been identified in the nervous system, present in nanomolar concentrations alongside various other biochemical molecules and minerals [Niy19]. For example, dopamine has many analogues, and some potential interferents with a similar chemical structure (Figure 2.1), which makes selective detection challenging [Liu21]. These neurotransmitters can be categorized into different classes based on their chemical structure, including amino acids, monoamines, neuropeptides, purines, gasotransmitters, and others [Niy19].
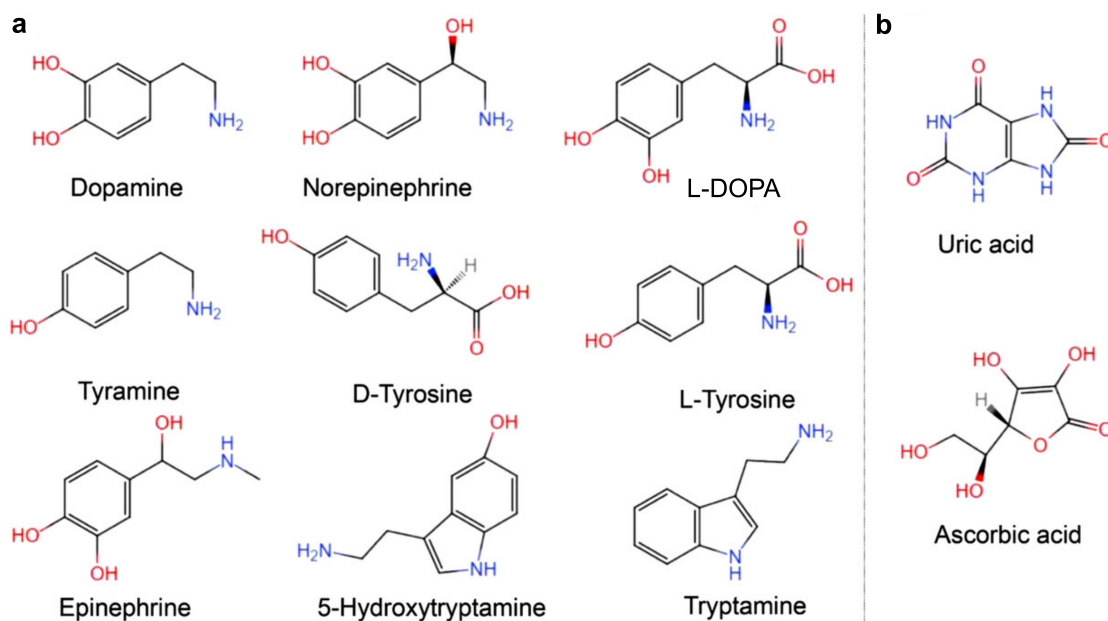
Figure 2.1: Molecular structures. The structures of a) dopamine and its analogs, and b) some interferents in biological samples. Adapted with permission from [Liu21]. Copyright © 2020, John Wiley & Sons, Ltd.

Neurotransmitters are endogenous electrochemical signaling molecules that act as messengers in the synaptic transmission process between neurons. They play a crucial role in the proper functioning of the brain and are closely linked to numerous bodily functions and cognitive behaviors, including motor control, sleep, perception, appetite, memory/learning, and emotions [Niy19, Tav19]. As such, they are a key factor in both physiological and psychological health. While all neurotransmitters contribute to the intricate interplay within the nervous system, a small group has emerged that is particularly involved in peripheral nervous system disorders [Niy19]. For instance, dopamine, which along with norepinephrine (noradrenaline) and epinephrine (adrenaline) is one of the catecholamines derived from the amino acid L-tyrosine, has been associated with these disorders. These catecholamines belong to the group of monoamine neurotransmitters, that are characterized by an amino group connected to an aromatic ring through a two-carbon chain. Dopaminergic neurons, localized in the *substantia nigra pars compacta* and the *ventral tegmental area*, play a central role in motivation and motor functions. However, there are other neurons that primarily contain other specific neurotransmitters, and are localized in different brain regions. They are all linked to specific brain functions. For example, norepinephrine and epinephrine can act as both neurotransmitters and stress hormones. In their role as neurotransmitters, they function in the autonomic nervous system, often referred to as the 'fight or flight' system, while serotonin, also known as 5-hydroxytryptamine (5-HT), is involved in a variety of behavioral functions, such as sleep, appetite, nausea, headaches or mood swings [Niy19].

A synapse consists of a presynaptic neuron and a postsynaptic neuron [Ou 19]. Neurons consist of a cell body and projections through which signals are supplied (dendrites) or transmitted (neurite, axon, Figure 2.2 a) [Hai18]. Axons are typically long and unbranched, sometimes surrounded by medullary sheaths interrupted by Ranvier nodes. These medullary sheaths are composed of lipid- and protein-rich myelin, which, together with the nodes, influence the speed of signal conduction [Hai18].
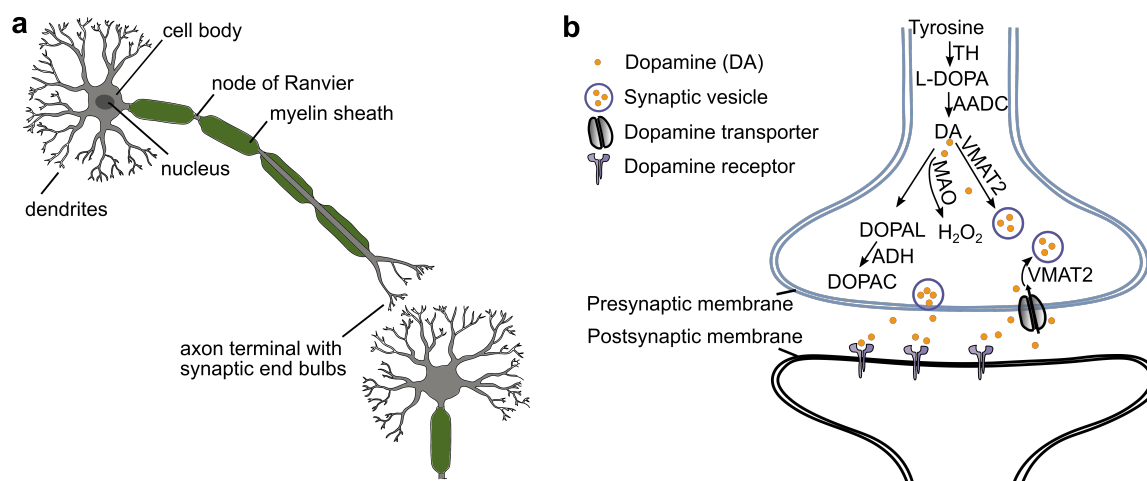
Figure 2.2: Neural communication. a) Structure of a neuron, b) dopamine metabolism in dopaminergic neurons. Adapted with permission from [Xu 22]. Copyright © 2022, Springer Nature.

The signal transduction process consists of several steps and is illustrated in the following on the basis of the signal transduction of dopamine (Figure 2.2 b).

1. **Synthesis and Storage:** For dopamine to function as an electrochemical signaling molecule in the synaptic transmission process between neurons, it must first be synthesized *via* presynaptic processes in dopaminergic neurons. The primary metabolic pathway involves a two-step synthesis in which tyrosine is first converted to levodopa (L-DOPA) by the enzyme tyrosine hydroxylase (TH), while L-DOPA is further converted to dopamine (DA) by aromatic amino acid decarboxylase (AADC) [Kle19, Xu 22]. Through vesicular monoamine transporters (VMAT2), the dopamine molecules are stored in synaptic vesicles. In norepinephrine and adrenergic neurons, dopamine can be further converted into norepinephrine and epinephrine [Kle19].

2. **Dopamine Release:** The release of neurotransmitters from the presynaptic cell into the synaptic cleft occurs through calcium ion (Ca^{2+})-initiated exocytosis [Hai18, Kle19, Dol20]. Here, Ca^{2+} channels are opened by an action potential in the neurite's cell membrane, allowing Ca^{2+} to enter and causing a change in membrane potential.

Ca^{2+} triggers fusion between the dopamine-containing vesicles and the presynaptic neuron membrane, leading to the release of dopamine into the synaptic cleft through exocytosis. In this process, dopamine acts by 'volume transfer', similar to other neuromodulators like serotonin, norepinephrine, and histamine. This means that dopamine molecules diffuse over a larger area, affecting multiple cells in a broader region.

3. **Receptor Binding:** Dopamine molecules diffuse across the synaptic cleft and bind to dopamine receptors on the postsynaptic cell or autoreceptors on the presynaptic cell [Kle19]. Dopamine receptors have several subtypes, including D1-like receptors (D1 and D5) and D2-like receptors (D2, D3, and D4) [Xu 22]. The binding of dopamine to its receptors can have different effects depending on the receptor subtype and the brain region involved. This process, known as neurotransmission or signal transmission, occurs within milliseconds. The remaining dopamine molecules in the synaptic cleft are taken back into the presynaptic cell with the help of dopamine transporters (DAT) and can be re-packaged into vesicles or degraded by enzymes such as monoamine oxidase (MAO). MAO cleaves dopamine to 3,4-dihydroxy-phenylacetaldehyde (DOPAL) and hydrogen peroxide (H_2O_2), while DOPAL is, in turn, degraded to 3,4-dihydroxy-phenylacetic acid (DOPAC) by the enzyme aldehyde dehydrogenase (ADH) [Xu 22].

4. **Equilibration:** The resting potential is restored by ion balance between the outer and inner cell membrane. Within this refractory period, a new stimulation is not possible [Pfa22].

For the described stimulation of neurons, a certain threshold value must be overcome. Prior to stimulation, the cell has a resting potential, where the cell interior is about $60 - 75$ mV more negative than the cell exterior [Pfa22]. This difference arises because the cell membrane is roughly a hundred times more permeable to potassium ions (K^+) than to sodium ions (Na^+), allowing K^+ to diffuse out of the cell while anions remain inside. In the cell experiments within this thesis, in both research manuscripts potassium chloride (KCl) is used to stimulate dopamine release from cells surrounded by phosphate-buffered saline (PBS) supplemented with calcium chloride ($CaCl_2$). The addition of KCl elevates the concentration of K^+ in the external medium, enabling K^+ to enter the neurons. Due to their size difference, chloride ions (Cl^-) have limited diffusion. As a result, the negative charge within the membrane increases, leading to cell depolarization. This, in turn, triggers the opening of voltage-gated Ca^{2+} channels in the membrane, facilitating the release of dopamine into the synaptic cleft, as described earlier. The addition of $CaCl_2$ to PBS ensures an adequate supply of Ca^{2+} for exocytosis.

2.2 Analyzing Neurotransmitters: A Critical Tool for Understanding, Diagnosing, and Treating Neurological and Mental Health Disorders

9

2.2 Analyzing Neurotransmitters: A Critical Tool for Understanding, Diagnosing, and Treating Neurological and Mental Health Disorders

Based on the previous Section 2.1, it becomes evident that neurotransmitters play a critical role in brain function. Consequently, disruption of these chemical messengers can lead to neurological disorders such as dementia, epilepsy, Parkinson's, Huntington's, and Alzheimer's disease, as well as severe mental health disorders like anxiety, depression, addiction, and schizophrenia [Niy19]. This affects numerous people in this world. The number of people suffering from neurological disorders has increased significantly in the last 30 years. Neurological disorders are the leading cause of disability and the second leading cause of death [Fei20]. The incidence of mental illness has increased by 13 % from 2007 to 2017, primarily due to demographic change, with every 5th child/adolescent worldwide also suffering from a mental illness [WHO22].

However, despite the substantial impact of these disorders, many of them lack well-defined diagnostic protocols and quantifiable chemical biomarkers [Ou 19]. This poses a major challenge to the accurate diagnosis and treatment of these disorders. Unlike physical diseases, for which measurable biomarkers often exist, the diagnosis of mental disorders relies heavily on subjective assessments and patient-reported symptoms, which can be influenced by a variety of factors. For example, antidepressants are ineffective in many patients [Hen17]. Moreover, while medications can help manage symptoms, most neurological disorders remain incurable, highlighting the need for more effective treatment options. For instance, even after more than 50 years, the gold standard treatment for Parkinson's disease, L-DOPA, has not been surpassed, despite it is known that movement disorders, initially well relieved by L-DOPA, return after some time [Pao19].

Consequently, addressing these challenges necessitates the development of precise detection methods in neuroscience. The availability of sensitive and selective measurement techniques capable of assessing the release of neurotransmitters from neurons in real time and quantifying the concentrations of neurotransmitters in various body fluids would have significant benefits. It would help to tackle these diseases at the root of their emergence, slow their progression, as well as develop effective drugs that ideally address the disease itself and not just the symptoms. In particular, simultaneous, specific detection of different compounds and neurotransmitters would be of enormous benefit in observing and understanding the complex metabolism and interplay of different neurotransmitters involved in these disorders. Thus, accurate detection of neurotransmitters is important for the following reasons:

1. **Research Advancements:** Detection of neurotransmitters in real-time can improve understanding of cellular communication and the underlying mechanisms of mental and neurological diseases [Leo19].

2. **Improved Drug Development:** Drug discovery involves the use of compounds that target different pathways of neurotransmitter metabolism to modulate their levels. Accurate neurotransmitter detection can help to identify specific neurotransmitter receptors or pathways and develop drugs that specifically target these areas [Hua19, Whi21].

3. **Early Intervention:** Monitoring neurotransmitter concentrations in urine or other body fluids allows early detection of imbalances before the onset of significant symptoms [Mar11].

4. **Personalized Treatment and Monitoring of Treatment Efficacy:** Personalized monitoring of neurotransmitter concentrations in urine or other body fluids can provide insight into the effectiveness of treatment interventions or whether dosage adjustments of medications or alternative strategies are needed to rebalance neurotransmitter concentrations over time [Yu 22].

2.3 State-of-the-Art and Current Restrictions in Neurotransmitter Detection

As previously mentioned in Section 2.1, neurotransmitters are present in the nervous system and other biological samples in very low concentrations, mixed with numerous other biochemical molecules and minerals. Moreover, neurotransmission occurs on short temporal (ms) and small spatial (nm) scales [Ou 19]. These factors present significant challenges in their detection, which is why neurotransmitter detection is the subject of ongoing research [Niy19]. Different detection methods exist, which are optimized for either *in vivo* or *in vitro* monitoring of neurotransmitters. Furthermore, these methods are typically tailored for specific neurotransmitters (monoamine and amino-acid groups and others such as acetylcholine), which have been identified as important candidates in neurological and mental health disorders [Niy19]. The objective of this section is to provide an overview of the commonly used detection methods that have already been established and to compare their strengths and weaknesses. In practice, however, two techniques are sometimes combined in order to obtain a better detection accuracy [Niy19].

Typical detection methods for neurotransmitters can be divided into five categories (Figure 2.3) and are as follows [Niy19]:
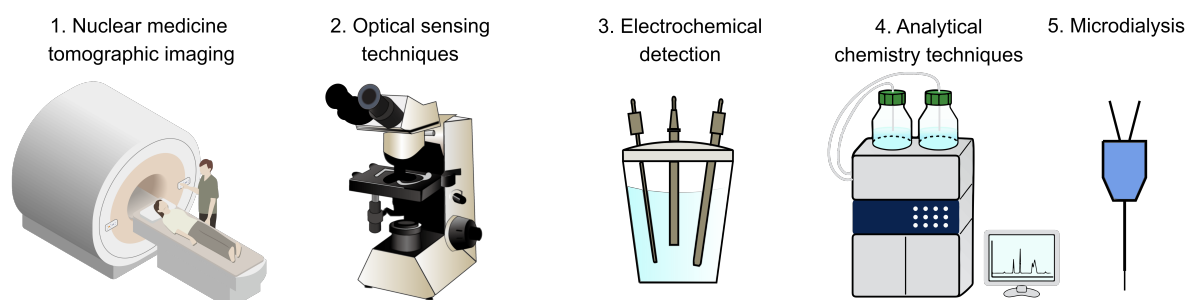
Figure 2.3: State-of-the-art in neurotransmitter detection. The images under no. 1, 2, and 4 taken from [Tog16]. Copyright © 2016, DBCLS TogoTV.

1. **Nuclear Medicine Tomographic Imaging**, including positron emission tomography (PET) and single photon emission computed tomography (SPECT)

2. **Optical Sensing**, including surface-enhanced Raman spectroscopy (SERS), fluorescence, CL, fiber optic biosensors, and colorimetry

3. **Electrochemical Detection**, including fast-scan cyclic voltammetry (FSCV) and amperometry

4. **Analytical Chemistry Techniques**, including high-performance liquid chromatography (HPLC) and mass spectrometry

5. **Microdialysis**

2.3.1 Nuclear Medicine Tomographic Imaging

Nuclear medical tomography, which includes both PET and SPECT, is a non-invasive *in vivo* neuroimaging technique [Niy19]. It indirectly measures brain activity and neurotransmitter release by employing short-lived radioactive tracers intravenously injected into the patient. The tracer competes with neurotransmitters for receptor binding, whose decay leads to the emission of radiation captured by a ring-shaped detector surrounding the patient. However, PET and SPECT differ in the radioactive product and detector setup [Niy19].

In PET, the decay of the isotope generates a positron (beta radiation) [Niy19]. The positron interacts with electrons in the body, leading to its annihilation and the production of two photons with an energy of 411 keV (gamma radiation), emitted in opposite directions. The detector captures these photons, and the position of annihilation is determined by measuring their time of flight before they reach the detector. The temporal and spatial distribution of these events is used to reconstruct a series of cross-sectional images with resolutions of about $4 - 6$ mm [Uni19] and $5 - 10$ s [Wan19].

Conversely, SPECT employs a tracer emitting single gamma photons, detected by a rotating gamma camera equipped with a collimator [Niy19]. Reconstruction algorithms create 3D images of the radiopharmaceutical's position, offering lower spatial resolution and two to three orders of magnitude lower sensitivity compared to PET. However, it is also less expensive due to its simpler setup [Niy19].

Both methods detect tracers indirectly rather than neurotransmitters directly [Niy19]. Despite their complexity and expertise demands, nuclear tomography is a standard method for *in vivo* neurotransmitter detection and is considered safe. One limitation is the complexity involved in developing new radioligands. In the clinical setting, PET is often combined with computed tomography (CT) to provide additional information on the appearance and shape of tissues and organs, improving spatial resolution [Uni19].

2.3.2 Optical Sensing Techniques

Various optical methods are employed for neurotransmitter detection, including SERS, where enhanced Raman scattering of molecules (up to 10^{11}, but very rare) is achieved through their interaction with metal nanostructures that support localized surface plasmon resonances [Sch14]. Molecules of interest can be adsorbed onto patterned metal surfaces made of noble metals such as gold/silver nanorods or particles. The amplification is based on two effects, electromagnetic amplification by surface plasmons and chemical amplification by the formation of charge transfer complexes. Due to its amplification capabilities, SERS offers high sensitivity (up to the femtomolar range) [Tan15]. However, detecting neurotransmitters in mixtures with interfering species can be challenging. This is because there can be an overlap of Raman signals and changes in bands due to intermolecular interactions, as illustrated in Figure 2.4 a) for a mixture of dopamine and ascorbic acid (AA) and their respective spectra alone [Fig20].

Fluorescence-based methods often combine a fluorescent nanomaterial with enzymes [Tan19], or aptamers [Ten22] for target recognition, which, for example, changes fluorescence through an electron transfer mechanism. Aptamers consist of ssDNA or RNA sequences that have high specificity for a particular target molecule due to their 3D folded shape [Dun17]. They are developed in iterative steps using a systematic evolution of ligands by exponential enrichment (SELEX) process in which a library of randomly generated aptamer sequences is synthesized and the sequences with the highest binding affinity to the target molecule are progressively separated and amplified. Their smaller size compared to antibodies allows them to detect smaller molecules. They can be produced synthetically and are cheaper and more stable than antibodies, making them a popular detection unit for biosensors.
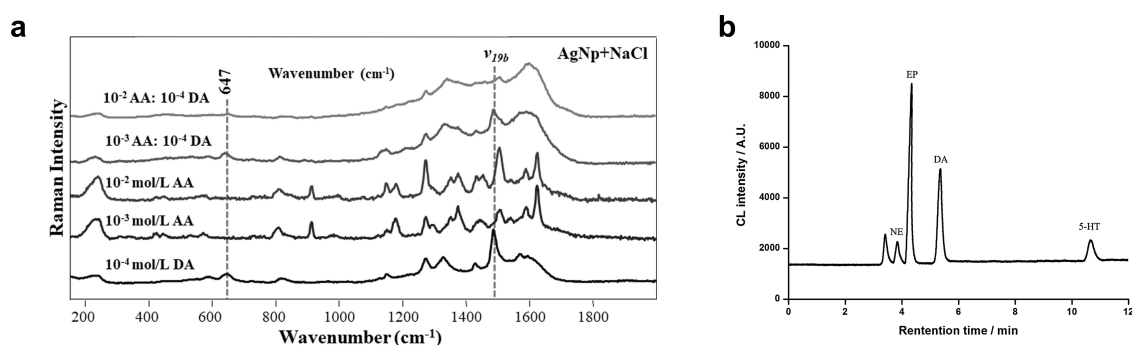
Figure 2.4: Experimental results for discrimination of different neurotransmitters/interfering molecules using optical methods. a) SERS based on silver nanoparticles for detection of dopamine (DA), ascorbic acid (AA), and their mixture. Adapted from [Fig20]. Copyright © 2020, with permission from Elsevier. b) HPLC in combination with chemiluminescence (CL) for detection of different neurotransmitters in a mixture (norepinephrine (NE), epinephrine (EP), DA, and serotonin (5-HT)). Reprinted with permission from [Wu 16]. Copyright © 2016, with permission from John Wiley & Sons, Ltd.

In addition, 'fluorescent false neurotransmitters' offer a unique approach as optical tracers, enabling the visualization of neurotransmitter release at individual presynaptic terminals [Gub09]. It is important to note, however, that this method is indirect and does not directly image the neurotransmitters themselves or their dynamics. Fluorescence resonance energy transfer (FRET) involves the radiation-free transfer of energy from an excited donor fluorophore to an acceptor fluorophore in close proximity. This leads to the quenching of the donor fluorophore, while the acceptor fluorophore emission intensity is increased. The quenchers are normally organic dyes, quantum dots, nanoparticles, or biological molecules with an absorption spectrum close to the emission spectrum of the donor [Niy19, Ten22]. They can specifically target certain molecules or biomolecules, making them highly selective.

CL methods are based on the emission of radiation due to a chemical reaction where a donor molecule in the excited state transfers its energy to an acceptor, which recombines under the emission of a photon. This is often combined with HPLC for the separation of biological samples [Rag00, Wu 16, Ma 20]. For example, Wu *et al.* achieved separation of the neurotransmitters norepinephrine (NE), epinephrine (EP), dopamine, and serotonin with HPLC within 11 min and the neurotransmitters showed an enhancing effect on the CL reaction between the Ag(III) complex $[Ag(HIO_6)_2]^{5-}$ and luminol in alkaline solution with a limit of detection in a low nanomolar regime (Figure 2.4 b [Wu 16]). Detection in combination with HPLC can thus be very specific, but is also more time-consuming and costly, while multiplexed detection without separation is challenging [Li 19a, Li 20].

Fiber optic biosensors exploit changes in refractive index [San21, Zha22] by, for example, an aptamer changing its conformation by binding, resulting in signal transduction [Zib16]. They can measure over longer distances or multiple measurements simultaneously.

Colorimetric methods, which are suitable for rapid, low-cost screening tests, rely on observable color changes caused by a color reaction between the target molecule and other compounds. They provide semi-quantitative information without additional equipment, since color and intensity may depend on the light conditions and the observer's perception, respectively [Jaf17, God18].

Overall, methods based on optical nanomaterials are particularly suitable for miniaturized assemblies. However, the biocompatibility and long-term effects of many nanomaterials used in optical methods remain largely unexplored or may even be toxic, rendering them unsuitable for *in vivo* applications at present [Niy19]. Furthermore, several fluorophores are not suitable for long-term imaging due to bleaching [Tyn12]. Additionally, autofluorescence and scattering from biological samples and tissues can impose limitations on the sensitivity of optical measurements [Hon17]. This is where NIR fluorescent SWCNTs exhibit advantages, which will be discussed in detail in the subsequent Section 2.4.

2.3.3 Electrochemical Detection

Neurotransmitter detection using electrochemical methods such as FSCV and amperometry is a powerful and widely used approach in the field of neuroscience, which relies on the measurement of electrical quantities such as current or potential with electrodes inserted into the samples [Niy19].

In FSCV, rapid voltage changes oxidize or reduce neurotransmitters located near the working electrode, revealing distinctive peak shapes and positions in current-voltage curves for identification. Distinguishing between different neurotransmitters and interfering molecules is a challenge, since the redox potential and thus the voltammograms are very similar. An enhanced distinction is achieved with optimized electrode materials like CNT yarn (Figure 2.5) [Sch13]. Amperometry, unlike FSCV, maintains a constant potential yielding superior temporal resolution for the dynamic detection of neurotransmitters that does not depend on the passage of a scan cycle as in FSCV. However, it does not provide current-voltage curves for the differentiation of neurotransmitters.

Overall, these methods offer high sensitivity and concentration measurements, but electrode fouling due to the adsorption of reactive species can occur which affects the sensitivity and thus results in necessary calibrations. Microelectrode arrays enhance spatial resolution for quantifying neurotransmitter release in cells [Che08, Whi21], although res-
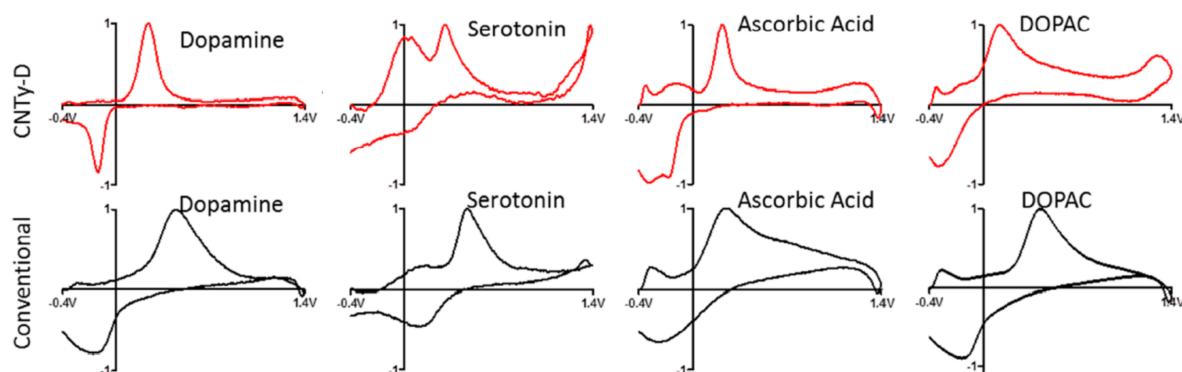
Figure 2.5: Experimental results for discrimination of different neurotransmitters/interfering molecules using electrochemical methods. Optimized electrochemical detection to discriminate different analytes by using CNT yarn compared to conventional carbon-fiber electrodes. Adapted with permission from [Sch13]. Copyright © 2013 American Chemical Society.

olution is limited by the number and size of electrodes. Despite optimized electrode materials, the key challenge is selectivity to interfering molecules such as ascorbic acid and discrimination of structurally similar neurotransmitters in mixtures.

2.3.4 Analytical Chemistry Techniques

HPLC separates molecules within a mixture by pumping them along with a mobile phase (a running medium) through a stationary phase composed of porous particles under high pressure [Niy19]. The molecules in the mixture interact differently with the stationary phase, causing them to separate based on the varying time spent in the column. The right choice of the mobile phase can improve separation [Wu 16]. HPLC is often coupled with techniques such as mass spectrometry, CL, or fluorescence for the simultaneous detection of multiple neurotransmitters, providing excellent selectivity and sensitivity. However, HPLC is not suitable for real-time detection, and the equipment can be costly.

2.3.5 Microdialysis

Microdialysis, an established *in vivo* technique for neurotransmitter detection, has been used for over 30 years [Niy19]. A probe consisting of a semipermeable membrane is inserted into the brain outside the synaptic cleft, which is continuously perfused with artificial cerebrospinal fluid. Molecules diffuse across the membrane driven by concentration gradients and are collected in vials or directed into an analytical system like HPLC and mass spec-

trometry for further analysis. The temporal resolution depends on offline (5 - 10 min) or online (less than 1 min) analysis [Liu14], offering an average value of molecules released into and removed from the extracellular space [Niy19]. The spatial resolution is thus low. It is an invasive technique that requires tissue healing after probe insertion [Liu14].

2.3.6 Comparative Analysis of All Methods

Table 2.1 contains a comparison of the various neurotransmitter detection methods discussed above to provide an overview with a qualitative ranking (green – good, yellow – medium, red – poor) for direct evaluation of their strengths and weaknesses. The values reported for individual parameters are intended as guidelines, were mostly obtained in buffer environments, implying that sensitivity values should be lower in more complex media such as serum, and are part of an individual publication/sub-method.

Overall, it is clear that there is no method yet that is strong in all areas, especially in the combination of high spatial and temporal resolution. Some of the given values in combination with the ranking may be surprising at first sight in direct comparison with other methods. For example, PET is ranked as 'green' with a spatial resolution of 4 – 6 mm, while FSCV and amperometry are ranked as 'yellow' with 220 µm and 30 µm, respectively. This is due to the overall resolution in terms of 'pixels'/area that contributes to imaging. While in PET the images are composed of the individual detected emissions of the radioactive tracers, which can be high in absolute numbers, the spatial resolution in electrochemical detection is limited by the number of electrodes. Resolution has already been increased here by the use of microelectrode arrays. For example, White *et al.* achieved a 32 x 32 array with a 30 µm electrode size by using complementary metal–oxide–semiconductor (CMOS) on-chip array technology [Whi21]. However, this still leaves the spatial resolution in terms of 1024 'pixels' behind those based on nanomaterials that can be densely coated onto surfaces. Furthermore, certain methods marked as 'yellow' in the table may have toxicity concerns for *in vivo* applications. And even though selectivity was ranked as 'green', distinguishing different neurotransmitters in complex mixtures with interfering molecules remains a challenge to be solved in general.

While tomographic imaging will remain a standard *in vivo* method for a long time, other methods based on fluorescence or CL have the potential to advance *in vitro* diagnostics with improved detection time, sensitivity, selectivity, and cost-effectiveness. The adoption of these novel methods as a standard for *in vivo* diagnostics may be limited (initially) due to material compatibility concerns, making it important to ensure their biocompatibility and rapid degradation in the body for non-invasive applications. This would provide a significant advantage over electrochemical methods and microdialysis, which are invasive

Table 2.1: Comparative analysis of all neurotransmitter detection methods. Ranking: green – good, yellow – medium, red – poor. The values given are from individual publications and can be seen as guide values. Sensitivity data refer to the detection of dopamine.

Method	Spatial Resolution	Temporal Resolution	Sensitivity	Selectivity	Equipment Costs	*In Vivo* Suitability
PET	🟢 4 – 6 mm [Uni19]	🟡 5 – 10 s [Wan19]	🟢 200 nM [Cec12]	🟢	🔴 1.8 Mio. € for PET/CT system [For08]	🟢
SPECT	🟡 8 mm [Her05]	🟡 10 s [Lin09]	🟡 a factor of $10^2 – 10^3$ lower than PET [Niy19]	🟢	🔴 460,000 € [For08]	🟢
SERS	🟢 10 µm [Plo21]	🟡 1 – 10 s [Lee21]	🟢 6 fM [Tan15]	🟢	🟡 >11,000 € [Emm21]	🟡
Fluorescence	🟢 130 nm – 400 nm*	🟢	🟡 20 pM [Wan15]	🟢	🟢	🟡
CL	🟡	🟡 seconds [Li 19a]	🟢 1.87 nM [Lan19]	🟢	🟢	🟡
Optical Fiber Sensing	🟡 <1 mm [Gru04]	🟢	🟢 0.1 pM [Hu 18]	🟢	🟢	🟢
Colorimetric	🟡	🟢	🟡 30 nM with analyzation device [Jaf17]	🟡	🟢	🔴
FSCV	🟡 220 µm [Che08]	🟢 100 ms [Put20]	🟢 10 nM [Put20]	🟡	🟡 8,400 € [Fos14]	🟡
Amperometry	🟡 30 µm [Whi21]	🟢 <1 ms [Put20]	🟢 25 nM [Put20]	🟡	🟢 1,700 € [Sci23]	🟡
Microdialysis + HPLC	🔴 mm region	🟡 <1 min [Liu14]	🟢	🟢	🔴 45,000 € HPLC [DeP21]	🟡

*For nanomaterials limited by the Rayleigh criterion as a function of the fluorescence wavelength.

techniques, as well as tomography methods, which are very expensive and bulky. However, there are additional challenges to overcome, such as achieving sufficient signal intensity in tissue and bleaching of fluorescent dyes. These factors should be taken into consideration when exploring the feasibility of such methods for neurotransmitter detection.

2.4 Single-Wall Carbon Nanotubes (SWCNTs) for Neurotransmitter Detection

In the previous Sections 2.2 and 2.3, it was highlighted that there is a significant need for new methods to detect neurotransmitters. In particular, biosensing approaches using nanomaterials have shown great potential. In this context, sensors based on fluorescent SWCNTs have emerged as promising candidates for the detection of various biomolecules, including neurotransmitters, based on their fluorescence in the NIR tissue transparency window. As the optimization of SWCNT sensors for the detection of rapid release processes such as neurotransmitters is the focus of this thesis, the current chapter aims to provide the scientific background of this technology.

Since the first synthesis of CNTs in 1991 by Iijima using arc-discharge evaporation [Iij91], the discovery of structure-dependent NIR fluorescence in 2002 [O'C02, Bac02], and the first observations of stepwise quenching of SWCNTs by single-molecule reactions in 2007 [Cog07], it has become clear that these building blocks offer multiple applications as optical sensors. A biosensor consists of a recognition unit that allows selective interaction with the analyte of interest and a transduction unit that converts a recognition event into a signal. In this context, SWCNTs serve as the transduction unit by altering their NIR fluorescence, and they can be functionalized with recognition units such as ssDNA sequences [Zhe03, Kru14, Nis20], aptamers [Din19, Nis20], or antibodies [Zha14, Wil18b].

SWCNT-based sensing has been a rapidly evolving research field for many years, and significant progress has been made. To provide an overview of the various developments in recent years and to capture the existing research gaps, challenges, and future trends, a comprehensive review manuscript was written under joint co-authorship at the beginning of the doctoral studies. This Review Manuscript, which is presented in the following Section 2.4.1, covers a wide range of topics and has gained considerable attention with a reasonably high number of citations (58 in 1.5 years). It begins with an introduction to the importance of biosensing in the biomedical context and discusses the unique features of SWCNT-based sensing (*Chapter 1*). The Review Manuscript then deals with a description of the structure and associated photophysical properties, surface functionalization approaches, and biocompatibility of SWCNTs (*Chapter 2*). It further explores chemical

design strategies and provides detailed insights into the development of sensors for various analyte classes, discussing parameters such as sensitivity, selectivity, spatiotemporal resolution, and reversibility of different sensor approaches. Underlying sensor mechanisms leading to fluorescence modulation, considerations of imaging and kinetics, their effects on temporal resolution, and various measurement variations like approaches to ratiometric and hyperspectral measurement are also covered (*Chapter 3* and the extensive *Tables* in the *Appendix*). Finally, the Review concludes with an outlook and perspectives (*Chapter 4*). Following the Review, the main points are summarized and discussed as a publication synopsis in Section 2.4.2.

Given the extensive scope of the Review Manuscript, the following chapters are particularly recommended to provide the scientific background within the context of this thesis:

- *1. Introduction*
- *2.1 SWCNT Structure and Photophysics*
- *2.2.1 Noncovalent Functionalization*
- *2.3 Biocompatibility*
- *3.2.2. Neurotransmitters* in combination with *Table 2* in the *Appendix*
- *3.3.2. Impact of Conformational Changes and Solvation*
- *3.4.1 Kinetics of Sensors and Impact of Spatiotemporal Resolution*
- *4. Outlook and Perspectives*

2.4.1 Biosensing with Fluorescent Carbon Nanotubes (Review Manuscript)

Graphical Abstract

Optical biosensors are important tools for basic research and non-invasive diagnostics. Carbon nanotubes are versatile near-infrared fluorescent and non-bleaching materials that can be chemically functionalized to detect a broad variety of biomolecules. This Review highlights chemical design strategies and provides a comprehensive overview of the recent developments in this dynamic field.
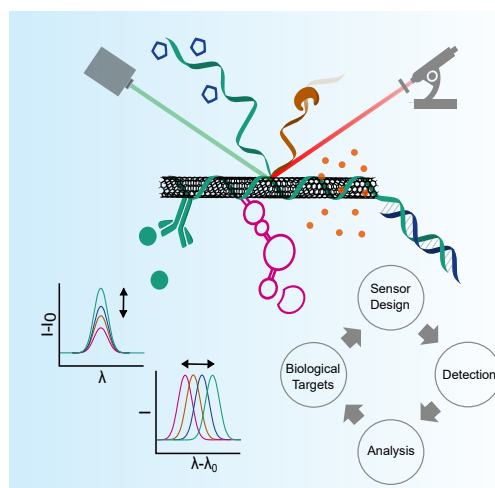
Reference

J. Ackermann[+], J. T. Metternich[+], S. Herbertz, S. Kruss: Biosensing with Fluorescent Carbon Nanotubes. *Angew. Chem. Int. Ed.* **2022**, 61(18):e202112372, doi.org/10.1002/anie.202112372

[+] These authors contributed equally to this work.

Copyright Statement

Contributions

S.H. wrote the initial draft of the *Introduction (1)*; J.T.M. wrote the initial draft of the sections on *Surface Functionalization (2 – 2.2)*, *Biocompatibility (2.3)* and *Mechanistic Insights (3.3)*. S.K. wrote the section on the *Development of Chemical Design Strategies (3.1)*. J.A. wrote the initial draft of the sections on *Biosensing of Target Analytes (3.2)* and *Considerations on Kinetics and Imaging (3.4)*. The *Conclusion and Outlook (4)* were jointly written by J.A. and J.T.M. Tables and figures in the respective sections were created by the respective authors. All authors contributed to the subsequent versions of the manuscript. S.K. coordinated the project and provided in-depth feedback on all sections. The table of content figure was prepared by J.T.M. The cover figure was designed by J.A. and J.T.M. and realized by J.T.M. All authors have given approval to the final version of the manuscript.

Biosensors

Biosensing with Fluorescent Carbon Nanotubes

Julia Ackermann+, Justus T. Metternich+, Svenja Herbertz, and Sebastian Kruss*

Angewandte
International Edition
Chemie
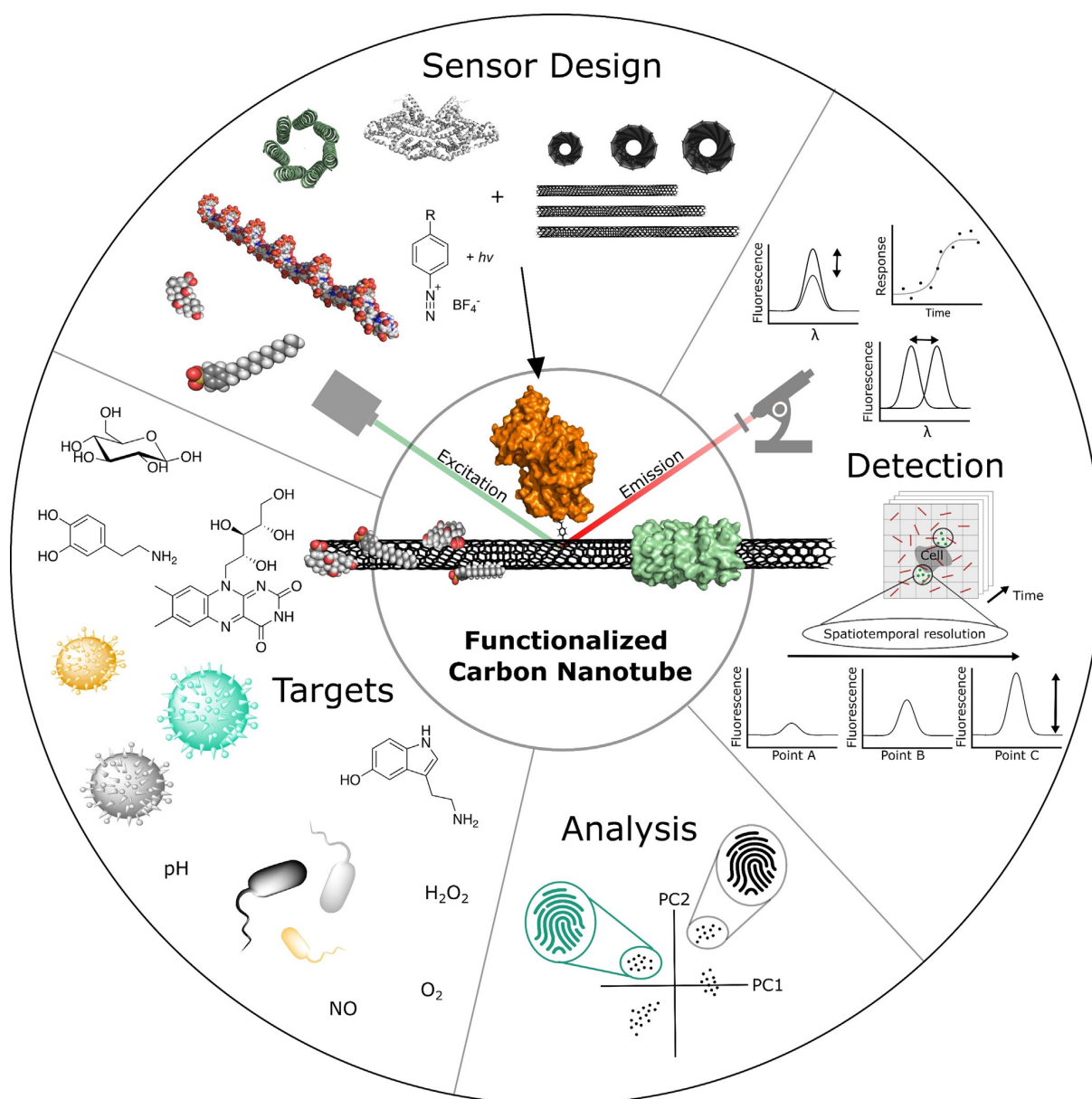
Biosensors are powerful tools for modern basic research and biomedical diagnostics. Their development requires substantial input from the chemical sciences. Sensors or probes with an optical readout, such as fluorescence, offer rapid, minimally invasive sensing of analytes with high spatial and temporal resolution. The near-infrared (NIR) region is beneficial because of the reduced background and scattering of biological samples (tissue transparency window) in this range. In this context, single-walled carbon nanotubes (SWCNTs) have emerged as versatile NIR fluorescent building blocks for biosensors. Here, we provide an overview of advances in SWCNT-based NIR fluorescent molecular sensors. We focus on chemical design strategies for diverse analytes and summarize insights into the photophysics and molecular recognition. Furthermore, different application areas are discussed—from chemical imaging of cellular systems and diagnostics to in vivo applications and perspectives for the future.

1. Introduction

Future challenges in medicine such as early disease detection, point-of-care diagnostics, and tailored therapies require novel methods of biosensing. Additionally, biosensors can provide insights into the complex dynamics of biological and chemical systems. Consequently, they are essential tools for both fundamental research and biomedicine. In particular, optical sensing approaches possess a great potential for contactless real-time readouts that are required in biomedical research, as well as industrial healthcare and agriculture applications.[1–3] During the last decade, the field of biosensors based on nanomaterials has seen vast improvements.[4,5] These materials include carbon-based nanomaterials such as graphene, graphene quantum dots, and carbon nanotubes (CNTs).[4,6–8] Here, single-walled carbon nanotubes (SWCNTs) are of particular interest. Their optoelectronic properties are sensitive to the surrounding environment, which makes them suitable for highly selective biosensing.[8–16] When dispersed in aqueous solutions, SWCNTs fluoresce without bleaching in the near-infrared region (NIR, around $\lambda = 870$–2400 nm).[17,18] This region of the electromagnetic spectrum is beneficial for detection and imaging as it offers an ultralow background and high penetration depths in biological tissues (tissue transparency window).[1,2,9,19–21] Fluorescence methods using common visible fluorophores often suffer from high scattering, absorption, and autofluorescence, which limits the penetration depth and signal to noise ratios.[1] Additionally, phototoxicity is increased by excitation of common fluorophores with visible (Vis) or ultraviolet (UV) light. Consequently, SWCNTs offer an advantage as they combine the biocompatibility and photostability required for optical sensing and imaging with emission in the NIR region.[14,22,23] Furthermore, the structural diversity of SWCNTs promises tunable emission wavelengths.[10,12] SWCNTs are highly sensitive to environmental changes, which is the basis for molecular recognition and was pioneered by optical sensors for glucose detection and DNA polymorphism.[24,25] Both covalent or noncovalent functionalization approaches play an essential role in tailoring molecular interactions close to the SWCNT surface.[10,14,17,23,26] By using such concepts, SWCNT-based biosensors for many highly important biomolecules have been developed.

More recently, this allowed chemical signaling to be mapped in a completely new manner, for example, release patterns of neurotransmitters from cells with high spatial and temporal resolution, which provides unique insights into fundamental biological questions.[27,28] Moreover, recent advances have been made in remote in vivo biosensing applications by the multimodal optical detection of several analytes. By combining multiple nanosensor elements and integrating them into functional arrays, analytes can be identified and distinguished on the basis of their characteristic image signatures.[29] Such a combination of optical nanosensors could pave the way for the next generation of fast and reliable in situ diagnostics. In addition, these approaches provide completely new opportunities for standoff process controlling, for example, fabrication of antibodies or monitoring in food and agriculture industries (smart plant sensors).[3,19,30–33]

In this Review we focus on optical biosensing with SWCNTs to give an update on this fast-evolving field. We evaluate in detail the specificity, sensitivity, spatial resolution, and biocompatibility of different SWCNT-based biosensors. This Review follows on from previous reviews,[2,10,14,23,34,35]

[*] J. T. Metternich,[+] Prof. Dr. S. Kruss
     Physical Chemistry, Ruhr-University Bochum
     Universitätsstrasse 150, 44801 Bochum (Germany)
     E-mail: Sebastian.Kruss@rub.de

     J. Ackermann,[+] J. T. Metternich,[+] Dr. S. Herbertz, Prof. Dr. S. Kruss
     Biomedical Nanosensors, Fraunhofer Institute for Microelectronic Circuits and Systems
     Finkenstrasse 61, 47057 Duisburg (Germany)

     J. Ackermann[+]
     Department EBS, University Duisburg-Essen
     Bismarckstrasse 81, 47057 Duisburg (Germany)

[+] These authors contributed equally to this work.

(iD) The ORCID identification number(s) for the author(s) of this article can be found under: https://doi.org/10.1002/anie.202112372.

Reviews

and discusses new chemical strategies developed in the last few years. SWCNTs can also serve as NIR labels. However, this is not discussed here and we refer to other excellent reviews.[1,2]

In Section 2, the basic structural properties and photophysics of SWCNTs as well as functionalization strategies are described. To conclude this section, we touch on the most important aspects of SWCNT biocompatibility. Section 3 contains an overview of general chemical recognition strategies. We provide a detailed and up-to-date summary of all currently accessible biomolecular target groups, including reactive oxygen species (ROS), neurotransmitters, proteins, antibodies, lipids, and sugars. This overview is complemented with mechanistic insights into how these sensors work. Finally, we provide a perspective on the field (Sections 3 and 4) and discuss possible future directions. This includes novel biological topics such as plants, advanced chemical tools (defects), methods for improved (hyperspectral) imaging, novel screening approaches, and multiplexing.

2. Functionalization Concepts

Since the report of their structure, CNTs have attracted wide interest within the scientific community and beyond. Their remarkable mechanical, electrical, and photophysical properties have paved the way for applications in the fields of advanced materials, microelectronics, biosensing, imaging, drug delivery, and many more.[8,36] Here, we will briefly describe the structure and photophysics of SWCNTs, followed by approaches to tailor their surface chemistry and biocompatibility.

2.1. SWCNT Structure and Photophysics

CNTs can be conceptualized as rolled-up cylinders of graphene.[37] Their properties are determined by the exact sp^2-hybridized carbon lattice as well as by the number of cylinders that are stacked into each other.[37] CNTs derived from a single graphene cylinder are called single-walled carbon nanotubes (SWCNTs),[38] whereas tubes consisting of multiple layers are called multiwalled carbon nanotubes (MWCNTs).[7] SWCNTs are commonly labeled using the chiral index (n,m), where n and m are integers that describe the carbon lattice structure (Figure 1a).[37,39] In this notation, the SWCNT is conceptually rolled up along the vector $c = na_1 + ma_2$ (a_1 and a_2 are the graphene lattice vectors). Consequently, the roll-up vector also determines the diameter. For SWCNTs, the reported diameters range from 0.4 nm to 10 nm.[8,40]

The roll-up vector affects the density and energy of the electronic states of SWCNTs and consequently the optoelectronic properties are directly related to chirality. As a result, for $n-m = 0$ (armchair configuration), SWCNTs are metallic, for $n-m = 3j$ ($j \in N\backslash\{0\}$), semimetallic, and semiconducting for all other (n,m) chiralities.[10] When SWCNTs are excited with light, an electron–hole pair (exciton) can be created and diffuses along the SWCNT axis.[41] For semiconducting SWCNTs,[18] the absorption of photons with energies corre-

Julia Ackermann received her M.Sc. in nano-engineering with a focus on nano-(opto)electronics at the university of Duisburg-Essen (Germany). Since 2020 she has been persuing her Ph.D. in the technology division of biomedical nanosensors of the Fraunhofer Institute for Microelectronic Circuits and Systems in Duisburg (Germany). Her work focuses on improving the overall selectivity of carbon nanotube based sensors by pattern recognition.

Svenja Herbertz received her Ph.D. in Physics at the Solid-State Physics Laboratory at the Heinrich-Heine-University in Düsseldorf (Germany) in 2019. During her years of study in Medical Physics she gained experience in the field of optical spectroscopy and use of semiconductor quantum dots for fluorescence labeling in biomedical applications. She is currently a researcher at the Fraunhofer Institute for Microelectronic Circuits and Systems in Duisburg (Germany) in the technology division of biomedical nanosensors.

Justus Metternich received his Bachelor's degree in biotechnology from the University of Applied Sciences Darmstadt. After a short stay at the Centro de Investigaciones Biológicas Margarita Salas in 2018, he continued with his Master's studies in chemistry at Uppsala University. Since November 2020, he has been part of the Attract group of Sebastian Kruss and pursuing his Ph.D. at Ruhr-University Bochum. His research focuses on the design of fluorescent carbon nanotube functionalizations for the detection of pathogens.

Sebastian Kruss received his Ph.D. in biophysical chemistry at Heidelberg University and the Max Planck Institute for Intelligent Systems (with Prof. Joachim Spatz). He then moved to the Massachusetts Institute of Technology (with Prof. Michael Strano), where he worked on carbon nanomaterials. After heading an independent research group at Göttingen University (2015–2020), he became professor of physical chemistry at Ruhr-Universität Bochum and Attract group leader at Fraunhofer IMS. His research focuses on novel materials, fluorescence spectroscopy and microscopy, biosensors, and cell biophysics.
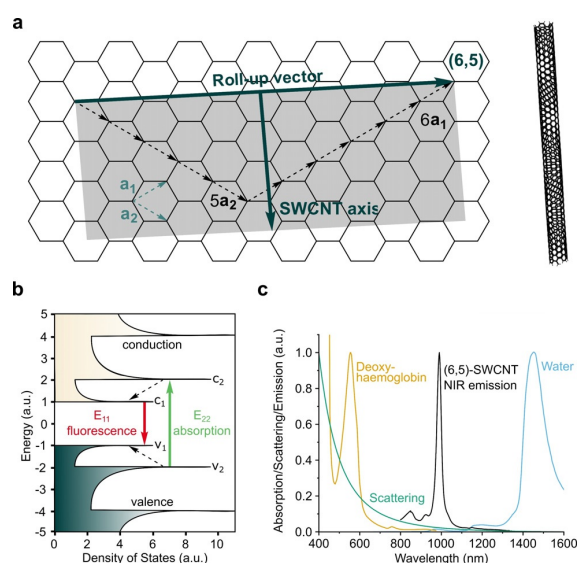
Figure 1. Structure and properties of single-walled carbon nanotubes (SWCNTs). a) The structure of SWCNTs can be rationalized by rolling a sheet of graphene along its roll-up vector, for example, $c = 6a_1 + 5a_2$. b) The band gap structure gives rise to fluorescence emission in the near-infrared (NIR) region. c) The E_{11} transition of SWCNTs[49] overlaps with the tissue transparency window, thus offering the advantage of reduced light absorption,[50] scattering (e.g. Rayleigh), and background fluorescence. Here, the emission spectrum of SWCNTs of (6,5)-chirality is shown, but the emission wavelength for other chiralities span the whole NIR region.

sponding to the visible spectrum of light typically leads to excitation to the second conducting band (Figure 1 b).[9,12]

Fast decay (femtosecond time scale) to the first conduction band followed by radiative recombination, then causes fluorescent emission in the NIR region (>870 nm),[18,42] a region that is particularly interesting for biological imaging (Figure 1 c). Quantum chemical considerations predict 4 singlet and 12 triplet excitonic states.[43,44] However, only the transition from the singlet state is optically allowed.[43,44] As the energy of this state is higher than the majority of other singlet and triplet states,[43,44] a variety of dark exciton decay pathways exist.[45] For (6,5)-SWCNTs, the size of an exciton is approximately 2 nm.[46] During their lifetimes they diffuse in the range of 100 nm along the SWCNT axis.[47,48] As all carbon atoms are located on the surface of the SWCNT, excitons are affected by the nanotube corona (i.e. the organic phase around the SWCNTs). Consequently, the photophysics of SWCNTs are highly influenced by chemical processes around their surfaces. This renders them ideal building blocks and transducers for chemical and biological sensing.

2.2. Surface Functionalization

The extended π-system makes SWCNTs hydrophobic and consequently they easily aggregate in solvents like water. Therefore, an important step in the preparation of SWCNT-based sensors is their functionalization to isolate, solubilize

and colloidally stabilize single SWCNTs. The functionalization also serves the purpose to a) interact (specifically) with other molecules and b) translate this interaction into a fluorescence change.

In the past years, different covalent and noncovalent modification strategies (Figure 2) have been developed. For a complete overview, we refer the reader to several excellent reviews and discuss only concepts relevant for sensing here.[26,51–53]

On a more abstract level, two strategies to assemble selective SWCNT-based sensors have been used, namely screening and rational design (Figures 3 and 5). The first one relies on permutations of the organic corona around the SWCNT (e.g. deoxyribonucleic acid (DNA) sequence) whereas the second one uses known recognition motifs (e.g. antibodies).

2.2.1. Noncovalent Functionalization

Noncovalent functionalization in aqueous solution is achieved by sonication with surfactants that form micellar structures around the SWCNT or through strong π-π inter-actions with the SWCNT surface (Figure 2). Prominent examples of surfactants are sodium dodecylsulfonate (SDS), sodium dodecylbenzenesulfonate (SDBS), sodium cholate (SC), sodium deoxycholate (DOC), lithium dodecyl sulfate, Triton X-100, and pluronic F127.[17,26] Additionally, functional surfactants—for example, with a perylene core together with a hydrophilic dendron—adsorb through π-π stacking and enable energy transfer.[54] In general, a surfactant concentration above the critical micelle concentration is required to stabilize dispersed SWCNTs in solution.[17] Thus, these approaches are limited with regards to experiments in complex (biological) systems.

In contrast, functionalization with larger biopolymers enables the formation of stable conjugates. Here, DNA and ribonucleic acid (RNA) form strong π-stacking interactions between the nucleobases and the SWCNT surface, thereby exposing their negatively charged phosphate backbones and solvating the SWCNT–nucleic acid complex (Figure 2).[22,55] As the conformation of the SWCNT–nucleic acid complex is affected by changes in the local ion concentration,[25,56,57] locked nucleic acids have been used as more rigid synthetic derivatives at higher salt concentrations.[57]

As alternative to nucleic acids,[25] certain polycyclic aromatic compounds carrying hydrophilic moieties have effectively solubilized SWCNTs. Similar to the π-stacking[51,58] of those compounds, the functionalization of SWCNTs with peptides,[59,60] proteins,[60,61] and other polymers[62,63] has been widely demonstrated (Figure 2). SWCNT-based biosensors have been rationally designed by the attachment of antibodies (or analogues; Figure 4 a,b,d)[64,65] and peptides (Figure 4 e)[66,67] to polymers or by the adsorption of boronic acids (Figure 4 c)[68] and aptamers (Figure 4 f) on SWCNTs.[27] In cases when sonication would destroy the structural integrity of the (bio-)polymers, primary suspension of the SWCNTs in a surfactant, followed by subsequent exchange to the polymer by dialysis has been employed.[24,60,69] An alternative to this rational design is the screening/search for

Reviews

Figure 2. Covalent and noncovalent (bio)functionalization of SWCNTs. Note that only covalent approaches that preserve the NIR fluorescence are included and that double bonds in the SWCNT carbon lattice are not shown for clarity.
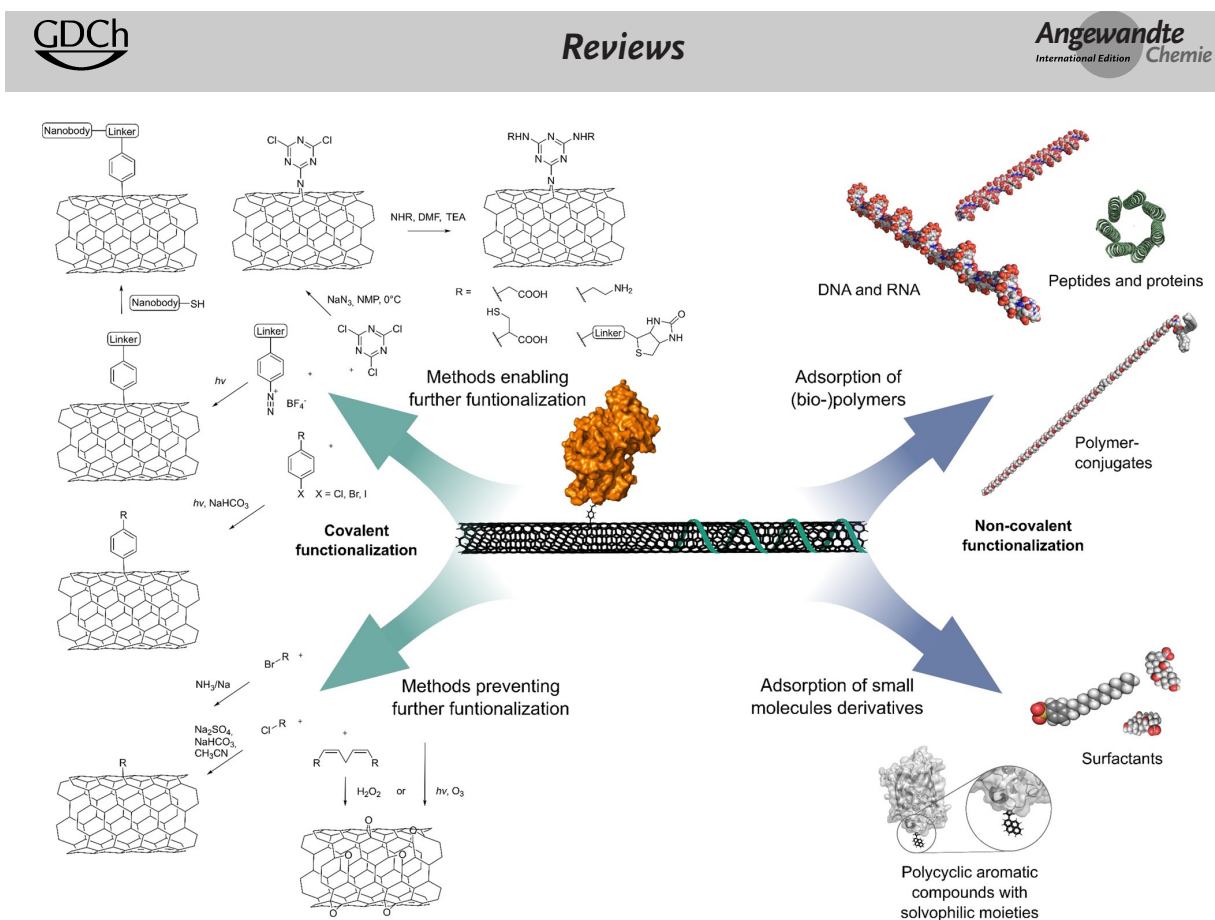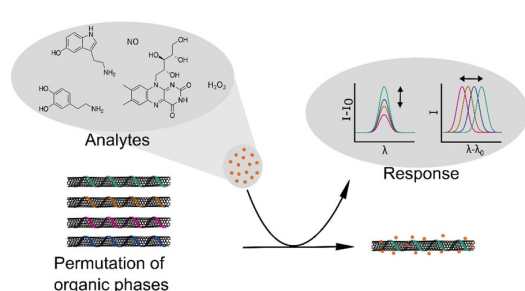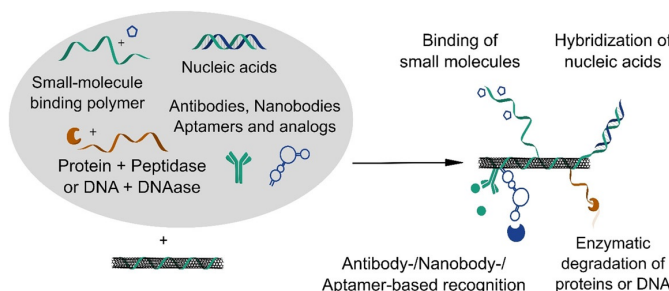
Figure 3. Chemical concepts for the design of SWCNT-based NIR fluorescent sensors. a) Screening of different organic phases identifies biopolymer/SWCNT conjugates with the desired analyte response. b) Rational concepts use known recognition motifs and assemble them on the SWCNT surface. Note that for both concepts colloidal stability in aqueous solution determines the usable reactions.

novel organic phases. This concept was named corona-phase molecular recognition (CoPhMoRe).[70] Here, a heteropolymer adsorbs onto the carbon nanotube surface and forms a new structure (corona) that serves as a molecular recognition site for interaction with an analyte. The biomolecules used are typically amphiphilic with hydrophobic domains that enable SWCNT adsorption and hydrophilic domains to be responsible for the entropic stabilization of the SWCNT in suspension and formation of a binding site for the analyte.[70]

It is important to note that the biomolecules/polymers alone do not necessarily need to interact selectively with the analyte of interest.[34,70] As such, the formation of these recognition sites cannot be predicted and are typically found by screening or high-throughput approaches. Prominent examples of CoPhMoRe screenings are the identification of SWCNT-based neurotransmitter sensors[15] as well as the adaptation of the CoPhMoRe concept to proteins[71] (Figure 5).
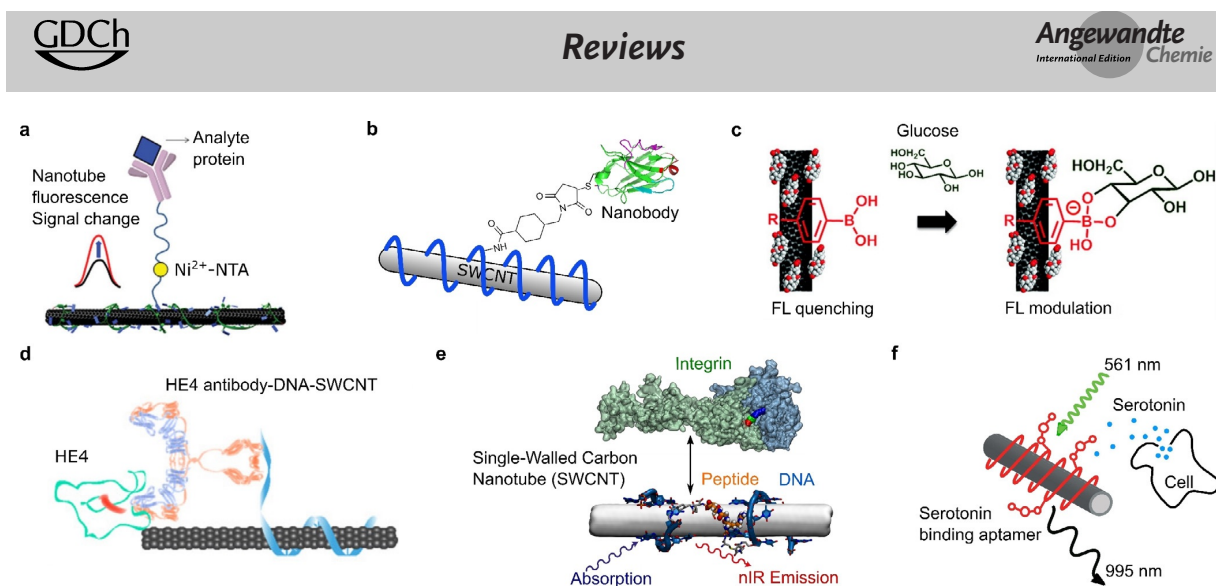
Figure 4. Rational molecular recognition concepts in SWCNT-based biosensors. a) Conjugation of His-tagged troponin antibodies to SWCNTs wrapped with Ni^{2+}-chelating chitosan for the detection of the cardiac biomarker troponin. Adapted from Ref. [64] with permission. Copyright 2014 John Wiley and Sons. b) Attachment of a nanobody against the green fluorescent protein (GFP) to DNA-functionalized SWCNTs to target GFP-tagged proteins in vivo. Adapted from Ref. [47] with permission. Copyright 2019 John Wiley and Sons. c) Adsorbed aryl boronic acids react with sugars, which modulates the SWCNT fluorescence. Adapted from Ref. [68] with permission. Copyright 2012 American Chemical Society. d) Antibody-DNA-SWCNT complex for the detection of the ovarian cancer biomarker human epididymis protein 4 (HE4). Adapted from Ref. [65] with permission. e) Short peptides conjugated to DNA adsorbed on SWCNTs enable the binding of cell adhesion receptors. Adapted from Ref. [66] with permission. Copyright 2018 American Chemical Society. f) Serotonin-binding aptamers on SWCNTs enable the detection of serotonin release from cells. Adapted from Ref. [27] with permission. Copyright 2019 American Chemical Society.
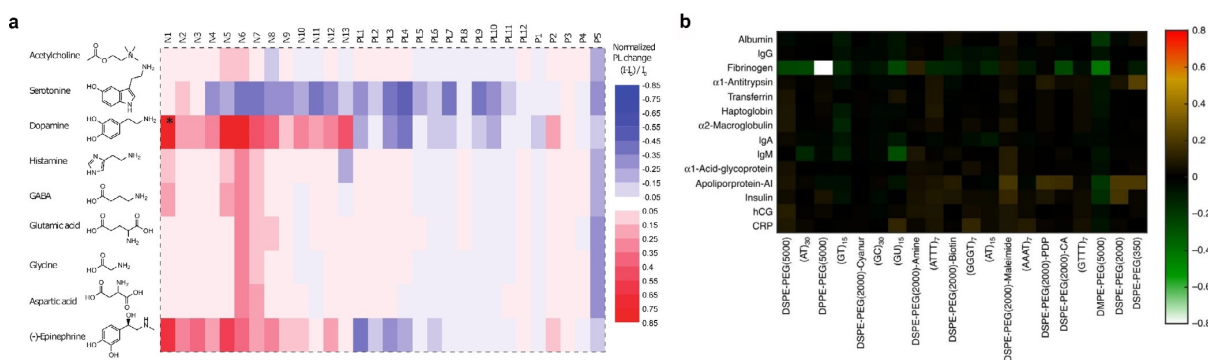
Figure 5. Screening approaches based on corona phase molecular recognition (CoPhMoRe). a) The screening of SWCNT–polymer conjugates (*x* axis, N1–N13: nucleic acids; PL1–PL12: phospholipids; P1–P5: amphiphilic polymers) identifies SWCNT-based sensor candidates with a strong fluorescence in response to different neurotransmitters (*y* axis). Reprinted from Ref. [15] with permission. Copyright 2014 American Chemical Society. b) CoPhMoRe screening procedure of SWCNT–polymer conjugates (*x* axis) for the detection of proteins (*y* axis). Reprinted from Ref. [71] with permission.

2.2.2. Covalent Functionalization

The covalent functionalization of SWCNTs introduces new σ-bonds into the sp^2-hybridized SWCNT structure. In contrast to noncovalent functionalization methods, the conjugates promise higher stability.[10] However, the uncontrolled introduction of covalent sp^3 bonds (defects) destroys the electronic and optical properties and diminishes the intrinsic NIR fluorescence.[10] One strategy to overcome this problem preserves the sp^2-hybridized structure of SWCNTs during their covalent functionalization.[72] In contrast, a certain number of sp^3 defects give rise to novel properties, such as

red-shifted emission features that are capable of single photon emission.[53,73–75] Therefore, these defects are also called quantum defects or quantum color centers.[53]

These sp^3 defects have, at low densities, been shown to increase the fluorescence of SWCNTs.[53,74,76] Incorporation of these defects at low concentrations leads to the trapping of excitons and an alternative decay pathway (E_{11}^*) that results in a new red-shifted fluorescence feature (Figure 6a).[74,76] A wide range of sp^3 defects has been incorporated into SWCNTs to increase the fluorescent properties by using diazo ether, aryl halide, (bis-)diazonium, as well as Billup-Birch and alkyl halide reductions.[53] Additionally, O-doping approaches using
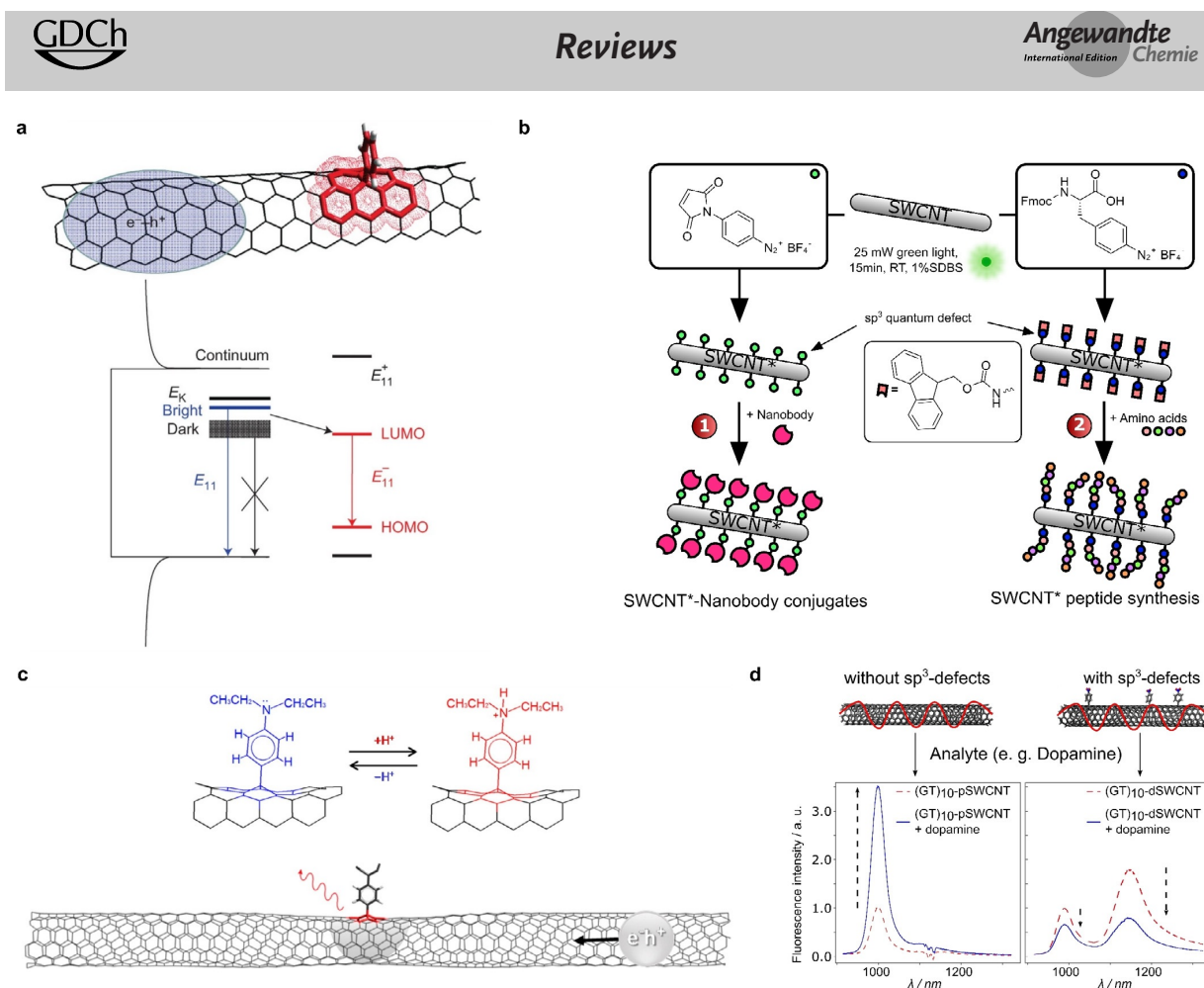
Figure 6. Covalent functionalization of SWCNTs. a) The controlled introduction of sp³ defects creates an alternative decay pathway that brightens dark excitons without destroying the normal E_{11} NIR fluorescence. Reprinted from Ref. [74] with permission. Copyright 2013 Nature Publishing Group. b) Introduction of certain aryl defects as generic handles to functionalize SWCNTs with biomolecules. Adapted from Ref. [79] with permission. c) The protonation of covalently attached aminobenzene groups modifies the energy level of the sp³ defect state and changes the photoluminescence. Adapted from Ref. [85] with permission. Copyright 2015 American Chemical Society. d) Quantum defects change the fluorescence response of DNA-functionalized SWCNTs to the important biomolecule and neurotransmitter dopamine. $(GT)_{10}$-functionalized pristine SWCNTs (pSWCNT) increase their fluorescence in response to dopamine. The same SWCNTs with sp³ defects (dSWCNT) decrease their fluorescence, which shows the strong impact of defects on the sensing mechanism. Adapted from Ref. [87] with permission. Copyright 2021 American Chemical Society.

ozone and light,[75] sodium hypochlorite,[77] as well as hydroperoxides of polyunsaturated fatty acids[78] have been reported to increase the red-shifted emission of SWCNTs at low defect concentrations (Figure 2).

Covalent functionalization approaches also offer opportunities beyond changes in the photophysics. Defects that can be further functionalized enable the conjugation of important biomolecules. Recently, maleimide defects were used to link proteins such as nanobodies and phenylalanine defects to grow peptides directly on the SWCNT surface, similar to a solid-phase peptide synthesis[79] (Figure 6b). The covalent conjugation approach with dichlorotriazine allows subsequent nucleophilic aromatic substitution of the chlorides using amine-containing linkers[72,80] (Figure 2). Another example are defects that are already able to interact with other biomolecules, such as phenyl boronic acids that interact

with saccharides, and change the E_{11}^* (S_{11}^*) and E_{11} (S_{11}) emissions.[81]

It is interesting to note that the resulting bathochromic shifts (E_{11}^*) caused by sp³ defects can be tuned using the electronic properties of the incorporated moieties.[74,76] That said, defects provide a rich chemical playground and interested readers are referred to several excellent reviews.[53,82] With regards to SWCNTs with aryl defects, electron-withdrawing substituents generally introduce red-shifts to the E_{11}^* emission that can be correlated to the Hammet constants (σ) of the substituents.[74,83] Furthermore, the E_{11}^* red-shift shows a $1/d^2$ dependence on the diameter (d) of the SWCNT.[74] The protonation of diethylamino-substituted aryl defects ($\sigma_{HR2N+} = +0.82$ vs. $\sigma_{R2N} = -0.66$)[84] is a good example of the effect caused by the inductive effects of substituents. Furthermore, this type of defects allows a precise sensing of

the pH value down to 0.2 units through the changes in the E_{11}^* emission (Figure 6c).[85] Apart from the introduction of defects for sensing, the covalent functionalization of SWCNTs can be used for site assembly using different (bio-)polymers and linkers.[86]

Defects also change the exciton decay pathways and, therefore, affect the photophysics and sensing mechanism of SWCNT-based sensors. This approach was recently used to perturb the sensing and elucidate the rate constants that are involved[87] (Figure 6d).

In this study it was also found that a small number of defects can inverse the sensing response from a strong increase to a strong decrease in fluorescence.

2.3. SWCNT Biocompatibility

Biocompatibility is highly important for materials in direct contact to biological matter. Even though many biocompatibility studies exist, the conclusions are difficult to compare.[88] The main reason is that different materials, surface reactions, and biological systems are compared, which leads to a noncoherent view. Moreover, the SWCNT field has evolved dramatically over the years and well-defined chirality pure SWCNTs-based sensors with ultrahigh purity are available today, whereas older studies used less well-defined materials.[49] In addition, the application itself determines the perspective.[89] As a research tool, SWCNTs should not affect the biological system in such a way that the results are biased. For long-term in vivo studies and applications in humans, the fate of SWCNTs in biological systems is highly relevant for their biocompatibility. SWCNTs have been shown to be susceptible to degradation by oxidative processes introduced by neutrophils[90] and macrophages.[91] Furthermore, the functionalization changes the surface properties of the nanotubes and, thus, ultimately the way SWCNTs interact with the molecules in a (biological) system.[92]

For example, endocytosis experiments have shown that the DNA sequence length plays an important role in endocytosis and retention time scales of DNA-functionalized SWCNTs within mammalian cells.[93] Additionally, experiments using a combination of NIR fluorescence spectroscopy and resonance Raman scattering have been used to analyze the fate of DNA-functionalized SWCNTs through the endosomal process.[94] Based on the experimental findings, the authors propose that DNA-SWCNTs enter the cell, where they are transported into early endosomes. Maturation of the endosome begins with a decrease in the luminal pH value, which is followed by a series of physicochemical processes that transform the endosome into a lysosome, where the SWCNTs finally aggregate.[94]

As correct functionalization has been shown to alleviate the pathogenicity of SWCNTs,[95] stable functionalization is one possible way to safeguard the future design of SWCNT-based sensors in environments where long-term stability is of the highest importance. Adequately functionalized SWCNTs have been shown to possess excellent biocompatible properties. A good example is the recently published long-term biodistribution and compatibility assessment of DNA-encapsulated SWCNTs after intravenous administration in mice.[96] After an initial increase in the SWCNT fluorescence in the liver, the SWCNT fluorescence decreased rapidly over the course of 14 days.[96] The same trend is also seen in the long-term SWCNT biodistribution in different organs. By using hyperspectral microscopy, low levels of SWCNTs were detected in murine hearts, lungs, livers, kidney, and spleen tissues one month after injection. Assessment of these tissues after three and five months showed no SWCNT fluorescence in lung tissue, or in heart and lung tissues.[96] Moreover, no abnormalities were found in chronically exposed tissues after hematoxylin and eosin (H&E) staining at all observed time points and the assessed biomarkers showed negligible changes up to four months, and minor changes after five months.[96]

The aforementioned studies suggest remarkable opportunities for SWCNTs in biomedical applications. As a consequence of the interplay between different materials, surface reactions, and biological systems it becomes evident that biofunctionalized SWCNTs represent a class of different materials. As for all new materials, the biocompatibility should be evaluated for every type of chirality, purity, functionalization, and route of administration.[96] The scientific community is well-aware of this problem and it has been pointed out that an assessment of these parameters in the context of biocompatibility depends on the context of the experiment, timescale, and the application of the nanomaterial.[88,97] As a consequence, it is fundamentally important to place experimental data in the right context.[88]

An important requirement for a biocompatible design of SWCNT-based sensors is an in-depth understanding of the composition of the protein corona in biological media. In this regard, a recent study characterized the enrichment of certain proteins in the SWCNT corona.[98]

In the future, long-term studies comparing the biocompatibility of different SWCNT subclasses (purity, chirality, surface chemistry) would be desirable to safeguard the development of biocompatible sensors. A foundation for the standardization of protocols could be the MIRIBEL (Minimum Information Reporting in Bio-Nano Experimental Literature) reporting standard.[99] As the functionalization of the SWCNT plays a critical role in the biocompatibility of SWCNT-based sensors, the design of stable SWCNT functionalizations needs to be carefully ensured for long-term applications. In particular, the recent advances in covalent functionalization strategies might, therefore, offer interesting starting points for future development.[79]

3. SWCNT-Based Sensors

3.1. Development of Chemical Design Strategies

The discovery of band gap fluorescence from SWCNTs and their structure-dependent NIR emission wavelength marks the starting point for SWCNT-based sensors.[12,18] Given the high surface to volume ratio of SWCNTs, it was quickly anticipated that SWCNT fluorescence would be sensitive to the chemical environment.[24] The first generation

of sensors targeted mainly smaller molecules including protons and reactive oxygen/nitrogen species (ROS/RNS). In these cases, the fluorescence changes were most likely caused by direct quenching. At the same time, it was discovered that different surface reactions with biopolymers lead to molecular interactions that are surprisingly specific even without using a standard approach with antibodies. This idea was conceptualized as corona-phase molecular recognition (CoPhMoRe).[70] During the last few years, great progress has been made in the chemical design of sensors for both biomedical and environmental applications. In the next sections we will give an overview on different sensing strategies, organized according to the molecular target. Here, sensing of the target molecule has partly environmental as well as biomedical applications. We focus on the advances in the last few years but also report previous studies (see Tables 1–9 in the Appendix).

3.2. Biosensing of Target Analytes

The ongoing advances in the development of recognition strategies have led to powerful biosensors based on SWCNTs. Various targets can be detected with high selectivity and sensitivity by combining a recognition unit with the SWCNTs. Recognition strategies (Figure 3) can mainly be categorized into a screening (Figure 5) and a rational approach (Figure 4). The first approach is in principle achieved with a library of synthetic organic phases (coronas) consisting of different amphiphilic polymers wrapped around SWCNTs and screened against a panel of various analytes to find a selective interaction.[15,70,71,100,101] The latter approach is mostly applied for the detection of larger molecules such as proteins[65,102–106] or sugars[11,107,108] by conjugating a known binding partner of the target analyte to the SWCNT surface. Several approaches are based on the use of SWCNTs wrapped by single-stranded DNA (ssDNA), whereby different lengths of the $(GT)_x$ sequence is probably the most used sequence up to now.

It has shown its versatility in the detection of divalent ions,[25,109] genotoxins,[110] NO,[20] H_2O_2,[20,32,110–112] riboflavin,[49,113,114] doxorubicin,[115] β-carotene,[116] endolysosomal lipids,[117] arsenite,[33] and neurotransmitters, especially dopamine.[15,49,63,80,87,118–121] This section highlights the major advances from the last few years for different categories of biomolecules. A detailed overview of most of the known fluorescent SWCNT-based sensors, subdivided into the target categories, can be found in Tables 1–9 in the Appendix.

3.2.1. ROS/RNS

ROS/RNS are important signaling molecules in many organisms,[122] but their detection is challenging because they diffuse fast and have short lifetimes due to their high reactivity with O_2 and other molecules.[10,123] Since the finding of the first NO sensor based on SWCNTs[124] the performance of SWCNT-based ROS sensors has grown from the first selective detection of NO and H_2O_2 at the single molecule level[13,125,126] and first in vivo applications[127] to a new approach to study NO generation and spatiotemporal imag-

ing of intracellular NO signaling.[128] Recently, a mathematical model that calculated the NO concentration based on the change in the SWCNT fluorescence was derived.[129] This was previously not possible due to a nonlinear fluorescence quenching rate in response to NO.[13]

ROS play a mediating role in the cell-to-cell communication of plants to activate defence mechanisms,[122] whereby it has become clear that H_2O_2 is the primary mediator that responds to different stresses in plants.[130] This has led to novel SWCNT sensor approaches to study ROS within plants.[19,20,31,32] Wu et al. demonstrated remote H_2O_2 monitoring of plant health with sensitivity in the plant physiological range by using fluorescent SWCNT-based sensors.[31] Their rational approach was based on a DNA aptamer that specifically binds to the porphyrin hemin (HeAptDNA-SWCNT). Hemin binds ferric ions, which undergo a Fenton-like reaction with H_2O_2 to produce hydroxyl radicals (Figure 7a) that directly quench the SWCNT fluorescence. For spatiotemporal in vivo monitoring, SWCNTs were embedded in leaves of plants and the plants exposed to different stresses such as UV-B, high light intensities, and a pathogen-associated peptide (flg22; Figure 7b). The decrease in fluorescence reported remotely different aspects of the stress. These differences in fluorescence intensity quenching offer the possibility to interpret stress patterns in plants.

Similar to this approach, Lew et al. developed a platform for H_2O_2 detection in leaves of different plant species.[32] This sensor platform used a ratiometric approach, with $(GT)_{15}$-SWCNTs (G-SWNT) that respond to H_2O_2 by quenching, possibly as a result of a charge-transfer phenomenon, and $(AT)_{15}$-(6,5)-SWCNTs (A-SWNT) as an invariant reference (Figure 7c). They infiltrated both G-SWNT and A-SWNT into spinach leaves and monitored the H_2O_2 signal with a standoff detection platform in real time (Figure 7d). In the presence of different stresses, for example, tissue wounding, distinct waveform characteristics were observed (Figure 7e), whereby the wave speeds in different plant species post-wounding differed in the range of 0.44 to 3.10 $cm\,min^{-1}$.

In the same manner, Lew et al. developed a SWCNT-based sensor system for the specific detection of arsenite in plants to monitor the uptake of the toxic heavy-metal pollutant arsenic by using a self-powered microfluidic system in real time.[33] For this purpose, they infiltrated the sensors and the invariant reference into leaves of spinach, rice plants, and hyperaccumulating fern, which is able to preconcentrate and extract arsenic from soil (Figure 8a). The intensity of the sensors increased steadily over several days, with the sensor response of the hyperaccumulating plant being significantly higher than those of the rice and spinach plants (Figure 8b). Based on a kinetic model, the arsenite concentration in the leaf and the limit of detection (LOD) were calculated to be 4.7 nM and 1.6 nM as a function of the root fresh weight and uptake solution volume after 7 and 14 days (Figure 8c). These examples show that SWCNT-based H_2O_2 sensors are able to report plant stress on a microscopic and macroscopic level with potential applications in smart agriculture.

Another macroscopic situation in which H_2O_2 plays an important role is wound healing. Safaee et al. developed
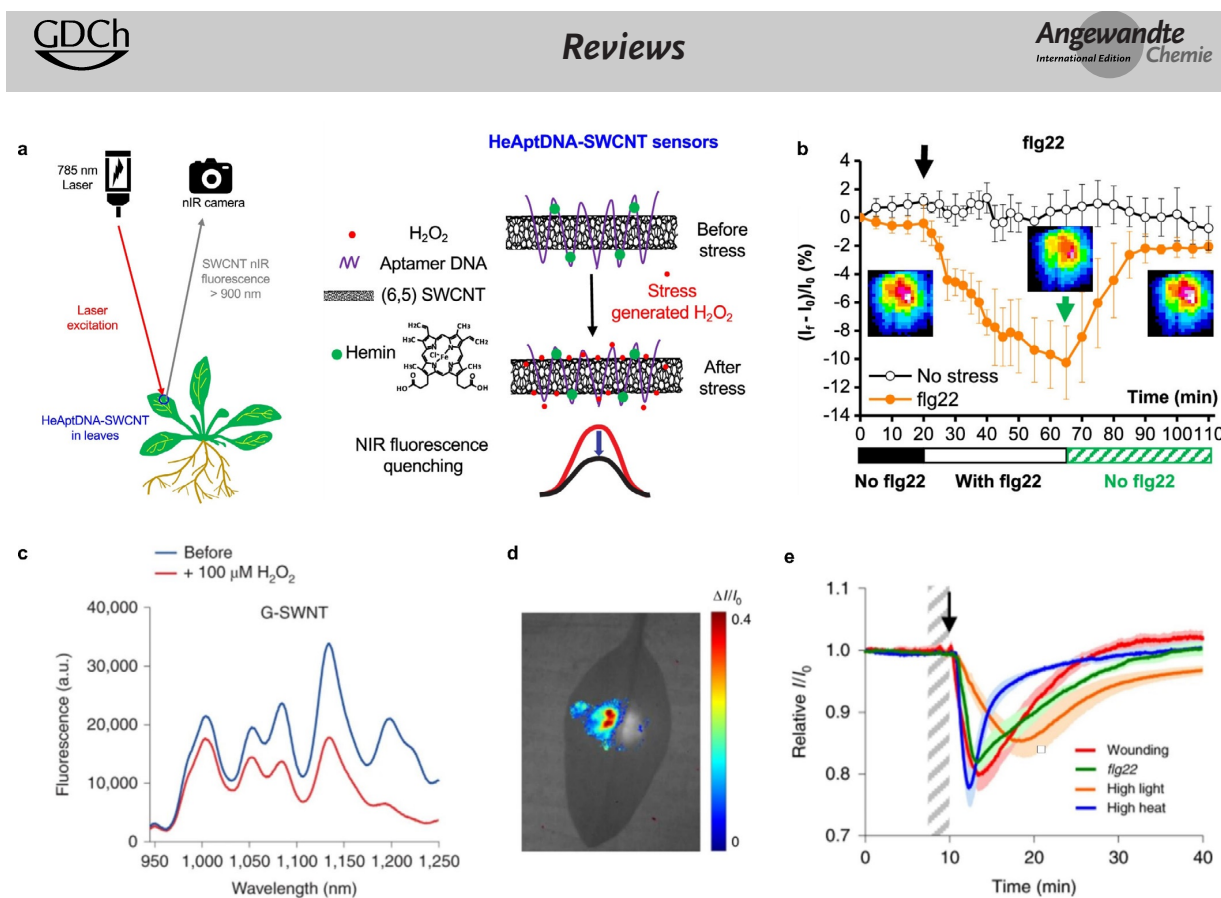
Figure 7. In vivo monitoring of plant health. a) SWCNTs functionalized with a DNA aptamer for hemin (HeAptDNA-SWCNT) serve as a sensor for H_2O_2, which is an important signaling molecule for plant stress. Hemin catalyzes the reaction of H_2O_2 to hydroxyl radicals, which quench the fluorescence of the SWCNT. Spatial and temporal changes in the NIR fluorescence intensity in leaves embedded with HeAptDNA-SWCNT sensors are remotely recorded by a NIR camera to assess plant health. b) The sensor's NIR fluorescence decreases reversibly in the presence of the peptide flg22, which mimics a pathogen attack. Reprinted from Ref. [31]. Copyright 2020 American Chemical Society. c) SWCNTs functionalized with $(GT)_{15}$-ssDNA (G-SWNT) respond to H_2O_2. d) Bright-field image of a spinach leaf infiltrated with G-SWNT (left) and nonresponsive A-SWNT (right) in combination with a false color plot after wounding shows that only the G-SWNT spot decreases in intensity. e) Ratiometric sensor response after application of different types of stress. Reprinted from Ref. [32] with permission. Copyright 2020 Springer Nature.

a wearable optical microfibrous material with encapsulated SWCNT-based sensors (Figure 8d) to monitor the H_2O_2 concentration in wounds.[112] Their approach was based on the ratiometric signal of (8,7)/(9,4)-SWCNT chiralities, which differed in their response to H_2O_2 (Figure 8e). The fluorescence signal was invariant to the excitation source distance, and exposure time, which enabled detection within commercial wound bandages with a wireless readout (Figure 8f). These microfibers encapsulated the SWCNTs for at least 21 days without structural changes.

Furthermore, Zheng et al. reported the selective interactions of SWCNTs coated with ten different ssDNA sequences in response to dissolved oxygen.[131] The SWCNT emission intensity was quenched between 9 to 40% depending on both the ssDNA sequence and SWCNT chirality in response to 1 atm O_2 compared to samples purged with 1 atm argon, thus indicating that stronger coating interactions lead to reduced O_2 access to the SWCNT surface. Since the quenching reversed completely after the removal of dissolved oxygen, it is probably based on physisorption on the SWCNT. Thus, the screening for fluorescence quenching by dissolved

oxygen provides a simple approach to explore the structure-selective interactions of ssDNA with SWCNTs.

ROS can also be generated by enzymes and SWCNTs. Yaari et al. demonstrated the first SWCNT-based sensor that reports the degree of enzymatic suicide inactivation.[201] The approach was based on enzyme-bound SWCNTs, which report fluorescence modulations by quenching and red-shifting selectively in response to substrate-mediated suicide inactivation of tyrosinase. Mechanistic insights revealed that the red-shifted response is most likely a result of the generation of singlet oxygen during the enzymatic reaction, which leads to the binding of ssDNA on the SWCNT surface.[132]

3.2.2. Neurotransmitters

Neurotransmitters are an important class of signaling molecules. To understand neuronal networks and linked neurological diseases, imaging with high selectivity and spatiotemporal resolution is necessary, which existing methods are currently not able to provide.[133] In the last few years

Reviews
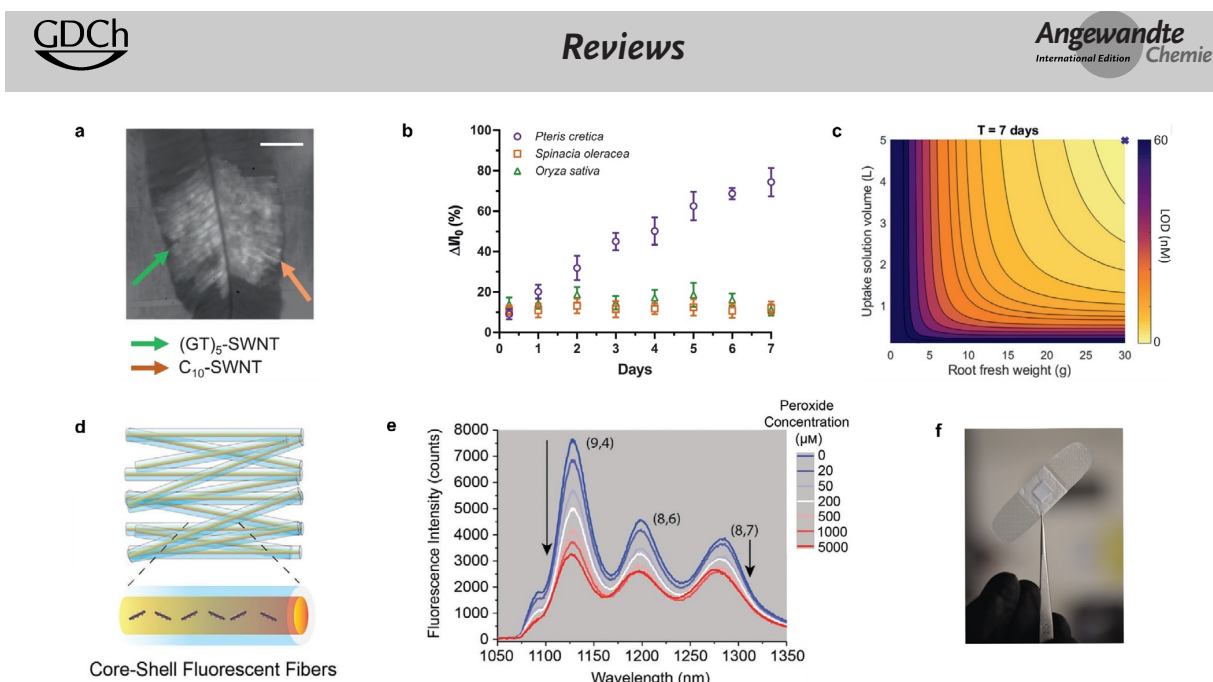
Figure 8. Macroscopic detection of small molecules. a) Bright-field image of leaf (arsenic hyperaccumulator plant Pteris cretica) infiltrated with (GT)$_5$-SWNT sensors and a C$_{10}$-SWNT reference. b) Fluorescence intensity change in response to 10 μM arsenite uptake through the roots of a hyperaccumulator, spinach, and rice plants. c) Theoretical LOD as a function of root fresh weight and uptake solution volume after 7 days. Reprinted from Ref. [33] with permission. Copyright 2020 John Wiley and Sons. d) Wireless monitoring of oxidative stress. Schematic representation of fabricated core–shell NIR fluorescent microfibers. e) Fluorescence spectra of the microfibrous material in response to different peroxide concentrations. f) Optical fibrous sample integrated into a commercial wound bandage for real-time wireless sensing. Adapted from Ref. [112] with permission. Copyright 2021 John Wiley and Sons.

several SWCNT-based sensors based on functionalization with DNA have been explored and it has been shown that sensitivity and selectivity depend on the exact DNA sequence.[100,118,119]

The first SWCNT-based sensors for the detection of neurotransmitters were reported by Kruss et al.[15] By using a screening approach, it was found that certain ssDNA-SWCNTs change their fluorescence in the presence of catecholamine neurotransmitters such as dopamine. These sensors were reversible and showed sensitivities in the nanomolar range. Similar sensors were used for the high-resolution imaging of cellular dopamine efflux from stimulated neuroprogenitor cells.[100] Here, the sensors were immobilized on a collagen-coated glass substrate to increase cell adhesion, and dopamine-releasing neuroprogenitor (PC12) cells were cultured on top. In response to a stimulation event, the fluorescence intensity of the sensor layer image consisting of up to 20000 pixels increased (Figure 9a,b). This allowed both the spatial and temporal dynamics of dopamine release events to be studied with extraordinary high resolution and to identify hotspots (Figure 9c,d).

This approach of imaging many nanosensors under cells is also applicable to other neurotransmitters. Dinarvand et al. imaged the release of serotonin from human blood platelets in real time,[27] as most of the serotonin is stored in blood platelets and not in the brain of humans. This serotonin sensor (NIRSer) consisted of a serotonin-binding aptamer on a SWCNT, which exhibited an increased fluorescence emission of up to 80% in response to serotonin (Figure 10a). High-resolution images of serotonin release patterns from

single cells were obtained by placing the sensors below and around serotonin-releasing cells (Figure 10b,c). This approach allows serotonin release to be studied with unprecedented resolution and the time delay between stimulation and release to be resolved.

In a similar fashion, artificially added serotonin was detected in acute brain slices by Jeong et al.[134] In this case, a DNA sequence was found by an expanded screening approach from a library of around 6.9×10^{10} different ssDNA-SWCNTs. These ssDNA-SWCNTs exhibited a selective response to serotonin over serotonin analogues, metabolites, and receptor-targeting drugs.

The high spatiotemporal resolution of SWCNT-based neurotransmitter sensors is especially useful when it comes to resolving parallel processes on the subcellular to cell-network length scale. However, placing the sensors below cells can be a drawback, especially with cells that need to differentiate on this layer for several weeks. Elizarova et al. developed a new sensor paint approach (AndromeDA) to use sensors and study the dopaminergic signaling in primary neurons.[135] In this case, the sensors were adsorbed ('painted') onto the complex cell networks, which included different cell types. This approach allowed the heterogeneity of dopamine release events to be quantified from up to 100 release sites (varicosities), which is highly important to understand the information processing and plasticity of neurons.

An effect that has to be accounted for in these studies is that SWCNT fluorescence is affected by changes in the local cation concentration, which is also a hallmark of neuronal activity.[56,57] To circumvent this problem, Gillen et al. used
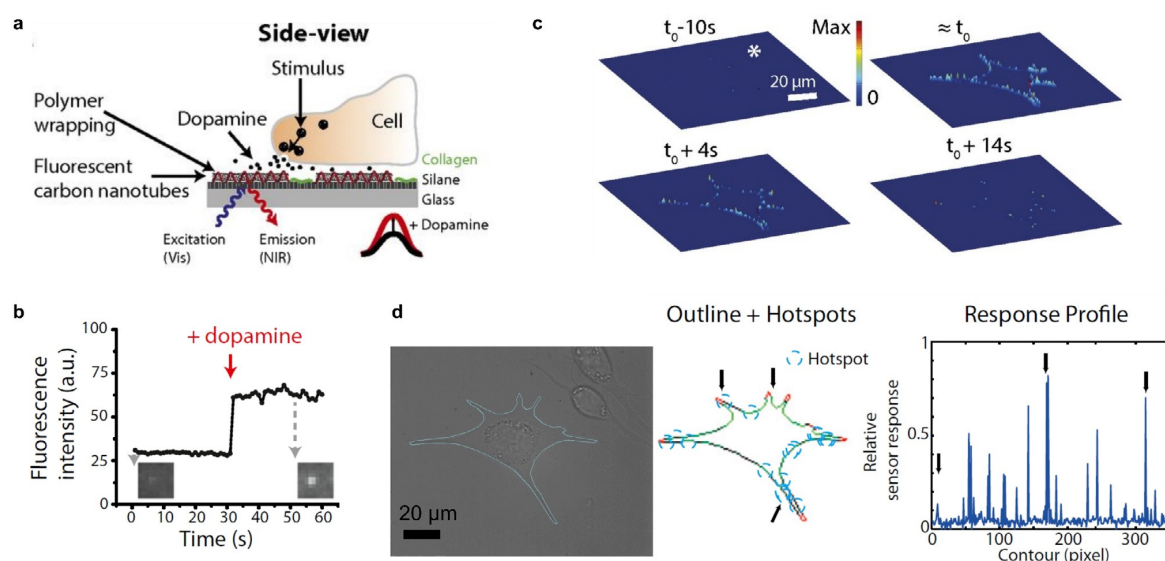
Figure 9. High-resolution imaging of dopamine using SWCNT-based sensor arrays. a) Specific ssDNA-functionalized fluorescent SWCNTs respond selectively to dopamine. Sensors are immobilized on a glass substrate and dopamine-releasing neuroprogenitor cells are cultivated on top. The SWCNT fluorescence changes in response to stimulation of the cells. b) Fluorescence intensity change of a single sensor in response to dopamine. c) Three-dimensional release profiles for dopamine along the border of neuroprogenitor (PC12) cells at different time points relative to the stimulation at t_0. The height and color indicate the relative fluorescence change normalized to the maximum fluorescence change. d) Bright-field image of the cell stimulated on top of the nanosensor array and corresponding hotspots (blue circles) along the cell border. Arrows indicate positions belonging to the hotspots in the response profile. Reprinted from Ref. [100] with permission.
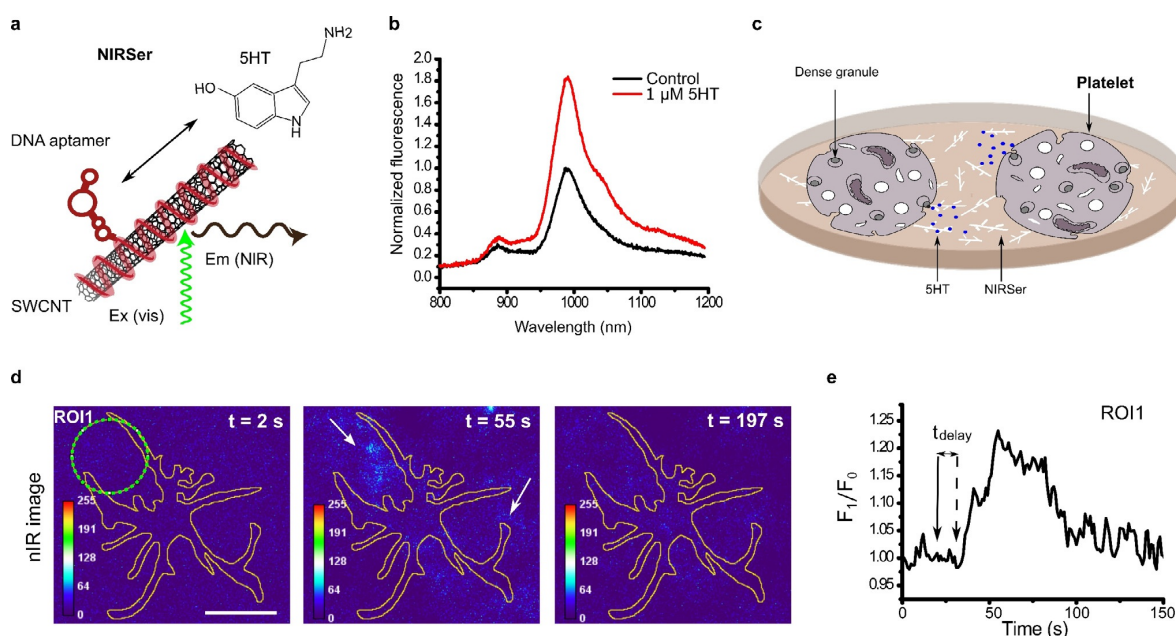
Figure 10. High-resolution imaging of serotonin (5HT) release from cells. a) NIRSer sensor: SWCNTs functionalized with a serotonin aptamer respond selectively to serotonin. b) NIRSer increases its fluorescence in response to serotonin. c) Sensors are immobilized on a surface and serotonin-releasing cells are cultured on top. Here, blood platelets are used, which contain most of the body's serotonin. d) Color-coded image of serotonin release from a single platelet at three time points (before, during, and after serotonin release). e) Fluorescence response from a region of interest (ROI, green circle in (d)). The activation and delay time of the onset of serotonin release are marked with arrows. Reprinted from Ref. [27] with permission. Copyright 2020 American Chemical Society.

Reviews

locked nucleic acids to develop sensors with improved stability to cation-induced fluctuations of the fluorescence intensity.[136] By systematically introducing locked bases along the $(GT)_{15}$-DNA sequence they found that the fluorescence stability in the presence of Ca^{2+} ions depends on the type of the locked bases. Certain SWCNT chiralities exhibited improved stability against Ca^{2+} ions and retained their ability to detect dopamine in the presence of Ca^{2+} ions, thus highlighting the importance of the exact conformation of the nucleic acid sequence. Moreover, the detection of both Ca^{2+} and dopamine was possible by monitoring multiple chiralities simultaneous.

Interestingly, the fluorescence responses of SWCNTs suspended in sodium cholate to dopamine and serotonin can be altered by modulating the exposed area by the surfactant concentration. However, such surfactants would not be compatible with cellular systems.[137]

A central challenge in biomedicine is the controlled delivery (uptake, transport, and release) of (nano)materials such as sensors and pharmaceuticals. Even whole cells can serve as vehicles to take up such materials. Certain immune cells (neutrophils) have been shown to be suitable for cargo delivery by hijacking a process known as neutrophil extracellular trap formation (NETosis). During NETosis, cells lyse after rupture of the cellular membrane by chromatin swelling.[138] Meyer et al. showed that human immune cells take up ssDNA-SWCNT-based sensors and can be triggered to release the cargo after a certain time by using NETosis.[139] Moreover, the sensors maintained their functionality to detect dopamine and H_2O_2, which offers opportunities for in vivo delivery.

All these discussed neurotransmitter sensors responded by a fluorescence increase. Interestingly, the introduction of a small number of aryl defects into ssDNA-functionalized SWCNTs completely reversed the sensing response (Figure 6d).[87] The E_{11} emission slightly decreased and strongly decreased the red-shifted E_{11}^* emission. Apart from new insights into the sensing, this approach enables ratiometric detection schemes. For a more detailed overview on the biological relevance of catecholamine neurotransmitters and alternative detection methods (e.g. electrochemical) readers are referred to the literature.[28,114]

3.2.3. *Other Small Molecules*

Beyond neurotransmitters, recognition strategies for other small molecules have been developed, for example, adenosine 5′-triphosphate,[140] nitroaromatics,[30,141] riboflavin,[49,70,142] L-thyroxine,[70] oestradiol,[70] doxorubicin,[115,143] and steroids.[144]

Finding a specific molecular recognition element is difficult for many of these biomolecules, such as hormones, due to their chemical similarity. Therefore, Lee et al. used a polymer self-templating synthetic approach, which is based on the attachment of a chemical appendage similar in molecular weight and structure to the target analyte to create a binding pocket within the corona. This approach reduced the library size for screening and led to implantable SWCNT-based sensors for the selective detection of the human steroid hormones cortisol and progesterone.[144]

Recently, the first reversible fluorescent SWCNT-based sensor for volatile organic compounds was also reported, which has potential for the detection of wine spoilage.[145] For this, Shumeiko et al. used peptide-encapsulated SWCNTs, which were adsorbed onto a polystyrene cuvette to detect low concentrations of acetic acid (down to 0.05 % (v/v)) in air. Using (6,5)-SWCNTs, which fluoresce below 1000 nm they demonstrated the detection with a low-cost Si-based camera (Figure 11a). The sensor was exposed to different concentrations of acetic acid, which quenched the fluorescence but was reversible when switching to clean air (Figure 11b). The ability to identify wine spoilage was investigated by using two wine types with and without the addition of acetic acid to simulate an undesirably high acetic acid concentration (Figure 11c).
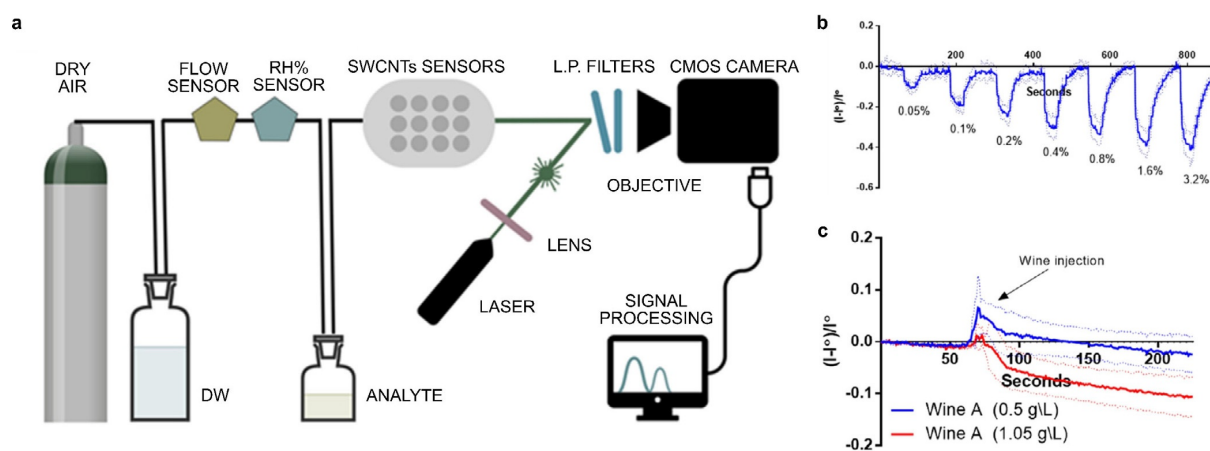
Figure 11. Detection of volatile compounds in the gas phase. a) Air with analyte (acetic acid) flows to the SWCNT-based sensors, which produces an optical readout. b) Dynamic response of the sensor to rising acetic acid concentrations. c) Dynamic response of the sensor to wine spiked with acetic acid. Reprinted from Ref. [145] with permission. Copyright 2021, Elsevier.

In an extension of this study, this system was expanded to an array of five different peptide-encapsulated SWCNTs on a nitrocellulose paper. The optical patterns enabled the distinction of volatile molecules such as ethanol, methanol, and 2-propanol as well as the aromas of red wine, beer, and vodka by linear discriminant analysis and machine learning.[146]

One way to detect or study small molecules is to mimic parts of larger biomolecules, such as enzymes. Dong et al. screened a library of 24 amphiphilic polymers to find a corona phase which demonstrates a binding specificity very similar to the enzyme phosphodiesterase type 5 (PDE5), which catalyzes the hydrolysis of secondary messengers.[147] The SWCNT-based sensor consisted of a poly(methacrylic acid-*co*-styrene) motif. This synthetic corona mimics the H loop of the native enzyme and is, thus, able to bind to Vardenafil, a PDE5 inhibitor, and its molecular variant as a result of the unique corona phase configuration. It is selective over other off-target inhibitors, but not completely over the chemically similar inhibitor Sildenafil.

One of the challenges in SWCNT-based sensing is the heterogeneous material that is used for most sensors. Even though purification has made tremendous progress, getting access to chirality-pure SWCNTs with a tailored surface chemistry has been a challenge. Nißler et al. showed sensing of small molecules such as riboflavin and ascorbic acid as well as pH value with chirality-pure SWCNTs by using aqueous two-phase extraction and a subsequent surface functionalization exchange process.[49] The chirality-pure sensors were up to ten-times brighter than mixtures of SWCNT chiralities, and enabled insights into the impact of chirality and handedness of SWNCTs and the sensing mechanism. Additionally, long-time stability over 14 days was demonstrated as well as ratiometric and multiplexed sensing based on the non-over-lapping fluorescence spectra (Figure 22b,c).

On a macroscopic level, monochiral SWCNTs were used by Nißler et al. to detect polyphenols in and around plants.[148] Polyphenols are secondary metabolites and messenger molecules that are released from leaves and roots as a chemical defence against pathogens and herbivores (Figure 12a). Certain polyethylene glycol phospholipids (PEG-PL) were identified for the selective detection of different polyphenols

over interfering molecules such as sugars or H_2O_2. The SWCNT-based sensors responded through quenching and red-shifting of up to 20 nm, for example, to tannic acid (TaA, Figure 12b). To image the plant polyphenol release over time, the sensors were embedded in agar, soybean seedlings were plated on top, and polyphenol secretion was triggered with a pathogen-derived elicitor, which resulted in a decrease in the NIR fluorescence over time (Figure 12c). These sensors help to understand this plant defence mechanism and could improve the breeding of stress-resistant plants for precision agriculture.

3.2.4. Lipids

The investigation of lipid-linked diseases is challenging because methods for accurate in vivo monitoring of lipid accumulation have been missing. The Heller group was the first to address this issue by developing a SWCNT-based optical sensor, which non-invasively detects the lipid flux within the lumen of endolysosomal vesicles in vitro and in vivo.[117,149] In a first approach, they used $(GT)_6$-functionalized (8,6)-SWCNTs, which fluoresce at 1200 nm and responded through a wavelength shift to biological lipids and water-soluble lipid analogues.[117]

By incubating the sensors with fibroblasts from a lysosomal storage disorder Niemann-Pick-type C patient in vitro, the sensors localized in the lumen of endolysosomal organelles without affecting their properties and resolved the lipid accumulation down to the subcellular level in real time. The authors proved the reversibility of this sensor by administering a drug which reverses the disease phenotype.

The second approach was based on the screening of several ssDNA-SWCNT chirality combinations to identify $CTTC_3TTC$-(9,4)-SWCNTs with the greatest wavelength shift of up to 8 nm in response to lipid accumulations.[149] The emission wavelength at 1125 nm is spectrally separated from the lipid absorption band at 1210 nm, thus facilitating promising in vivo applications. Molecular dynamics calculations led to the assumption that the lipid molecules sphingomyelin and cholesterol bind to the SWCNT surface by hydrophobic interactions, thereby decreasing the water density in the SWCNT environment and leading to the
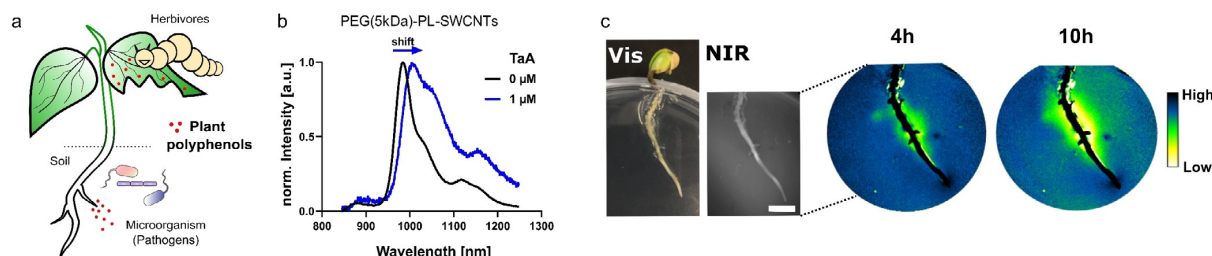
Figure 12. Detection and imaging of plant polyphenols. a) Polyphenols from leaves and roots are released in the immediate vicinity in response to pathogens or herbivores as a defence mechanism. b) SWCNTs functionalized with polyethylene glycol phospholipids (PEG-PL) respond selectively to polyphenols such as tannic acid (TaA) through a red-shift and decrease in the fluorescence emission. c) Visible and NIR images of a soybean root plated on top of the sensors (embedded in agar). The plant is challenged with a pathogen elicitor and the NIR fluorescence intensity decreases over time in response to the release of polyphenols in the immediate vicinity of the root. Reprinted from Ref. [148] with permission.
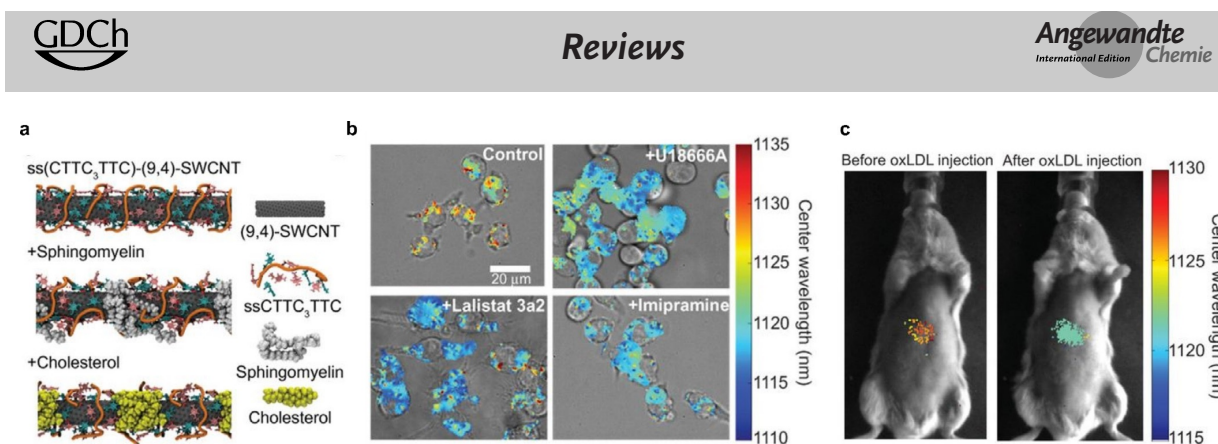
Figure 13. In vivo detection of lipid accumulation. a) Molecular dynamics simulations of ssCTTC$_3$TTC-(9,4)-SWCNTs that serve as a sensor for the lipids cholesterol and sphingomyelin through a change in the SWCNT emission wavelength. b) Bright-field images overlaid with hyperspectral NIR images of the sensors in RAW 264.7 macrophages with or without the chemical inhibitors U18666A, Lalistat 3a2, and Imipramine that change the intracellular lipid levels. c) Hyperspectral NIR images of the sensor before and after injection of oxLDL in mice report the in vivo lipid status. Reprinted from Ref. [149] with permission.

observed blue shift (Figure 13 a). To validate the sensor functionality in live cells, endolysosomal lipid accumulation was induced in macrophage cells with chemical inhibitors to mimic different lipid phenotypes. After sensor incubation, a blue-shift was observed for all sensors within the drug-treated cells compared to the control (Figure 13 b). For in vivo applications, two mouse models were used with lipid accumulation within the organelles of many cell types, for example, in Kupffer cells. By intravenously injecting the SWCNT-based sensors, a rapid decrease of the SWCNT fluorescence and consequently removal of SWCNTs from all parts of the mice except for the liver were observed. The sensors were also able to report uptake and endolysosomal lipid accumulation of oxidized low-density lipoprotein (oxLDL; Figure 13 c). Therefore, these types of sensors provide novel insights into the complexity of lipid metabolism and related health states.

3.2.5. Proteins

Proteins are one of the major biomacromolecules. Consequently, the study of protein–protein interactions helps to understand the function of proteins or to find novel drugs.[150] As discussed above, the detection of proteins with SWCNTs is either based on attaching a known natural recognition element[21, 64, 65, 102–106, 151] or a synthetic heteropolymer to the SWCNT surface (Figure 3).[71, 101, 152, 153] Such studies go beyond detecting the presence of a whole protein.

Williams et al. developed the first label-free optical sensor for the detection of glutathione-S-transferase (GST) fusion proteins based on glutathione-(TAT)$_6$-SWCNTs (GSH-DNA-SWCNTs; Figure 14 a).[154] The system used distinct differences in the emission wavelength and intensity of SWCNT chiralities in response to GST and, consequently, the ratiometric intensity of two chiralities (8,6)/(9,1) (Figure 14 b). The functionality of this sensor in response to four different GST fusion proteins was tested, which all showed a similar ratiometric response and a LOD in the low nanomolar regime. This approach has potential for the tracking of protein expressions in real time.

The detection of insulin is essential for diabetes as it controls the glucose levels in blood. The first optical SWCNT-based sensor approach for detecting insulin was realized in 2010 by Cha et al.[155] They used an insulin-binding aptamer, which showed a highly specific and sensitive decrease in the fluorescence intensity on forming a guanine quadruplex. Furthermore, they incorporated these sensors in a collagen extracellular matrix and demonstrated sensor reversibility with enzymatic proteolysis and the detection of insulin secreted by pancreatic β-cells.[156]

Recently, insulin detection was enabled by screening a library of PEG-conjugated lipids. It was found that the C$_{16}$-PEG(2000 Da)-Ceramide-SWCNT complex causes a significant decrease in the fluorescence intensity in the presence of insulin compared to other relevant proteins present in human whole blood.[101] Additionally, nonspecific recognition mechanisms such as hydrophobicity or molecular weight were ruled out. For example, the sensor response to shorter insulin fragments was measured, however no correlation to the molecular weight was observed (Figure 14 c). The analysis of insulin fragments was further supported by enthalpy measurements that showed no affinity of the PEG-conjugated lipid itself, which highlights that the exact CoPhMoRe phase bound to the SWCNT is responsible for the insulin binding. In more complex environments, such as serum, the sensor affinity was lower but still sensitive enough (Figure 14 d).

The application of sensors in complex biological samples is often challenging. The spontaneous adsorption of proteins onto all kind of materials changes the actual corona structure and might affect sensing. To improve the performance of sensors in those protein-rich environments, a fundamental understanding of the interaction between sensors and their biological environment is necessary. Pinals et al. addressed this issue by studying the protein corona formation on (GT)$_{15}$-SWCNTs in cerebrospinal fluid and blood plasma by mass spectroscopy.[98]

Their results showed strong binding to fibrinogen and other proteins involved in blood clotting, lipid transport, and complement activation. The identification of interactions responsible for the formation of protein corona revealed that
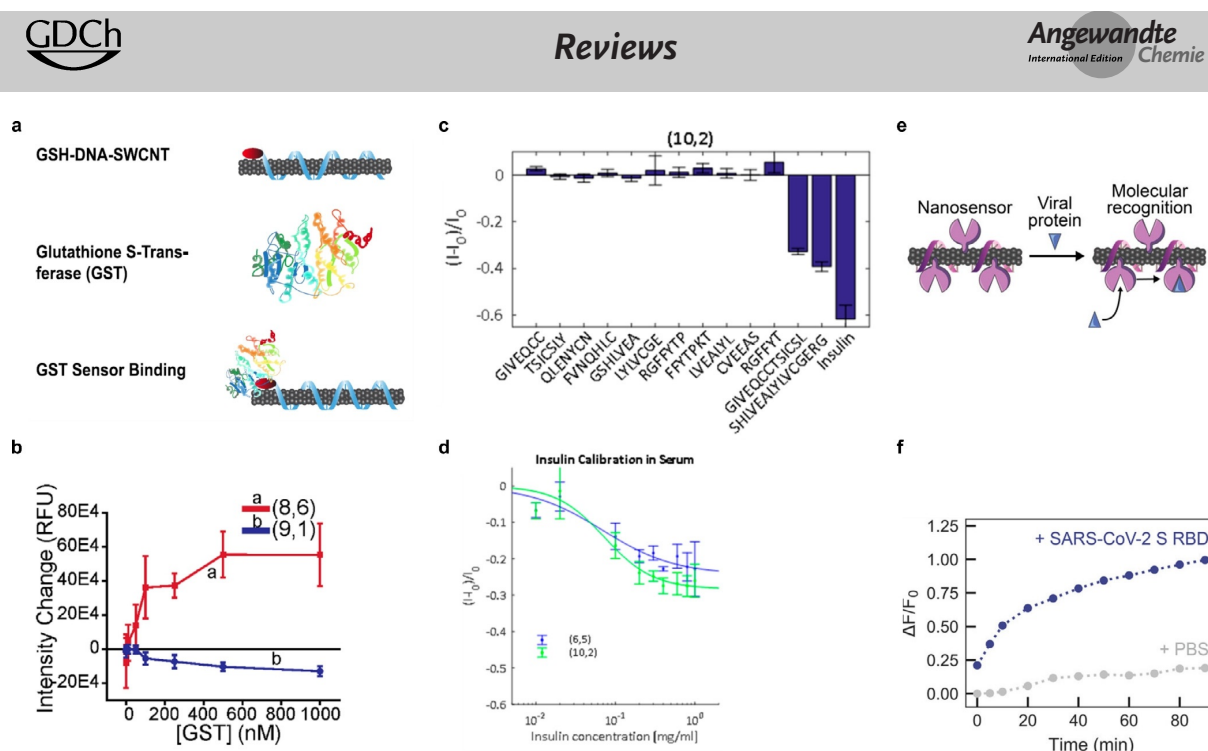
Figure 14. Detection of proteins. a) SWCNT-based sensor design for the detection of glutathione-S-transferase (GST) fusion proteins. b) Monotonic intensity changes of (8,6) and (9,1) sensors with increasing GST concentration. Reprinted from Ref. [154] with permission. Copyright 2020 American Chemical Society. c) Detection of insulin by SWCNTs functionalized with a PEG-conjugated lipid. Intensity change of the sensor in response to insulin and shorter insulin fragments. d) Insulin calibration curve in serum. Reprinted from Ref. [101] with permission. Copyright 2018 American Chemical Society. e) Detection of the SARS-CoV-2 spike protein. ACE2-(GT)$_6$-SWCNTs interact with the SARS-CoV-2 spike protein receptor-binding domain (S RBD). f) Time-dependent change in the relative fluorescence intensity of the sensor in response to the viral protein S RBD. Reprinted from Ref. [157] with permission. Copyright 2021 American Chemical Society.

the outer corona formation can be reduced by optimizing the electrostatic interactions through the sensor design and dynamic flow conditions (e.g. with lateral flow assays or microfluidic systems), while entropic calculations must be considered for the inner corona. This study highlights the urgent need to investigate sensors not only in simple buffers but biologically complex environments. Most recently, Ehrlich et al. developed a complementary approach using an insulin aptamer (found within the natural insulin gene promoter) functionalized to the SWCNT surface through a $(AT)_{15}$ ssDNA anchor sequence.[158] In contrast to the synthetic PEGylated-lipid, which has no prior affinity to insulin, this aptamer possesses a known affinity to insulin. However, the observed sensitivity was lower than the previous approach.

Most of the SWCNT-based sensors that have been discussed so far were measured in solution. The immobilization of SWCNTs on different porous paper matrices, for example, nitrocellulose, has several advantages for a robust assay.[116] Paper-based immobilization enabled analyte detection within non-aqueous solvents such as edible oil, which was previously not possible. To further extend this system the authors used wax to pattern hydrophobic regions onto the paper to create a multiplexed one-dimensional sensor barcode consisting of different ssDNA-wrapped SWCNTs.

Another important class in biomedical diagnostics are antibodies. The detection of immunoglobulin G (IgG) with

SWCNTs was realized by using chitosan-wrapped SWCNT noncovalently modified with immunoglobulin-binding proteins.[104,151] Recently, Kozawa et al. designed a flexible fiber optic interface coupled to nanosensors that was capable of detecting the aggregation status of human IgG by reporting the relative fraction of monomers and dimer aggregates with sizes of 5.6 and 9.6 nm.[159] For this purpose, the SWCNT-based sensors were incorporated into a hydrogel (HG) and attached to the end of a fiber waveguide. Proteins are also part of pathogens and consequently disease markers. Pinals et al. developed a SWCNT-based sensor which is functionalized with the angiotensin-converting enzyme 2 (ACE2), a host protein which shows a high binding affinity for the SARS-CoV-2 spike protein (Figure 14e).[157] A twofold NIR fluorescence increase was detected 90 min after the addition of the purified spike protein (Figure 14f). Passivation with a hydrophilic polymer was used to enable detection of the spike protein in saliva and viral transport medium.

However, antibodies are not always available for all targets. In addition, the development of new recognition units can be expensive and tedious, which is why new approaches are directed to the development of multiplexed sensor arrays[146,151] to overcome the limited selectivity of existing single sensors. Recently, Yaari et al. developed a SWCNT solution-based sensor platform to detect multiple gynecologic cancer biomarkers in uterine lavage samples.[160] The array consisted of eleven different ssDNA-SWCNT sensors, and the

optical change in the intensity and wavelength was extracted for twelve chiralities present in the sample, which resulted in 132 individual ssDNA-SWCNT complexes. With machine learning algorithms a classification accuracy (F1 score) of 0.95 was achieved. With retraining, this sensor platform may not be limited to the detection of cancer biomarkers. The large variety of possible SWCNT chiralities in combination with unlimited SWCNT wrappings opens possibilities to meet the rising demand of new recognition strategies.

3.2.6. Sugars

Sugars are important building blocks and metabolites. Glucose, in particular, is a major target, for which continuous monitoring of the glucose level in blood is desired. SWCNT-based sensing ranges from the use of glucose-specific enzymes[24,161,162] or proteins[108] to the first affinity sensor based on the competitive binding between glucose and its polymer dextran.[11] Although improvements were made, the first approaches suffered from limited reversibility and/or physiological detection range. One sensor that meets the requirements is based on the functionalization of SWCNTs with glucose oxidase (GOX), a glucose-specific enzyme.[161] The addition of glucose causes an increase in fluorescence emission. The proposed mechanism is based on SWCNT fluorescence being quenched by defect sites on the SWCNT surface, which are hole-doped through oxygen adsorption. The addition of glucose causes an oxidation of the GOX wrapping, which behaves as an electron donor and passivates the oxygenated sites of the SWCNT, thereby resulting in a fluorescence increase. This effect is reversible by removing the glucose. The sensor showed responses to five other tested saccharides, but with the highest response to glucose.

Another recognition element for saccharides is phenylboronic acids, which have been used to functionalize SWCNTs noncovalently for the detection of sugars.[68] Recently, covalent aryl-boronic acid defects were also incorporated in SWCNTs.[81] Upon interaction with fructose and glucose, these sensors decreased in fluorescence intensity and the E_{11}^* signal shifted, which can be used for spectrally encoded sensing.

3.2.7. DNA/RNA

One of the most abundant and important types of biomacromolecules are nucleic acids that store and process genetic information. Using a construct of a complementary capture sequence connected to a $(GT)_{15}$-sequence serving as an anchor, thus providing colloidal stability, SWCNTs were recently used to detect hybridization events of microRNA and other oligonucleotides directly in serum, urine, and in mice in vivo.[163] Upon the addition of complementary nucleic acids, a specific blue-shift for different chiralities upon hybridization was observed. Additionally, the sensor response was reversible through toehold-mediated strand displacement and the sensors possessed a LOD in the picomolar range.

Further development of this sensor led to the first SWCNT-based sensor for the detection of HIV in serum.[164] Harvey et al. discovered that SDS-denatured serum proteins lead to an enhanced optical response of the SWCNTs in response to DNA hybridizations. They hypothesized that the addition of SDS ensured both the liberation of the viral RNA genome and the denaturation of the proteins which competitively bind to the freed surface of the sensor. The interaction leads to a blue-shift in the SWCNT emission (Figure 15a). This was first shown for hybridization with complementary target miR-19 DNA compared to control R23 DNA (Figure 15b). A dose-dependent enhancement of the blue-shift occurred in the region of the critical micelle concentration of SDS; thus, the denaturation of proteins by SDS is considered to involve an unfolding process of the tertiary structure of the protein to complete denaturation. As the SDS concentration was increased, the amount of denatured protein absorbed onto the SWCNT surface after hybridization of the DNA increased and saturated at 2% SDS. For HIV detection, the recognition strategy was based on a sensor consisting of $(GT)_{15}$-T_{15}-SWCNTs, which hybridize with the polyadenylation elements of HIV RNA (Figure 15c). In a similar way, a control sensor with the noncomplementary capture sequence, namely $(GT)_{15}$-A_{15}-DNA, was constructed. The wavelength shifts of both the sensor and negative control in the presence of HIV particles treated with 1% SDS were recorded over time and and the sensor displaying the complementary capture sequence showed a blue-shift of around 3 nm after 180 min.
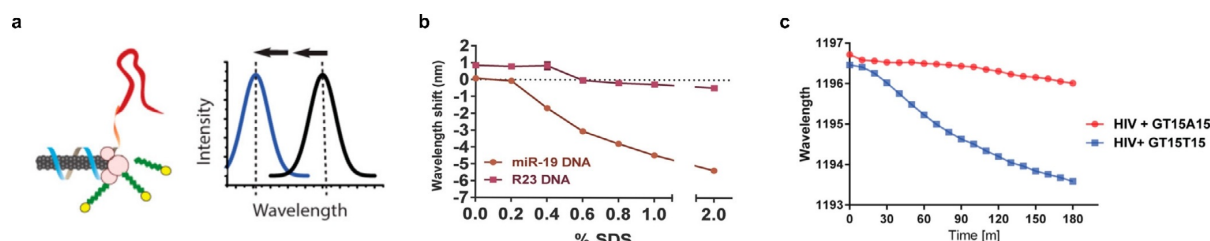
Figure 15. Detection of viral (HIV) RNA. a) Detection of viral RNA using a HIV lentivirus model. The virus is denatured by SDS, which liberates the RNA genome. It hybridizes to the complementary ssDNA on the SWCNT-based sensor and increases the free surface area, which is then occupied by serum proteins and causes a blue-shift of the spectrum. b) Wavelength shift in response to the target miR-19 DNA or control R23 DNA in bovine serum albumin with various SDS concentrations. c) Kinetics of the response of sensors with complementary $((GT)_{15}T_{15})$ and negative control $((GT)_{15}A_{15})$ ssDNA in the presence of HIV particles, FBS, and 2% SDS. Reprinted from Ref. [164] with permission. Copyright 2019 American Chemical Society.

A completely different application of DNA chemistry on SWCNTs was established by Cha et al. Based on the consumption of chemical energy delivered by the RNA molecules, they developed a synthetic motor that transports nanoparticles through the mechanical motion of DNA conformation changes along the SWCNTs.[165] Movements of the motor of over 3 µm with a speed of 1 nm min^{-1} were observed.

3.2.8. Enzymes

So far, the detection of enzymes with SWCNTs has been shown for the characterization of proteases and DNases as well as cellulases and pectinases. The hydrolytic enzyme activity was measured by Kallmyer et al., who used hydrolytic enzyme wrapped SWCNTs that respond to the target enzyme with a fluorescent intensity quenching because of the degradation of the enzyme-wrapping.[166] Different polymer wrappings consisting of polysaccharides and polypeptides were used to study cellulase, pectinase, and bacterial protease. Most recently, they used this approach to evaluate the enzyme activity in soil using a low-cost multiplexed and portable fluorimeter able to perform the measurement outside the laboratory only minutes after extraction from the field.[167] As a consequence of the fresh nature of the soil sample, field tests indicated activities an order of magnitude larger than those obtained in benchtop experiments.

Enzymes are also released by microorganisms, which can be used to fingerprint them. Nißler et al. chemically tailored SWCNTs to detect enzymes such as DNases and proteases.[29] For targeting extracellular proteases, SWCNTs were modified with bovine serum albumin (BSA), which serves as an enzymatic substrate, while SWCNTs were functionalized with calf thymus (CT) DNA for reporting DNase I and *S. aureus* nuclease activity. The sensors showed a fluorescence decrease, most likely as a result of decomposition of the BSA surface coating. These SWCNT-based sensors were further used for the discrimination of bacteria, which are known to alter their chemical environment through the release of signaling molecules, enzymes, and metabolites (see section below).

In contrast, Shumeiko et al. used peptide-encapsulated SWCNTs, which also responded through a fluorescence decrease upon enzymatic digestion of the SWCNT wrapping.[168] They utilized a low-cost paper-based dipstick system, with which they evaluated the trypsin activity in urine samples as a mimic for acute pancreatitis, where abnormal trypsin concentrations are common.

To study the enzyme myeloperoxidase, which is involved in the regulation of inflammation processes, He et al. used a ratiometric system based on graphene oxide (GO) wrapped SC-SWCNT sensors and GO-wrapped carboxymethylcellulose (CMC)-SWCNTs as a reference.[169] GO and SC-SWCNTs showed an opposed fluorescence signal in response to enzymatic degradation. Whereas the blue fluorescence intensity of GO was increased due to oxidation and degradation of GO leading to the formation of graphene quantum dots, the NIR emission of SWCNTs decreased due to the generation of defects on the SWCNT surface. In contrast, the CMC-SWCNT reference was almost stable as a result of the better surface protection of the CMC-wrapping.

3.2.9. Epitopes and Metabolites from Pathogens

Microbial infections are one of the major causes of mortality worldwide. Currently, the limited number of diagnostic methods in combination with increasing antibiotic resistances demonstrate the rising need for the rapid, contactless, and specific detection of pathogens such as bacteria. The optical properties of SWCNTs promise advantages for pathogen detection. Bardhan et al. developed M13 bacteriophage functionalized SWCNTs (M13-SWNTs, Figure 16a), which are able to distinguish F′-positive and F′-negative bacterial strains by modulation of the fluorescence intensity.[170] The M13 bacteriophage has a known binding affinity to F′-positive *E. coli* strains. Therefore, they intramuscularly infected the right flank of living mice with *E. coli* strains, either F′-negative DH5-α strains (Figure 16b, left) or targeted F′-positive JM109 strains (Figure 16b, right) and observed a 1.6-fold intensity increase over the nonspecific DH5-α strains. Injection of PBS into the right flank served as a control. To extend this SWCNT-based label to a wider range of bacterial strains lacking F′-pili, they additionally attached an antibacterial antibody on those M13-SWCNTs (anti-*S. aureus*-M13-SWNT) through a streptavidin–biotin reaction.
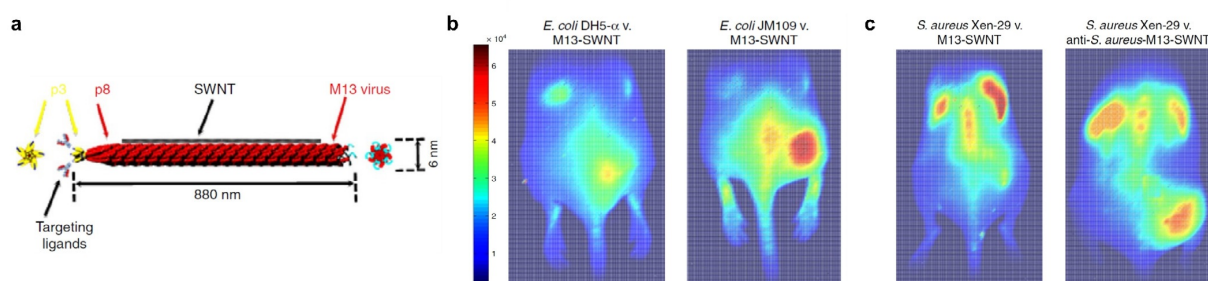
Figure 16. Labeling of bacteria. a) The bacteriophage M13 and its proteins p8 and p3 are used to longitudinally functionalize the SWCNT and to bind a target. b) Fluorescence image of M13-SWCNTs, intravenously injected into mice infected with *E. coli* strains. The right flank is either infected with F′-negative *E. coli* DH5-α strains (left) or the targeted F′-positive *E. coli* JM109 strains (right). The left flank serves as a control (PBS). c) Fluorescence images of mice infected with *S. aureus* strain Xen-29. The left mouse received M13-SWCNTs, while the right mouse received antibody labelled sensors (anti-*S. aureus*-M13-SWNTs). Adapted from Ref. [170] with permission. Copyright 2014 Nature Publishing Group.

Reviews
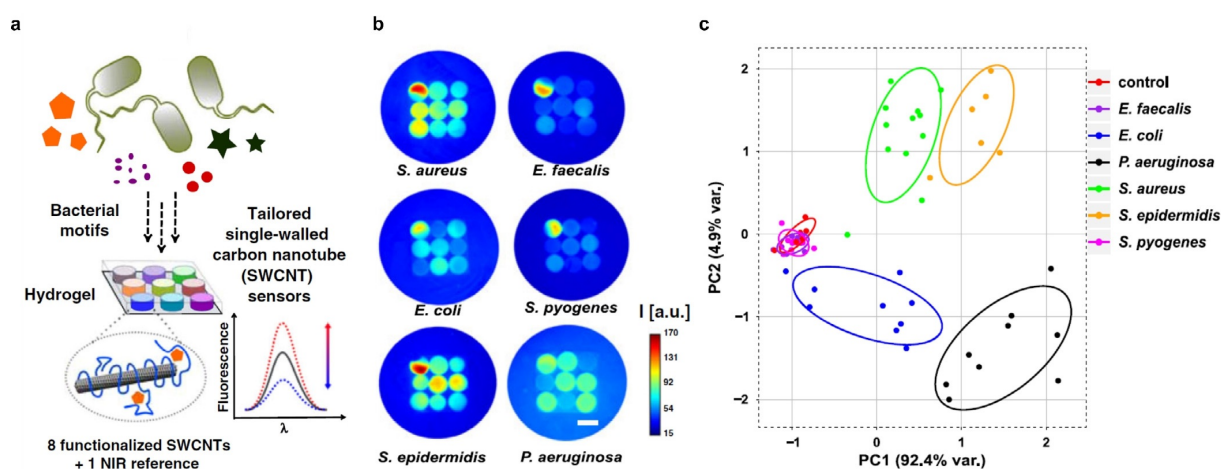
Figure 17. Remote detection of pathogens. a) Eight fluorescent SWCNT-based nanosensors and one NIR fluorescent reference material are incorporated into a polyethylene glycol hydrogel (HG) array that is remotely monitored in the NIR region. The sensors change their fluorescence signal in response to bacterial metabolites and virulence factors, which are released by bacteria growing on top of this HG. b) The unique NIR fingerprint of the multiplexed sensor array allows important pathogens to be differentiated. c) Principal component analysis (PCA) of the fluorescence fingerprint of all the analyzed strains (72 h). Each point represents one bacterial sample, including clinical isolates from different patients. The clusters show that different bacteria can be identified and distinguished. Control = medium only. Reprinted from Ref. [29] with permission.

This complex specifically detected *S. aureus* intramuscular infections in a mouse model in vivo (3.1-fold intensity increase over the nontargeted M13-SWCNTs, Figure 16c).

This approach is a NIR labeling rather than sensing. In contrast, Nißler et al. created a concept to remotely distinguish six important pathogens using an array of SWCNT-based sensors:[29] four for specific bacterial target detection based on a rational approach and four generic lower sensitivity sensors together with an invariant reference consisting of NIR fluorescent Egyptian Blue nanosheets (Figure 17a).[171]

To overcome unspecific effects arising from the complex composition of bacterial media, the sensors were incorporated into a hydrogel (HG) array, in which the pore size was varied in accordance to the size of the analyte. For the detection of small molecules (such as siderophores), HGs with a low porosity were used, whereas HGs with a high porosity allowed large enzymes to diffuse to the sensors. The sensors were exposed to clinical isolates of bacteria and the unique change in the fluorescence intensity for each sensor was monitored remotely. Within 24–72 h, a unique fingerprint in response to the tested pathogens was visible (Figure 17b), which further allowed differentiation of the pathogens by principal component analysis (PCA; Figure 17c). Besides this spatially encoding, spectral multiplexing was implemented to differentiate *S. aureus* and *P. aeruginosa* by using two mono-chiral SWCNT-based sensors with different wavelengths compared to the reference. Moreover, the signal of the sensor could be detected through tissue to a depth of > 7 mm, which highlights the potential for biomedical in vivo applications.

3.3. Mechanism of Fluorescence Modulation

In SWCNT-based sensors or probes, the SWCNTs serve as transducer elements that translate chemical changes caused by an analyte in the vicinity of the SWCNT into a fluorescent signal. Thus, SWCNT-based sensing involves molecular recognition and signal transduction. The precise mechanisms are most likely different for different analytes and different surfaces. However, from the literature one can distinguish several possible generic mechanisms (Figure 18).

3.3.1. Direct Quenching

Direct quenching, that is, the decrease of fluorescence, is caused by adsorption of the analyte onto the SWCNT surface. Changes in the pH value caused by the addition of an acid can cause protonation of the SWCNT sidewall and result in direct, reversible quenching of the SWCNT fluorescence (Figure 19a). Mechanistically, this can be explained by the injection of an electron hole into the π-system near the protonation site.[47] Excitons encountering such an electron hole will be quenched through a nonradiative Auger process.[172] Furthermore, electron transfer between the valence band of 3,4-diaminophenyldextran-functionalized SWCNTs and the lowest unoccupied molecular orbital (LUMO) of nitrogen oxide results in rapid, reversible quenching of the SWCNT fluorescence.[124] Both of these interactions take part in the vicinity of the SWCNT and, consequently, solvent effects should play a large role.

3.3.2. Impact of Conformational Changes and Solvation

Within the dimensions of the exciton, the fluorescence of SWCNTs is very sensitive to the surrounding environment. To
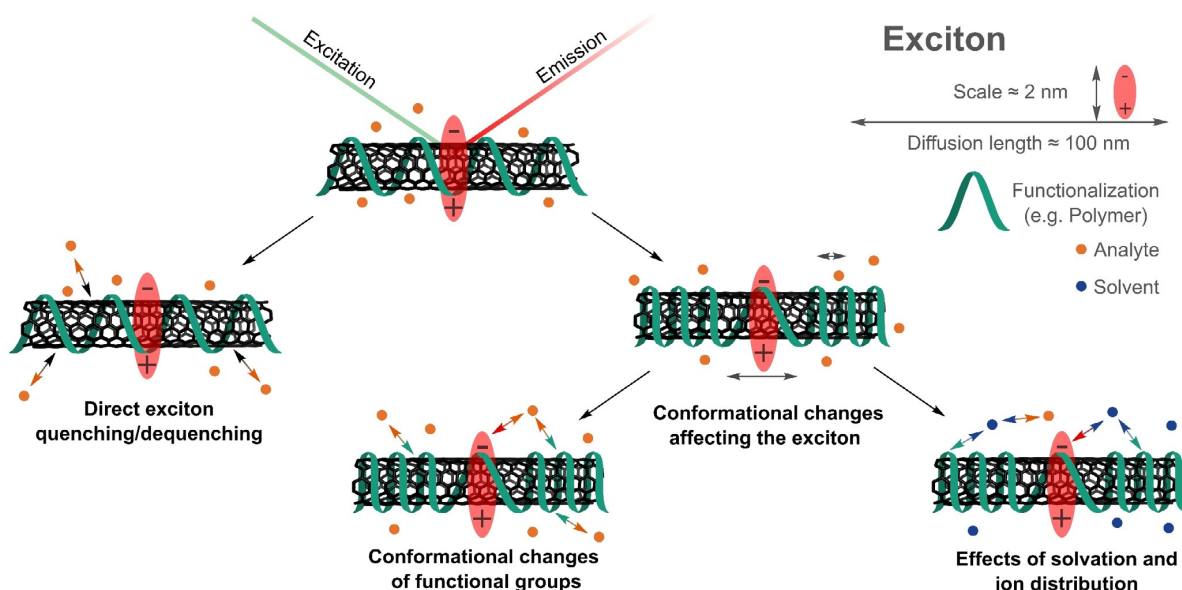
Figure 18. Mechanisms of fluorescence modulation in SWCNT-based biosensors. Note that the size of the objects and their arrangement is simplified and not to scale.

study the contributions of the solvent to the fluorescence of SWCNTs, fluorescence spectra were analyzed in different dielectric environments.[173,174] By using the solvatochromic shifts, a semiempirical scaling model was developed that linked optical with structural parameters and suggested an inverse dependence of exciton polarizability on the diameter and the square of the transition energy.[173] In nonpolar solvents, the solvatochromic modulation of the fluorescence intensity becomes more pronounced for larger diameters.[174] Changes in the solvatochromic shift, on the other hand, were more pronounced for SWCNTs with smaller diameters.[174]

In general, the displacement of H_2O or DNA from the surface of SWCNTs by surfactants leads to a strong blue-shift and increase in the fluorescence intensity. Interestingly, the change in the fluorescence characteristics of pristine SWCNTs and DNA-coated SWCNTs immobilized in gel are highly similar. This suggests that considerable portions of the nanotube surface are exposed to H_2O.[175] However, to date, a local model of solvatochromism that accounts for the nonhomogeneous structure around SWCNTs is missing.

One of the best understood systems is the recognition of small molecules by DNA-functionalized SWCNTs. Here, the mechanism of sensors for catecholamine neurotransmitters such as dopamine have been studied in greater detail (Figure 19d,e).

As these molecules are redox-active, they could reduce or oxidize either the SWCNT or the surrounding organic phase, thereby affecting the fluorescent properties. To study this potential mechanism, the redox potential and the fluorescent response of certain analytes were correlated. This study showed that molecules with a negative redox potential are more likely to increase the SWCNT fluorescence (Figure 19b).[63] However, as molecules of the same redox potential can induce drastically different fluorescence

responses, the redox potential alone cannot account for the fluorescence changes observed.[63] Likewise, fluorescent responses of ssDNA-functionalized SWCNTs to dopamine and riboflavin cannot be correlated to the amount of adsorbed nucleotides/DNA molecules on the SWCNT surface (Figure 19c), which suggests that more complex conformational changes are responsible for the change in the SWCNT fluorescence.[176] Molecular dynamics simulations showed that a stacking of dopamine with DNA-functionalized SWCNTs leads to interactions between the phosphate backbone of the DNA as well as the hydroxy and amine groups of dopamine (Figure 19d,e).[100] As a result of this interaction, the phosphate backbone moves toward the SWCNT surface and the electrostatic potential at the SWCNT surface changes (Figure 19d,e).[100] It is also known that the diffusion coefficient of the excitons in surfactant-containing systems changes with the surfactant identity and, furthermore, correlates with the fluorescence intensity.[48]

As pristine SWCNTs do not show any fluorescence response to dopamine[100] and differently functionalized SWCNTs display different affinities to neurotransmitters,[118] it follows that the organic phase (DNA) governs both the sensitivity as well as selectivity for this neurotransmitter.[118] The used biopolymers are typically charged and, consequently, electrostatic interactions play an integral part for biosensing.[177] It has been shown that the presence of certain salts alters the conformation of the DNA wrapping on the SWCNT[56,57] and decreases the electrostatic repulsions between equally charged molecules.[177] To reduce ion-induced fluorescence effects, the flexibility of the DNA can be altered by using xeno nucleic acids.[57] A good example of the influence of electrostatic repulsion and screening effects is the increased SWCNT surface accessibility at higher salt concentrations (Figure 19f).[177] In a surfactant-containing
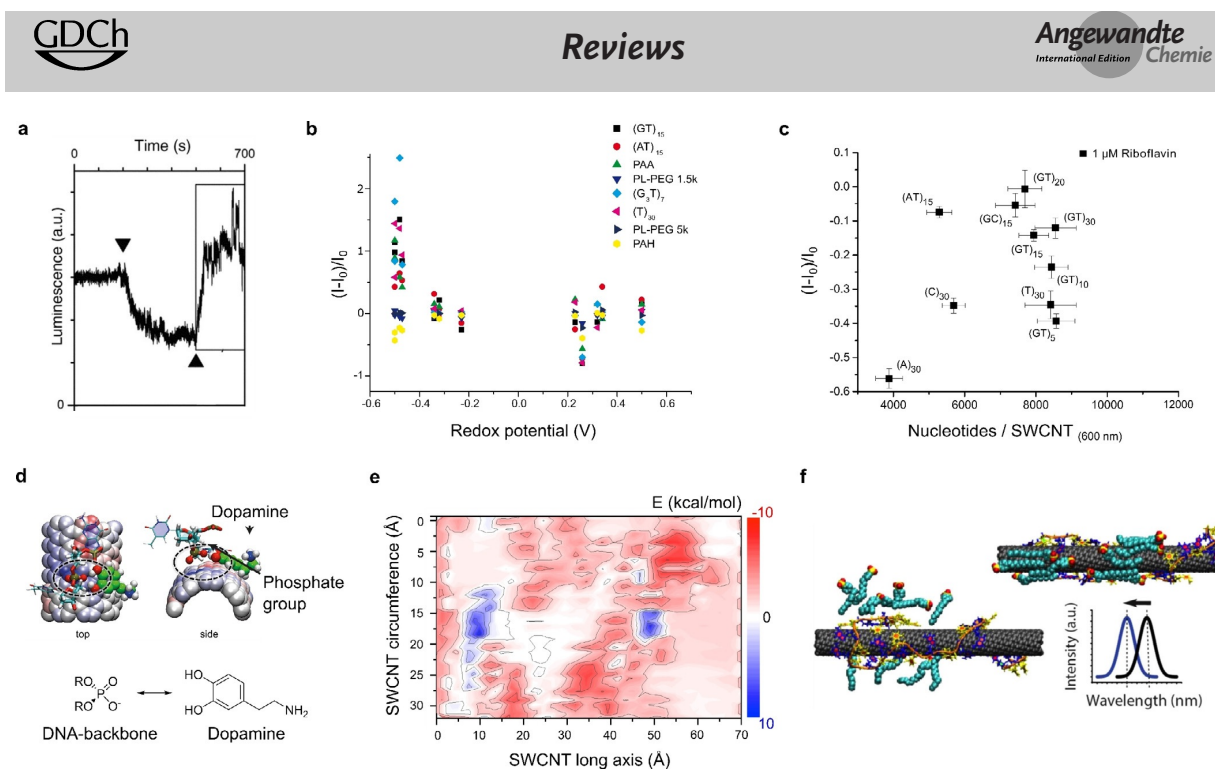
Figure 19. Insights into the mechanism of SWCNT-based sensors. a) Change in the fluorescence signal of an individual (7,6)-SWCNT upon successive addition of acid (▼) and base (▲). Luminescence recovery is observed after base addition, which indicates direct quenching by protons. Adapted from Ref. [47] with permission. b) Correlation between the fluorescence response of different SWCNT/polymer conjugates for different analytes (replicate symbols), such as dopamine and ascorbic acid, and the redox potential. The spread along the y axis indicates that the redox potential alone cannot explain the fluorescence change. Adapted from Ref. [63] with permission. Copyright 2016 American Chemical Society. c) There is also no simple correlation between the fluorescence response and surface coverage, shown here for ssDNA-functionalized SWCNTs and the response to riboflavin. Adapted from Ref. [176] with permission. Copyright 2019 American Chemical Society. d) Mode of interaction between dopamine and DNA-functionalized SWCNTs. The hydroxy groups of dopamine interact with the phosphate groups of the DNA backbone, which pulls them closer to the SWCNT surface. Most likely, solvation effects play an important role. e) Corresponding potential landscape on a SWCNT functionalized with $(GT)_{15}$ DNA. The blue regions with changed potential colocalize with the dopamine interactions site and affect the exciton fate. In this particular case, the fluorescence quantum yield increases. Adapted from Ref. [100] with permission. f) Wavelength shift in response to an interaction between ssDNA-suspended SWCNTs with SDBS, a surfactant. The hybridization of ssDNA is influenced by the salt concentration and changes the surface accessibility of the SWCNT. Reprinted from Ref. [177] with permission. Copyright 2018 American Chemical Society.

system, the exposed surface is covered by the surfactant, which causes a blue-shift of the NIR fluorescence, again demonstrating that the dynamics of the organic phase around the SWCNT is crucial for the sensing mechanism.[177]

By modulating the exposed surface area, it is furthermore possible to tune surfactant-suspended SWCNTs to respond to different bio-analytes.[137] Together, these findings indicate that fluorescence is modulated by the precise 3D arrangement of the molecules, ions, and water molecules in the vicinity of the nanotube.

3.3.3. Exciton Decay and Defects

As described above, the introduction of certain sp^3 defects into the carbon lattice of SWCNTs can increase the NIR fluorescence through the trapping of excitons.[53,74] The defined introduction of quantum defects, thus, provides a way to perturb the exciton decay and elucidate the involved processes that ultimately affect the fluorescent response. As the NIR fluorescent response of SWCNT-based sensors to

dopamine in H_2O and D_2O did not show major differences, electronic-to-vibrational energy transfer (EVET)[178] seems not to be a main factor in (dopamine) sensing.[87] In contrast, the correlation between the length of the SWCNTs and their fluorescent response seems to indicate that quenching at the ends plays a role. However, the fluorescence response was independent of the variation of defect density.[87] Together with the finding that a small number of quantum defects reverse the fluorescent response of DNA-functionalized SWCNTs to dopamine (Figure 6d), it follows that multiple rate constants are affected by the analyte.[87] Computationally, the experiments were best explained by a three rate constant model (3RC) that includes a decrease in the nonradiative decay from the E_{11} state (k_{nr}), an increase in the exciton diffusion constant (D_e), and an increase in the nonradiative decay constant from the E_{11}^* (k_{nr}^*) caused by dopamine.[87] Together, these insights highlight the complex interplay between photophysics and molecular recognition as well as new avenues to tailor sensing using defects.

3.4. Considerations on Kinetics and Imaging

The processes related to sensing happen on a certain time scale. How fast an analyte binds or dissociates from a sensor is determined by its kinetics. Additionally, the optical signal is detected in setups that determine aspects such as spatial resolution or imaging speed. In the following sections we discuss how these hallmarks of fluorescence sensors affect their performance.

3.4.1. Kinetics of Sensors and Impact on Spatiotemporal Resolution

Chemical imaging with many SWCNT-based sensors at one time is a highly effective strategy to gain chemical information from a sample with outstanding spatial and temporal resolution.[179] To understand how the collective image of such an array of sensors reflects the concentration of an analyte, Meyer et al. used stochastic Monte Carlo simulations to study the kinetic requirements for spatiotemporal chemical imaging with nanoscale sensors such as SWCNTs.[180]

The subject of the simulation was a nanosensor array being exposed to a changing concentration gradient of an analyte. To predict the image one gains from many sensors, single sensor responses were first simulated. In a typical scenario, the time-dependent concentration/diffusion profile of a dynamic process, such as release of signaling molecules (e.g. neurotransmitters) from cells and the stochastic binding site state of the sensors for certain rate constants, was simulated to calculate the expected fluorescence change of single sensors (Figure 20 a,b). The overall image was then calculated considering the individual fluorescence emission point spread functions and technical considerations, such as the frame rate of the camera. This simulation allows the prediction of how the rate constants of a sensor (k_{on}, k_{off}) and other factors affect the spatiotemporal resolution, for example, to resolve fast concentration changes such as neurotransmitter release from cells. It can serve as guiding principle for the chemical design but also for the interpretation of signals from a given biological problem. Phase diagrams

(Figure 20 c) indicated that the senors need a surprisingly low affinity ($K_d = 100$ µM) to resolve fast processes.

3.4.2. Ratiometric Detection

So far, optical biosensors based on SWCNTs have mainly been fabricated from mixtures of multiple chiralities. This leads to a large spectral overlap in the fluorescence emission, which complicates multiplexing and reduces sensitivity.

Advances in the separation and functionalization of SWCNTs have recently enabled the sole use of SWCNTs emitting below 1000 nm together with low-cost silicon-based detectors[145,181] for the development of ratiometric sensors,[20,29,30,32,33,112,121,154,169] in which two or more distinct NIR signals are detected simultaneously. Here, one SWCNT chirality is typically not responsive to the analyte and acts as a reference. Besides the fact that single chirality SWCNTs lead to six- to tenfold higher fluorescence intensities compared to multichirality SWCNT mixtures at the same concentration,[49,182] ratiometric approaches are more stable to external noise. Despite the clear advantages, the implementation was not possible for a long time because of difficulties in gaining chirality-pure SWCNTs.

Although progress was made in the synthesis of chirality-enriched SWCNT samples,[183] only a few chirality-enriched samples are commercially available. Different separation and purification methods have been developed. They range from density gradient centrifugation,[184] gel chromatography,[185] ion-exchange chromatography,[55] and aqueous two-phase extraction[186] to wrappings of special macromolecules that preferably solubilize certain chiralities.[22,187] What they all have in common is that the resulting pure chiralities are solubilized in certain polymers or surfactants. However, for a biosensing application it is necessary to tailor the surface chemistry. Therefore, straightforward processes are required that yield chirality-pure SWCNTs with tunable functionalization.[121]

The first ratiometric SWCNT-based sensor was demonstrated by Giraldo et al., who integrated into the leaves of plants two sensors: one for the detection of H_2O_2 and one for
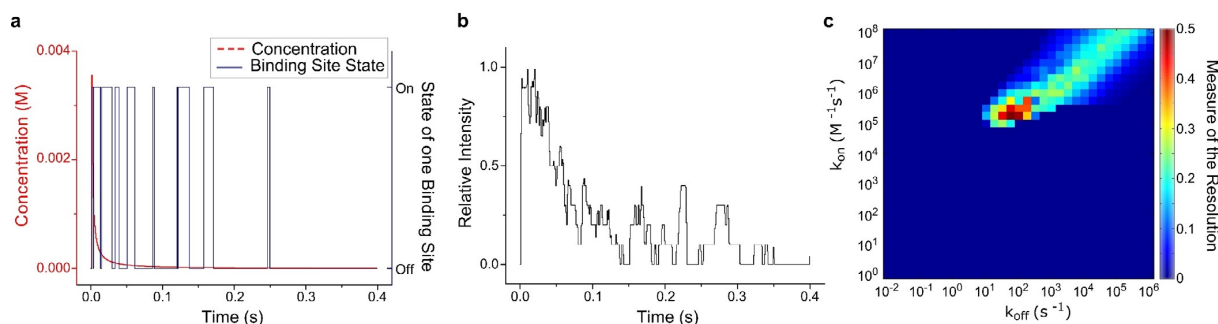
Figure 20. Kinetic requirements of sensors for spatiotemporal imaging. a) A stochastic-kinetic simulation allows the binding states (blue) to be predicted and consequently the fluorescence traces of single sensors in response to a changing concentration profile (red), for example, release of molecules from a cell. b) Relative intensity response of a single sensor over time based on the concentration profile shown in (a) and the assumption of 10 binding sites. c) Spatial and temporal resolution phase diagram as a function of rate constants. The red regions show combinations of rate constants that allow the detection of the biological events (here, release of molecules from a cell). Reprinted from Ref. [180] with permission. Copyright 2017 American Chemical Society.

Reviews
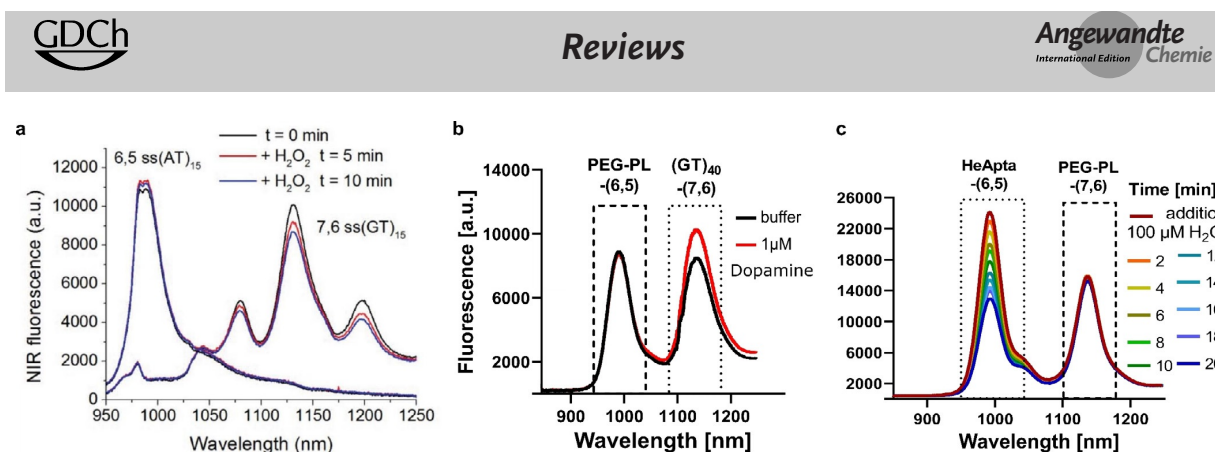
Figure 21. Ratiometric sensing. a) NIR fluorescence of $(GT)_{15}$-(7,6)-SWCNTs in response to H_2O_2 compared to the nearly invariant $(AT)_{15}$-(6,5)-SWCNT reference at different time points. Reprinted from Ref. [20] with permission. b,c) Ratiometric sensing of dopamine and H_2O_2 using PEG-PL as a reference and $(GT)_{40}$-SWCNTs or SWCNTs functionalized with the hemin-binding aptamer (HeApta). The reference sensor can be made from different colors of SWCNTs ((6,5) or (7,6) chirality). Adapted from Ref. [49] with permission. Copyright 2021 American Chemical Society.

NO.[20] The sensor system was based on the ratio of the distinct emission bands of two chirality species (Figure 21 a). Whereas the $(GT)_{15}$-(7,6)-SWCNT-based sensor was quenched by 20 % within 10 min in the presence of 100 µM H_2O_2, the reference sensor remained mostly invariant to the analyte. The overall sensor response was similar to in vitro tests.

Most recently, Nißler et al. combined the isolation of specific SWCNTs and their subsequent functionalization for the detection of neurotransmitters and other small molecules.[49] They used aqueous two-phase extraction to obtain chirality-pure (6,5)-, (7,5)-, (9,4)-, and (7,6)-SWCNTs and applied a surface exchange through dialysis to remove the DOC wrapping of the SWCNTs and replace it with specific ssDNA sequences or aptamers. This approach enabled the fabrication of ratiometric sensors, for example, for the detection of dopamine and H_2O_2 (Figure 22 b,c). For these sensors, SWCNTs were functionalized either with a $(GT)_{40}$ sequence or, in the case of H_2O_2 detection, with an aptamer (hemin binding aptamer, HeApta) that binds the protoporphyrin hemin and catalyzes the decomposition of H_2O_2. PEG-

PL-functionalized SWCNTs of another chirality served as an invariant reference. These examples show the potential of ratiometric or multiplexed sensing and given the large wavelength range of SWCNT fluorescence, there are plenty of opportunities for advanced sensing schemes.

3.4.3. *Remote Imaging and Alternative Excitation Pathways*

Remote imaging—the spatial separation of molecular sensors and detectors—is particularly beneficial to observe biochemical processes non-invasively, for example, in biomanufacturing or in vivo. As only a small portion of the emitted light is captured by a camera within a certain distance to the sensors, remote detection requires either bright fluorophores or cameras with a high quantum yield in the spectral window of the fluorophore emission.

An example for remote imaging are NIR fluorescent nanosheets, which were remotely detected in a customized portable setup.[171, 188] Due to the high brightness and emission closer to the visible range (910 nm), a low-cost CMOS camera (Complementary Metal Oxide Semiconductor, Si based),
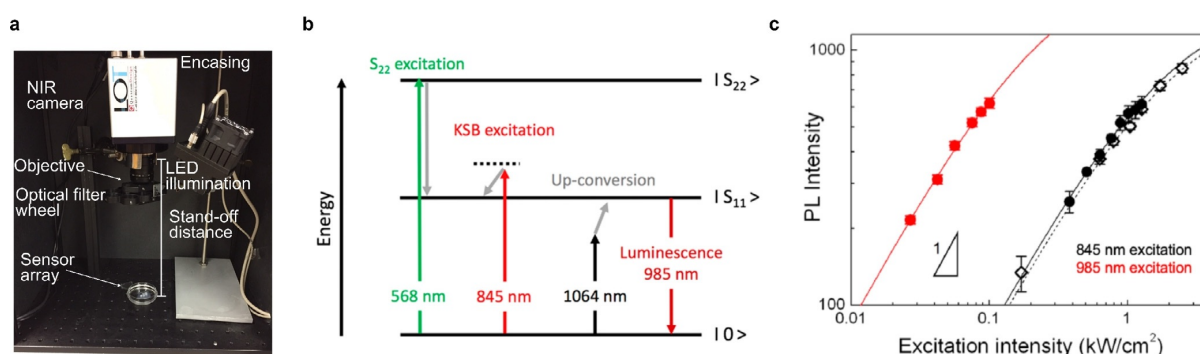
Figure 22. Imaging and excitation approaches. a) Customized portable NIR standoff device enables remote detection (25 cm) by fluorescence sensors, for example, of bacteria.[29, 171, 188] Adapted from Ref. [29] with permission. b) Different possible excitation pathways for fluorescent (6,5)-SWCNTs. Reprinted from Ref. [189] with permission. Copyright 2018 American Chemical Society. c) Comparison of fluorescence brightness of *p*-nitroaryl SWCNTs with introduced sp³ defects wrapped with PEG-PL (solid circles) on excitation of the KSB (845 nm) or E_{11} (985 nm) with PEG-PL-SWCNTs (open diamonds, KSB excitation). Reprinted from Ref. [190] with permission.

which typically has a low quantum efficiency of around 5 % in the NIR region, could be used here.

Additionally, this setup was modified for SWCNT detection by using an NIR-sensitive InGaAs camera, a white-light LED, and corresponding filters for wavelength-specific excitation and detection of emission (Figure 22 a). Up to now, remote imaging of fluorescent SWCNT-based sensors has been used for the identification of bacteria[29] and monitoring of plant health,[30–32,148] for which resolutions in the (sub-)-millimeter range were achieved with standoff distances of up to 1 m.

Apart from exploiting the decreasing sensitivity of Si-detectors in the NIR, efforts have been made to promote NIR-fluorescent transducers using straightforward designs for inexpensive NIR fluorimeters.[167] Instead of using high-cost InGaAs photodiode arrays, single InGaAs diodes were combined with a motorized stage controlled with an open source programming language. The robustness of these devices outside of the laboratory was demonstrated in a high-throughput format with field-side measurements of soil samples. Future developments might also show remote detection using pure (6,4)-SWCNTs with Si-based cameras and also versatile use as smart surfaces, for example, for monitoring contamination with pathogens, such as bacteria, on medical surfaces or even implants.

Fluorophore brightness is not the only performance-related factor when measurements in live biological tissues are carried out. Fluorophore stability as well as wavelength-dependent tissue scattering, absorption, and the background originating from autofluoresence must also be considered. From this point of view, SWCNTs have excellent photophysical properties.

However, imaging at the single molecule level is always accompanied by considerations to achieve a high signal to noise ratio. Long-term single SWCNT imaging has, in particular, become established for (6,5)-SWCNTs in living cells[191] and brain tissue.[192]

Although the second-order excitonic transition, E_{22} (S_{22}), is typically used for excitation, alternative excitation pathways such as the K-momentum exciton-phonon sideband (KSB) excitation[193] and up-conversion excitation[194] have been successfully demonstrated, but excitation efficiency, photostability, as well as absorption and scattering of molecules in tissue differ depending on the excitation wavelength. Danné et al. evaluated the different excitation options (Figure 22 b) for optimal single (6,5)-SWCNT imaging.[189] Here, E_{22} excitation of PEG-PL SWCNTs was found to be four times more efficient than KSB excitation and an order of magnitude more efficient than 1064 nm up-conversion excitation, while the signal to noise ratio was more than five times higher for KSB and up-conversion excitation. However, the excitation at the E_{22} transition is not ideal due to limited tissue penetration depth and autofluorescence. In addition, simulations to quantify the impact of tissue absorption showed that a higher temperature rise of the tissue induced by up-conversion excitation might be an issue, thus suggesting that KSB excitation is the best choice when considering all the factors. Nevertheless, it still requires relatively high excitation doses in the $kW\,cm^{-2}$ regime.

Recently, single SWCNT imaging was performed in brain tissue in vivo by using ultralow excitation doses of $0.1\ kW\,cm^{-2}$ (Figure 22 c).[190] To achieve this, sp^3 defects were introduced into (6,5)-SWCNTs, which lead to a fluorescence emission at E_{11}^* (1160 nm) when exciting at the first-order excitonic transition E_{11} (985 nm). This approach is beneficial as a result of excitation in the NIR window, but also because of the increased brightness by channeling free excitons to defect sites and subsequent E_{11}^* emission.

Another way to both excite and detect in the NIR region is the use of multiphoton microscopy. This technique relies on the nonlinear excitation of at least two photons and is optimal for in vivo tissue applications when using NIR radiation. Del Bonis-O'Donnell et al. demonstrated two-photon 1560 nm excitation of dopamine-sensitive SWCNT-based sensors, which showed only 4 % scattering (one-photon excitation: 42 % scattering).[195] However, the frame rate is significantly reduced for single sensor imaging compared to wide-field one-photon excitation.[196]

3.4.4. *Hyperspectral and Spinning Disc Microscopy*

Hyperspectral microscopy (i.e. simultaneous imaging at different wavelengths) provides another approach to exploit the spectral variety for multiplexed SWCNT imaging. Roxbury et al. resolved up to 17 distinct chiralities with single nanotube spatial resolution.[197] In contrast to organic fluorophores, more chiralities can be imaged simultaneously in a certain emission window due to the narrow emission bands of SWCNTs. The hyperspectral imaging is based on the use of a volume Bragg grating (VBG) placed between the emission port of an inverted fluorescence microscope and the NIR camera. The VBG filters one specific emission wavelength depending on optical properties such as the incident angle θ and the grating period Λ (Figure 23 a).

The spatial imaging of different chiralities is then achieved by measuring a continuous stack of 152 images within a time frame of 20 s and 10 min depending on the signal intensity and, thus, the integration time. By using this approach 12 different chiralities from DOC-SWCNTs in live human cervical cancer cells could be detected (Figure 23 b). Additionally, individual SWCNTs adsorbed on a surface in live mammalian cells, murine tissues ex vivo, and zebrafish endothelium in vivo were imaged.

Another challenge of typical wide-field microscopy setups is the poor z-resolution. To improve this limitation, a NIR spinning-disc confocal laser microscope with an increased resolution and imaging contrast was demonstrated by Zubkovs et al. (Figure 23 c).[198] The custom-built microscope was based on a spinning-disc module integrated between a cooled InGaAs camera and the microscope body, which rejects out of focus light.

To achieve a maximized photon intensity, the lenses in the spinning disc unit were optimized for the NIR region. The authors showed in different biological applications the advantages of an improved lateral/axial resolution of $0.5 \pm 0.1\ \mu m\,/0.6 \pm 0.1\ \mu m$ (enhancement of 17 % /45 %) compared to the wide-field configuration, reaching from single-particle tracking over the spatial distribution of nanoparticles within

Angew. Chem. Int. Ed. **2022**, 61, e202112372 (24 of 50)

© 2022 The Authors. Angewandte Chemie International Edition published by Wiley-VCH GmbH

Reviews
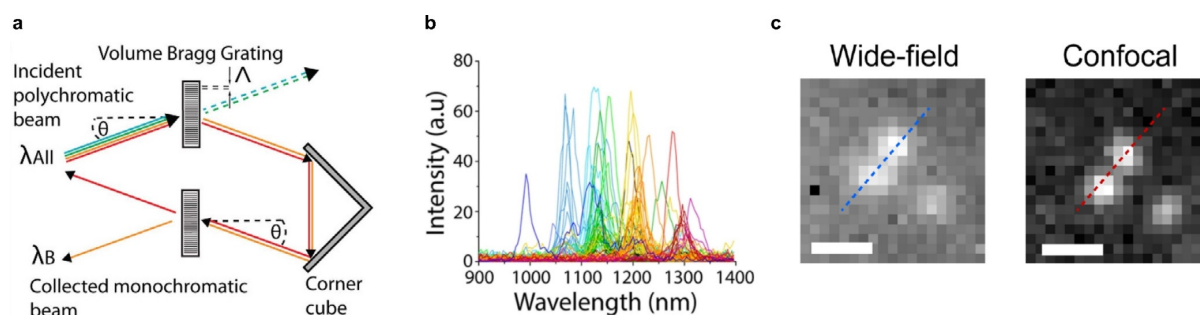
Figure 23. Advances in spatial and spectral resolution. a) A Volume Bragg grating filters one specific emission wavelength depending on the incident angle θ, refractive index n, and grating period Λ, which enables hyperspectral imaging. b) Detection of 12 different SWCNT chiralities without deconvolution in live human cervical cancer cells. Reprinted from Ref. [197] with permission. c) Improved NIR image contrast of NIR fluorescent beads with a spinning disc NIR fluorescence microscope in comparison to wide-field microscopy. Reprinted from Ref. [198] with permission.

an organelle to the optical in situ monitoring of glucose by GOx-SWCNT-based sensors embedded within an agarose gel. Overall, this approach showcases the opportunities for in vitro and in vivo imaging and sensing with improved spatiotemporal resolution.

4. Outlook and Perspectives

SWCNTs have shown their large potential as versatile building block for biosensors. The last few years have provided fundamental mechanistic insights, novel recations, and novel applications such as sensing in plants or primary cells. The advent of covalent quantum defect chemistry as well as the broader availability of monochiral samples will further advance typical figures of merit such as selectivity and robustness in demanding biochemical environments. One of the key challenges remains a basic understanding of molecular recognition and also signal transduction in the organic phase around these materials. Advances in this space can directly translate into superior selectivities. Additionally, high-throughput or screening approaches will increase the speed of chemical discoveries. This is particularly interesting for applications in complex biological environments, where interactions become too complex to be predicted. Several milestones remain to be achieved before transfer into commercially available products. In vivo applications require long-term evaluation of each sensor's toxicology and stability profile. Here, new covalent quantum defect functionalization strategies as well as the standardization of protocols and the purity of SWCNTs offer promising opportunities. Additionally, higher degrees of multiplexing and the adaptation of conventional cameras and readout systems will increase the application potential of SWCNT-based sensors. In summary, SWCNT-based biosensors offer a rich playground for chemistry and related disciplines and promise further advances and breakthroughs in the near future.

Appendix

Table 1: Detailed overview of fluorescent SWCNT-based sensors of ROS/RNS.[a]

Target	Biological system	Recognition strategy	Sensitivity	Selectivity	SWCNT chirality/wavelength	Spatial resolution	Temporal resolution	Reversibility
Arsenite[33]	In buffer (NaCl, MES, TES), embedded in plant tissue by syringe infiltration, uptake by plants through the roots	Screening approach: (GT)$_5$-SWCNTs FI increase TO-PRO-1-(GT)$_5$-SWCNTs (dye) FI decrease	In buffer (NaCl) LOD 122 nM In hyperaccumulator plants theoretical LOD 4.7 nM/1.6 nM after 7/14 days	Over other heavy-metal ions present in soil, e.g. Mn^{2+}, Cd^{2+}, Pb^{2+}, Ni^{2+}, Hg^{2+}	HiPCO (9,4) at 1128 nm Dye for additional fluorescence in the visible range: 540 nm	Sub-mm for a standoff distance of 1 m Subcellular with TO-PRO-1-(GT)$_5$-SWCNTs (visible confocal microscopy)	Real time Intensity increase of sensors in plants 30 min after 10 μM arsenic introduction, after 5 h 11—15% increase	No
Group 2 and 12 metal ions[199]	In solution (NH$_4$OH, NaOH)	SDBS-SWCNTs FI decrease	0.5—5 mM tested	Varying quenching efficiency for different ions and SWCNT chiralities	HiPCO Analysis of each individual chirality at 925—1425 nm	ND	Measurement after 1 h of metal ion addition	ND
Divalent ions[25,109]	In Tris buffer, blood, black ink, tissue, within living mammalian cells	ssDNA-SWCNTs ssDNA tested: (GT)$_{15}$, (GC)$_{15}$, 5'-TAG CTA TGG AAT TCC TCG TAG GCA-3' Red-shift	Concentration and chirality dependent red-shift for different cations Hg^{2+} > Cu^{2+} > Co^{2+} > Ca^{2+} > Mg^{2+}[131] LOD 3.5 mM/8 mM in blood/tissue	Responds to different divalent ions	Chirality mix (6,5) peak mostly analyzed	ND	Within minutes	Yes, with dialysis to remove ions
H$_2$O$_2$, H$^+$, Fe(CN)$_6$$^{3-}$[200]	Embedded in collagen film	Collagen-SWCNTs FI changes in discrete quenching steps	Single molecule	Different quenching equilibrium constants: 1.59/1.37 for H$_2$O$_2$/Fe(CN)$_6$$^{3-}$ at 20 μM, similar constant for H$^+$ at 0.1 M	HiPCO (6,5), (10,2), (9,2), (8,7) 900—1600 nm	Single molecule 4 pixels, 900 nm × 900 nm**	Real time 1 s**	H$_2$O$_2$- and H$^+$-induced quenching reversible with MnO$_2$ catalyst for H$_2$O$_2$/NaOH decomposition
H$_2$O$_2$[125]	H$_2$O$_2$ emitted from A431 human epidermal carcinoma cells	Collagen-SWCNTs FI changes in discrete quenching steps	Single molecule	Over H$^+$, NO, NO$_2$$^-$, NO$_3$$^-$, Dulbecco modified Eagle's medium (DMEM), L-15, ^{1}O$_2$, O$_2$ NO: largest forward rate constant, but binds nearly irreversibly, nitrites and nitrates: small rate constants	HiPCO	Sub-μm	Real time Typical observation time 3000 s	Yes
H$_2$O$_2$[126]	H$_2$O$_2$ generated from live human umbilical vein endothelial cells stimulated by vascular endothelial growth factor (VEGF) and artificial proangiogenic factor Eu(OH)$_3$ nanorods	Collagen-SWCNTs FI changes in discrete quenching steps	Single molecule 12.5—400 nM	see Ref. [125]	Chirality mix	Single molecule 300 nm pixel size**	Real time 1 s**	Yes

Reviews

Table 1 (Continued)

Analyte [ref]	Setup	SWCNTs / mechanism	µmol L⁻¹ range tested	Selectivity	Chirality / emission	Spatial resolution	Temporal	Reversibility
H_2O_2[111]	Incubated in gemcitabine/irinotecan-treated Pancreatic ductal adenocarcinoma (PDAC) cells, implanted in tumors of PDAC murine model in response to gemcitabine	(GT)$_{15}$-SWCNTs Fl quenching Alteration of Raman G-band intensity		ND	HiPCO Raman G-band intensity at 1590 cm⁻¹	µm	Real time Measurement after 0–48 h of gemcitabine-/irinotecan-treatment	Yes
H_2O_2[31]	Embedded in leaves of Arabidopsis plants, in vivo monitoring of stresses (UV-B light, high intensity light, pathogen-related peptide)	Rational approach: Hemin-binding-aptamer SWCNTs Hemin binds Fe^{3+}, which catalyzes a Fenton-like reaction of H_2O_2 into hydroxyl radicals that quench fluorescence	10—100 µM	Over Ca^{2+}, sugar (sucrose, glucose), plant hormone levels (methyl salicylate, abscisic acid (ABA), jasmonate (JA)), mechanical wounding	HiPCO >900 nm	Sub-mm with standoff detection	Real time 60/120 min for saturation after pathogen-/environmental-related stress (UV-B-/high intensity light)	Yes
H_2O_2[32]	Embedded in leaves of plants, in vivo monitoring of wound-induced H_2O_2 waves and other stresses (high intensity light, heat stress, pathogen-related peptide)	(GT)$_{15}$-SWCNTs Fl decrease	µM—mM	Over other plant analytes (JA, auxin, ABA, salicylic acid, glutamates, Ca^{2+} ions), NO, NO_3^-, antioxidant O_2, OH caused Fl decrease, but not reversible	HiPCO 950 nm—1250 nm	Sub-mm for a standoff distance of 1 m Wave speeds due to different stress treatments from 0.44 to 3.10 cm min⁻¹	Real time Response within 4 min after wound infliction, recovery after 10–20 min	Yes, due to unbinding or consumption by antioxidants and peroxidases
H_2O_2[112]	Embedded in wearable microfibrous textiles, in presence of peroxide-producing macrophages, incorporated in wound bandages	(GT)$_{15}$-SWCNTs Chiralities show different quenching degree in response to H_2O_2	5 µM–5 mM	See Refs. [20, 32, 110]	HiPCO (8,7)/(9,4)	Sub-µm	Real time within 5—30 min	Yes, within 50 min
NO/H_2O_2[20]	Leaves mounted on microfluidic chamber, in vivo in leaves of Arabidopsis plants	(GT)$_{15}$-SWCNTs Fl decrease	Tested: NO in vitro/in vivo 500 µM/50 mM, H_2O_2 in vitro/in vivo 10 mM/100 µM	See Ref. [110]	Monochiral (7,6) 1135 nm/1131 nm for NO/H_2O_2	Sub-µm	Real time in vitro/in vivo: >600 s/50 s for saturation	Yes
NO[124]	In PBS, macrophage cells, mouse model	Rational approach: 3,4-diaminophenyldextran-SWCNTs Fl decrease	LOD in solution/cells 70 nM/200 nM	Over other ROS/RNS (e.g. NO_2^-, NO_3^-, ONO_2^-, HNO, OCl^-, OH*, H_2O_2)	Chirality mix 950—1350 nm	Sub-µm in cells	Real time Bleaching rate $k=0.856$ s⁻¹ for (10,5)-SWCNTs	With reducing agent
NO[13]	Immobilized	Screening approach: (AT)$_{15}$-SWCNTs Fl changes in discrete quenching steps	Single molecule LOD 300 nM	Over other ROS/RNS, dopamine, NADH, L-ascorbic acid, riboflavin	HiPCO 900—1400 nm	Single molecule 4 pixels, 580 nm × 580 nm**	Real time Response time for NO: 1.1 s	Yes

GDCh   *Reviews*   **Angewandte** *Chemie* — International Edition

Table 1 (Continued)

	Application	Sensor	LOD / Response	Selectivity	Nanotube / chirality	Spatial resolution	Temporal resolution	Reversible
NO[127]	Intravenous injection into mice, localization within the liver. Implantation of alginate-encapsulated SWCNTs within specific tissue	PEG-(AAAT)$_7$-SWCNTs FI decrease	LOD 1 μM	Less quenching with other ROS/RNS	CoMoCAT-SWCNTs (6,5) at 990 nm	Sub-mm	For injection/implantation within s min⁻¹ (93 % quenching after 30 min)	Yes
NO[128]	In cultures of A375 melanoma cells through micropinocytosis, NO production using NO-releasing anticancer drug JS-K. VEGF-mediated NO production in endothelial cells	(AT)$_{15}$-SWCNTs FI decrease	JS-K concentrations of 16–28 μM tested. VEGF concentrations between 10 ng mL⁻¹ (LOD) and 100 ng mL⁻¹	See Ref. [13]	HiPCO	Sub-μm	Real time 400 s to reach steady state (after JS-K addition)	Yes
NO[19]	In extracted chloroplasts and leaves of Arabidopsis plants, in vivo by infiltration through the leaf lamina	(AT)$_{15}$-SWCNTs FI decrease	40%—60% FI decrease	See Ref. [13]	HiPCO (8,6), (12,1), (11,3), (8,7), (10,5) 1150—1450 nm	Sub-μm	Real time. Less than 150 s for reaching steady state (after NO exposure)	ND
^{1}O$_2$[131]	In buffer (NaH$_2$PO$_4$/Na$_2$HPO$_4$)	Screening approach: 10 ssDNA sequences tested, e.g. (GT)$_{10}$, (GT)$_{20}$, (ATT)$_4$, (GT)$_4$-SWCNTs FI decrease	Depending on ssDNA and SWCNT chirality, 9—40% quenching with 1 atm O$_2$ compared to samples purged with 1 atm Ar	Relatively insensitive to pH	HiPCO	ND	Within seconds	yes
^{1}O$_2$[20]	SWCNTs challenged with different tyrosinase substrates for enzyme-catalyzed reactions	Tyrosinase-conjugated-PEG$_{12}$-(GT)$_{15}$-amine-SWCNTs Red-shift and FI decrease	0.01–1 mm of tyrosinase substrates. Response curves for different tyrosinase inhibitors measurable, IC$_{50}$ values of suicide inactivation, e.g. 0.5 mm for kojic acid	For tyrosinase inhibitors which induce suicide inactivation of the enzyme	HiPCO 950—1350 nm	Single-sensor	Within minutes 0.0281 nm min⁻¹ with L-tyrosine, 0.75 nm min⁻¹ with pyrogallol	ND
Single protons/pH[47]	Embedded in agarose gel	SDBS-SWCNTs FI changes in discrete steps	Single molecule	Response to chemical reactions with acid, base, diazonium reactants	HiPCO individual chiralities, e.g. (8,6) at 1175 nm, (8,3), (11,1)	Single molecule 4 pixels, 670 nm × 670 nm **	Real time 54 ms **	For acid reactions

[a] FI: fluorescence intensity, ND: not determined, **: limited by the Abbe limit, diffusion, and detection speed.

GDCh   *Reviews*   Angewandte
International Edition   Chemie

Table 2: Detailed overview of fluorescent SWCNT-based sensors for neurotransmitters.[a]

Target	Biological system	Recognition strategy	Sensitivity	Selectivity	SWCNT chirality/ wavelength	Spatial resolution	Temporal resolution	Reversibility
Dopamine (DA)[15]	In PBS, immobilized	Screening approach: (GT)$_{15}$-SWCNTs and other candidates FI increase	Depending on chirality LOD in solution 11 nM	Response to other catecholamines with different magnitude	HiPCO (6,5) at 991 nm, (7,5) at 1044 nm, (10,2) at 1077 nm, (9,4) at 1132 nm, (8,6) at 1203 nm	Single sensor 4 pixels, 585 nm × 585 nm**	Real time Within seconds	Yes
Reducing and oxidizing molecules, e.g. ascorbic acid/oxidized ascorbic acid, cysteine/cystine, DA, epinephrine (EPI), glutathione/oxidized glutathione, riboflavin, trolox[63]	In PBS	FI increase with negatively charged polymer wrapping (e.g. ssDNA, poly(acrylic acid)) FI decrease with positively charged wrapping (polyallylamine-SWCNTs) No FI change with PL-PEG-SWCNTs	100 µM tested Polymer-wrapped SWCNTs that respond to reducing molecules (e.g. +141%, ascorbic acid) also respond to oxidizing molecules (e.g. 81%, riboflavin) Up to 250% FI increase with reducing molecules such as ascorbic acid, EPI, trolox with negatively charged wrapping, but redox potential alone cannot explain FI changes	Different responses for different small molecules	CoMoCAT (6,4), (8,3), (9,1), (6,5), (7,5) 800—1050 nm	ND	ND	ND
Catecholamine (DA, EPI, norepinephrine (NE), amino acids, saccharides, riboflavin[202]	In PBS	ssDNA-SWCNTs (24 sequences tested, e.g. (ATT)$_4$, (TAT)$_4$, (ATTT)$_3$) FI increase for catechol-amines and ascorbic acid	Chirality-dependent FI change, e.g. smaller diameter SWCNTs with (TAT)$_4$ wrappings are less responsive than larger diameter SWCNTs	Different responses for different small molecules	HiPCO (8,3), (6,5), (7,5), (10,2), (9,4), (7,6), (12,1), (11,3)	ND	ND	ND
DA[100]	Collagen-coated SWCNTs for increased cell adhesion, immobilized on glass, PC12 neuroprogenitor cells cultivated on top	Screening approach: (GA)$_{15}$-SWCNTs FI increase Interaction of hydroxy groups of DA with phosphate groups of DNA backbone pulls phosphate groups closer to the SWCNT surface, which increases the FI.	Single molecule LOD 100 pM	Not over catecholamine homologues (e.g. EPI, NE, L-ascorbic acid), but PC12 cells mainly release dopamine	(6,5)-enriched chiralities (6,5) at 980 nm	>20,000 sensors per cell 850 nm pixel size**	<100 ms	Yes

Table 2 (Continued)

Analyte	Sample/condition	Approach	LOD / Performance	Selectivity / Notes	SWCNT	Spatial resolution	Temporal resolution	In vivo
Catecholamine (DA, EPI, NE)[118]	In PBS, DA in presence of NE	Screening approach: different ssDNA-SWCNTs, e.g. A_{30}, $(GT)_{10}$, $(GC)_{15}$, $(AT)_{15}$, $(GT)_{10}$, for different selectivity and sensitivity FI increase $(GT)_{10}$-SWCNTs for sensing DA in presence of NE	LOD mostly in single-digit nM regime LOD of dopamine in presence of NE 4.9 nM, without NE 0.1 nM	Dissociation constants vary between 2.3 nM ($(GC)_{15}$-SWCNTs + NE) and 9.4 µM ($(AT)_{15}$-SWCNTs + DA)	(6,5)-enriched at 987 nm	Single nano-sensor	Real time Within seconds	Yes
Catecholamine release, e.g. DA[120]	Brain slices from dorsal striatum of mouse incubated in artificial cerebro-spinal fluid (ACSF)	$(GT)_6$-SWCNT FI increase	10 nM—100 µM	Over γ-aminobutyric acid, glutamate, acetylcholine In the presence of pharmacological DA receptor ligands Not for DA over NE	HiPCO (9,4) at 1128 nm	µm	Sub-second	Yes
DA[121]	In PBS	$(GT)_{10}$-SWCNTs FI increase	>20% intensity increase (100 nM)	ND	Monochiral (6,5) at 980 nm	ND	ND	ND
DA, riboflavin, H_2O_2, pH[176]	In PBS	ssDNA-SWCNTs, e.g. $(GT)_5$, $(GT)_{15}$, A_{30}, T_{30}, C_{30}	In most cases FI change does not correlate with the number of adsorbed ssDNA molecules	Different responses for different small molecules	CoMoCAT	ND	ND	ND
DA[203]	Acute mouse brain slices in ACSF, electrically evoked neurotransmitter release	PEG_{2000}-PL-$(GT)_6$-SWCNTs FI increase Improved sensor response due to PL-induced quenching of SWCNT baseline FI	In vitro: increased sensor response to 200 µM DA of $\Delta I/I_0=2.01$ compared to nonpassivated sensors $I_0=1.44$ Ex vivo in brain slices: increased responsivity by $52\pm8\%$ and improved number of identified ROI by $160\pm50\%$	Reduced protein adsorption of 28% compared to nonpassivated sensors	HiPCO	Sub-µm	Real time 111 ms**	Yes
DA[80]	Self-assembled on neutravidin-coated microscopy slides	Screening approach: Combination of covalent and noncovalent SWCNT functionalization $(GT)_{15}$-amine-PEG2k-biotin-SWCNTs $(GT)_{15}$ is able to detect DA, while biotin is able to detect neutravidin and streptavidin	$\Delta I/I_0=0.8658\pm0.1986$ for 25 µM DA	ND	HiPCO (10,2) at 1053 nm	ND	Real time Sub-seconds	Yes

Table 2 (Continued)

Analyte [ref]	Description	Sensor	Range / LOD	Selectivity	Nanotube	Resolution	Time	In vivo
DA, H$_2$O$_2$ [139]	SWCNT uptake, transport, and programmed release by human immune cells (neutrophilic granulocytes, neutrophils)	DA: (GT)$_{15}$-SWCNTs, FI increase; H$_2$O$_2$: Heminaptamer-SWCNTs, FI decrease	100 nM DA and 100 μM H$_2$O$_2$ tested; Sensors functional after cargo transport and release	ND	CoMoCAT	ND	Within seconds	ND
DA [136]	Immobilized on surface in complex medium (e.g. Schneider's medium); In presence of CaCl$_2$; Drosophila neurons	Locked nucleic acid bases incorporated into (GT)$_{15}$ sequence	LOD 10 nM; Superior compared to (GT)$_{15}$-SWCNTs in presence of CaCl$_2$/Schneider's medium	Over Ca^{2+}	HiPCO (7,5), (7,6)	ND	Measurement after 5 min—24 h	ND
DA, NE [119]	In PBS, NaCl, protein-rich media (DMEM + 10% fetal bovine serum (FBS)) and ACSF	Screening approach of (GT)$_x$ sequences: (GT)$_6$-SWCNTs FI increase	Down to 100 nM tested 3500%/2300% increase to 100 μM NE/DA in PBS 143%/260% increase to 100 μM DA in DMEM + FBS/ ACSF	Over acetylcholine, serotonin, histamine, γ-aminobutyric acid, glutamate, glycine, aspartate, DA transporter inhibitor nomifensine, DA receptor agonist quinpirole, antagonist sulpiride, and haloperidol	HiPCO (9,4) at 1127 nm	ND	Measurement after 5 min/ 1 h of analyte incubation	ND
DA, riboflavin, pH, H$_2$O$_2$ [49]	Immobilized	DA: (GT)$_{40}$ SWCNTs, Riboflavin: (GT)$_{40}$ SWCNTs, pH: PEG-PL-SWCNTs, H$_2$O$_2$: hemin-binding aptamer-SWCNTs	Higher brightness of monochiral sensors, μM range for H$_2$O$_2$ detection	Affected by surfactant residues, differences in sensing magnitudes for different sequences/ analytes	Monochiral (6,5) at 990 nm, (7,6) at 1130 nm	ND	ND	ND
DA [135]	Release from primary neurons (varicosities) using a sensor paint (AndromeDA)	(GT)$_{10}$-SWCNTs FI increase; Sensors are applied on top of cells as sensor coating/paint (AnromeDA)	1 nM—100 μM EC$_{50}$: 299 nM	Over neurons treated with inhibitor reserpine (depletes DA)	CoMoCat	Subcellular Discriminates individual varicosities (up to 100 within a single imaging field)	Real time 15 images s^{-1}	Yes
Serotonin [27]	Release from human blood platelets	Serotonin-binding-aptamer-SWCNTs FI increase	100 nM—10 μM	Over tryptophan, histamine, tyrosine, glucose 11% increase to 100 nM DA compared to 45% increase to serotonin	(6,5)-enriched chiralities (6,5) at 995 nm	Subcellular 63 nm pixel size**	Real time (Sub)second	Yes
Serotonin [134]	Acute striatal brain slices of mice and exogenous addition of serotonin	Screening approach: Identification of polynucleotides by exponential enrichment for selective ssDNA-SWCNTs	100 nM—50 μM	Over serotonin analogues, metabolites, and receptor-targeting drugs (e.g. 5-hydroxytryptophan, 5-methoxytryptophan, fluoxetine) FI increase due to DA of 1400%	HiPCO (8,6) at 1195 nm	Sub-μm	Real time (Sub)second	Yes

[a] FI: fluorescence intensity, ND: not determined, **: limited by the Abbe limit, diffusion and detection speed.

Table 3: Detailed overview of fluorescent SWCNT-based sensors for other small molecules.[a]

Target	Biological system	Recognition strategy	Sensitivity	Selectivity	SWCNT chirality/wavelength	Spatial resolution	Temporal resolution	Reversibility
Acetic acid[145]	In DI water, wine; Analytes injected into glass bottle with inlet and outlet tubes	Screening approach: Peptide-encapsulated SWCNTs (YK-SWCNT) detect volatile molecules; Synthesized peptide (YK): contains positive charge to potentially improve acetic acid binding to the sensor and aromatic amino acids to enhance π-π interaction and binding to SWCNTs	In DI water: concentrations of 0.05%–3.2% (v/v) tested; In wine: 0.05% (v/v) and 0.1% (v/v) tested	Slightly increased sensor response at higher humidity results in stronger quenching due to additional binding of water molecules to the sensor; In wine, other volatile compounds interfere with sensor	CoMoCAT (6,5) at 970–1050 nm	ND	Real time; Steady state after 40 s; In wine: no steady state after 90 s, but significant Fl change	Yes, but slow. Illumination with UV light enhances recovery speed
Adenosine-5'-triphosphate (ATP)[140]	In Tris-HCl buffer, cellular ATP detection in living HeLa cells	Rational approach: PL-PEG-functionalized SWCNT/luciferase enzyme conjugate; Fl quenched by the luciferase-mediated bioluminescence reaction product oxyluciferin in the presence of ATP and D-luciferin; Fl decrease	LOD 240 nM	Over Adenosine 5'-monophosphate, adenosine 5'-diphosphate, cytidine 5'-triphosphate, guanosine 5'-triphosphate	Chirality mix	μm	Real time; Measurement after 15 min of analyte addition	No
DA, riboflavin, pH, H2O2[49]	Immobilized	DA: (GT)40-SWCNTs; Riboflavin: (GT)40-SWCNTs; pH: PEG-PL-SWCNTs; H2O2: hemin-binding aptamer-SWCNTs	Higher brightness of monochiral sensors, μM range for H_2O_2 detection	Affected by surfactant residues, differences in sensing magnitudes for different sequences/analytes	Monochiral (6,5) at 990 nm, (7,6) at 1130 nm	ND	ND	ND
Doxorubicin[143]	In water or water/DMSO mixture, human blood plasma, mouse tissue	Screening approach: CCCCCCCCAGAATTACTTCCCCCCCC-SWCNTs; Fl change and red-shift (shift for readout)	In buffer: LOD 8 μM	Over dacarbazine (chemotherapeutic, commonly co-injected with doxorubicin); Not over other anthracycline chemotherapeutic drugs (epirubicin, daunorubicin)	Chirality mix (7,6), (6,5)	ND	Steady state within minutes; 20 min for diffusion of doxorubicin into tissue	Yes
Doxorubicin[115]	In saline-sodium citrate buffer, FBS, intracellularly (incubated in Raw 264.7 murine macrophage cells), incorporated into membrane and implanted into peritoneal cavity of living mice	(GT)15-SWCNTs; Fl decrease and red-shift	In buffer: 500 nM–50 μM; In serum: LOD 5 μM; In vivo: LOD 50 μM	Not over other DNA-intercalating agents (SYBR green, Hoechst 33258, ethidium bromide, 1-pyrenebutyric acid)	HiPCO (9,4)	Sub-μm	Real time; Within minutes	No

GDCh   *Reviews*   **Angewandte** *International Edition* *Chemie*

Table 3 (Continued)

Analyte	Setup	Approach/Sensor	Selectivity	Response	SWCNT	Resolution	Time	Reversible
Human steroid hormones (cortisol, progesterone)[144]	In DMSO, PBS, 10% mouse serum, subcutaneously implanted in mice (progesterone detection, SWCNTs in HG)	Semirational approach: Cortisol sensor: p(AA$_{197}$-ran-AC$_5$)-SWCNTS Progesterone sensor: p(AA$_{53}$-ran-S$_{22}$-ran-AC$_4$)-SWCNT Fl increase	Over other steroids by a factor of 2 Progesterone additionally over other small molecules and large proteins	In solution: cortisol: 10–100 μM, progesterone: 5–100 μM In serum: 12% fluorescence increase at 100 μm progesterone In HGs inside dialysis bag: three times higher sensor response (22.1%) compared to control Single molecule	HiPCO (6,5) for cortisol sensor, (7,6) for progesterone sensor	Sub-mm	3 h needed for stabilization of fluorescence signal in HG	Yes
Nitroaromatics[141]	In solution, immobilized on glass in Tris buffer	Screening approach: Bombolitin II-SWNTs (AT)$_{15}$-SWCNTs for TNT detection Wavelength shift Fl changes in discrete quenching steps	Distinction with PCA possible: over several containing nitro-aromatic and non-aromatic compounds containing nitro groups, e.g. picric acid, cyclotrimethylenetrinitramine, 2,4-dinitrophenol, over other nitroaromatics (e.g. RDX, TFM) but 2,4-dinitrotoluene and 2-nitrophenol show quenching to a lesser degree ND	HiPCO Analyzation of 8 chiralities, e.g. (7,5), (11,3)	Single molecular	Real time 500 ms–1 s	Yes
Nitroaromatics/ picric acid[30]	Within spinach plant leaf mesophyll by root uptake or through direct uptake through leaf surface	Bombolitin II-SWNTs Fl quenching	85%/78% quenching with 400 μM picric acid by root/leaf uptake	HiPCO (6,5)-enriched chiralities	0.5 mm pixel size for a stand-off distance of 0.85 m	Real time 5–15 min transport time of picric acid uptake from the roots to the leaves, 40–50 min for saturation Sensor response after 10 s by leaf uptake	No

Table 3 (Continued)

Odors, volatile molecules[146] Alcoholic vapors (ethanol, methanol, propanol, 2-propanol) Distinction between aromas of red wine, beer, vodka Distinction between limonene, undecanal, and geraniol vapors	Analytes injected into glass bottle with inlet and outlet tubes	Array of five different peptide-encapsulated SWCNTs adsorbed on a nitrocellulose paper, recognition by LDA and machine learning FI increase	LOD around 216 ppm of ethanol	Slightly increased sensor response at higher humidity Discrimination of a mixture of ethanol and methanol	CoMoCAT (6,5) at 1000 nm	ND	Real time Response within seconds Steady state after 24 s, some continue to rise after 45 s	Yes, within 160 s
Phosphodiesterase type 5 (PDE5) inhibitor Vardenafil[147]	In PBS	Screening approach: Poly(methacrylic acid-*co*-styrene)-SWCNTs with methacrylic acid and styrene at 90:10 ratio Synthetic corona mimics H loop of native enzyme PDE5 FI decrease	LOD 0.02–0.2 µM by varying the polymer length Sensor has smaller binding affinity than the enzyme, interaction is disrupted in the presence of PDE5a	Over 22 tested small molecules, not over inhibitor Sildenafil (chemical similar), but smaller emission modulation	HiPCO (8,3), (6,5)	ND	5 min incubation time	ND
Polyphenols (tannins, flavonoids, ...)[148]	In plant extracts, tissue culture media Sensors embedded in agar, pathogen-induced release from soybean roots (stimulated with pathogen-derived elicitor or mechanical wounding)	PEG-PL-SWCNTs FI decrease, red-shift	K_d = 90 nM, saturation in lower µM range (−80% FI change, 20 nm wavelength shift) Differences for different polyphenols	Over potential interferant molecules from the root such as sugar, H_2O_2	CoMoCAT, HiPCO, and monochiral (6,5)	Sub-mm with standoff detection	Real time (s)	ND
Porphyrins/heme[204]	Detection of plasma samples with solvent extraction method	Heme-binding-aptamer-SWCNTs FI decrease	LOD 20 nM	Over other porphyrins, BSA, lysozyme, phthalocyanine	CoMoCAT (7,5)	ND	Real time Immediately	ND

Table 3 (Continued)

Riboflavin, L-thyroxine, oestradiol[70]	In buffer. Riboflavin imaging in live Raw 264.7 macrophage cells	Screening approach: Oestradiol: Rhodamine isothiocyanate-difunctionalized poly(ethylene glycol)-SWCNTs FI decrease. L-thyroxine: Fmoc-L-phenylalanine PEG-SWCNTs FI decrease. Aliphatic chain and Fmoc group adsorb onto SWCNT, strong interaction between Fmoc and L-thyroxine leads to molecular recognition. Riboflavin: 53 mol/mol boronic-acid-substituted phenoxydextran-wrapped-SWCNTs (BA-PhO-Dex-SWCNTs) Red-shift through polymer dielectric change	0.6 FI change to 100 μM oestradiol/L-thyroxine and 11 nm shift to riboflavin	Over 35 biological molecules	Chirality mix Deconvoluted into 8 chiralities (7,6) at 1147 nm for tracking of riboflavin in macrophage cells	Sub-μm	In macrophage cells within seconds	Yes, for riboflavin through riboflavin-binding protein
Riboflavin[113]	SWCNTs embedded in HG with water and barium chloride, subcutaneously implanted into mice	(GT)$_{15}$-SWCNTs FI decrease	10 mM riboflavin results in 48% quenching for HG SWCNTs with a concentration of 10 mg L^{-1}. LOD in 5.4 mm depth tissue	Pore size of HG can be engineered to exclude large molecular weight interfering molecules, average pore size: 3.2 nm	(6,5)-enriched SWCNTs (6,5)	Sub-mm	Two characteristic quenching times: 14.1 min (riboflavin-SWCNT reaction), 5.8 h (riboflavin diffusion) for HGs with 10 mg L^{-1} SWCNT concentration	ND
Riboflavin[142]	In HG for in vitro and ex vivo tissue measurement of marine organisms (Sparus aurata, Stenotomus chrysops, Galeus melastormus)	(AC)$_{15}$-SWCNTs FI decrease	In vitro: 1–100 μM. in vivo: LOD in 7 mm skin and muscle tissue	Pore size of HG can be engineered to exclude large molecular weight interfering molecules, average pore size: 15 nm	CoMoCAT	mm	In vitro: immediate response, fluorescence decreases continuously while riboflavin diffuses to sensors	ND

[a] FI: fluorescence intensity, ND: not determined, HG: hydrogel.

Table 4: Detailed overview of fluorescent SWCNT based sensors for lipids.[a]

Target	Biological system	Recognition strategy	Sensitivity	Selectivity	SWCNT chirality/wavelength	Spatial resolution	Temporal resolution	Reversibility
Endolysosomal lipids[117]	In PBS, in fibroblasts from an NPC patient (Niemann-Pick type C, lysosomal storage disease)	Screening approach: $(GT)_6$-SWCNTs Wavelength shift	For lipid analogues, e.g. PEG-cholesterol: 10 nM—1 μM	Over BSA, double-stranded DNA from salmon, carboxymethyl cellulose (CMC)	HiPCO (8,6) at 1200 nm	Subcellular	< 2 min for incubation of fibroblasts from NPC patient with SWCNTs Measurement after 24 h	Yes, upon administration of a drug (hydroxypropyl)-β-cyclodextrin) that reverses disease phenotype
Endolysosomal lipids[149]	In cell culture medium with 10% FBS, intravenous injected into mice with NPA/B and NPC disease to detect lipid accumulation in the Kupffer cell endolysosomal organelles	Screening approach: $CTTC_3TTC$-SWCNTs Blue-shift	In cell culture medium 6–8 nm blue shift In vivo 4.2–5.3 nm blue shift	Minimal response to BSA, genomic DNA, CMC Not over different lipid types	Chirality mix (9,4) at 1125 nm	μm	Within min–h	ND

[a] FI: fluorescence intensity, ND: not determined.

Table 5: Detailed overview of fluorescent SWCNT based sensors for proteins.[a]

Target	Biological system	Recognition strategy	Sensitivity	Selectivity	SWCNT chirality/wavelength	Spatial resolution	Temporal resolution	Reversibility
β-Carotene[116]	In canola oil	Screening approach: $(GT)_{15}$-SWCNTs adsorbed onto nitrocellulose paper	Dissociation constant 2.2 μM	Less FI increase to fat-soluble vitamins (menadione, retinyl acetate and α-tocopherol)	CoMoCAT	ND	Real time	ND
Aggregation status of human IgG[159]	In HG	Chitosan-SWCNTs modified with Cu^{2+}-NTA/His-tagged protein A interacting with human IgG leading to ion based proximity quenching	LOD below 660 nM	ND	CoMoCAT (6,5)	mm	Real time Within 5 min	Usable twice
Albumin[152]	In clinical urine samples of patients with micro-albuminuria Samples need to be filtered to remove small interfering molecules	Screening approach: Constructed polymer mimics fatty binding to albumin Carboxylate-functionalized poly-carbodiimide polymer-SWCNTs incorporated into acrylic-based paint Blue-shift, FI increase	LOD 3 mg L^{-1}	Potential interfering proteins such as transferrin, γ-globulins, degraded albumin showed either negligible change or red-shift	HiPCO (9,4)	ND	Saturation after 20 min FI change: 0.214 min^{-1} Wavelength change: 0.1845 min^{-1}	ND
Avidin	In solution	SWCNTs noncovalently bound to dye-ligand conjugates (biotinylated anthracene), which are covalently bound to a biological receptor ligand (biotin), which binds to the analyte FI increase	LOD 1–5 nM	Response to BSA, but with three orders less sensitivity	HiPCO 900—1500 nm	ND	ND	Yes

Reviews

Table 5 (Continued)

Analyte	Condition	Approach / Mechanism	Sensitivity / LOD	Selectivity / Notes	SWCNT	Spatial resolution	Temporal	In vivo
Cardiac biomarker troponin T[64]	In HG	Rational approach: Chitosan-wrapped SWCNTs non-covalently modified with troponin antibody using a Ni^{2+}-NTA/hexa-histidine-tagged protein mechanism for divalent ion-based proximity quenching Fl increase	LOD 2.5 nM	Over BSA, IgG, cancer biomarker Pisum sativum agglutinin (PSA), 10000 times diluted human plasma (7 μg mL^{-1} proteins) Affected by viscosity change (e.g. 100 times diluted plasma), unable to quantitatively detect in full plasma	Chirality mix 1000–1400 nm	ND	Real time Within 5 min saturation	Yes
Cell surface receptors CD20, HER2/neu[205]	Incubation of cells in SWCNT solution	Rational approach: PL-PEG-NH$_2$-SWCNTs conjugated to antibodies Rituxan antibody to recognize CD20 cell surface receptor on B-cell lymphoma Herceptin to recognize HER2/neu positive breast cancer cells	ND	Rituxan-SWCNTs: over T-cell lymphoma Herceptin-SWCNTs: over HER2/neu negative cell line	HiPCO 900–2200 nm	Sub-μm	1 h incubation time before measurement	ND
Electrostatic charge accumulation mediated by cell membrane proteins[206]	SWCNTs in contact with cell monolayer (HeLa cells, murine fibroblast cell line (NIH/3T3), human lymphocyte cell line (Jurkat))	(AT)$_{15}$-SWCNTs Wavelength shift Determined between membrane-bound SWCNTs and SWCNTs in serum-free solution	Emission energy correlated with the degree to which a cell adheres to a substrate and the zeta potential of the cell Jurkat cells: $\Delta\lambda = 6.02 \pm 0.28$ nm NIH/3T3: $\Delta\lambda = 4.97 \pm 0.23$ nm HeLa cell: $\Delta\lambda = 2.72 \pm 0.12$ nm	Cell type dependent trend	HiPCO 900–1600 nm	20 μm pixel size**	ND	ND
Fibrinogen[71]	In serum (10% FBS in PBS)	Screening approach: Dipalmitoyl-phosphatidylethanolamine (DPPE)-PEG (5 kDa)-SWCNT	Lowest concentration tested 0.05 mg ml^{-1}	Negligible response of < 5% intensity to 13 proteins (some are highly abundant in blood and others are relatively rare but of clinical significance)	HiPCO (9,4), (7,6)	Single sensor	Real time Signal quenching occurs rapidly (within seconds), Saturation within minutes	ND
Glutathione-S-transferase (GST) fusion proteins[154]	In solution	Glutathione-(TAT)$_6$-SWCNTs Modulation of Fl and wavelength in response to GST and GST fusions depending on SWCNT structure	LOD 10 nM	Responds to multiple classes of GST-tagged proteins (e.g. cell-cycle proteins, RNA-binding proteins, ovarian cancer protein biomarkers) Affected by powdered milk (protein blocking agent), BSA	HiPCO (8,6), (9,1)	ND	Real time 5 min incubation time	ND

Table 5 (Continued)

Analyte	Sample	Approach / Mechanism	LOD	Selectivity	Chirality	Spatial resolution	Time	
Green fluorescent protein (GFP), GFP-fusion proteins[79]	Incubation with GFP	GFP-binding nanobody-SWCNTs, covalently bound aryl maleimide Quantum defects introduced by light-driven diazonium chemistry serve as anchor points for peptides and proteins, conjugation of cysteine-containing proteins to maleimide	ND	Over negative control, where no diazonium salt was added	E_{11}^{*} at 1135 nm	μm	ND	ND
Gynecologic cancer biomarker human epididymis protein 4, cancer antigen 125, chitinase-3-like protein, mesothelin[160]	In 10% FBS, uterine lavage samples	Machine-perception-based sensor array consisting of 132 distinct DNA-SWCNT complexes: 11 ssDNA-SWCNT-based sensors with 12 chiralities, e.g. $(AT)_{11}$, $(GT)_{12}$, $(ATT)_{4}$, $(TCT)_{5}$-SWCNTs Fl increase/decrease and wavelength shift	LOD in pM range	Simultaneous distinction / detection of biomarkers with classification accuracy (F1-score) of ca. 0.95	HiPCO Deconvoluted to extract individual chiralities, e.g. (6,5), (8,4), (10,3), (7,5), (7,6), (8,3)	ND	ND	ND
Human α-thrombin[207]	In PBS	Rational approach: Dye (FAM) labelled human α-thrombin binding aptamer-SWCNTs Fl increase	LOD 1.8 nM Dynamic range 4–150 nM	In presence of 100 nM of other proteins (BSA, HAS, IgG)	HiPCO	ND	Incubation of target 2–3 h	ND
Immunoglobulin IgG[104]	In HG	Rational approach: Chitosan-wrapped SWCNT non-covalently modified with immunoglobulin-binding proteins A using a Cu^{2+}-NTA/His-tagged protein mechanism for divalent ion based proximity quenching Fl increase	LOD 10 ng mL^{-1}	ND	HiPCO	ND	Real time Within seconds Equilibrium reached within 5 min	ND
Immunoglobulin (human IgG, mouse IgM, rat IgG2a, human IgD)[151]	Ink printed	Rational approach: Chitosan-SWCNTs noncovalently modified with immunoglobulin-binding proteins. Cu-NTA chelating chemistry with histidine tag for divalent ion based proximity quenching Binding proteins: protein A, protein G, protein L Fl increase	LOD 25 μg mL^{-1} of human IgG, 2.5 μg mL^{-1} at 20x magnification	Different association constants for different antibody/binding proteins	CoMoCAT (6,5) at 980 nm	Sub-mm	Real time 1 s** Response within seconds	Yes
Insulin[155]	In buffer	Insulin-binding aptamer-SWCNTs Fl quenching	Lowest concentration tested: 9 nM	Over BSA, proteinase K	HiPCO (6,5)	Sub-μm	ND	ND

Table 5 (Continued)

Target	Sample/conditions	Mechanism/approach	LOD	Selectivity	SWCNT	Spatial resolution	Temporal resolution	Reversibility
Insulin[156]	In collagen extracellular matrix. Insulin secreted by pancreatic β-cells due to glucose addition	Insulin-binding aptamer-SWCNTs. Fl quenching upon analyte binding by photoinduced charge-transfer mechanism (electron transfer from conduction band of SWCNTs to LUMO of the bound insulin)	LOD 10 nm	Over BSA, proteinase K, cell culture media RPMI 1640, glucose	CoMoCAT (7,5) at 1044 nm	Sub-μm	Real time. Within seconds. Fl quenching rate 5.85×10^{14} M^{-1} s^{-1} diffusion reaction rate 0.129 s^{-1}	Yes, through enzymatic proteolysis within 1 h. enzyme: α-chymotrypsin
Insulin[101]	In PBS, blood serum (10% FBS in PBS)	Screening approach of PEG-conjugated lipids. C_{16}-PEG(2000 Da)-ceramide-SWCNTs. Fl decrease	180 pM—3.5 μM tested. In FBS reduced response	Over library of proteins (<5% intensity change). Not over apolipoproein A-I and longer fragments of isolated α- and β-peptide chains of insulin	HiPCO (10,2)	ND	Measurement after 30 min of insulin addition	ND
Insulin[158]	In PBS, Krebs-Ringer HEPES buffer (KRHB), secreted by pancreatic β-cells due to glucose addition	C_{16}-PEG(2000 Da)-ceramide-SWCNTs. $(AT)_{15}$-Insulin-binding aptamer-SWCNT. Fl decrease	8.1 nM—74 mM tested. C_{16}-PEG-ceramide-SWCNTs: response stable and reproducible. $(AT)_{15}$-Insulin aptamer-SWCNT: diminishing response over time, batch-to-batch variations	Over BSA, KRHB, IBMX, glucose	HiPCO (10,2) (6,5)	ND	5 min incubation time. Detection in real time	ND
Integrins[66] Human platelet integrin $\alpha_{IIb}\beta_3$	Immobilized on epithelial cells	Arg-ly-Asp (RGD) peptide conjugated to different ssDNA sequences in linear ssDNA-RGD or bridged ssDNA-RGD-ssDNA geometries. Integrin affinity of RGD motif depends on its conformational freedom due to ssDNA-RGD geometry	IC_{50} values varied from 309 nm for C_{20}-RGD-SWCNTs to 29 nm for $(GT)_{15}$-SWCNTs	DNA sequence affects overall RGD affinity	CoMoCat	ND	ND	ND
Green fluorescent protein (GFP), GFP-fusion proteins[67]	Tracking of motor protein (Kinesin-5-GFP) in embryos of Drosophila melanogaster	Rational approach: GFP binding nanobodies conjugated to DNA-wrapped SWCNT GBP-$(GT)_{20}$-SWCNTs	ND		CoMoCAT (6,5)	Single sensor	Real time. Resolving the velocity of a molecular motor in vivo at 1340 nms^{-1}	ND
Ovarian cancer biomarker HE4 (human epididymis protein 4)[65]	In serum (10% FBS), living mice, sensors loaded into semipermeable PVDF membrane capillary	Rational approach: HE4 Antibody (Ab) is goat polyclonal anti-HE4 IgG antibody Ab-$(TAT)_6$-amine-SWCNT passivated with BSA	In serum: 10 nm—500 nm	Mostly over nontarget proteins like uPA, CA-125 (another ovarian biomarker), BSA or 93% FBS	HiPCO 900—1400 nm	Single sensor	Change after 1 min, stabilized signal after 1 h	ND

GDCh   *Reviews*   **Angewandte** *International Edition* *Chemie*

Table 5 (Continued)

Target	Media	Approach	LOD	Notes	SWCNT	Spatial	Temporal	
Prostate cancer biomarker uPA[106]	In PBS, blood, FBS, plasma	Rational approach: Mouse monoclonal IgG anti-uPA-(TAT)$_6$-SWCNTs passivated with BSA to increase sensitivity. Red-shift	In buffer 100 pM In serum 25 nM In plasma 100 nM	Increased selectivity in complex protein environment due to BSA passivation of SWCNTs	HiPCO (9,4), (8,6), (8,7)	ND	Saturation after 30/90 min in human serum/plasma	ND
Prostate tumors[21]	In tissues/ tissue-like phantoms, serum (FBS), incubated on human prostate cancer cell lines, in vivo in mice (intravenous injection)	Rational approach: Prostate specific membrane antigen (PSMA) antibody conjugated to M13-phage SWCNTs	At 2 µg ml^{-1} SWCNTs detection depth up to 2.5 cm in tissue-like phantoms	4-fold improved uptake in PSMA positive prostate tumors compared to control, stable in serum	HiPCO	mm in vivo	After 2–4 h post injection	ND
RAP1[105]	Release from *E. coli* cell lysates	Rational and screening approach: RAP1-aptamer-(AT)$_{11}$-SWCNT With spacers between (AT)$_{11}$ enhanced FI increase (4x) due to less adhesion of aptamer to SWCNT surface	Zeptomolar protein detection	Over eight tested other proteins	Chirality mix (6,5)	Single cell	ms**	Yes
SARS-CoV-2 spike protein[157]	In saliva, viral transport medium	Rational approach: ACE2-(GT)$_6$-SWCNTs, passivation with PE-PEG FI increase	LOD 12.6 nM/ 10^4–10^6 viral copies per µL in solution/on surface	Less increase with other viral spike-like proteins (SARS-CoV-1 S RBD, MERS S RBD, FLU hemagglutinin subunit, serum albumin), in biological fluids (e.g. saliva, viral transport medium)	HiPCO 1130 nm	ND	Within 90 min/ 5 s in solution/ immobilized	ND
Wheat germ agglutinin (WGA) (sugar-binding lectin protein)[153] **Sugars/N-acetylglutamic acid (GlcNAc) and N-acetylneuraminic acid (Neu5Ac)**	In buffer, complex biological media, immobilized	Screening approach: Peptoid-SWCNT FI decrease in response to WGA Sensor shows preserved protein activity and is able to bind its target sugars	LOD 3.4 µM	Minor responses to protein A, BSA, NeutrAvidin, lysozyme FI increase to peanut agglutinin, ConA Attenuated ability to detect WGA in complex biological media (DMEM, FBS) Over other sugars commonly bound by lectins (fructose, galactose, glucose, mannitol mannose, sucrose), but not fucose	HiPCO (7,6)	Single sensor	Equilibrium reached within 1 h	ND

[a] FI: fluorescence intensity, ND: not determined, HG: hydrogel.

Table 6: Detailed overview of fluorescent SWCNT based sensors for sugar.[a]

Target	Biological system	Recognition strategy	Sensitivity	Selectivity	SWCNT chirality/ wavelength	Spatial resolution	Temporal resolution	Reversibility
D-glucose[24,208]	SWCNT solution loaded into dialysis capillary imaged through human epidermal tissue sample	Rational approach: GOX-SWCNTs with Fe(CN)$_6^{3-}$ addition as electroactive species results in Fl decrease or Fermi level shift into the VB due to irreversible adsorption on the SWCNT surface. Addition of analyte results in increasing restored Fl. GOX catalyzes the reaction of D-glucose to D-glucono-1,5-lactone with a H$_2$O$_2$ co-product	LOD 34.7 μM	ND	HiPCO	μm	Within 80 s	ND
D-glucose[108]	In PBS, immobilized	Rational approach: Glucose-binding protein (GBP) covalently conjugated to PVA-SWCNTs. Quenching in discrete steps in response to glucose due to conformation change of GBP	2.5–50 mM Linear until 10 mM	Over fructose, mannose	CoMoCAT (8,3), (6,5), (7,5)	Single-sensor 500 nm pixel size**	Immediately (s)	Yes
Glucose[11]	In BSA + PBS BSA to prevent concanavalin A (ConA, lectin with four glucose-binding sites) adsorption to the walls of the cuvette	Rational approach: Phenoxydextran-SWCNTs with ConA. Competitive binding between target analyte and dextran, ConA introduces protein-controlled aggregation and Fl decrease, introduction of glucose causes dissolution of aggregate and Fl recovery	LOD 3.8 nM Response range based on ConA concentration	Over glycerol (hydrogen-bond-breaking agent)	Chirality mix	ND	3–28 min to reach steady state	Yes
Glucose[162]	In solution, 36°C	Rational approach: GOX-DNA-SWCNTs with 2 mM/5 mM potassium ferricyanide (PFC) as electron transfer mediator. Fl increase	LOD 1 mM With increasing amount of glucose portions (1–2 mM) less sensitive (Fl restoration decreases)	ND	HiPCO (9,2) at 1136 nm	ND	Within minutes	No
Glucose[68]	In solution	Screening approach: Boronic acid derivatives complexed with SC-SWCNTs. Identified derivatives: 4-cyanophenylboronic acid, 4-chlorophenylboronic acid. Blue-shift and Fl increase	5–30 mM	ND	CoMoCAT (6,5)	ND	Within seconds	Yes
Glucose, fructose[81]	In solution	SWCNTs locally functionalized with a phenylboronic acid group. Blue-shift and Fl decrease	13.5 nm shift with 8.8 mM fructose/ 19 mM glucose	ND	CoMoCAT E$_{11}$* of (6,5) at 1138 nm	ND	ND	ND
Glucose[161]	In PBS, human serum, incorporated into membrane device	Rational approach: GOX-SWCNTs. Fl increase	In PBS: 3 mM—30 mM tested. In serum: 3.3 mM—7.8 mM tested	Different Fl increase to mannose, galactose, xylose. Over maltose, fructose	CoMoCAT (6,5) at 995 nm	ND	Without/ with membrane setup saturation after 1/12–15 min	Yes

Table 6 (Continued)

Glycan[107] Free biotinylated glycans, glycans tethered to streptavidin; Explored glycan-lectin pairs: fucose to PA-IIL lectins and N-acetyl-glucosamine to GafD lectins	In HG	Rational approach: Chitosan-SWCNTs noncovalently modified with lectins using a Ni^{2+}-NTA/His-tagged protein mechanism for divalent ion based proximity quenching; FI increase	LOD 2 μg/100 ng of glycosylated protein/free glycan to 20 μg of lectin	Greater response of known high affinity pairs than to cross reactions	CoMoCAT (6,5)	Single sensor	Within seconds	Yes
Glycoforms with high mannose content[209]	In PBS, metabolically induced hypermannosylation of human IgG from CHO cells, SWCNTs in HG	Rational approach: Chitosan-SWCNTs noncovalently modified with PSA-lectin using a Ni^{2+}-NTA/His-tagged protein conjugation for divalent ion based proximity quenching; FI increase	Dissociation constant 1.3–55 μM	Over human/mouse IgG with absent mannose content	HiPCO	ND	Within 5 min	ND
Saccharide[210]	In PBS	Semirational approach: Phenylboronic acid (PBA) grafted, polyethylene glycol 8-membered branched polymers (PPEG8) wrapped SWCNTs. Three PBAs to measure saccharide binding: 4-carboxyphenylboronic acid, N-(4-phenylboronic)- succinamic acid, 3-carboxy-5-nitrophenylboronic acid; FI quenching	FI changes varied for different saccharide, e.g. 4-carboxyphenylboronic acid-PPEG8-SWCNTs respond with −20% FI change upon 10 mM ribose and 15% upon arabinose	Not selective over DA; Most responsive to pentoses, such as arabinose, ribose, and xylose	Chirality mix (9,4)	ND	1 h incubation of analytes	ND
Saccharide[211]	In DMSO/PBS	Screening approach: Polymer or surfactant SWCNTs modified with noncovalent adsorption of PBAs. Saccharide responses occur only within corona phases that have allowed PBAs to adsorb and prequench SWCNT emission (e.g. most PBAs fail to penetrate SDBS corona). Recognition upon saccharide adsorption into SWCNT corona, followed by surface reaction of PBA	mM range tested	Corona-phase environment has a profound effect on selectivity of saccharide binding	Chirality mix	ND	Within minutes	ND

[a] FI: fluorescence intensity, ND: -not determined, HG: hydrogel, ***: limited by the Abbe limit, diffusion and detection speed.

Table 7: Detailed overview of fluorescent SWCNT based sensors for DNA/RNA.[a]

Target	Biological system	Recognition strategy	Sensitivity	Selectivity	SWCNT chirality/ wavelength	Spatial resolution	Temporal resolution	Reversibility
DNA hybridization[212]	In Tris buffer	Rational approach: ssDNA-SWCNTs Hybridization of 24-mer oligonucleotide sequence with its complement causes blue-shift	LOD 6 nM	Over noncomplementary DNA	HiPCO (6,5)	ND	13 h to reach steady state (for 625 nM DNA)	ND
MicroRNA/ DNA hybridization[163]	In urine, serum, implanted in live mice by using a semi-permeable membrane capillary	Rational approach: SWCNTs functionalized with 23-mer microRNA capture sequence (complementary to target oligonucleotide and (GT)$_{15}$ (for SWCNT colloidal stability) Low concentrations of SDBS (5.7 mM) cause an increased blue-shift (and Fl enhancement) by an order of magnitude	In buffer: 10 pM–1 µM In urine: LOD 1 nM In serum: similar, but addition of proteinase K necessary for detection of RNA (to deactivate RNase, which can degrade RNA sequence) In vivo: LOD 100 pM	Over random 23-mer sequences and similar sequences	Chirality mix	Single sensor	Within 10 min/ 120 min in buffer/ in vivo Kinetics are 1.8 × faster for DNA vs. RNA	Yes, by toe-hold-mediated strand displacement, but slower than detection in forward direction
Single nucleotide polymorphism (SNP)[213]	In Tris buffer	Rational approach: TAG CTA TGG AAT TCC TCG TAG GCA -SWCNTs Blue-shift upon SNP detection Not all ssDNA sequences can be used for SNP detection, surface coverage of SWCNTs with ssDNA shouldn't be too high	0.8 meV blue-shift	Distinction from response caused by complementary DNA due to higher energy shift of 1.2 meV	HiPCO (6,5)	ND	8 h to reach steady state	ND
ssRNA genome of intact HIV[164]	In PBS, FBS	Rational approach: (GT)$_{15}$(T)$_{15}$-SWCNTs SDS for blocking nonspecific binding in serum and denaturation of virus RNA genome hybridizes to sensor, freeing space on the SWCNT surface, denatured viral proteins bind to the surface, eliciting an enhanced blue-shift	3–9 nm blue-shift depending on chirality	Control DNA causes slight red-shift	HiPCO (8,6)	ND	Wavelength shift within 20 min (after 180 min 3 nm shift)	ND

[a] Fl: fluorescence intensity, ND: not determined.

Table 8: Detailed overview of fluorescent SWCNT based sensors for enzymes.[a]

Target	Biological system	Recognition strategy	Sensitivity	Selectivity	SWCNT chirality/ wavelength	Spatial resolution	Temporal resolution	Reversibility
Enzyme activity[166]	In solution	BSA-SWCNTs for bacterial protease, citrus pectin-SWCNTs for pectinase, carboxymethylcellulose (CMC)-SWCNTs for cellulase Target enzyme degrades the polymer-wrapping, resulting in FI quenching	LOD 5 fM Sensitivity and repeatability of sensors varies due to affinity of polymers to the SWCNT	ND	CoMoCAT, (6,5) at 975 nm	ND	Real time Signal stabilized 1–3 h after incubation (24–29 h for 5 fM)	No
Enzyme activity[167]	In soil, diluted with DI water	Albumin-SWCNTs for proteolytic activity, lignosulfonic acid (LSA)-SWCNTs for lignin-modifying activity, CMC-SWCNTs for cellulolytic activity Target enzyme degrades the polymer-wrapping resulting in FI quenching or target enzyme further protects the SWCNT resulting in FI increase	ND	LSA-SWCNTs respond to pH changes CMC-SWCNTs to nonspecific binding of proteins	Chirality mix, (6,5)	ND		ND
Myeloperoxidase (MPO)[169]	MPO/H$_2$O$_2$/Cl$^-$ system	GO-SC-SWCNTs Increasing FI at 420/430 nm due to oxidation and degradation of GO Decreasing NIR SWCNT FI due to generation of defects on the SWCNT surface	Linear response to MPO-catalyzed degradation	ND	CoMoCAT, 998 nm GO: 420 nm	ND	Real time, within 5 days	No
Trypsin[168]	SWCNTs drop-casted and dried on glass fiber paper, fixed on plastic strips Urine samples diluted in PBS	Screening approach: Peptide-SWCNTs (HexCoil-Ala) Target enzyme degrades the peptide-wrapping resulting in FI quenching	1–20 µg mL^{-1} Urine samples: reduced sensitivity	8.3 %/33 % urine (without trypsin) caused 33 %/50 % FI decrease over urea	CoMoCAT, (6,5)	ND	Significant FI decrease after 2 h/1 h of incubation at concentrations of 1/5–20 µg mL^{-1}	No

[a] FI: fluorescence intensity, ND: not determined.

Reviews

Angewandte *Chemie*
International Edition

Table 9: Detailed overview of fluorescent SWCNT based sensors for epitopes and metabolites from pathogens.[a]

Target	Biological system	Recognition strategy	Sensitivity	Selectivity	SWCNT chirality/ wavelength	Spatial resolution	Temporal resolution	Reversibility
Distinction between F'-positive and F'-negative bacterial strains, specific F'-negative bacteria[170]	In tissue phantom, mice, SWCNTs injected intravenously	Rational approach: For distinction: M13 bacteriophage-SWCNTs. F'-negative bacteria: Anti-bacterial antibody-SWCNTs via streptavidin-biotin reaction	F'-negative bacteria: Detection of S. aureus intramuscular infections with 3400% FI enhancement	Over control (injection of PBS)	HiPCO	μm	Imaging of mice 8–48 h after injection	ND
Distinction between pathogens: S. aureus, S. epidermidis, S. pyogenes, E. faecalis, E. coli, P. aeruginosa[29]	SWCNTs in HG array with low porosity for small molecules (e.g. siderophores) and high porosity for large enzymes, bacteria plated on top, in human synovial fluid, tissue phantom	1) Lipopolysaccharides (LPS) sensor: LPS-binding peptide linked to NH_2-(GT)$_{10}$-SWCNTs, FI increase 2) Siderophore sensor: hemin-binding aptamer- (HeApta)SWCNTs, HeApta binds to hemin, which brings Fe^{3+} into proximity of the SWCNT and quenches it. Siderophore can reverse this effect by removing iron, which increases FI again 3) Nuclease activity sensor: calf-thymus-(CT-)DNA-SWCNTs, report to DNase I and S. aureus nuclease activity due to degradation of CT-DNA via FI modulation 4) Protease sensor: BSA-SWCNTs, FI decrease in response to protease Generic lower-selectivity sensors to increase the discrimination power of the sensor array: (GT)$_{10}$, C$_{30}$, (GC)$_{15}$, PEG-PL-SWCNTs react to changes in pH, oxygen or protein concentration For spectrally encoding: LPS-(6,5)-SWCNTs, PEG-PL-(9,4),-(8,6),(9,5)-SWCNTs and EB-NS reference	LPS sensor: up to 12.5 μM. Siderophore sensor: up to 10 μM. LOD in > 7 mm depth tissue	Distinction of P. aeruginosa, S. aureus, S. epidermidis, E. coli and of 43 different clinical isolates of S. aureus and S. epidermidis with 80% likelihood. E. faecalis and S. pyogenes not distinguishable. Over human synovial fluid. LPS sensor: responds to different LPS structures with different sensitivity, siderophore sensor: not responsive to weaker chelators such as ethylenediaminetetraacetic acid citrate	Spatial encoding: CoMoCAT, >900 nm. Spectral encoding: EB-NS: 920 nm, (6,5): 920 nm, (9,4), (8,6), (9,5) > 1110 nm	mm for a stand-off distance of ≥ 25 cm	Limited by diffusion of analytes through HG. Within 24–72 h distinction possible	ND

[a] FI: fluorescence intensity, ND: not determined, HG: hydrogel.

GDCh Reviews Angewandte

Conflict of Interest

The authors declare no conflict of interest.

Keywords: biosensors · carbon nanotubes · imaging · molecular recognition · near-infrared fluorescence

[1] G. Hong, A. L. Antaris, H. Dai, *Nat. Biomed. Eng.* **2017**, *1*, 0010.

[2] G. Hong, S. Diao, A. L. Antaris, H. Dai, *Chem. Rev.* **2015**, *115*, 10816.

[3] J. P. Giraldo, H. Wu, G. M. Newkirk, S. Kruss, *Nat. Nanotechnol.* **2019**, *14*, 541.

[4] T. M. Swager, *Angew. Chem. Int. Ed.* **2018**, *57*, 4248; *Angew. Chem.* **2018**, *130*, 4325.

[5] a) P. D. Howes, R. Chandrawati, M. M. Stevens, *Science* **2014**, *346*, 1247390; b) P. D. Howes, S. Rana, M. M. Stevens, *Chem. Soc. Rev.* **2014**, *43*, 3835; c) C. D. Spicer, C. Jumeaux, B. Gupta, M. M. Stevens, *Chem. Soc. Rev.* **2018**, *47*, 3574; d) C. Cheng, S. Li, A. Thomas, N. A. Kotov, R. Haag, *Chem. Rev.* **2017**, *117*, 1826.

[6] a) V. Schroeder, S. Savagatrup, M. He, S. Lin, T. M. Swager, *Chem. Rev.* **2019**, *119*, 599; b) D. Tasis, N. Tagmatarchis, A. Bianco, M. Prato, *Chem. Rev.* **2006**, *106*, 1105; c) G. Reina, J. M. González-Domínguez, A. Criado, E. Vázquez, A. Bianco, M. Prato, *Chem. Soc. Rev.* **2017**, *46*, 4400; d) H. Ali-Boucetta, K. Kostarelos, *Adv. Drug Delivery Rev.* **2013**, *65*, 1897.

[7] S. Iijima, *Nature* **1991**, *354*, 56.

[8] R. H. Baughman, A. A. Zakhidov, W. A. de Heer, *Science* **2002**, *297*, 787.

[9] A. A. Boghossian, J. Zhang, P. W. Barone, N. F. Reuel, J.-H. Kim, D. A. Heller, J.-H. Ahn, A. J. Hilmer, A. Rwei, J. R. Arkalgud, et al., *ChemSusChem* **2011**, *4*, 848.

[10] S. Kruss, A. J. Hilmer, J. Zhang, N. F. Reuel, B. Mu, M. S. Strano, *Adv. Drug Delivery Rev.* **2013**, *65*, 1933.

[11] P. W. Barone, M. S. Strano, *Angew. Chem. Int. Ed.* **2006**, *45*, 8138; *Angew. Chem.* **2006**, *118*, 8318.

[12] S. M. Bachilo, M. S. Strano, C. Kittrell, R. H. Hauge, R. E. Smalley, R. B. Weisman, *Science* **2002**, *298*, 2361.

[13] J. Zhang, A. A. Boghossian, P. W. Barone, A. Rwei, J.-H. Kim, D. Lin, D. A. Heller, A. J. Hilmer, N. Nair, N. F. Reuel, et al., *J. Am. Chem. Soc.* **2011**, *133*, 567.

[14] J. Pan, F. Li, J. H. Choi, *J. Mater. Chem. B* **2017**, *5*, 6511.

[15] S. Kruss, M. P. Landry, E. Vander Ende, B. M. A. Lima, N. F. Reuel, J. Zhang, J. Nelson, B. Mu, A. Hilmer, M. Strano, *J. Am. Chem. Soc.* **2014**, *136*, 713.

[16] C. Farrera, F. Torres Andón, N. Feliu, *ACS Nano* **2017**, *11*, 10637.

[17] J. N. Coleman, *Adv. Funct. Mater.* **2009**, *19*, 3680.

[18] M. J. O'Connell, S. M. Bachilo, C. B. Huffman, V. C. Moore, M. S. Strano, E. H. Haroz, K. L. Rialon, P. J. Boul, W. H. Noon, C. Kittrell, et al., *Science* **2002**, *297*, 593.

[19] J. P. Giraldo, M. P. Landry, S. M. Faltermeier, T. P. McNicholas, N. M. Iverson, A. A. Boghossian, N. F. Reuel, A. J. Hilmer, F. Sen, J. A. Brew, et al., *Nat. Mater.* **2014**, *13*, 400.

[20] J. P. Giraldo, M. P. Landry, S.-Y. Kwak, R. M. Jain, M. H. Wong, N. M. Iverson, M. Ben-Naim, M. S. Strano, *Small* **2015**, *11*, 3973.

[21] H. Yi, D. Ghosh, M.-H. Ham, J. Qi, P. W. Barone, M. S. Strano, A. M. Belcher, *Nano Lett.* **2012**, *12*, 1176.

[22] M. Zheng, A. Jagota, E. D. Semke, B. A. Diner, R. S. McLean, S. R. Lustig, R. E. Richardson, N. G. Tassi, *Nat. Mater.* **2003**, *2*, 338.

[23] S. F. Oliveira, G. Bisker, N. A. Bakh, S. L. Gibbs, M. P. Landry, M. S. Strano, *Carbon* **2015**, *95*, 767.

[24] P. W. Barone, S. Baik, D. A. Heller, M. S. Strano, *Nat. Mater.* **2004**, *4*, 86.

[25] D. A. Heller, E. S. Jeng, T.-K. Yeung, B. M. Martinez, A. E. Moll, J. B. Gastala, M. S. Strano, *Science* **2006**, *311*, 508.

[26] A. J. Gillen, A. A. Boghossian, *Front. Chem.* **2019**, *7*, 612.

[27] M. Dinarvand, E. Neubert, D. Meyer, G. Selvaggio, F. A. Mann, L. Erpenbeck, S. Kruss, *Nano Lett.* **2019**, *19*, 6604.

[28] M. Dinarvand, S. Elizarova, J. Daniel, S. Kruss, *ChemPlusChem* **2020**, *85*, 1465.

[29] R. Nißler, O. Bader, M. Dohmen, S. G. Walter, C. Noll, G. Selvaggio, U. Groß, S. Kruss, *Nat. Commun.* **2020**, *11*, 5995.

[30] M. H. Wong, J. P. Giraldo, S.-Y. Kwak, V. B. Koman, R. Sinclair, T. T. S. Lew, G. Bisker, P. Liu, M. S. Strano, *Nat. Mater.* **2017**, *16*, 264.

[31] H. Wu, R. Nißler, V. Morris, N. Herrmann, P. Hu, S.-J. Jeon, S. Kruss, J. P. Giraldo, *Nano Lett.* **2020**, *20*, 2432.

[32] T. T. S. Lew, V. B. Koman, K. S. Silmore, J. S. Seo, P. Gordiichuk, S.-Y. Kwak, M. Park, M. C.-Y. Ang, D. T. Khong, M. A. Lee, et al., *Nat. Plants* **2020**, *6*, 404.

[33] T. T. S. Lew, M. Park, J. Cui, M. S. Strano, *Adv. Mater.* **2021**, *33*, 2005683.

[34] M. P. Landry, S. Kruss, J. T. Nelson, G. Bisker, N. M. Iverson, N. F. Reuel, M. S. Strano, *Sensors* **2014**, *14*, 16196.

[35] A. Hendler-Neumark, G. Bisker, *Sensors* **2019**, *19*, 5403.

[36] M. F. L. de Volder, S. H. Tawfick, R. H. Baughman, A. J. Hart, *Science* **2013**, *339*, 535.

[37] M. S. Dresselhaus, G. Dresselhaus, J. C. Charlier, E. Hernández, *Philos. Trans. A* **2004**, *362*, 2065.

[38] S. Iijima, T. Ichihashi, *Nature* **1993**, *363*, 603.

[39] M. S. Dresselhaus, G. Dresselhaus, R. Saito, *Carbon* **1995**, *33*, 883.

[40] J. Ma, J. N. Wang, X. X. Wang, *J. Mater. Chem.* **2009**, *19*, 3033.

[41] F. Wang, G. Dukovic, L. E. Brus, T. F. Heinz, *Science* **2005**, *308*, 838.

[42] C. Manzoni, A. Gambetta, E. Menna, M. Meneghetti, G. Lanzani, G. Cerullo, *Phys. Rev. Lett.* **2005**, *94*, 207401.

[43] H. Zhao, S. Mazumdar, *Phys. Rev. Lett.* **2004**, *93*, 157402.

[44] T. Ando, *J. Phys. Soc. Jpn.* **2006**, *75*, 024707.

[45] a) C. D. Spataru, S. Ismail-Beigi, R. B. Capaz, S. G. Louie, *Phys. Rev. Lett.* **2005**, *95*, 247402; b) S. Berciaud, L. Cognet, B. Lounis, *Phys. Rev. Lett.* **2008**, *101*, 77402; c) A. Srivastava, H. Htoon, V. I. Klimov, J. Kono, *Phys. Rev. Lett.* **2008**, *101*, 87402.

[46] L. Lüer, S. Hoseinkhani, D. Polli, J. Crochet, T. Hertel, G. Lanzani, *Nat. Phys.* **2009**, *5*, 54.

[47] L. Cognet, D. A. Tsyboulski, J.-D. R. Rocha, C. D. Doyle, J. M. Tour, R. B. Weisman, *Science* **2007**, *316*, 1465.

[48] A. J. Siitonen, D. A. Tsyboulski, S. M. Bachilo, R. B. Weisman, *Nano Lett.* **2010**, *10*, 1595.

[49] R. Nißler, L. Kurth, H. Li, A. Spreinat, I. Kuhlemann, B. S. Flavel, S. Kruss, *Anal. Chem.* **2021**, *93*, 6446.

[50] a) L. Kou, D. Labrie, P. Chylek, *Appl. Opt.* **1993**, *32*, 3531; b) Scott Prahl, "Tabulated Molar Extinction Coefficient for

Hemoglobin in Water", can be found under https://omlc.org/spectra/hemoglobin/summary.html, **2018**.

[51] N. Karousis, N. Tagmatarchis, D. Tasis, *Chem. Rev.* **2010**, *110*, 5366.

[52] a) P. Singh, S. Campidelli, S. Giordani, D. Bonifazi, A. Bianco, M. Prato, *Chem. Soc. Rev.* **2009**, *38*, 2214; b) A. Hirsch, *Angew. Chem. Int. Ed.* **2002**, *41*, 1853; *Angew. Chem.* **2002**, *114*, 1933; c) P. Bilalis, D. Katsigiannopoulos, A. Avgeropoulos, G. Sakellariou, *RSC Adv.* **2014**, *4*, 2911; d) C. A. Dyke, J. M. Tour, *J. Phys. Chem. A* **2004**, *108*, 11151; e) H.-C. Wu, X. Chang, L. Liu, F. Zhao, Y. Zhao, *J. Mater. Chem.* **2010**, *20*, 1036; f) Z. Liu, S. M. Tabakman, Z. Chen, H. Dai, *Nat. Protoc.* **2009**, *4*, 1372.

[53] A. H. Brozena, M. Kim, L. R. Powell, Y. Wang, *Nat. Rev. Chem.* **2019**, *3*, 375.

[54] a) F. Ernst, T. Heek, A. Setaro, R. Haag, S. Reich, *Adv. Funct. Mater.* **2012**, *22*, 3921; b) F. Ernst, T. Heek, A. Setaro, R. Haag, S. Reich, *J. Phys. Chem. C* **2013**, *117*, 1157.

[55] X. Tu, S. Manohar, A. Jagota, M. Zheng, *Nature* **2009**, *460*, 250.

[56] D. P. Salem, X. Gong, A. T. Liu, V. B. Koman, J. Dong, M. S. Strano, *J. Am. Chem. Soc.* **2017**, *139*, 16791.

[57] A. J. Gillen, J. Kupis-Rozmysłowicz, C. Gigli, N. Schuergers, A. A. Boghossian, *J. Phys. Chem. Lett.* **2018**, *9*, 4336.

[58] a) Y. Tomonari, H. Murakami, N. Nakashima, *Chemistry* **2006**, *12*, 4027; b) Y.-L. Zhao, L. Hu, J. F. Stoddart, G. Grüner, *Adv. Mater.* **2008**, *20*, 1910; c) P. Petrov, F. Stassin, C. Pagnoulle, R. Jérôme, *Chem. Commun.* **2003**, 2904.

[59] a) S. Wang, E. S. Humphreys, S.-Y. Chung, D. F. Delduco, S. R. Lustig, H. Wang, K. N. Parker, N. W. Rizzo, S. Subramoney, Y.-M. Chiang, et al., *Nat. Mater.* **2003**, *2*, 196; b) V. Zorbas, A. Ortiz-Acevedo, A. B. Dalton, M. M. Yoshida, G. R. Dieckmann, R. K. Draper, R. H. Baughman, M. Jose-Yacaman, I. H. Musselman, *J. Am. Chem. Soc.* **2004**, *126*, 7222; c) G. R. Dieckmann, A. B. Dalton, P. A. Johnson, J. Razal, J. Chen, G. M. Giordano, E. Muñoz, I. H. Musselman, R. H. Baughman, R. K. Draper, *J. Am. Chem. Soc.* **2003**, *125*, 1770; d) F. A. Mann, J. Horlebein, N. F. Meyer, D. Meyer, F. Thomas, S. Kruss, *Chemistry* **2018**, *24*, 12241.

[60] A. Antonucci, J. Kupis-Rozmysłowicz, A. A. Boghossian, *ACS Appl. Mater. Interfaces* **2017**, *9*, 11321.

[61] S. S. Karajanagi, H. Yang, P. Asuri, E. Sellitto, J. S. Dordick, R. S. Kane, *Langmuir* **2006**, *22*, 1392.

[62] T. Fujigaya, N. Nakashima, *Sci. Technol. Adv. Mater.* **2015**, *16*, 024802.

[63] E. Polo, S. Kruss, *J. Phys. Chem. C* **2016**, *120*, 3061.

[64] J. Zhang, S. Kruss, A. J. Hilmer, S. Shimizu, Z. Schmois, F. de La Cruz, P. W. Barone, N. F. Reuel, D. A. Heller, M. S. Strano, *Adv. Healthcare Mater.* **2014**, *3*, 412.

[65] R. M. Williams, C. Lee, T. V. Galassi, J. D. Harvey, R. Leicher, M. Sirenko, M. A. Dorso, J. Shah, N. Olvera, F. Dao, et al., *Sci. Adv.* **2018**, *4*, eaaq1090.

[66] E. Polo, T. T. Nitka, E. Neubert, L. Erpenbeck, L. Vuković, S. Kruss, *ACS Appl. Mater. Interfaces* **2018**, *10*, 17693.

[67] F. A. Mann, Z. Lv, J. Großhans, F. Opazo, S. Kruss, *Angew. Chem. Int. Ed.* **2019**, *58*, 11469; *Angew. Chem.* **2019**, *131*, 11591.

[68] K. Yum, J.-H. Ahn, T. P. McNicholas, P. W. Barone, B. Mu, J.-H. Kim, R. M. Jain, M. S. Strano, *ACS Nano* **2012**, *6*, 819.

[69] T.-W. Tsai, G. Heckert, L. F. Neves, Y. Tan, D.-Y. Kao, R. G. Harrison, D. E. Resasco, D. W. Schmidtke, *Anal. Chem.* **2009**, *81*, 7917.

[70] J. Zhang, M. P. Landry, P. W. Barone, J.-H. Kim, S. Lin, Z. W. Ulissi, D. Lin, B. Mu, A. A. Boghossian, A. J. Hilmer, et al., *Nat. Nanotechnol.* **2013**, *8*, 959.

[71] G. Bisker, J. Dong, H. D. Park, N. M. Iverson, J. Ahn, J. T. Nelson, M. P. Landry, S. Kruss, M. S. Strano, *Nat. Commun.* **2016**, *7*, 10241.

[72] A. Setaro, M. Adeli, M. Glaeske, D. Przyrembel, T. Bisswanger, G. Gordeev, F. Maschietto, A. Faghani, B. Paulus, M. Weinelt, et al., *Nat. Commun.* **2017**, *8*, 14281.

[73] a) X. He, H. Htoon, S. K. Doorn, W. H. P. Pernice, F. Pyatkov, R. Krupke, A. Jeantet, Y. Chassagneux, C. Voisin, *Nat. Mater.* **2018**, *17*, 663; b) Y. Miyauchi, M. Iwamura, S. Mouri, T. Kawazoe, M. Ohtsu, K. Matsuda, *Nat. Photonics* **2013**, *7*, 715.

[74] Y. Piao, B. Meany, L. R. Powell, N. Valley, H. Kwon, G. C. Schatz, Y. Wang, *Nat. Chem.* **2013**, *5*, 840.

[75] S. Ghosh, S. M. Bachilo, R. A. Simonette, K. M. Beckingham, R. B. Weisman, *Science* **2010**, *330*, 1656.

[76] Q. H. Wang, M. S. Strano, *Nat. Chem.* **2013**, *5*, 812.

[77] C.-W. Lin, S. M. Bachilo, Y. Zheng, U. Tsedev, S. Huang, R. B. Weisman, A. M. Belcher, *Nat. Commun.* **2019**, *10*, 2874.

[78] C. F. Chiu, W. A. Saidi, V. E. Kagan, A. Star, *J. Am. Chem. Soc.* **2017**, *139*, 4859.

[79] F. A. Mann, N. Herrmann, F. Opazo, S. Kruss, *Angew. Chem. Int. Ed.* **2020**, *59*, 17732; *Angew. Chem.* **2020**, *132*, 17885.

[80] L. Chio, R. L. Pinals, A. Murali, N. S. Goh, M. P. Landry, *Adv. Funct. Mater.* **2020**, *30*, 1910556.

[81] T. Shiraki, H. Onitsuka, T. Shiraishi, N. Nakashima, *Chem. Commun.* **2016**, *52*, 12972.

[82] a) D. Janas, *Mater. Horiz.* **2020**, *7*, 2860; b) T. Shiraki, *Chem. Lett.* **2021**, *50*, 397.

[83] T. Shiraki, S. Uchimura, T. Shiraishi, H. Onitsuka, N. Nakashima, *Chem. Commun.* **2017**, *53*, 12544.

[84] C. Hansch, A. Leo, R. W. Taft, *Chem. Rev.* **1991**, *91*, 165.

[85] H. Kwon, M. Kim, B. Meany, Y. Piao, L. R. Powell, Y. Wang, *J. Phys. Chem. C* **2015**, *119*, 3733.

[86] a) M. Freeley, H. L. Worthy, R. Ahmed, B. Bowen, D. Watkins, J. E. Macdonald, M. Zheng, D. D. Jones, M. Palma, *J. Am. Chem. Soc.* **2017**, *139*, 17834; b) P. Clément, P. Trinchera, K. Cervantes-Salguero, Q. Ye, C. R. Jones, M. Palma, *ChemPlusChem* **2019**, *84*, 1235; c) G. Amoroso, Q. Ye, K. Cervantes-Salguero, G. Fernández, A. Cecconello, M. Palma, *Chem. Mater.* **2019**, *31*, 1537.

[87] A. Spreinat, M. M. Dohmen, J. Lüttgens, N. Herrmann, L. F. Klepzig, R. Nißler, S. Weber, F. A. Mann, J. Lauth, S. Kruss, *J. Phys. Chem. C* **2021**, *125*, 18341.

[88] D. A. Heller, P. V. Jena, M. Pasquali, K. Kostarelos, L. G. Delogu, R. E. Meidl, S. V. Rotkin, D. A. Scheinberg, R. E. Schwartz, M. Terrones, et al., *Nat. Nanotechnol.* **2020**, *15*, 164.

[89] K. Aoki, N. Saito, *Nanomaterials* **2020**, *10*, 264.

[90] V. E. Kagan, N. V. Konduru, W. Feng, B. L. Allen, J. Conroy, Y. Volkov, I. I. Vlasova, N. A. Belikova, N. Yanamala, A. Kapralov, et al., *Nat. Nanotechnol.* **2010**, *5*, 354.

[91] D. Elgrabli, W. Dachraoui, C. Ménard-Moyon, X. J. Liu, D. Bégin, S. Bégin-Colin, A. Bianco, F. Gazeau, D. Alloyeau, *ACS Nano* **2015**, *9*, 10113.

[92] M. P. Monopoli, C. Aberg, A. Salvati, K. A. Dawson, *Nat. Nanotechnol.* **2012**, *7*, 779.

[93] M. Gravely, M. M. Safaee, D. Roxbury, *Nano Lett.* **2019**, *19*, 6203.

[94] M. Gravely, D. Roxbury, *ACS Nano* **2021**, *15*, 12388.

[95] H. Ali-Boucetta, A. Nunes, R. Sainz, M. A. Herrero, B. Tian, M. Prato, A. Bianco, K. Kostarelos, *Angew. Chem. Int. Ed.* **2013**, *52*, 2274; *Angew. Chem.* **2013**, *125*, 2330.

[96] T. V. Galassi, M. Antman-Passig, Z. Yaari, J. Jessurun, R. E. Schwartz, D. A. Heller, *PLoS One* **2020**, *15*, e0226791.

[97] B. Fadeel, K. Kostarelos, *Nat. Nanotechnol.* **2020**, *15*, 164.

[98] R. L. Pinals, D. Yang, D. J. Rosenberg, T. Chaudhary, A. R. Crothers, A. T. Iavarone, M. Hammel, M. P. Landry, *Angew. Chem. Int. Ed.* **2020**, *59*, 23668; *Angew. Chem.* **2020**, *132*, 23876.

[99] M. Faria, M. Björnmalm, K. J. Thurecht, S. J. Kent, R. G. Parton, M. Kavallaris, A. P. R. Johnston, J. J. Gooding, S. R. Corrie, B. J. Boyd, et al., *Nat. Nanotechnol.* **2018**, *13*, 777.

[100] S. Kruss, D. P. Salem, L. Vuković, B. Lima, E. Vander Ende, E. S. Boyden, M. S. Strano, *Proc. Natl. Acad. Sci. USA* **2017**, *114*, 1789.

[101] G. Bisker, N. A. Bakh, M. A. Lee, J. Ahn, M. Park, E. B. O'Connell, N. M. Iverson, M. S. Strano, *ACS Sens.* **2018**, *3*, 367.

[102] B. C. Satishkumar, L. O. Brown, Y. Gao, C.-C. Wang, H.-L. Wang, S. K. Doorn, *Nat. Nanotechnol.* **2007**, *2*, 560.

[103] J.-H. Ahn, J.-H. Kim, N. F. Reuel, P. W. Barone, A. A. Boghossian, J. Zhang, H. Yoon, A. C. Chang, A. J. Hilmer, M. S. Strano, *Nano Lett.* **2011**, *11*, 2743.

[104] J. T. Nelson, S. Kim, N. F. Reuel, D. P. Salem, G. Bisker, M. P. Landry, S. Kruss, P. W. Barone, S. Kwak, M. S. Strano, *Anal. Chem.* **2015**, *87*, 8186.

[105] M. P. Landry, H. Ando, A. Y. Chen, J. Cao, V. I. Kottadiel, L. Chio, D. Yang, J. Dong, T. K. Lu, M. S. Strano, *Nat. Nanotechnol.* **2017**, *12*, 368.

[106] R. M. Williams, C. Lee, D. A. Heller, *ACS Sens.* **2018**, *3*, 1838.

[107] N. F. Reuel, J.-H. Ahn, J.-H. Kim, J. Zhang, A. A. Boghossian, L. K. Mahal, M. S. Strano, *J. Am. Chem. Soc.* **2011**, *133*, 17923.

[108] H. Yoon, J.-H. Ahn, P. W. Barone, K. Yum, R. Sharma, A. A. Boghossian, J.-H. Han, M. S. Strano, *Angew. Chem. Int. Ed.* **2011**, *50*, 1828; *Angew. Chem.* **2011**, *123*, 1868.

[109] H. Jin, E. S. Jeng, D. A. Heller, P. V. Jena, R. Kirmse, J. Langowski, M. S. Strano, *Macromolecules* **2007**, *40*, 6731.

[110] D. A. Heller, H. Jin, B. M. Martinez, D. Patel, B. M. Miller, T.-K. Yeung, P. V. Jena, C. Höbartner, T. Ha, S. K. Silverman, et al., *Nat. Nanotechnol.* **2009**, *4*, 114.

[111] S. Bhattacharya, X. Gong, E. Wang, S. K. Dutta, J. R. Caplette, M. Son, F. T. Nguyen, M. S. Strano, D. Mukhopadhyay, *Cancer Res.* **2019**, *79*, 4515.

[112] M. M. Safaee, M. Gravely, D. Roxbury, *Adv. Funct. Mater.* **2021**, *31*, 2006254.

[113] N. M. Iverson, G. Bisker, E. Farias, V. Ivanov, J. Ahn, G. N. Wogan, M. S. Strano, *J. Biomed. Nanotechnol.* **2016**, *12*, 1035.

[114] E. Polo, S. Kruss, *Anal. Bioanal. Chem.* **2016**, *408*, 2727.

[115] J. D. Harvey, R. M. Williams, K. M. Tully, H. A. Baker, Y. Shamay, D. A. Heller, *Nano Lett.* **2019**, *19*, 4343.

[116] D. P. Salem, X. Gong, A. T. Liu, K. Akombi, M. S. Strano, *Anal. Chem.* **2020**, *92*, 916.

[117] P. V. Jena, D. Roxbury, T. V. Galassi, L. Akkari, C. P. Horoszko, D. B. Iaea, J. Budhathoki-Uprety, N. Pipalia, A. S. Haka, J. D. Harvey, et al., *ACS Nano* **2017**, *11*, 10689.

[118] F. A. Mann, N. Herrmann, D. Meyer, S. Kruss, *Sensors* **2017**, *17*, 1521.

[119] A. G. Beyene, A. A. Alizadehmojarad, G. Dorlhiac, N. Goh, A. M. Streets, P. Král, L. Vuković, M. P. Landry, *Nano Lett.* **2018**, *18*, 6995.

[120] A. G. Beyene, K. Delevich, J. T. Del Bonis-O'Donnell, D. J. Piekarski, W. C. Lin, A. W. Thomas, S. J. Yang, P. Kosillo, D. Yang, G. S. Prounis, et al., *Sci. Adv.* **2019**, *5*, eaaw3108.

[121] R. Nißler, F. A. Mann, H. Preiß, G. Selvaggio, N. Herrmann, S. Kruss, *Nanoscale* **2019**, *11*, 11159.

[122] R. Mittler, S. Vanderauwera, N. Suzuki, G. Miller, V. B. Tognetti, K. Vandepoele, M. Gollery, V. Shulaev, F. Van Breusegem, *Trends Plant Sci.* **2011**, *16*, 300.

[123] I. S. Zulfugarov, A. Tovuu, J.-H. Kim, C.-H. Lee, *J. Plant Biol.* **2011**, *54*, 351.

[124] J.-H. Kim, D. A. Heller, H. Jin, P. W. Barone, C. Song, J. Zhang, L. J. Trudel, G. N. Wogan, S. R. Tannenbaum, M. S. Strano, *Nat. Chem.* **2009**, *1*, 473.

[125] H. Jin, D. A. Heller, M. Kalbacova, J.-H. Kim, J. Zhang, A. A. Boghossian, N. Maheshri, M. S. Strano, *Nat. Nanotechnol.* **2010**, *5*, 302.

[126] J.-H. Kim, C. R. Patra, J. R. Arkalgud, A. A. Boghossian, J. Zhang, J.-H. Han, N. F. Reuel, J.-H. Ahn, D. Mukhopadhyay, M. S. Strano, *ACS Nano* **2011**, *5*, 7848.

[127] N. M. Iverson, P. W. Barone, M. Shandell, L. J. Trudel, S. Sen, F. Sen, V. Ivanov, E. Atolia, E. Farias, T. P. McNicholas, et al., *Nat. Nanotechnol.* **2013**, *8*, 873.

[128] Z. W. Ulissi, F. Sen, X. Gong, S. Sen, N. Iverson, A. A. Boghossian, L. C. Godoy, G. N. Wogan, D. Mukhopadhyay, M. S. Strano, *Nano Lett.* **2014**, *14*, 4887.

[129] J. Meier, J. Stapleton, E. Hofferber, A. Haworth, S. Kachman, N. M. Iverson, *Nanomaterials* **2021**, *11*, 243.

[130] V. D. Petrov, F. Van Breusegem, *AoB PLANTS* **2012**, *2012*, pls014.

[131] Y. Zheng, S. M. Bachilo, R. B. Weisman, *J. Phys. Chem. Lett.* **2017**, *8*, 1952.

[132] Y. Zheng, S. M. Bachilo, R. B. Weisman, *ACS Nano* **2019**, *13*, 8222.

[133] S. D. Niyonambaza, P. Kumar, P. Xing, J. Mathault, P. de Koninck, E. Boisselier, M. Boukadoum, A. Miled, *Appl. Sci.* **2019**, *9*, 4719.

[134] S. Jeong, D. Yang, A. G. Beyene, J. T. Del Bonis-O'Donnell, A. M. M. Gest, N. Navarro, X. Sun, M. P. Landry, *Sci. Adv.* **2019**, *5*, eaay3771.

[135] S. Elizarova, A. Chouaib, A. Shaib, F. Mann, N. Brose, S. Kruss, J. A. Daniel, *bioRxiv* **2021**, DOI 10.1101/2021.03.28.437019.

[136] A. J. Gillen, A. Antonucci, M. Reggente, D. Morales, A. A. Boghossian, *bioRxiv* **2021**, DOI 10.1101/2021.02.20.428669.

[137] A. J. Gillen, D. J. Siefman, S.-J. Wu, C. Bourmaud, B. Lambert, A. A. Boghossian, *J. Colloid Interface Sci.* **2020**, *565*, 55.

[138] a) E. Neubert, D. Meyer, F. Rocca, G. Günay, A. Kwaczala-Tessmann, J. Grandke, S. Senger-Sander, C. Geisler, A. Egner, M. P. Schön, et al., *Nat. Commun.* **2018**, *9*, 3767; b) V. Brinkmann, U. Reichard, C. Goosmann, B. Fauler, Y. Uhlemann, D. S. Weiss, Y. Weinrauch, A. Zychlinsky, *Science* **2004**, *303*, 1532.

[139] D. Meyer, S. Telele, A. Zelená, A. J. Gillen, A. Antonucci, E. Neubert, R. Nißler, F. A. Mann, L. Erpenbeck, A. A. Boghossian, et al., *Nanoscale* **2020**, *12*, 9104.

[140] J.-H. Kim, J.-H. Ahn, P. W. Barone, H. Jin, J. Zhang, D. A. Heller, M. S. Strano, *Angew. Chem. Int. Ed.* **2010**, *49*, 1456; *Angew. Chem.* **2010**, *122*, 1498.

[141] D. A. Heller, G. W. Pratt, J. Zhang, N. Nair, A. J. Hansborough, A. A. Boghossian, N. F. Reuel, P. W. Barone, M. S. Strano, *Proc. Natl. Acad. Sci. USA* **2011**, *108*, 8544.

[142] M. A. Lee, F. T. Nguyen, K. Scott, N. Y. L. Chan, N. A. Bakh, K. K. Jones, C. Pham, P. Garcia-Salinas, D. Garcia-Parraga, A. Fahlman, et al., *ACS Sens.* **2019**, *4*, 32.

[143] J. T. Del Bonis-O'Donnell, R. L. Pinals, S. Jeong, A. Thakrar, R. D. Wolfinger, M. P. Landry, *Biochemistry* **2019**, *58*, 54.

[144] M. A. Lee, S. Wang, X. Jin, N. A. Bakh, F. T. Nguyen, J. Dong, K. S. Silmore, X. Gong, C. Pham, K. K. Jones, et al., *Adv. Healthc. Mater.* **2020**, *9*, 2000429.

[145] V. Shumeiko, E. Malach, Y. Helman, Y. Paltiel, G. Bisker, Z. Hayouka, O. Shoseyov, *Sens. Actuators B* **2021**, *327*, 128832.

[146] V. Shumeiko, Y. Paltiel, G. Bisker, Z. Hayouka, O. Shoseyov, *Biosens. Bioelectron.* **2021**, *172*, 112763.

[147] J. Dong, M. A. Lee, A. G. Rajan, I. Rahaman, J. H. Sun, M. Park, D. P. Salem, M. S. Strano, *Proc. Natl. Acad. Sci. USA* **2020**, *117*, 26616.

[148] R. Nißler, A. T. Müller, F. Dohrman, L. Kurth, H. Li, E. G. Cosio, B. S. Flavel, J. P. Giraldo, A. Mithöfer, S. Kruss, *Angew. Chem. Int. Ed.* **2022**, *61*, e202108373; *Angew. Chem.* **2022**, *134*, e202108373.

[149] T. V. Galassi, P. V. Jena, J. Shah, G. Ao, E. Molitor, Y. Bram, A. Frankel, J. Park, J. Jessurun, D. S. Ory, et al., *Sci. Transl. Med.* **2018**, *10*, eaar2680.

[150] V. S. Rao, K. Srinivas, G. N. Sujini, G. N. S. Kumar, *Int. J. Proteomics* **2014**, *2014*, 147648.

[151] J. Dong, D. P. Salem, J. H. Sun, M. S. Strano, *ACS Nano* **2018**, *12*, 3769.

Reviews

[152] J. Budhathoki-Uprety, J. Shah, J. A. Korsen, A. E. Wayne, T. V. Galassi, J. R. Cohen, J. D. Harvey, P. V. Jena, L. V. Ramanathan, E. A. Jaimes, et al., *Nat. Commun.* **2019**, *10*, 3605.

[153] L. Chio, J. T. Del Bonis-O'Donnell, M. A. Kline, J. H. Kim, I. R. McFarlane, R. N. Zuckermann, M. P. Landry, *Nano Lett.* **2019**, *19*, 7563.

[154] R. M. Williams, J. D. Harvey, J. Budhathoki-Uprety, D. A. Heller, *Nano Lett.* **2020**, *20*, 7287.

[155] T.-G. Cha, B. A. Baker, M. D. Sauffer, J. H. Choi in *2010 18th Biennial University/Government/Industry Micro/Nano Symposium*, IEEE, **2010-2010**, pp. 1–4.

[156] T.-G. Cha, B. A. Baker, M. D. Sauffer, J. Salgado, D. Jaroch, J. L. Rickus, D. M. Porterfield, J. H. Choi, *ACS Nano* **2011**, *5*, 4236.

[157] R. L. Pinals, F. Ledesma, D. Yang, N. Navarro, S. Jeong, J. E. Pak, L. Kuo, Y.-C. Chuang, Y.-W. Cheng, H.-Y. Sun, et al., *Nano Lett.* **2021**, *21*, 2272.

[158] R. Ehrlich, A. Hendler-Neumark, V. Wulf, D. Amir, G. Bisker, *Small* **2021**, *17*, 2101660.

[159] D. Kozawa, S.-Y. Cho, X. Gong, F. T. Nguyen, X. Jin, M. A. Lee, H. Lee, A. Zeng, G. Xue, J. Schacherl et al., *ACS Nano* **2020**, *14*, 10141.

[160] Z. Yaari, Y. Yang, E. Apfelbaum, C. Cupo, A. H. Settle, Q. Cullen, W. Cai, K. L. Roche, D. A. Levine, M. Fleisher, et al., *Sci. Adv.* **2021**, *7*, eabj0852.

[161] V. Zubkovs, N. Schuergers, B. Lambert, E. Ahunbay, A. A. Boghossian, *Small* **2017**, *13*, 1701654.

[162] V. A. Karachevtsev, A. Glamazda, V. S. Leontiev, O. S. Lytvyn, U. Dettlaff-Weglikowska, *Chem. Phys. Lett.* **2007**, *435*, 104.

[163] J. D. Harvey, P. V. Jena, H. A. Baker, G. H. Zerze, R. M. Williams, T. V. Galassi, D. Roxbury, J. Mittal, D. A. Heller, *Nat. Biomed. Eng.* **2017**, *1*, 0041.

[164] J. D. Harvey, H. A. Baker, M. V. Ortiz, A. Kentsis, D. A. Heller, *ACS Sens.* **2019**, *4*, 1236.

[165] T.-G. Cha, J. Pan, H. Chen, J. Salgado, X. Li, C. Mao, J. H. Choi, *Nat. Nanotechnol.* **2014**, *9*, 39.

[166] N. E. Kallmyer, J. Musielewicz, J. Sutter, N. F. Reuel, *Anal. Chem.* **2018**, *90*, 5209.

[167] N. E. Kallmyer, M. S. Abdennadher, S. Agarwal, R. Baldwin-Kordick, R. L. Khor, A. S. Kooistra, E. Peterson, M. D. McDaniel, N. F. Reuel, *Anal. Chem.* **2021**, *93*, 4800.

[168] V. Shumeiko, Y. Paltiel, G. Bisker, Z. Hayouka, O. Shoseyov, *Sensors* **2020**, *20*, 5247.

[169] X. He, D. L. White, A. A. Kapralov, V. E. Kagan, A. Star, *Anal. Chem.* **2020**, *92*, 12880.

[170] N. M. Bardhan, D. Ghosh, A. M. Belcher, *Nat. Commun.* **2014**, *5*, 4918.

[171] G. Selvaggio, A. Chizhik, R. Nißler, L. Kuhlemann, D. Meyer, L. Vuong, H. Preiß, N. Herrmann, F. A. Mann, Z. Lv, et al., *Nat. Commun.* **2020**, *11*, 1495.

[172] F. Wang, G. Dukovic, E. Knoesel, L. E. Brus, T. F. Heinz, *Phys. Rev. B* **2004**, *70*, 241403(R).

[173] J. H. Choi, M. S. Strano, *Appl. Phys. Lett.* **2007**, *90*, 223114.

[174] C. A. Silvera-Batista, R. K. Wang, P. Weinberg, K. J. Ziegler, *Phys. Chem. Chem. Phys.* **2010**, *12*, 6990.

[175] F. F. Bergler, F. Schöppler, F. K. Brunecker, M. Hailman, T. Hertel, *J. Phys. Chem. C* **2013**, *117*, 13318.

[176] R. Nißler, F. A. Mann, P. Chaturvedi, J. Horlebein, D. Meyer, L. Vuković, S. Kruss, *J. Phys. Chem. C* **2019**, *123*, 4837.

[177] J. D. Harvey, G. H. Zerze, K. M. Tully, J. Mittal, D. A. Heller, *J. Phys. Chem. C* **2018**, *122*, 10592.

[178] X. He, K. A. Velizhanin, G. Bullard, Y. Bai, J.-H. Olivier, N. F. Hartmann, B. J. Gifford, S. Kilina, S. Tretiak, H. Htoon, et al., *ACS Nano* **2018**, *12*, 8060.

[179] M. Schäferling, *Angew. Chem. Int. Ed.* **2012**, *51*, 3532; *Angew. Chem.* **2012**, *124*, 3590.

[180] D. Meyer, A. Hagemann, S. Kruss, *ACS Nano* **2017**, *11*, 4017.

[181] A. L. Antaris, O. K. Yaghi, G. Hong, S. Diao, B. Zhang, J. Yang, L. Chew, H. Dai, *Small* **2015**, *11*, 6325.

[182] A. L. Antaris, J. T. Robinson, O. K. Yaghi, G. Hong, S. Diao, R. Luong, H. Dai, *ACS Nano* **2013**, *7*, 3644.

[183] a) F. Yang, X. Wang, D. Zhang, J. Yang, D. Luo, Z. Xu, J. Wei, J.-Q. Wang, Z. Xu, F. Peng, et al., *Nature* **2014**, *510*, 522; b) H. An, A. Kumamoto, H. Takezaki, S. Ohyama, Y. Qian, T. Inoue, Y. Ikuhara, S. Chiashi, R. Xiang, S. Maruyama, *Nanoscale* **2016**, *8*, 14523.

[184] a) S. Ghosh, S. M. Bachilo, R. B. Weisman, *Nat. Nanotechnol.* **2010**, *5*, 443; b) M. S. Arnold, A. A. Green, J. F. Hulvat, S. I. Stupp, M. C. Hersam, *Nat. Nanotechnol.* **2006**, *1*, 60.

[185] a) H. Liu, D. Nishide, T. Tanaka, H. Kataura, *Nat. Commun.* **2011**, *2*, 309; b) B. S. Flavel, M. M. Kappes, R. Krupke, F. Hennrich, *ACS Nano* **2013**, *7*, 3557; c) K. Tvrdy, R. M. Jain, R. Han, A. J. Hilmer, T. P. McNicholas, M. S. Strano, *ACS Nano* **2013**, *7*, 1779.

[186] a) J. A. Fagan, C. Y. Khripin, C. A. Silvera Batista, J. R. Simpson, E. H. Hároz, A. R. Hight Walker, M. Zheng, *Adv. Mater.* **2014**, *26*, 2800; b) C. Y. Khripin, J. A. Fagan, M. Zheng, *J. Am. Chem. Soc.* **2013**, *135*, 6822; c) H. Li, G. Gordeev, O. Garrity, S. Reich, B. S. Flavel, *ACS Nano* **2019**, *13*, 2567.

[187] a) M. Zheng, A. Jagota, M. S. Strano, A. P. Santos, P. Barone, S. G. Chou, B. A. Diner, M. S. Dresselhaus, R. S. McLean, G. B. Onoa, et al., *Science* **2003**, *302*, 1545; b) A. Nish, J.-Y. Hwang, J. Doig, R. J. Nicholas, *Nat. Nanotechnol.* **2007**, *2*, 640; c) H. Ozawa, N. Ide, T. Fujigaya, Y. Niidome, N. Nakashima, *Chem. Lett.* **2011**, *40*, 239; d) A. Graf, Y. Zakharko, S. P. Schießl, C. Backes, M. Pfohl, B. S. Flavel, J. Zaumseil, *Carbon* **2016**, *105*, 593.

[188] G. Selvaggio, M. Weitzel, N. Oleksiievets, T. A. Oswald, R. Nißler, I. P. Mey, V. Karius, J. Enderlein, R. Tsukanov, S. Kruss, *Nanoscale Adv.* **2021**, *3*, 4541.

[189] N. Danné, A. G. Godin, Z. Gao, J. A. Varela, L. Groc, B. Lounis, L. Cognet, *ACS Photonics* **2018**, *5*, 359.

[190] A. K. Mandal, X. Wu, J. S. Ferreira, M. Kim, L. R. Powell, H. Kwon, L. Groc, Y. Wang, L. Cognet, *Sci. Rep.* **2020**, *10*, 5286.

[191] N. Fakhri, A. D. Wessel, C. Willms, M. Pasquali, D. R. Klopfenstein, F. C. MacKintosh, C. F. Schmidt, *Science* **2014**, *344*, 1031.

[192] A. G. Godin, J. A. Varela, Z. Gao, N. Danné, J. P. Dupuis, B. Lounis, L. Groc, L. Cognet, *Nat. Nanotechnol.* **2017**, *12*, 238.

[193] S. M. Santos, B. Yuma, S. Berciaud, J. Shaver, M. Gallart, P. Gilliot, L. Cognet, B. Lounis, *Phys. Rev. Lett.* **2011**, *107*, 187401.

[194] a) N. Akizuki, S. Aota, S. Mouri, K. Matsuda, Y. Miyauchi, *Nat. Commun.* **2015**, *6*, 8920; b) S. Aota, N. Akizuki, S. Mouri, K. Matsuda, Y. Miyauchi, *Appl. Phys. Express* **2016**, *9*, 045103.

[195] J. T. Del Bonis-O'Donnell, R. H. Page, A. G. Beyene, E. G. Tindall, I. R. McFarlane, M. P. Landry, *Adv. Funct. Mater.* **2017**, *27*, 1702112.

[196] C. Paviolo, L. Cognet, *Neurobiol. Dis.* **2021**, *153*, 105328.

[197] D. Roxbury, P. V. Jena, R. M. Williams, B. Enyedi, P. Niethammer, S. Marcet, M. Verhaegen, S. Blais-Ouellette, D. A. Heller, *Sci. Rep.* **2015**, *5*, 14167.

[198] V. Zubkovs, A. Antonucci, N. Schuergers, B. Lambert, A. Latini, R. Ceccarelli, A. Santinelli, A. Rogov, D. Ciepielewski, A. A. Boghossian, *Sci. Rep.* **2018**, *8*, 13770.

[199] J. J. Brege, C. Gallaway, A. R. Barron, *J. Phys. Chem. C* **2007**, *111*, 17812.

[200] H. Jin, D. A. Heller, J.-H. Kim, M. S. Strano, *Nano Lett.* **2008**, *8*, 4299.

[201] Z. Yaari, J. M. Cheung, H. A. Baker, R. S. Frederiksen, P. V. Jena, C. P. Horoszko, F. Jiao, S. Scheuring, M. Luo, D. A. Heller, *Nano Lett.* **2020**, *20*, 7819.

[202] D. P. Salem, M. P. Landry, G. Bisker, J. Ahn, S. Kruss, M. S. Strano, *Carbon* **2016**, *97*, 147.

[203] D. Yang, S. J. Yang, J. T. Del Bonis-O'Donnell, R. L. Pinals, M. P. Landry, *ACS Nano* **2020**, *14*, 13794.

[204] J. Pan, H. Zhang, T.-G. Cha, H. Chen, J. H. Choi, *Anal. Chem.* **2013**, *85*, 8391.

[205] K. Welsher, Z. Liu, D. Daranciang, H. Dai, *Nano Lett.* **2008**, *8*, 586.

[206] D. Roxbury, P. V. Jena, Y. Shamay, C. P. Horoszko, D. A. Heller, *ACS Nano* **2016**, *10*, 499.

[207] R. Yang, Z. Tang, J. Yan, H. Kang, Y. Kim, Z. Zhu, W. Tan, *Anal. Chem.* **2008**, *80*, 7408.

[208] P. W. Barone in *AIP Conference Proceedings*, AIP, **2005**, pp. 193–197.

[209] N. F. Reuel, B. Grassbaugh, S. Kruss, J. Z. Mundy, C. Opel, A. O. Ogunniyi, K. Egodage, R. Wahl, B. Helk, J. Zhang, et al., *ACS Nano* **2013**, *7*, 7472.

[210] B. Mu, T. P. McNicholas, J. Zhang, A. J. Hilmer, Z. Jin, N. F. Reuel, J.-H. Kim, K. Yum, M. S. Strano, *J. Am. Chem. Soc.* **2012**, *134*, 17620.

[211] B. Mu, J. Ahn, T. P. McNicholas, M. S. Strano, *Chemistry* **2015**, *21*, 4523.

[212] E. S. Jeng, A. E. Moll, A. C. Roy, J. B. Gastala, M. S. Strano, *Nano Lett.* **2006**, *6*, 371.

[213] E. S. Jeng, J. D. Nelson, K. L. J. Prather, M. S. Strano, *Small* **2010**, *6*, 40.

2.4.2 Publication Synopsis

The comprehensive overview in the previous Section 2.4.1 describes the main advantages, methods, and developed biosensors of SWCNT-based sensing, as well as existing challenges. Key points relevant to this work are listed along with a brief discussion of previous SWCNT sensors for neurotransmitter detection to place them in the state-of-the-art.

SWCNTs emit in the NIR range, which falls within the tissue transparency window. This allows for detection at high signal-to-noise ratio (SNR), as scattering, autofluorescence, and absorption of biological samples are low in this range [Hon17]. Consequently, the penetration depth into tissue is increased. Unlike other fluorophores SWCNTs exhibit excellent photostability [Hon15]. These properties make them promising for long-term and/or *in vivo* applications. However, commercially available SWCNTs are only offered in mixtures of different chiralities [Yan20a], resulting in a broad fluorescence spectrum instead of single peak wavelengths, compromising sensitivity when used as a sensor. To access a specific chirality, separation techniques like density gradient ultracentrifugation (DGU) [Arn06, Gho10], aqueous two-phase extraction (ATPE) [Gui15, Li 19b], or gel chromatography [Liu11, Fla13] exist. However, depending on the method, this requires expensive equipment, expertise, and/or time. On the other hand, this offers the opportunity for spectral multiplexing by functionalizing different SWCNT chiralities and characterizing them based on their emission wavelength [Nis20]. Due to their fluorescence in the NIR and the fact that conventional cameras based on Si technology have a sensitivity limit up to a maximum of 1000 nm, the detection of SWCNT sensors requires expensive indium gallium arsenide (InGaAs) cameras ($> 21{,}000$ €) [Smi09], often in combination with lasers (561 nm, approx. 7,300 € [Opt23]) for excitation, to compensate for higher fluorescence signals due to the relatively low quantum efficiency of SWCNTs with $1 - 5$ % [Mal13].

From a chemical perspective, SWCNTs can be functionalized in a modular way. Functionalization serves to stabilize SWCNTs colloidally but also to create a sensor. The key expertise lies in selectively designing the surface chemistry of SWCNTs to achieve a desired sensor. Two main strategies for developing new sensor units are the screening and the rational approach. In the screening approach, a change in SWCNT fluorescence is observed when screening different analytes against arbitrarily functionalized sensors (e.g., with ssDNA sequences). Surprisingly selective units have been identified in the past using this method [Zha13, Bis16]. The biomolecule/polymer used for functionalization usually has no affinity to the target analyte, but selective binding sites are created by the resulting structure through the functionalization of the SWCNTs. The rational approach involves using known recognition entities, such as antibodies [Zha14, Wil18b], nanobodies [Man19], or aptamers [Din19, Nis20]. The former has the advantage that sensors for a target molecule

can be developed even without knowledge of a specific recognition unit. However, the screening process can be time-consuming. Establishing high-throughput screening in combination with assisted machine learning can be beneficial here [Gon22, Kel22].

Different mechanisms exist that lead to signal changes in SWCNT sensors. The change in sensor signal can be a shift in wavelength or a change in intensity. The SWCNT sensors for dopamine detection used in this thesis are functionalized non-covalently with ssDNA consisting of $(GT)_{10}$ sequences, which were identified by a screening procedure [Man17]. These sensors show a reversible fluorescence increase in the presence of dopamine and have sensitivities in the 100 pM range at the single SWCNT level [Eli22]. However, they also respond to similar molecules like epinephrines, norepinephrines, and ascorbic acid with smaller increases in fluorescence [Man17, Kru17], as is the case with many other detection methods from Section 2.3. Molecular dynamics simulations have revealed that the fluorescence change is caused by a conformational change [Kru17]. Dopamine interacts with its hydroxy and amine groups with the phosphate backbone of the ssDNA-functionalized SWCNTs, moving the ssDNA closer to the SWCNT surface. This changes the electrostatic potential at the SWCNT surface, which alters the exciton diffusion and thus the fluorescence (compare with *Figure 19 d, e* in the Review Manuscript).

The biocompatibility of SWCNTs is a matter of context. In principle, biocompatibility must be evaluated separately for each type of SWCNT (chirality, purity and biofunctionalization) [Gal20]. However, SWCNTs with stable functionalization show promising results in this regard even in permanent contact with cells [Gao17] or in *in vivo* studies [Gal20]. The increasing development of covalent functionalization strategies could contribute to the development of more stable conjugates for long-term applications in the future.

Due to their nanoscale dimensions with diameters of about 0.78 nm for CoMoCAT SWCNTs at lengths of 600 – 1000 nm after functionalization [Nis19, Nis21], sensors based on SWCNTs can achieve high spatial resolutions by simultaneously measuring multiple SWCNTs (e.g. by coating surfaces). The resolution is primarily limited by the optical resolution in microscopy and the pixel sizes of InGaAs camera technology, which is currently still rather large. To achieve resolution beyond the refraction limit super-resolution microscopy with SWCNTs has also been performed recently [Kag22, Nan22]. In terms of time, resolutions of <100 ms have been possible experimentally [Kru17]. These properties have already been exploited to image release processes of dopamine and serotonin in cells [Kru17, Din19, Eli22] and brain slices [Bey19] using SWCNT sensors increasing in fluorescence intensity (compare *Figure 9* and *Figure 10* in the Review Manuscript).

By coating the surfaces with sensors and then seeding cells on top, the increase in fluorescence intensity at local hotspots adjacent to and below the cells following cell stimulation

can be attributed to neurotransmitter release and mapped chemically. In addition to the dopamine sensors identified *via* the above screening procedure, a rational approach by functionalizing SWCNTs with a serotonin aptamer was used for the detection of serotonin [Din19], but the review reports a ssDNA sequence identified by a screening procedure as well [Jeo19]. However, even these two sequences are not fully selective compared with dopamine homologs (e.g., 11 % increase for dopamine vs. 45 % increase for serotonin) [Din19]. However, the high spatial resolution allows to analyze how the cell morphology affects the location of dopamine release [Kru17]. Another approach is to use SWCNT sensors as 'paint' applied to the cellular network [Eli22]. The sensors do not adhere to the cellular network itself, but surround it. This offers the advantage that in the case of prolonged cell cultivation, such as with neurons, the sensors are added only at the beginning of the experiment. Thus, possible influences on the viability of the cells and the sensitivity of the sensor are prevented. In addition to cross-selectivity to other neurotransmitters, local changes in ion concentrations may also affect sensor responses [Sal17]. In this regard, ssDNA sequences with locked nucleic acid (LNA) (containing a 2'-O, 4'-C methylene bridge which reduces flexibility) can provide an improvement [Gil18, Gil21].

How fast such chemical images assembled from a variety of SWCNT sensors can map changes in molecular concentrations depends not only on the frame rate of the camera but also on the kinetics of the sensors, i.e., how fast an analyte binds or dissociates from the sensor [Mey17]. Knowledge of these rate constants can thus predict how quickly concentration changes of molecules can be resolved. According to a simulation by Meyer *et al.*, the optimal dissociation constant K_d is in the range of 100 µM (e.g., k_{on} of 10^6 $M^{-1}s^{-1}$ and k_{off} of 10^2 s^{-1}) for imaging neurotransmitter release processes [Mey17].

Table 2.2 provides the ranking of SWCNTs for neurotransmitter detection compared to the state-of-the-art. SWCNTs outperform other technologies in terms of high spatial and temporal resolution and compete with the best methods in the literature in terms of sensitivity. However, the equipment required for SWCNT detection includes specialized cameras and lasers, which add to the overall cost in addition to standard microscopy equipment (included in this calculation as minimum costs). Moreover, the resolution achieved by SWCNTs is not limited by the Rayleigh criterion of optical microscopy, but rather by the currently InGaAs camera technology. There is a need for further optimization to enhance the selectivity of SWCNT sensors towards dopamine homologs, but this challenge is also faced by other technologies, as discussed in Section 2.3. The issue of toxicity is another point that must be addressed for each application in combination with the specifically used SWCNT sensors. Nonetheless, as a research tool, SWCNTs should not significantly influence the biological system to the extent that it biases the results.

Table 2.2: Performance parameter of fluorescent SWCNT sensors for neurotransmitter detection. Ranking: green – good, yellow – medium, red – poor. Sensitivity data refer to the detection of dopamine.

Method	Spatial Resolution	Temporal Resolution	Sensitivity	Selectivity	Equipment Costs	*In Vivo* Suitability
	🟢	🟢	🟢	🟡	🔴	🟡
SWCNT	850 nm* [Kru17]	< 100 ms [Kru17]	100 pM [Kru17]		58,000 €	

*Limited by the pixel size of indium gallium arsenide (InGaAs) cameras.

In a Nutshell

✓ SWCNTs fluoresce in the NIR (850 – 1700 nm) tissue transparency window (reduced scattering and autofluorescence of biological samples)

✓ Optically stable (no bleaching or blinking)

✓ Adaptable surface chemistry exploitable for the development of various sensors; reversible sensor response depending on sensor design

✓ High spatial and temporal resolution

✓ High sensitivity in the single-molecule regime

✓ Cross sensitivities to dopamine homologs in current SWCNT sensors for dopamine detection

Chapter 3

Results

In this chapter, the most significant results obtained during the course of this doctoral thesis are presented. The chapter is divided into two sections, each focusing on a research objective aimed at enhancing the sensitivity of fluorescent SWCNT-based sensors. Each section includes a previously published research manuscript, accompanied by a brief introduction and a publication synopsis that summarizes the research objectives, the methodology used, the major findings or results as well as the implications or significance of the work.

3.1 Cost-Effective Neurotransmitter Detection with Standard Microscopes

Chapter 2 has explained the crucial role of neurotransmitters in cell communication. To comprehensively understand and effectively address such complex biological processes, as well as the formation and progression of neurological disorders, it is essential to capture the dynamic behavior of cellular release events and their response to various stimuli.

As mentioned in Section 2.4, fluorescent SWCNT-based sensors possess an exceptional spatial and temporal resolution, making them capable of imaging this dynamic behavior. Previous publications have demonstrated the potential of SWCNT-based sensors in high-resolution imaging of cellular release processes of neurotransmitters like dopamine and serotonin [Kru17, Din19, Eli22]. These studies employed more than 20,000 sensors per cell, achieving a temporal resolution of less than 100 ms [Kru17]. However, specialized and expensive microscope equipment was used.

For SWCNT excitation, a laser with a wavelength of 561 nm and a high power of 500 mW was employed [Kru17, Din19, Eli22], while fluorescence detection relied on an InGaAs camera, which exhibits sensitivity in the range of approximately 900 − 1700 nm [Xen].

Although the performance of InGaAs detectors has shown improvement in recent years, they still have limitations compared to the well-established Si technology [Hon17]. The fabrication process of InGaAs detectors is complex, making them expensive and bulky. Additionally, these detectors exhibit high dark current/noise levels due to the small direct bandgap of InGaAs, while their resolution in terms of absolute pixel number remains low (320 x 256 pixels or 640 x 512 pixels, which is up to 50 times lower compared to Si cameras) [Hon17]. Typical dark current values for InGaAs cameras are around 10,000 electrons $(s \cdot pixel)^{-1}$ at -50 °C [Xen], whereas Si cameras exhibit dark currents of only 0.6 electrons $(s \cdot pixel)^{-1}$ at 10 °C [Ham23]. For further reductions in dark current, thermoelectric cooling is not sufficient and liquid-nitrogen cooling must be used to achieve temperatures as low as -190 °C [Hon17]. These factors in turn limit the practicability, high sensitivity, and spatial resolution of SWCNT-based sensing and prompts the question of which camera system can effectively provide higher SNR for imaging a specific fluorophore/emission wavelength within a specific biological context.

To make this technology more accessible, it would be advantageous to utilize standardized microscope equipment, such as a white LED for fluorescence excitation, along with cost-effective Si-based cameras. Si cameras offer a decreasing quantum efficiency towards the NIR, and (6,4)-SWCNTs, emitting at 880 nm, are thus the most suitable NIR emitters among SWCNTs. Antari *et al.* have already investigated the detection of pure (6,4)-SWCNTs with Si cameras by using DGU to extract (6,4)-SWCNTs from commercially available SWCNT mixtures [Ant15]. They subsequently employed these (6,4)-SWCNTs for immunohistochemical staining of cells and cancer tissue. However, this possibility of using (6,4)-SWCNTs in combination with Si cameras has not been demonstrated for a sensor application, nor has it been pursued otherwise. This limitation may be attributed to the lack of an easily accessible protocol for (6,4)-SWCNT separation.

DGU requires expensive equipment for the separation through a density-gradient medium under fast centrifugation, while ATPE is generally regarded as a cost-effective and simple method for the separation of surfactant- or ssDNA-dispersed SWCNTs between two immiscible polymers [Gui15, Li 19b, Lyu19]. By changing the overall conditions within this mixture, SWCNTs can be selectively partitioned between these phases. However, existing protocols for the separation of (6,4)-SWCNTs have been predominantly based on a sequential separation approach [Li 19b], involving multiple steps and resulting in a time-consuming process, which may be the reason why sensors based on (6,4)-SWCNTs have not yet been developed. In this context, however, other chirality-pure SWCNT sensors have demonstrated significantly stronger fluorescence emission, up to 10-fold, and in some cases larger intensity changes during detection, which is thus very promising [Nis21].

The study presented in the subsequent Section 3.1.1 (Research Manuscript I) was therefore guided by the following questions:

- Can the separation procedure for (6,4)-SWCNTs be optimized to provide simple, rapid, and highly scalable access to this specific SWCNT chirality?

- Within which fluorescence wavelength range should biological samples be detected to achieve an optimal signal-to-background ratio (SBR), considering the reduced detection efficiency but also the low dark current of Si cameras and the increasing benefits of reduced autofluorescence and scattering in the NIR?

- Can monochiral (6,4)-SWCNTs, when used with Si cameras, enhance analyte sensitivity compared to unpurified, commercially available SWCNTs? How does their sensitivity compare to InGaAs cameras?

- What is the speed of microscopic image acquisitions achievable with a 'standard' microscope setup?

- Can (6,4)-SWCNT-based sensors successfully image cellular release processes?

3.1.1 High Sensitivity Near-Infrared Imaging of Fluorescent Nanosensors (Research Manuscript I)

Graphical Abstract

(6,4)-SWCNTs fluoresce in the near-infrared (880 nm) and can be chemically functionalized with DNA to act as sensors. They provide access to the sweet spot between the efficiency of Si cameras of standard microscope equipment and the advantages of the near-infrared, which is shown by high-resolution mapping of dopamine release from cells.

Reference

Copyright Statement

Contributions

The research was designed and conceived by J.A. and S.K., with input from S.H., L.E., and K.S. S.K. coordinated the project. J.S. conducted the simulation of the SBR, while T.S. and E.R. performed part of the ATPE experiments. S.J. was responsible for cell cultivation and seeding of the cells on the sensors. A.S. conducted single SWCNT dopamine detection experiments at setup 2. All other experiments were carried out by J.A. Data analysis and manuscript writing were performed by J.A., with contributions from J.S., S.J., A.S., S.H., and S.K.

RESEARCH ARTICLE

High Sensitivity Near-Infrared Imaging of Fluorescent Nanosensors

Julia Ackermann, Jan Stegemann, Tim Smola, Eline Reger, Sebastian Jung, Anne Schmitz, Svenja Herbertz, Luise Erpenbeck, Karsten Seidl, and Sebastian Kruss*

Biochemical processes are fast and occur on small-length scales, which makes them difficult to measure. Optical nanosensors based on single-wall carbon nanotubes (SWCNTs) are able to capture such dynamics. They fluoresce in the near-infrared (NIR, 850–1700 nm) tissue transparency window and the emission wavelength depends on their chirality. However, NIR imaging requires specialized indium gallium arsenide (InGaAs) cameras with a typically low resolution because the quantum yield of normal Si-based cameras rapidly decreases in the NIR. Here, an efficient one-step phase separation approach to isolate monochiral (6,4)-SWCNTs (880 nm emission) from mixed SWCNT samples is developed. It enables imaging them in the NIR with high-resolution standard Si-based cameras (>50× more pixels). (6,4)-SWCNTs modified with (GT)$_{10}$-ssDNA become highly sensitive to the important neurotransmitter dopamine. These sensors are 1.7× brighter and 7.5× more sensitive and allow fast imaging (<50 ms). They enable high-resolution imaging of dopamine release from cells. Thus, the assembly of biosensors from (6,4)-SWCNTs combines the advantages of nanosensors working in the NIR with the sensitivity of (Si-based) cameras and enables broad usage of these nanomaterials.

1. Introduction

Cells use biomolecules to transmit information. This communication occurs in waves of biomolecules from a transmitter cell through the extracellular space to other (receiver) cells. This type of signal transmission takes place in many biological situations, such as the communication of neurons[1] via the release of neurotransmitters or in cells of the immune system,[2] which form reactive oxygen and nitrogen species in inflammatory processes to destroy microorganisms. The concentration of the released substances changes spatially and temporally and is a biochemical fingerprint of the biological state. However, such biologically relevant processes occur on temporal (ms) and spatial (nm) scales that are difficult to access using established methods.[3] For example, electrochemical methods, such as amperometry or voltammetry, lack the required spatial resolution determined by the number of electrodes and are invasive as the microelectrodes penetrate the tissue.[4] On the other hand, optical methods provide often only indirect information, for example, by labeling cellular components[5,6] or suffering from photobleaching.[7]

In this context, nanomaterials, such as single-wall carbon nanotubes (SWCNTs), have emerged as promising building blocks to capture these dynamics.[3,8] In addition to a high surface-to-volume ratio that makes them sensitive to single-molecule detection,[9–12] their surface can be chemically tailored.[13–17] Thus, SWCNTs have already been used for several bioimaging studies[18,19] and the detection of numerous analytes such as reactive oxygen species,[20–23] small molecules like nitroaromatics[24,25] or neurotransmitters,[26,27] proteins,[28–30] sugars,[31] enzymes,[32] or bacteria.[33] Due to their fluorescence in the near-infrared (NIR, 850–1700 nm), which shows no bleaching or blinking, they represent stable fluorophores, whose emission falls within the biological transparency window.[34] Here,

J. Ackermann, J. Stegemann, T. Smola, E. Reger, S. Herbertz, K. Seidl, S. Kruss
Fraunhofer Institute for Microelectronic Circuits and Systems
Finkenstrasse 61, 47057 Duisburg, Germany
E-mail: sebastian.kruss@rub.de

J. Ackermann, T. Smola, E. Reger, K. Seidl
Department EBS
University Duisburg-Essen
Bismarckstrasse 81, 47057 Duisburg, Germany

The ORCID identification number(s) for the author(s) of this article can be found under https://doi.org/10.1002/smll.202206856.

J. Stegemann, S. Kruss
Department of Chemistry
Ruhr-University Bochum
Universitätsstrasse 150, 44801 Bochum, Germany

S. Jung
ZEMOS Center for Solvation Science
Ruhr-University Bochum
Universitätsstrasse 150, 44801 Bochum, Germany

A. Schmitz, L. Erpenbeck
Department of Dermatology
University Hospital Münster
Von-Esmarch-Strasse 58, 48149 Münster, Germany

K. Seidl, S. Kruss
Center for Nanointegration Duisburg-Essen (CENIDE)
Carl-Benz-Strasse 199, 47057 Duisburg, Germany

reduced scattering and autofluorescence of biological samples allow for increased signal-to-noise ratios (SNR) during detection as well as deeper tissue penetration compared to UV or visible wavelength fluorophores.[35] Recently, their outstanding potential in detecting the cellular release of the neurotransmitters dopamine[36–38] and serotonin[39] was demonstrated with an unprecedentedly high spatiotemporal resolution, which also allowed observation of dopamine release from over 100 dopaminergic varicosities simultaneously.

However, one major drawback for scientists wishing to use such fluorophores is that a specialized NIR detector is required. NIR emission is usually collected with indium gallium arsenide (InGaAs) detectors. Their fabrication process is complex, the resolution in terms of absolute pixel numbers is low, and the sensor must be cooled, for example, with liquid nitrogen to reduce the high dark current.[35,40] This makes these cameras impractical and expensive (>40 000 €) compared to the widely used silicon (Si) cameras, which have a rapidly decreasing sensitivity in the NIR and therefore have problems detecting signals >950 nm.[41,42]

The exact fluorescence wavelength of SWCNTs depends on their chirality (n,m).[43] (6,4)-SWCNTs, which are the species emitting closest to visible light with emission around 880 nm, would be well-suited for detection with commercial Si cameras while still taking advantage of the NIR. However, (6,4)-SWCNTs are not yet available in their pure form.

In general, the fabrication of sensors based on SWCNTs has so far been mainly based on mixtures of different chiralities, as the synthesis of pure species has not yet been performed on larger scales.[44] Advances in synthesis have led to the preparation of chirality-enriched SWCNT samples,[45–47] as a result of which (6,5)-enriched CoMoCAT-SWCNTs with the main emission around 985 nm are already commercially available. Recently, they have been used for detection with Si cameras.[48,49] Although CoMoCAT-SWCNTs also contain some amount of (6,4)-SWCNTs, the sensitivity in combination with Si detectors is not as good because high concentrations have to be used that lead to a nonlinear signal increase due to reabsorption.[50] Xu et al. succeeded for the first time in preparing preferably (6,4)-SWCNTs with a purity of ≈57% by adjusting the oxidation state of the cobalt catalyst.[51] However, as long as high-purity SWCNTs are not yet commercially available, post-growth separation based on solution sorting techniques will remain a focus.[52] Here, various methods, such as density gradient ultracentrifugation,[53,54] ion-exchange[55] or gel column chromatography,[56,57] enrichment over polymers,[58–60] and aqueous two-phase extraction (ATPE),[61,62] have become established in recent years. ATPE, in particular, has proven to be fast, selective, cost-effective, and easily scalable. This method is usually based on two polymers, dextran and polyethylene glycol (PEG), added in a ratio where they are immiscible and thus form two phases.[63] SWCNTs are then dispersed using surfactants such as sodium deoxycholate (DOC), sodium cholate (SC), or sodium dodecyl sulfate (SDS), whereby separation is driven between the two phases by the properties of the resulting surfactant phase at the SWCNT surface, and then based on the exchange of phases of unwanted SWCNT chiralities for empty phases.[64] Li et al. recently published a simple pH-controlled method that separated (6,4)-SWCNTs and ten other species.[65] Subsequently,

Nißler et al. used this method for chirality-pure sensors for the detection of various small molecules and also ratiometric sensing with different wavelengths.[66] Furthermore, Antaris et al. used (6,4)-SWCNTs obtained from density gradient ultracentrifugation in combination with Si-detectors for immunohistochemical staining of cells and cancer tissue sections.[67]

Surprisingly, sensing with (6,4)-SWCNTs using low-cost Si cameras has not yet been demonstrated. This is likely because a fast method for large-scale extraction of (6,4)-SWCNTs has been missing so far, as well as a simple process for subsequent SWCNT functionalization to tailor their surface chemistry.[52,66] Routes for easy exchange have now been developed, such as methanol-assisted surfactant exchange[68] or dialysis,[52] leaving the obstacle of a rapid process for (6,4)-SWCNT extraction to make this material accessible to the broader community.

Here, we address this challenge and separate (6,4)-SWCNTs (emission at 880 nm) from commercial SWCNT mixtures ((6,5)-enriched CoMoCAT-SWCNTs) by tailoring an ATPE protocol[65] to obtain (6,4)-SWCNTs for the first time quickly and easily scalable in only one single step. By replacing the surfactant shell around the SWCNTs with $(GT)_{10}$-single-stranded(ss)DNA sequences, we tailor these SWCNTs exemplarily as dopamine sensors. Hereby, the optimum between detection with standard Si cameras and the use of NIR fluorescence imaging is achieved. We investigate the detection efficiency of these (6,4)-SWCNTs compared to the parental SWCNT mixture with both Si and InGaAs detectors. Finally, we demonstrate sensing of cellular dopamine release with high spatiotemporal resolution using standard microscope equipment (**Figure 1**). This method thus makes SWCNT-based nanosensors or labels accessible to a much larger community.

2. Results and Discussion

2.1. (6,4)-SWCNT Separation and Optical Characterization

To shift the overall SWCNT emission closer to the visible wavelength region, (6,4)-SWCNTs as the shortest SWCNT NIR emitter need to be separated from commercially available mixtures containing multiple chiralities. We decided to use ATPE as a scalable separation approach and used a pH-driven protocol.[65] The original protocol used a two-step separation with a mixture of 0.025% DOC, 0.05% SDS, and 0.5% SC but we did not get reproducible results. All of our experiments were carried out at room temperature (20 °C). In the first step, pH-driven separation of (6,4)-SWCNTs from the remaining semiconducting SWCNTs should be performed, in which the (6,4)-SWCNTs accumulated together with metallic SWCNTs in the dextran-rich bottom phase. However, we were unable to separate (6,4)-SWCNTs from semiconducting (7,3)-SWCNTs with this mixture, despite testing different additions of hydrochloric acid (HCl, Figure S1a, Supporting Information). This is mainly because these two SWCNT chiralities are difficult to separate due to their extremely similar diameters.[65] In addition, even slight variations in surfactant conditions can lead to altered experimental results.

Therefore, we modified it accordingly and finally developed a protocol achieving single-chirality (6,4)-SWCNTs in only
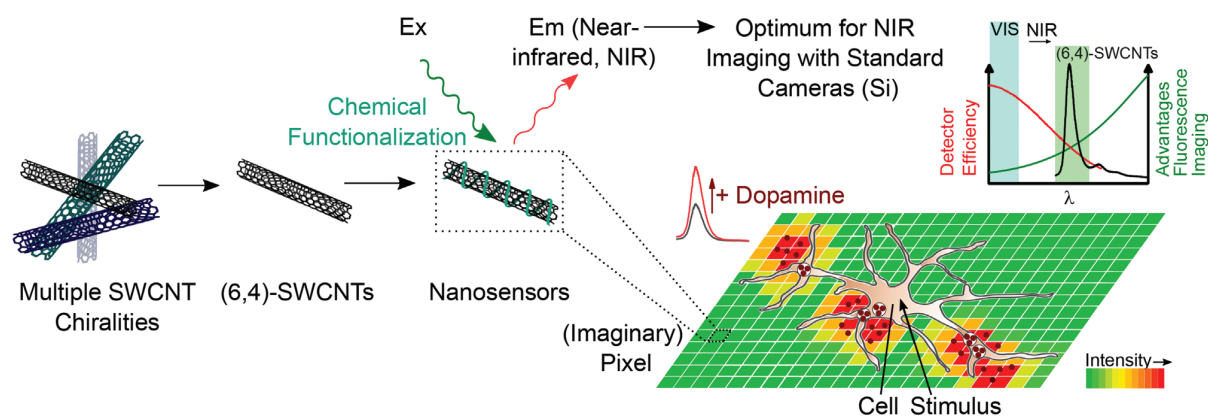
Figure 1. High sensitivity NIR imaging of molecular sensors. NIR fluorescent monochiral (6,4)-SWCNTs separated via ATPE from standard SWCNT samples with multiple chiralities are used to visualize biomolecules such as the neurotransmitter dopamine. Their emission is in the sweet spot between high camera quantum yields of high-resolution and cost-effective (Si-based) cameras and the increasing advantages of the NIR (reduced scattering and autofluorescence). These sensors are rendered sensitive to dopamine by specific surface functionalization with ssDNA. The nanosensors are immobilized on a glass surface and dopamine-releasing cells are cultured on top. Upon stimulation, the sensors acting as imaginary pixels report the release of dopamine by a fluorescence increase.

one step, which makes it simple to reproduce and scale up (**Figure 2**a). Since SC is known to have a chirality-dependent affinity,[65] we systematically increased the SC content within this mixture and found that an increase in SC content (0.6–0.9% SC tested) lead to an optimized separation of (6,4)- and (7,3)-SWCNTs at 0.7% SC and higher (Figure S1b–e, Supporting Information). It appeared that with increasing SC concentration, higher amounts of HCl addition were required to separate the (6,4)- from the (7,3)-SWCNTs (Figure S1f, Supporting Information). However, this trend is not entirely clear, since at 0.8% SC, the peak ratio hardly changed with varying HCl content. For subsequent experiments, the SC content of 0.7% with lower HCl addition was chosen because, on the one hand, the risk of surfactant flocculation and thus SWCNT precipitation rises with an increasingly acidic environment, and, on the other hand, the peak ratio of (6,4)-/(7,3)-SWCNTs was highest.

After finding the optimal surfactant conditions, the second separation step of the published protocol was followed, which consisted of the addition of sodium hypochlorite (NaClO), which is known to separate metallic from semiconducting SWCNTs.[65] Here, we found that after increasing the SC content to 0.7%, the addition of NaClO caused the separation of (6,4)-SWCNTs into the dextran-rich bottom phase (instead of the PEG-rich top phase at 0.5% SC content), whereas metallic SWCNTs migrated mostly into the interfacial layer and the PEG-rich top phase (Figure S2a–e, Supporting Information). Furthermore, the addition of NaClO further improved the peak ratio of (6,4)-/(7,3)-SWCNTs, and based on the absorbance spectrum of the final bottom phase (Figure S2d, Supporting Information), nearly all peaks could be assigned to (6,4)-SWCNTs. The two large peaks at 586 and 885 nm correspond to the E_{22} and E_{11} excitonic transitions of (6,4)-SWCNTs, while the peak at 414 nm could result from incomplete separation of metallic SWCNTs as the E_{33} transition is located at wavelengths <400 nm and the peak intensity further decreased after metallic separation. The small peaks at 534 and 773 nm are known to be phonon sidebands of (6,4)-SWCNTs.[43,69,70] Based on fitting all semiconducting chiralities present in the starting material compared to the final bottom phase and comparing the resulting area of each peak assuming simplified the same absorption cross section for all SWCNTs, the purity of the material thus improved from 9.4% containing (6,4)-SWCNTs to >95% (Figure S2a,d, Supporting Information).
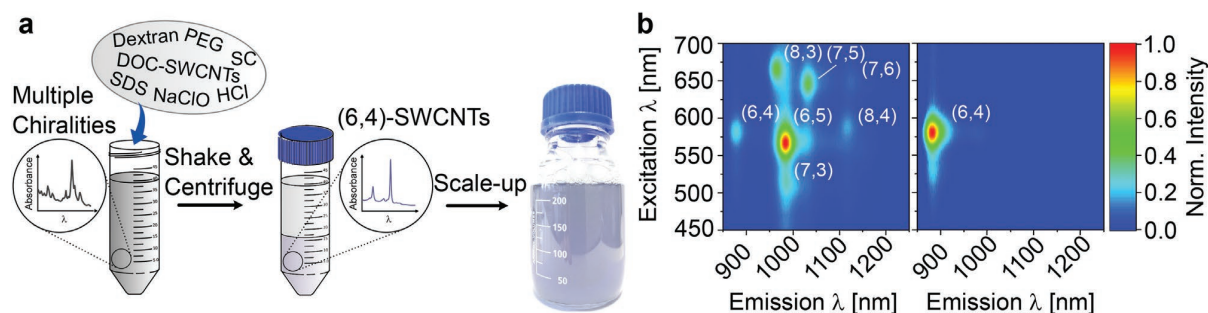
Figure 2. One-step large-scale isolation of (6,4)-SWCNTs. a) One-step ATPE is used to isolate (6,4)-SWCNTs from other chiralities, providing a highly scalable approach. b) 2D excitation–emission plot before (CoMoCAT-SWCNTs) and after phase separation ((6,4)-SWCNTs).

Since in the optimized surfactant mixture, (6,4)-SWCNTs remained in the bottom phase after metallic separation and did not migrate into the top phase, the next step was to test whether the two-step separation procedure could be reduced to a one-step separation by the simultaneous addition of HCl and NaClO at the beginning. Interestingly, based on characterization via absorption spectra, this led to the same but a faster result, and pure (6,4)-SWCNTs remained in the bottom phase (Figures S2f and S3, Supporting Information). As a result, this process also did not require a mimic phase and we were able to extract large amounts of (6,4)-SWCNTs (Figure 2a). To further confirm the purity of the (6,4)-SWCNTs, 2D excitation–emission plots were acquired before (CoMoCAT-SWCNTs) and after phase separation, in which the individual chiralities can be uniquely assigned based on their associated transitions (Figure 2b). It is evident that the main emission at 980 nm, originating from the (6,5)-enriched CoMoCAT-SWCNTs, shifted after phase separation to the (6,4)-SWCNT emission around 880 nm. In addition, there is a very weak emission at 985 nm, which is identical in emission to that of (6,5)-SWCNTs. However, the excitation wavelength shifted from 567 to 580 nm, and therefore, it is more likely that this feature corresponds to the phonon sideband of (6,4)-SWCNTs.[69]

Moreover, Raman spectra were acquired before and after (6,4)-SWCNT separation (Figure S4, Supporting Information), and the intensity ratios of Raman G/D bands were calculated, which are generally used to monitor covalent sidewall reactions in SWCNTs and are thus a measure of the defect number on the SWCNT surface.[71] The results indicate a lower defect ratio after SWCNT purification (increase from 15.1 to 18.3) due to the sorting out of impurities.

Since it is known that additional separation steps lead to stronger interfacial trapping of SWCNTs between the dextran and PEG phase,[64,65] the extraction yield between the two- and one-step separation was calculated and compared. For this purpose, the absorption spectra are additionally shown rescaled in Figure S2a–f, Supporting Information, (right axis), so that the different volumes of the two separation phases and dilutions during absorption measurements were quantitatively considered. While in the two-step separation, about 10.8% of all (6,4)-SWCNTs remained in the bottom phase without metallic separation and thus were accessible for (6,4)-SWCNT separation, 70.9% migrated to the top phase, and 18.3% of the non-extractable (6,4)-SWCNT were lost in the interfacial layer. After the second separation step, approximately half of the 10.8% (6,4)-SWCNTs got lost in the bottom phase, so the extraction yield was calculated as 5.1%. Reduction to a one-step separation approach resulted in a direct effect on the yield of extractable (6,4)-SWCNTs with an increase from 5.1 ± 0.3% to 7.4 ± 1.0% (Figure S2g, Supporting Information). The higher standard derivative in the one-step approach can probably be attributed to the inclusion of two different batches of DOC-SWCNTs for the calculation, which may have slightly different DOC concentrations and thus direct effects on the yield. A precise understanding of the interfacial losses would be necessary for further improvement of the extraction yield. For example, it has been shown that the molecular weight of the commonly used 6 kDa PEG/70 kDa dextran ATPE system can be changed, which also affects interfacial trapping.[72,73] However, this one-step ATPE can be scaled up to extract (6,4)-SWCNTs easily, quickly, and inexpensively on a large scale (Figure 2a). Furthermore, the remaining SWCNTs in the top phase could be recycled. This was demonstrated by precipitation, washing, and filtering of the SWCNTs in the ATPE top phase to remove the surfactant shell surrounding the SWCNTs and then drying them, which provided the SWCNT material for other sensing or ATPE experiments (Figure S5, Supporting Information). Here, we showed the redispersion of these SWCNTs in 1% DOC, using a superacid-surfactant exchange based on previous literature,[74] avoiding further SWCNT shortening by tip-sonication.

2.2. Comparison of Detection Efficiency

The use of NIR fluorophores for biomedical imaging is a steadily growing trend due to advantages such as lower scattering and autofluorescence of biological samples leading to higher signal-to-background ratios (SBR). While NIR imaging has long been limited to the so-called NIR-I window (700–900 nm), the discovery of new NIR-II (1000–1700 nm) fluorophores and improvements on the detector side are now extending imaging to the NIR-II window, which is expected to further improve the SBR due to further reduced scattering and autofluorescence in this wavelength range enabling deeper tissue imaging.[35] However, the detector side must also be considered, and for NIR-II imaging, InGaAs cameras must inevitably be used. Even though their performance has improved in recent years, Si cameras are still the best developed and are superior in all aspects such as quantum efficiency, resolution, and noise (dark current).

The main advantage of using (6,4)-SWCNTs compared to conventional NIR-I fluorophores, such as indocyanine green (ICG) or methylene blue (MB), is their very modular surface chemistry and that they can be used not only as labels but also as sensors.[75] Non-specific passive labels suffer from high background fluorescence signals, especially in vivo due to non-specific protein binding.[35] In addition, many NIR-I fluorophores like IRDye 800CW or Alexa 790 are often not very stable and bleach.[76] SWCNTs are excellent long-term fluorophores, which is especially advantageous for in vivo imaging. However, the quantum efficiency of (6,4)-SWCNTs with 2.3% is lower compared to many other NIR-I fluorophores (for ICG or MB around 9.5%).[35,67] On the other side, they can be excited with a very large Stokes shift between excitation and emission (≈300 nm), largely preventing the excitation light from passing through the filters to the detector. In addition, their fluorescence emission is further in the NIR compared to other NIR-I fluorophores like ICG (822 nm) or IRDye800CW (789 nm), which results in further reduced autofluorescence of biomolecules and tissue.[35] Although SWCNT-based labels/sensors are not clinically approved yet, which is also the case for many other NIR-I fluorophores, initial studies show promising results.[77,78]

To find the optimal fluorophore for the desired application, we developed a simulation, considering the parameters of fluorophores and biological samples based on a specific biological scenario and typical parameters on the detector side (InGaAs vs Si camera). In our scenario, SWCNTs are present in solution and it is assumed that their fluorescence can be selected
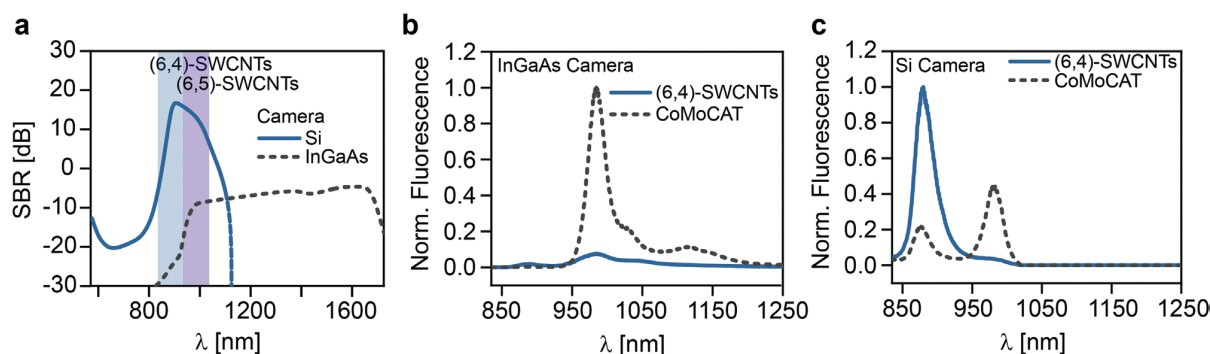
Figure 3. Increased signals by using (6,4)-SWCNTs. a) Simulation of the wavelength-dependent SBR when imaging fluorophores in biological tissue in PBS using a Si or InGaAs camera. Autofluorescence of soft tissue (100 μm thickness) and typical autofluorescence from biological samples as well as absorption of water are included. The wavelength refers to the peak wavelength of SWCNTs. Highlighted areas show the main emission of (6,4)- and (6,5)-SWCNTs. b) Normalized fluorescence spectra of (6,4)-, and CoMoCAT-SWCNTs collected with an InGaAs detector weighted with the quantum efficiency of a typical InGaAs camera. Concentration was adjusted based on the area under the curve of the E_{11} transitions in a range of 810–1350 nm. c) Normalized fluorescence spectra of the same data weighted with the quantum efficiency of a Si camera.

arbitrarily in wavelength while retaining their advantage of a large Stokes shift between excitation and emission. Furthermore, components of a standard microscope, such as the typical wavelength-dependent power density of an LED for excitation, wavelength-dependent transmission curves of necessary optics, optical interference factors such as the dark current of the detectors, as well as autofluorescence and absorption of biological samples, were considered (Figure S6, Supporting Information). Here, the scenario is focused on imaging cells in phosphate-buffered saline (PBS) buffer as we will show experimentally in the further course. Detailed assumptions and calculations can be found in the Supporting Information (Table S1, Supporting Information).

For comparison, the respective SBR of the two camera types when imaging cells in PBS with SWCNTs is shown (**Figure 3**a). Here, the wavelength refers to the peak wavelength of SWCNTs. For Si cameras, a sweet spot is obtained at about 906 nm, thus SWCNTs with (6,4)-chirality are an excellent fit. For InGaAs cameras, there is no real sweet spot since no autofluorescence was included/exists for the NIR region. In addition, the quantum efficiency increases steadily over a wide wavelength range (slightly increasing from 985 to 1575 nm) while the scattering from soft tissue and of other typical fluorophores present in cell cultures decreases. The drop in SBR around 1435 nm results from the absorption of water at this position. The highest SBR occurs at about 1629 nm before the quantum efficiency of the camera drops sharply. Overall, the SBR is lower for InGaAs cameras due to the higher impact of black body radiation and dark current (Figure S6, Supporting Information), which is mainly determined by the band gap of the material system used.

However, every simulation is a specific scenario and here imaging of cells in a thin tissue-like environment is mimicked. Since the background signal of Si cameras is reduced compared to InGaAs cameras, Si cameras are more sensitive to weak signals, while InGaAs cameras approach the same SBR with increasing signal strength.

To evaluate the detection efficiency of the obtained (6,4)-SWCNTs independently of the dark current of both camera systems and only based on the differences in quantum efficiency, they are compared with the parental (6,5)-enriched CoMoCAT-SWCNTs. For this purpose, their surface functionalization after ATPE was exchanged for 1% DOC, and the concentration of each SWCNT material was adjusted by matching the area under the absorbance curve of the E_{11} transitions in a range of 810–1350 nm (Figure S7a,b, Supporting Information). The wavelength-dependent fluorescence of these SWCNTs excited with a 561 nm laser and recorded with an InGaAs detector is shown after conversion based on the typical quantum efficiency of an InGaAs camera and a standard Si camera, normalized to the respective maximum (Figure 3b,c).

For CoMoCAT-SWCNTs, which are best detected with an InGaAs camera, the (6,5)-SWCNTs emitting around 980 nm contribute to around 2/3 of the fluorescence signal with the Si camera, despite the higher sensitivity of the camera to lower wavelengths. This is based on the simplified assumption that the area under the curve can be considered a measure of signal strength. While the (6,4)-SWCNTs are barely detected by the InGaAs camera, the comparison using a Si camera shows that they appear 1.7× brighter than CoMoCAT-SWCNTs. Although CoMoCAT-SWCNTs detected with an InGaAs detector show higher absolute intensity values (Figure S7c–e, Supporting Information), it makes detection with Si cameras using (6,4)-SWCNTs promising.

Another advantage in terms of imaging and sensing applications is the significantly higher resolution of Si cameras in relation to the absolute number of pixels (here 2048 × 2048 vs 320 × 256 pixels). Even though higher resolution InGaAs cameras (640 × 512 pixels) are now available, this means that Si cameras have about 13–51× higher resolution. In general, SWCNTs as nanoscale devices (dimensions 0.78 nm × 600–1000 nm) are limited by the resolution limit of optical microscopy. According to the Abbe/Rayleigh criterion, the smaller the wavelength is, the smaller the resolution limit becomes. For example, the maximum resolution for fluorescence microscopy with (6,4)-SWCNTs using a good 100× oil immersion objective (here λ = 885 nm, NA = 1.45) is about 372 nm, which decreases with increasing wavelength (412 nm for (6,5)-SWCNTs with λ = 980 nm).

Especially for imaging applications, resolution thus plays an important role, and it is not surprising that super-resolution microscopy, also with SWCNTs,[79–81] is increasingly used. According to the Nyquist criterion, SWCNTs must therefore be at least 2.3 pixels apart to still be perceived as separate structures.[82] In the case of InGaAs cameras, the optical resolution limit is thus further limited due to the low pixel number. While two parallel, single (6,4)-SWCNTs at a distance of 372 nm can still be separately resolved with a typical Si camera (here 1 px ≈ 65 nm at 100× magnification), this is not the case with typical InGaAs cameras (here 1 px ≈ 444 nm, **Figure 4**a). The required pixel size would have to be at least 162 nm or smaller. Further details of the simulation can be found in the Supporting Information.

Since we wanted to use SWCNTs to capture the dynamics of biological processes in time and space, the next step was to evaluate the imaging quality of individual SWCNTs and how sensitive they act as dopamine sensors on the single sensor level with the two camera systems. For this purpose, SWCNTs were rendered sensitive to dopamine by exchanging the surface functionalization from surfactant to $(GT)_{10}$-ssDNA, which is known from other studies[37,58,83] to respond to dopamine with an increase in intensity (Figure 4b).

Subsequently, both dopamine-responsive $(GT)_{10}$-(6,4)-SWCNTs and $(GT)_{10}$-CoMoCAT-SWCNTs were immobilized on

glass and the same image section was imaged at 100× magnification in a standard microscope using both an InGaAs and Si camera. Compared to the wavelength-dependent images in Figures 3 and 4b, a conventional white-light LED was used for excitation instead of a specific laser, and images were acquired before and after the addition of 10 μm dopamine with an exposure time of 1 s (Figure 4c,d).

The images show that SWCNTs are randomly arranged on the surface, but when looking at individual SWCNTs, the higher resolution of the Si camera compared to the InGaAs camera becomes directly apparent. Comparison of absolute fluorescence brightnesses between the two camera systems must be considered cautiously because it depends on the choice of pixels to be analyzed. However, the comparison of the absolute intensities of SWCNTs before dopamine addition again shows that, based on the InGaAs camera, CoMoCAT-SWCNTs appear significantly brighter compared to (6,4)-SWCNTs, and in terms of sensitivity, show a larger intensity change after dopamine addition (6.7% increase compared to 2.1%, Figure 4e). In contrast to the previous findings (Figure 3) $(GT)_{10}$-(6,4)-SWCNTs appear only slightly brighter than the CoMoCAT-SWCNTs imaged with the Si camera, but show a significantly higher sensitivity for dopamine (51.3% increase instead of 13.2%). The differences in intensity comparison between the two SWCNT materials could be due to
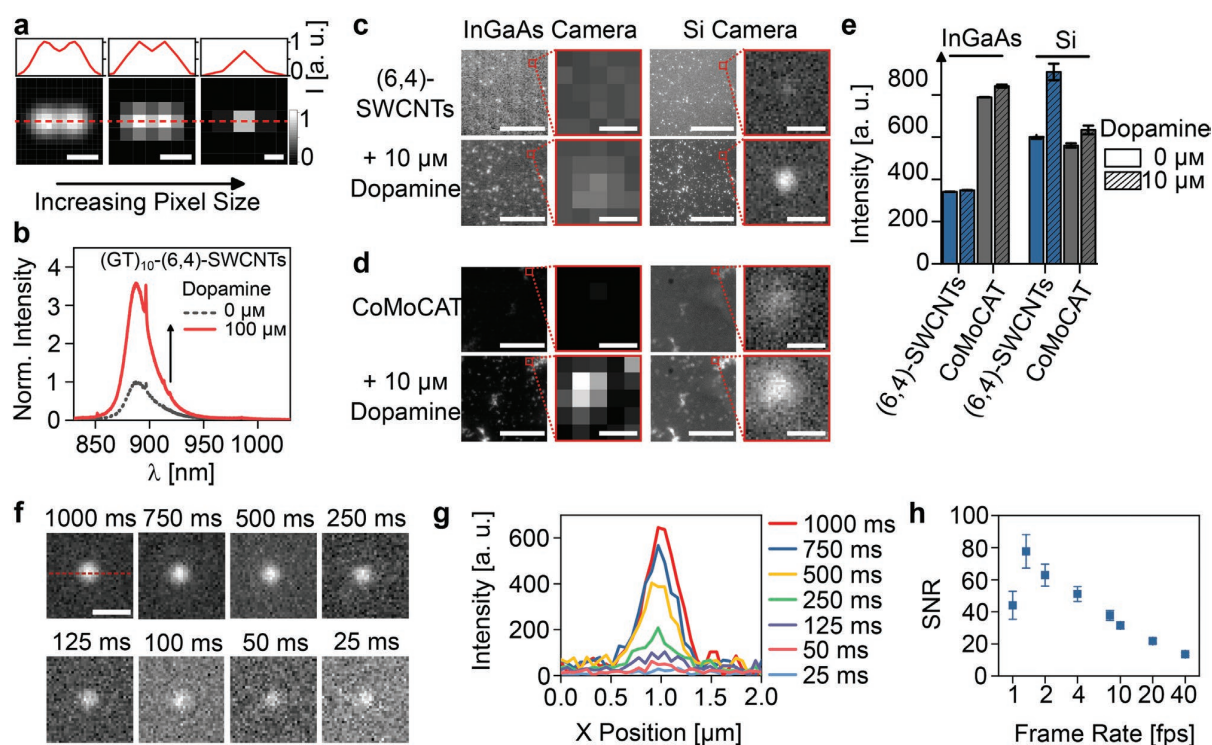
Figure 4. Increase of sensitivity and resolution. a) Simulation of the camera signal of two fluorescent point sources (880 nm) whose structure sizes (diameter 100 nm) are below the resolution limit of optical microscopy. With increasing pixel size/decreasing resolution (left to right), the structures can no longer be imaged separately. From left to right with 100× objective (NA = 1.45): 65 nm (pixel size Si camera), 162 nm (theoretical Nyquist pixel size), 444 nm (pixel size InGaAs camera). Scale bars represent 400 nm. b) $(GT)_{10}$-(6,4)-SWCNTs in solution show a fluorescence increase after the addition of 100 μm dopamine. c) Comparison of the sensitivity of single $(GT)_{10}$-(6,4)- and d) $(GT)_{10}$-CoMoCAT-SWCNTs (multiple SWCNTs and one inset of a single SWCNT) immobilized on a glass surface. Fluorescence images are recorded with an InGaAs and a Si camera before and after adding 10 μm dopamine at 1 s exposure time. e) Corresponding fluorescence intensities of single SWCNTs from (c) and (d), mean ± SE, *n* = 10. f) Fluorescence images of a single $(GT)_{10}$-(6,4)-SWCNT captured with a Si camera at different exposure times. g) Corresponding height traces and h) signal-to-noise ratio (SNR) of the images in (f) (mean ± SE, *n* = 6). Scale bars of multiple SWCNT images represent 20 μm, and of single SWCNT images represent 1 μm.

the exchanged functionalities, as Figure 3 compares surfactant-dispersed SWCNTs and here ssDNA-wrapped SWCNTs are compared. In general, surfactant-dispersed SWCNTs are brighter.[84] In addition, in a previous study, it was shown that the sensor response was in some cases enhanced for monochiral sensors.[66] This may be because the exact replacement process does not appear to be identical between the different fabrication routes (direct sonication for $(GT)_{10}$-CoMoCAT-SWCNTs and functionalization exchange for $(GT)_{10}$-(6,4)-SWCNTs).[85]

Lower exposure times for $(GT)_{10}$-(6,4)-SWCNTs were tested to see how fast SWCNTs could be imaged with the Si camera (Figure 4f). Down to 50 ms, single SWCNTs can be sufficiently distinguished from the background, which is also shown in the intensity traces (Figure 4g and Movie S1, Supporting Information). In addition, at these higher frame rates, dopamine could still be detected (Figure S8a, Supporting Information). This was also possible for a second standard microscope setup (see Experimental Section for details) equipped with a Si camera that had a higher quantum efficiency in the wavelength region of interest but only a 60× objective, which is common among scientists studying cell cultures (Figure S8b, Supporting Information). Here, dopamine detection at frame rates between 4 and 10 fps was easily possible with both setups, but at higher frame rates single SWCNT traces showed higher noise. For further quantification, we calculated the SNR based on previous literature[86,87] by taking images with and without illumination and dividing the averaged signal $Mean_{Signal}$ minus the mean noise $Mean_{Noise}$ without illumination by the standard derivation of the signal SD_{Signal} (Equation (1), Figure 4h).

$$SNR = \frac{Mean_{Signal} - Mean_{Noise}}{SD_{Signal}} \qquad (1)$$

As the frame rate increases, the SNR decreases, but still has high values of >30 at 10 fps. A similar procedure was followed with the $(GT)_{10}$-CoMoCAT-SWCNTs images with the InGaAs camera. Here, the single SWCNT contrast was less good because of the lower resolution (Figure S9a,b, Supporting Information). In addition, although the SNR showed higher values for lower frame rates compared to the imaged (6,4)-SWCNTs with the Si camera, both camera systems performed equivalently with the respective SWCNT material at high frame rates of 20 and 40 fps (Figure S9c, Supporting Information). This is probably due to the fact that the Si camera has a lower dark current, which was also evident when measuring the noise of the two camera systems, which increased for the InGaAs camera with increasing exposure time, while it remained constant for the Si camera (Figure S9d, Supporting Information).

Overall, the (6,4)-SWCNTs in combination with a Si camera and a standard LED for excitation are thus well-suited to keep up in performance with previous studies in which single SWCNTs were imaged with InGaAs cameras using high laser powers (≈ 500 mW) and frame rates of 10–15 fps.[36,37]

2.3. High-Sensitivity Imaging of Cellular Dopamine Release

Finally, to test the (6,4)-SWCNT sensors in a biological application, dopamine-releasing pheochromocytoma cells (PC12) were cultured on nanosensors immobilized on glass. To improve cell adhesion, the sensor layer was additionally coated with collagen, which did not alter the sensitivity for dopamine detection (Figure S10a, Supporting Information). **Figure 5**a shows the bright field image of such cells.
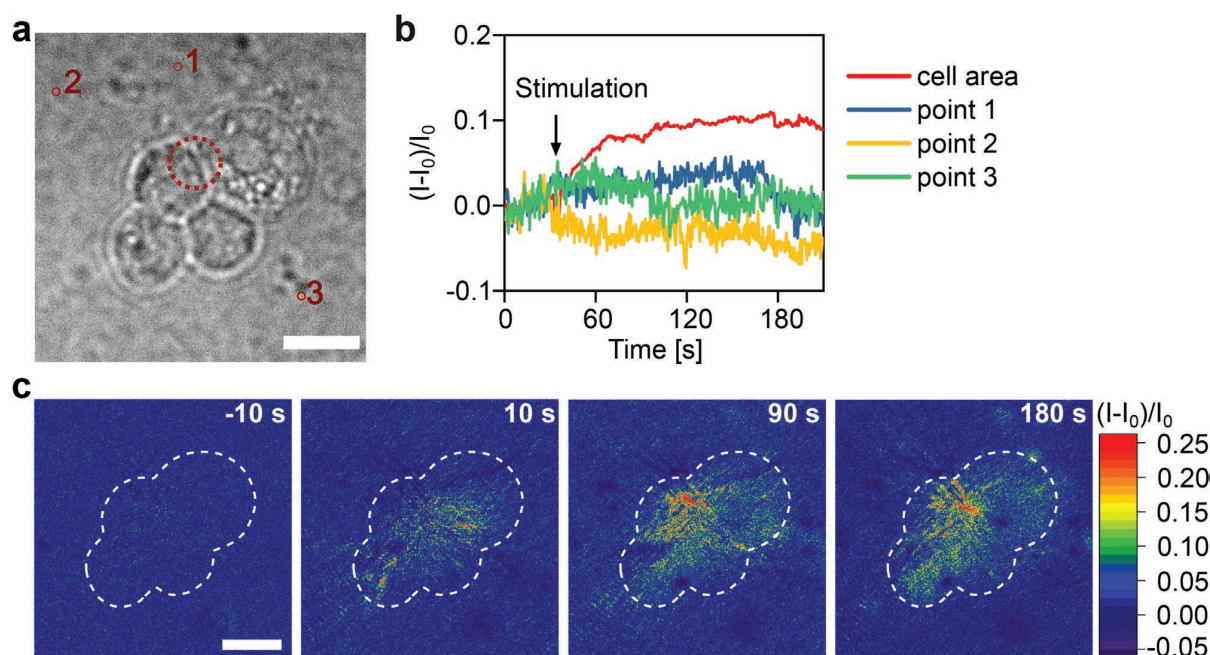
Figure 5. Spatiotemporal imaging of dopamine release from neural progenitor cells. a) Bright field image of PC12 cells cultured on glass coated with $(GT)_{10}$-SWCNTs and b) SWCNTs intensity change from ROIs (red circles in (a)) during cell stimulation imaged with a Si camera. c) Color-coded normalized intensity changes at different time points show a steady increase of SWCNT fluorescence at the cell area, which indicates continued dopamine release. All scale bars represent 10 µm.

After stimulation of cells with potassium buffer, there was an immediate increase in SWCNT fluorescence that occurred only locally at the cell surface, indicating dopamine release from cells (Figure 5b,c and Movie S2, Supporting Information). Here, each detector pixel was treated as a sensor to respond to the intensity changes over time. The increase in intensity occurred over several minutes, which can be attributed to continuous dopamine release. Such temporal dopamine release is also consistent with amperometric measurements, in which the release lasted for ≈ 3 min[88] or continued for several minutes with subsequent stimuli.[89,90] Moreover, a control experiment in which the same stimulus was added to the sensors without cell cultivation showed no signal change in the sensors (Figure S10b, Supporting Information), suggesting triggered dopamine release by dopaminergic PC12 cells.

In previous studies that used only InGaAs cameras + powerful laser excitation for cell experiments, high frame rates between 10 and 15 fps have been used, which is the same order of magnitude as (6,4)-SWCNTs + Si cameras.[36,37,39] Especially, the higher spatial resolution of Si cameras could have many benefits for example in localization of biological events or for super-resolution approaches. However, for in vivo experiments in deeper tissue layers, the NIR-II is still the better choice. This shows the need for further improvement and standardization of NIR cameras.

3. Conclusion

In summary, we tailored NIR fluorescent nanosensors for optimized imaging and sensing applications with Si cameras. The simple and fast protocol for separating large amounts of monochiral (6,4)-SWCNTs make these SWCNTs now accessible to the broader community because they can be detected and imaged in "normal" optical microscopes. In addition, the exemplary tailoring of SWCNTs for dopamine detection demonstrates the potential to resolve processes with a high spatial and temporal resolution with increased sensitivity. This method thus makes SWCNTs accessible as NIR building blocks for sensors and labels for the entire field of (bio)imaging.

4. Experimental Section

Materials: All materials were purchased from Sigma-Aldrich unless specified otherwise.

SWCNT Surface Modification: Surface modification of (6,5) chirality-enriched CoMoCAT-SWCNTs (Sigma-Aldrich, product no. 773 735) with 1% DOC was performed by mixing SWNCTs (1 mL, 4 mg mL^{-1} in DI water) with aqueous DOC (1 mL, 2% m/m). This mixture was tip sonicated in an ice bath (36 W output power – 25 min at 30% amplitude, Fisherbrand Model 120 Sonic Dismembrator) and centrifuged (2 × 30 min, 16 100 g, 4 °C) to remove aggregates. The supernatant yielded homogenously dispersed 1% DOC-SWCNTs for further experiments.

For surface modification of CoMoCAT-SWCNTs with (GT)$_{10}$-ssDNA, a recently published protocol was used.[91] SWCNTs (100 µL, 2 mg mL^{-1} in PBS) were mixed with ssDNA (100 µL, 2 mg mL^{-1} in PBS), followed by tip sonication (ice bath, 10 min at 30% amplitude) and centrifugation (2 × 30 min, 16 100 g, 4 °C).

For recycling of SWCNTs after ATPE, SWCNTs were precipitated with methanol, washed with isopropanol and water, and filtered. After drying

overnight (oven, 40 °C), SWCNTs were collected and represented the SWCNT material for further experiments. SWCNTs were resuspended in 1% DOC with superacid-surfactant exchange based on previous literature.[74] In short, SWCNTs were dissolved in chlorosulfonic acid (0.5 mg mL^{-1}). Droplets of 10 µL each were added to an aqueous solution of NaOH (0.5 м) and DOC (1 wt/v%) until the pH reached a value of 11.

SWCNT Separation: Separation of (6,4)-SWCNTs was based on a modified ATPE protocol by Li et al.[65] To find the optimal parameters, SWCNTs were separated in a two-phase aqueous system containing the polymers PEG (MW 6 kDa, 8% m/v) and dextran (Carl Roth, MW 70 kDa, 4% m/v) and the surfactants DOC (0.025% m/v), SDS (0.5% m/m), and SC (varying from 0.5% to 0.9% m/m in 0.1% steps), with DOC added via CoMoCAT-SWCNTs dispersed in 1% DOC. A certain volume of HCl (0.5 м) was added for pH-driven separation (here: 110–190 µL in 20 µL steps for an 8 mL batch). After the addition of all chemicals, the mixture was homogeneously mixed for 60 s and phase separation was accelerated by subsequent centrifugation at room temperature (30 min at 3046 g, 20 °C).

After finding the optimal SC concentration, (6,4)-SWCNTs were separated from all other semiconducting and metallic chiralities in a one-step approach by simultaneously adding a certain volume of HCl and NaClO (Honeywell) with 10–15% available chlorine for pH-driven and electronic separation (here: HCl (750 µL, 0.5 м) and NaClO (170 µL) for a 40 mL batch, resulting in a pH of 5.9 for the bottom phase). The final bottom phase yielded monochiral (6,4)-SWCNTs.

The bottom phase was dialyzed against 1% DOC for at least 3 days (300 kDa dialysis bag, Spectra/Por Spectrum Labs). The 1% DOC solution was renewed daily to replace the residual dextran with DOC and to obtain a stable 1% DOC-(6,4)-SWCNT solution.

Monochiral SWCNT Surface Exchange to ssDNA: Exchange of 1% DOC-(6,4)-SWCNT to ssDNA-(6,4)-SWCNTs was based on the kinetic exchange via dialysis. Purified (6,4)-SWCNTs were concentrated to an absorbance of 2.0 at the E$_{11}$ transition (880 nm) using molecular weight cut-off centrifugal filters (Amicon Ultra-15, 30 kDa). 1 mL of these SWCNTs was mixed with ssDNA (100 µL of (GT)$_{10}$, 2 mg mL^{-1} in PBS) and dialyzed against 1× PBS for 3 days (1 kDa dialysis bag, Spectra/Por Spectrum Labs). 1× PBS was renewed daily. After completion of dialysis, the solution within the dialysis bag was centrifuged (15 min at 16 100 g). The supernatant yielded the material for further experiments.

NIR Spectroscopy: Absorption spectra for the characterization of SWCNT samples were recorded using a JASCO V-780-ST spectrophotometer in the wavelength range of 400–1350 nm in 0.5 nm steps in quartz cuvettes (Hellma, 10 mm optical path).

1D NIR fluorescence spectra were recorded with 1 s integration time using a spectrometer (Shamrock 193i, Andor Technology Ltd.) connected to a microscope (IX53, Olympus) and a 561 nm laser at 100 mW (Gem 561, Laser Quantum) for excitation.

2D NIR fluorescence spectra were recorded with 10 s integration time using a spectrometer (Shamrock 193i, Andor Technology Ltd.) connected to a microscope (Olympus IX73). A lamp (LSE341, LOT-Quantum Design) was used in combination with a monochromator (MSH-150, LOT-Quantum Design) for excitation in the range of 400–700 nm in 5 nm steps.

Raman Spectroscopy: Raman and dopamine response fluorescence measurements were carried out using a confocal Raman microscope (inVia InSpect from Renishaw) at an excitation of 532 nm (10 mW laser power) with an integration time between 10 and 60 s. For dopamine response measurements in solution, a freshly prepared dopamine solution (2 µL of dopamine hydrochloride in 1× PBS) was added to (GT)$_{10}$-(6,4)-SWCNTs (200 µL) in a 96-well plate, resulting in a concentration of 100 µм dopamine.

SWCNT Immobilization for Single SWCNT Imaging: Glass bottom Petri dishes (ibidi) were treated with oxygen plasma (Atto B, Diener electronic, 0.6 mbar, 20 s). Directly after plasma cleaning, surfaces were coated with an APTES solution (300 µL of 1 wt% APTES/H$_2$O in ethanol) and incubated for 1 h at room temperature. Petri dishes were washed with ethanol and subsequently H$_2$O and dried with N$_2$. SWCNT solution

(150 µL, 0.1 nm) was added and incubated overnight at 4 °C. To remove non-immobilized SWCNTs, the surface was rinsed three times with 1× PBS.

Imaging of Single SWCNTs: SWCNTs were imaged in two different setups. The first setup consisted of an inverted microscope (Nikon Eclipse Ti2) equipped with a 100× objective (CFI Plan Apochromat Lambda D 100x Oil/1.45/0.13). A white LED (CoolLED pE300 Lite, 100% power) was used in combination with a 560 ± 40 nm bandpass filter for the excitation of SWCNTs via the E_{22} transitions. Excitation light was eliminated from emission via an 840 nm long-pass filter. The NIR fluorescence was imaged either with a Si camera (Hamamatsu Orca Flash 4.0) with 2048 × 2048 pixels or an InGaAs camera (Xeva 1.7 320 TE3 USB 100 Xenics) with 320 × 256 pixels, cooled down to 190 K.

The second setup consisted of an inverted microscope (Nikon Eclipse Ti2) equipped with a 60× objective (CFI P-Apo 60× Lambda Oil/1.40/0.13). A green LED emitting at 555 nm (Lumencor Spectrax Chroma, six independently controllable light sources, 100% power) was used in combination with a 550 ± 49 nm bandpass filter for SWCNT excitation. Excitation light was eliminated from emission via a bandpass filter in the range of 785–1000 nm. The NIR fluorescence was imaged with a Si camera (Hamamatsu Orca Fusion BT) with 2304 × 2304 pixels. For dopamine response measurements with immobilized SWCNTs, 20 µL of a freshly prepared dopamine solution (dopamine hydrochloride in 1× PBS) was added to 2 mL of PBS in the petri dish, resulting in a concentration of 10 µm dopamine.

The third setup used to perform the cell experiments consisted of an inverted microscope (Olympus IX73) equipped with a 100× objective (UPlanSApo/1.35/0.13-0.19). A 561 nm laser at 250 mW (Gem 561, Laser Quantum) was used for SWCNT excitation. Excitation light was eliminated from emission via a 780 nm long pass filter. The NIR fluorescence was imaged with a Si camera (PCO edge 4.2 bi) with 2048 × 2048 pixels at 500 ms exposure time.

Cell Experiments: PC12 cells were purchased from ATCC (CRL-1721) and cultivated according to the supplier's protocol. In short, cells were cultivated in a humidified 5% CO_2 atmosphere at 37 °C in T-75 flasks (Sarstedt) with a sub-cultivation ratio of 1:4 every 4 days. Cells were grown in 16 mL RPMI-1640 medium (Thermo Fisher Scientific) supplemented with heat-inactivated horse serum (10%, Thermo Fisher Scientific), fetal bovine serum (5%), penicillin (100 units mL^{-1}), and streptomycin (100 µg mL^{-1}, Thermo Fisher Scientific).

For cultivation and differentiation of PC12 cells on top of SWCNT-coated glass surfaces, surfaces were incubated overnight at 4 °C with a collagen solution (Bornstein and Traub Type I) for better cell adhesion.

200 000 cells were plated on SWCNT-coated glass surfaces and incubated for 4–7 days in RPMI-1640 medium supplemented with horse serum (1%), penicillin (100 units mL^{-1}), streptomycin (100 µg mL^{-1}), and nerve growth factor (100 ng mL^{-1}) in a humidified 5% CO_2 atmosphere at 37 °C. For dopamine release experiments, the cell medium was exchanged to 1× PBS (1 mL) supplemented with $MgCl_2$ and $CaCl_2$. To stimulate dopamine release, a potassium chloride (KCl) solution (18.68 µL of 3 м) was added, resulting in a final concentration of 55 mм KCl.

Purity and Yield Calculation of Separated SWCNTs: For characterization of the resulting bottom and top phases, absorption spectra were recorded with a corresponding mimic (without SWCNTs) for baseline subtraction. For better comparison, spectra were subsequently background corrected in the form of $Ae^{-b\lambda}$ based on previous literature.[92,93] The purity was calculated by fitting the respective SWCNT E_{11} chirality peaks under the absorbance curve from each ATPE phase and dividing the area of the (6,4)-SWCNT peak by the total area of all peaks. The extraction yield was calculated by determining the concentration of (6,4)-SWCNTs in the respective ATPE phase. This was calculated based on a previously published method.[91,94–96] Mean ± SD were then calculated based on $n = 4$ values for the 2-step separation and $n = 9$ values for the 1-step separation.

Intensity Change of Single SWCNTs: For characterization of the resulting intensity change after dopamine addition in the single SWCNT experiments, the initial (I_0) and final intensity after dopamine addition

(I) were calculated based on averaging $n = 60$ frames of recorded video. Mean ± SE of the absolute intensity change was calculated as $(I−I_0)/I_0$ for $n = 10$ individual SWCNTs.

SNR Calculation: To characterize the SNR at different frame rates, the noise and signal in each experiment were calculated based on averaging $n \geq 30$ frames at six equal positions in each video. The mean ± SE of the resulting SNR was calculated.

Fiji was used for image data processing and OriginPro for statistical analysis.

Supporting Information

Supporting Information is available from the Wiley Online Library or from the author.

Acknowledgements

Conflict of Interest

The authors declare no conflict of interest.

Data Availability Statement

The data that support the findings of this study are available from the corresponding author upon reasonable request.

Keywords

[1] T. B. Kornberg, S. Roy, *Trends Cell Biol.* **2014**, *24*, 583.
[2] J. C. Rieckmann, R. Geiger, D. Hornburg, T. Wolf, K. Kveler, D. Jarrossay, F. Sallusto, S. S. Shen-Orr, A. Lanzavecchia, M. Mann, F. Meissner, *Nat. Immunol.* **2017**, *18*, 583.
[3] M. Dinarvand, S. Elizarova, J. Daniel, S. Kruss, *ChemPlusChem* **2020**, *85*, 1465.
[4] A. Yakushenko, E. Kätelhön, B. Wolfrum, *Anal. Chem.* **2013**, *85*, 5483.
[5] M. R. Post, D. Sulzer, *Cell Chem. Biol.* **2021**, *28*, 748.
[6] N. G. Gubernator, H. Zhang, R. G. W. Staal, E. V. Mosharov, D. B. Pereira, M. Yue, V. Balsanek, P. A. Vadola, B. Mukherjee, R. H. Edwards, D. Sulzer, D. Sames, *Science* **2009**, *324*, 1441.
[7] K. S. Hettie, T. E. Glass, *ACS Chem. Neurosci.* **2016**, *7*, 21.

[8] J. Ackermann, J. T. Metternich, S. Herbertz, S. Kruss, *Angew. Chem., Int. Ed.* **2022**, *61*, e202112372.

[9] J. Zhang, A. A. Boghossian, P. W. Barone, A. Rwei, J.-H. Kim, D. Lin, D. A. Heller, A. J. Hilmer, N. Nair, N. F. Reuel, M. S. Strano, *J. Am. Chem. Soc.* **2011**, *133*, 567.

[10] H. Jin, D. A. Heller, M. Kalbacova, J.-H. Kim, J. Zhang, A. A. Boghossian, N. Maheshri, M. S. Strano, *Nat. Nanotechnol.* **2010**, *5*, 302.

[11] J.-H. Kim, C. R. Patra, J. R. Arkalgud, A. A. Boghossian, J. Zhang, J.-H. Han, N. F. Reuel, J.-H. Ahn, D. Mukhopadhyay, M. S. Strano, *ACS Nano* **2011**, *5*, 7848.

[12] M. Card, M. Gravely, S. Z. M. Madani, D. Roxbury, *ACS Appl. Mater. Interfaces* **2021**, *13*, 31986.

[13] F. A. Mann, N. Herrmann, F. Opazo, S. Kruss, *Angew. Chem., Int. Ed.* **2020**, *59*, 17732.

[14] A. J. Gillen, A. A. Boghossian, *Front. Chem.* **2019**, *7*, 612.

[15] A. Setaro, M. Adeli, M. Glaeske, D. Przyrembel, T. Bisswanger, G. Gordeev, F. Maschietto, A. Faghani, B. Paulus, M. Weinelt, R. Arenal, R. Haag, S. Reich, *Nat. Commun.* **2017**, *8*, 14281.

[16] A. Spreinat, M. M. Dohmen, J. Lüttgens, N. Herrmann, L. F. Klepzig, R. Nißler, S. Weber, F. A. Mann, J. Lauth, S. Kruss, *J. Phys. Chem. C* **2021**, *125*, 18341.

[17] P. Bilalis, D. Katsigiannopoulos, A. Avgeropoulos, G. Sakellariou, *RSC Adv.* **2014**, *4*, 2911.

[18] K. Huth, M. Glaeske, K. Achazi, G. Gordeev, S. Kumar, R. Arenal, S. K. Sharma, M. Adeli, A. Setaro, S. Reich, R. Haag, *Small* **2018**, *14*, 1800796.

[19] A. Antonucci, M. Reggente, C. Roullier, A. J. Gillen, N. Schuergers, V. Zubkovs, B. P. Lambert, M. Mouhib, E. Carata, L. Dini, A. A. Boghossian, *Nat. Nanotechnol.* **2022**, *17*, 1111.

[20] H. Wu, R. Nißler, V. Morris, N. Herrmann, P. Hu, S.-J. Jeon, S. Kruss, J. P. Giraldo, *Nano Lett.* **2020**, *20*, 2432.

[21] T. T. S. Lew, V. B. Koman, K. S. Silmore, J. S. Seo, P. Gordiichuk, S.-Y. Kwak, M. Park, M. C.-Y. Ang, D. T. Khong, M. A. Lee, M. B. Chan-Park, N.-H. Chua, M. S. Strano, *Nat. Plants* **2020**, *6*, 404.

[22] J. P. Giraldo, M. P. Landry, S.-Y. Kwak, R. M. Jain, M. H. Wong, N. M. Iverson, M. Ben-Naim, M. S. Strano, *Small* **2015**, *11*, 3973.

[23] J. Meier, J. Stapleton, E. Hofferber, A. Haworth, S. Kachman, N. M. Iverson, *Nanomaterials* **2021**, *11*, 243.

[24] D. A. Heller, G. W. Pratt, J. Zhang, N. Nair, A. J. Hansborough, A. A. Boghossian, N. F. Reuel, P. W. Barone, M. S. Strano, *Proc. Natl. Acad. Sci. U. S. A.* **2011**, *108*, 8544.

[25] M. H. Wong, J. P. Giraldo, S.-Y. Kwak, V. B. Koman, R. Sinclair, T. T. S. Lew, G. Bisker, P. Liu, M. S. Strano, *Nat. Mater.* **2017**, *16*, 264.

[26] S. Kruss, M. P. Landry, E. Vander Ende, B. M. A. Lima, N. F. Reuel, J. Zhang, J. Nelson, B. Mu, A. Hilmer, M. Strano, *J. Am. Chem. Soc.* **2014**, *136*, 713.

[27] S. Jeong, D. Yang, A. G. Beyene, J. T. Del Bonis-O'Donnell, A. M. M. Gest, N. Navarro, X. Sun, M. P. Landry, *Sci. Adv.* **2019**, *5*, eaay3771.

[28] G. Bisker, J. Dong, H. D. Park, N. M. Iverson, J. Ahn, J. T. Nelson, M. P. Landry, S. Kruss, M. S. Strano, *Nat. Commun.* **2016**, *7*, 10241.

[29] R. Ehrlich, A. Hendler-Neumark, V. Wulf, D. Amir, G. Bisker, *Small* **2021**, *17*, e2101660.

[30] R. M. Williams, C. Lee, D. A. Heller, *ACS Sens.* **2018**, *3*, 1838.

[31] V. Zubkovs, N. Schuergers, B. Lambert, E. Ahunbay, A. A. Boghossian, *Small* **2017**, *13*, 1701654.

[32] S. Agarwal, N. E. Kallmyer, D. X. Vang, A. V. Ramirez, M. M. Islam, A. C. Hillier, L. J. Halverson, N. F. Reuel, *Anal. Chem.* **2022**, *94*, 856.

[33] R. Nißler, O. Bader, M. Dohmen, S. G. Walter, C. Noll, G. Selvaggio, U. Groß, S. Kruss, *Nat. Commun.* **2020**, *11*, 5995.

[34] M. J. O'Connell, S. M. Bachilo, C. B. Huffman, V. C. Moore, M. S. Strano, E. H. Haroz, K. L. Rialon, P. J. Boul, W. H. Noon, C. Kittrell, J. Ma, R. H. Hauge, R. B. Weisman, R. E. Smalley, *Science* **2002**, *297*, 593.

[35] G. Hong, A. L. Antaris, H. Dai, *Nat. Biomed. Eng.* **2017**, *1*, 0010.

[36] S. Kruss, D. P. Salem, L. Vuković, B. Lima, E. Vander Ende, E. S. Boyden, M. S. Strano, *Proc. Natl. Acad. Sci. U. S. A.* **2017**, *114*, 1789.

[37] S. Elizarova, A. A. Chouaib, A. Shaib, B. Hill, F. Mann, N. Brose, S. Kruss, J. A. Daniel, *Proc. Natl. Acad. Sci. U. S. A.* **2022**, *119*, e2202842119.

[38] A. G. Beyene, K. Delevich, J. T. Del Bonis-O'Donnell, D. J. Piekarski, W. C. Lin, A. W. Thomas, S. J. Yang, P. Kosillo, D. Yang, G. S. Prounis, L. Wilbrecht, M. P. Landry, *Sci. Adv.* **2019**, *5*, eaaw3108.

[39] M. Dinarvand, E. Neubert, D. Meyer, G. Selvaggio, F. A. Mann, L. Erpenbeck, S. Kruss, *Nano Lett.* **2019**, *19*, 6604.

[40] R. Guntupalli, R. Allen, *Proc. SPIE* **2006**, *6294*, 1.

[41] A. M. Smith, M. C. Mancini, S. Nie, *Nat. Nanotechnol.* **2009**, *4*, 710.

[42] B. Song, B. Shi, S. T. Suran-Brunelli, S. Zhu, J. Klamkin, *IEEE J. Sel. Top. Quantum Electron.* **2022**, *28*, 1.

[43] S. M. Bachilo, M. S. Strano, C. Kittrell, R. H. Hauge, R. E. Smalley, R. B. Weisman, *Science* **2002**, *298*, 2361.

[44] F. Yang, M. Wang, D. Zhang, J. Yang, M. Zheng, Y. Li, *Chem. Rev.* **2020**, *120*, 2693.

[45] M. He, A. I. Chernov, P. V. Fedotov, E. D. Obraztsova, J. Sainio, E. Rikkinen, H. Jiang, Z. Zhu, Y. Tian, E. I. Kauppinen, M. Niemelä, A. O. I. Krause, *J. Am. Chem. Soc.* **2010**, *132*, 13994.

[46] H. An, A. Kumamoto, H. Takezaki, S. Ohyama, Y. Qian, T. Inoue, Y. Ikuhara, S. Chiashi, R. Xiang, S. Maruyama, *Nanoscale* **2016**, *8*, 14523.

[47] F. Yang, X. Wang, D. Zhang, J. Yang, D. Luo, Z. Xu, J. Wei, J.-Q. Wang, Z. Xu, F. Peng, X. Li, R. Li, Y. Li, M. Li, X. Bai, F. Ding, Y. Li, *Nature* **2014**, *510*, 522.

[48] V. Shumeiko, Y. Paltiel, G. Bisker, Z. Hayouka, O. Shoseyov, *Biosens. Bioelectron.* **2021**, *172*, 112763.

[49] V. Shumeiko, E. Malach, Y. Helman, Y. Paltiel, G. Bisker, Z. Hayouka, O. Shoseyov, *Sens. Actuators, B* **2021**, *327*, 128832.

[50] X. Wei, T. Tanaka, S. Li, M. Tsuzuki, G. Wang, Z. Yao, L. Li, Y. Yomogida, A. Hirano, H. Liu, H. Kataura, *Nano Lett.* **2020**, *20*, 410.

[51] B. Xu, T. Kaneko, Y. Shibuta, T. Kato, *Sci. Rep.* **2017**, *7*, 11149.

[52] R. Nißler, J. Ackermann, C. Ma, S. Kruss, *Anal. Chem.* **2022**, *94*, 9941.

[53] S. Ghosh, S. M. Bachilo, R. B. Weisman, *Nat. Nanotechnol.* **2010**, *5*, 443.

[54] M. S. Arnold, A. A. Green, J. F. Hulvat, S. I. Stupp, M. C. Hersam, *Nat. Nanotechnol.* **2006**, *1*, 60.

[55] M. Zheng, A. Jagota, E. D. Semke, B. A. Diner, R. S. McLean, S. R. Lustig, R. E. Richardson, N. G. Tassi, *Nat. Mater.* **2003**, *2*, 338.

[56] B. S. Flavel, M. M. Kappes, R. Krupke, F. Hennrich, *ACS Nano* **2013**, *7*, 3557.

[57] H. Liu, D. Nishide, T. Tanaka, H. Kataura, *Nat. Commun.* **2011**, *2*, 309.

[58] R. Nißler, F. A. Mann, H. Preiß, G. Selvaggio, N. Herrmann, S. Kruss, *Nanoscale* **2019**, *11*, 11159.

[59] H. Ozawa, N. Ide, T. Fujigaya, Y. Niidome, N. Nakashima, *Chem. Lett.* **2011**, *40*, 239.

[60] A. Nish, J.-Y. Hwang, J. Doig, R. J. Nicholas, *Nat. Nanotechnol.* **2007**, *2*, 640.

[61] C. Y. Khripin, J. A. Fagan, M. Zheng, *J. Am. Chem. Soc.* **2013**, *135*, 6822.

[62] J. A. Fagan, C. Y. Khripin, C. A. S. Batista, J. R. Simpson, E. H. Hároz, A. R. H. Walker, M. Zheng, *Adv. Mater.* **2014**, *26*, 2800.

[63] M. Iqbal, Y. Tao, S. Xie, Y. Zhu, D. Chen, X. Wang, L. Huang, D. Peng, A. Sattar, M. A. B. Shabbir, H. I. Hussain, S. Ahmed, Z. Yuan, *Biol. Proc. Online* **2016**, *18*, 18.

[64] N. K. Subbaiyan, S. Cambré, A. N. G. Parra-Vasquez, E. H. Hároz, S. K. Doorn, J. G. Duque, *ACS Nano* **2014**, *8*, 1619.

[65] H. Li, G. Gordeev, O. Garrity, S. Reich, B. S. Flavel, *ACS Nano* **2019**, *13*, 2567.

[66] R. Nißler, L. Kurth, H. Li, A. Spreinat, I. Kuhlemann, B. S. Flavel, S. Kruss, *Anal. Chem.* **2021**, *93*, 6446.

[67] A. L. Antaris, O. K. Yaghi, G. Hong, S. Diao, B. Zhang, J. Yang, L. Chew, H. Dai, *Small* **2015**, *11*, 6325.

[68] J. K. Streit, J. A. Fagan, M. Zheng, *Anal. Chem.* **2017**, *89*, 10496.

[69] J. L. Blackburn, J. M. Holt, V. M. Irurzun, D. E. Resasco, G. Rumbles, *Nano Lett.* **2012**, *12*, 1398.

[70] W. Zhou, D. Nakamura, H. Liu, H. Kataura, S. Takeyama, *Sci. Rep.* **2014**, *4*, 6999.

[71] M. S. Dresselhaus, G. Dresselhaus, R. Saito, A. Jorio, *Phys. Rep.* **2005**, *409*, 47.

[72] M. Lyu, B. Meany, J. Yang, Y. Li, M. Zheng, *J. Am. Chem. Soc.* **2019**, *141*, 20177.

[73] C. M. Sims, J. A. Fagan, *Carbon* **2022**, *191*, 215.

[74] P. Wang, M. Kim, Z. Peng, C.-F. Sun, J. Mok, A. Lieberman, Y. Wang, *ACS Nano* **2017**, *11*, 9231.

[75] J. Pan, F. Li, J. H. Choi, *J. Mater. Chem. B* **2017**, *5*, 6511.

[76] C. J. Tynan, D. T. Clarke, B. C. Coles, D. J. Rolfe, M. L. Martin-Fernandez, S. E. D. Webb, *PLoS One* **2012**, *7*, e36265.

[77] M. Gravely, M. M. Safaee, D. Roxbury, *Nano Lett.* **2019**, *19*, 6203.

[78] T. V. Galassi, M. Antman-Passig, Z. Yaari, J. Jessurun, R. E. Schwartz, D. A. Heller, *PLoS One* **2020**, *15*, e0226791.

[79] S. Nandi, K. Caicedo, L. Cognet, *Nanomaterials* **2022**, *12*, 1433.

[80] B. Kagan, A. Hendler-Neumark, V. Wulf, D. Kamber, R. Ehrlich, G. Bisker, *Adv. Photonics Res.* **2022**, *3*, 2200244.

[81] K. Otsuka, A. Ishii, Y. K. Kato, *Opt. Express* **2019**, *27*, 17463.

[82] A. Ehrmann, T. Blachowicz, in *Examination of Textiles with Mathematical and Physical Methods* (Eds: A. Ehrmann, T. Blachowicz), Springer, New York **2017**, pp. 55–73.

[83] F. A. Mann, N. Herrmann, D. Meyer, S. Kruss, *Sensors* **2017**, *17*, 1521.

[84] J. G. Duque, L. Oudjedi, J. J. Crochet, S. Tretiak, B. Lounis, S. K. Doorn, L. Cognet, *J. Am. Chem. Soc.* **2013**, *135*, 3379.

[85] Y. Yang, A. Sharma, G. Noetinger, M. Zheng, A. Jagota, *J. Phys. Chem. C* **2020**, *124*, 9045.

[86] J. Lu, B. Gu, X. Wang, Y. Zhang, *PLoS One* **2017**, *12*, e0169358.

[87] K. V. Vienola, M. Damodaran, B. Braaf, K. A. Vermeer, J. F. de Boer, *Opt. Lett.* **2015**, *40*, 5335.

[88] H.-F. Cui, J.-S. Ye, Y. Chen, S.-C. Chong, F.-S. Sheu, *Anal. Chem.* **2006**, *78*, 6347.

[89] K. D. Kozminski, D. A. Gutman, V. Davila, D. Sulzer, A. G. Ewing, *Anal. Chem.* **1998**, *70*, 3123.

[90] B. Zhang, K. L. Adams, S. J. Luber, D. J. Eves, M. L. Heien, A. G. Ewing, *Anal. Chem.* **2008**, *80*, 1394.

[91] R. Nißler, F. A. Mann, P. Chaturvedi, J. Horlebein, D. Meyer, L. Vuković, S. Kruss, *J. Phys. Chem. C* **2019**, *123*, 4837.

[92] A. V. Naumov, S. Ghosh, D. A. Tsyboulski, S. M. Bachilo, R. B. Weisman, *ACS Nano* **2011**, *5*, 1639.

[93] M. Pfohl, D. D. Tune, A. Graf, J. Zaumseil, R. Krupke, B. S. Flavel, *ACS Omega* **2017**, *2*, 1163.

[94] F. Schöppler, C. Mann, T. C. Hain, F. M. Neubauer, G. Privitera, F. Bonaccorso, D. Chu, A. C. Ferrari, T. Hertel, *J. Phys. Chem. C* **2011**, *115*, 14682.

[95] J. K. Streit, S. M. Bachilo, S. Ghosh, C.-W. Lin, R. B. Weisman, *Nano Lett.* **2014**, *14*, 1530.

[96] S. R. Sanchez, S. M. Bachilo, Y. Kadria-Vili, C.-W. Lin, R. B. Weisman, *Nano Lett.* **2016**, *16*, 6903.

NANO **|** MICRO

small

Supporting Information

## High Sensitivity Near-Infrared Imaging of Fluorescent Nanosensors

Julia Ackermann, Jan Stegemann, Tim Smola, Eline Reger, Sebastian Jung, Anne Schmitz, Svenja Herbertz, Luise Erpenbeck, Karsten Seidl, and Sebastian Kruss*
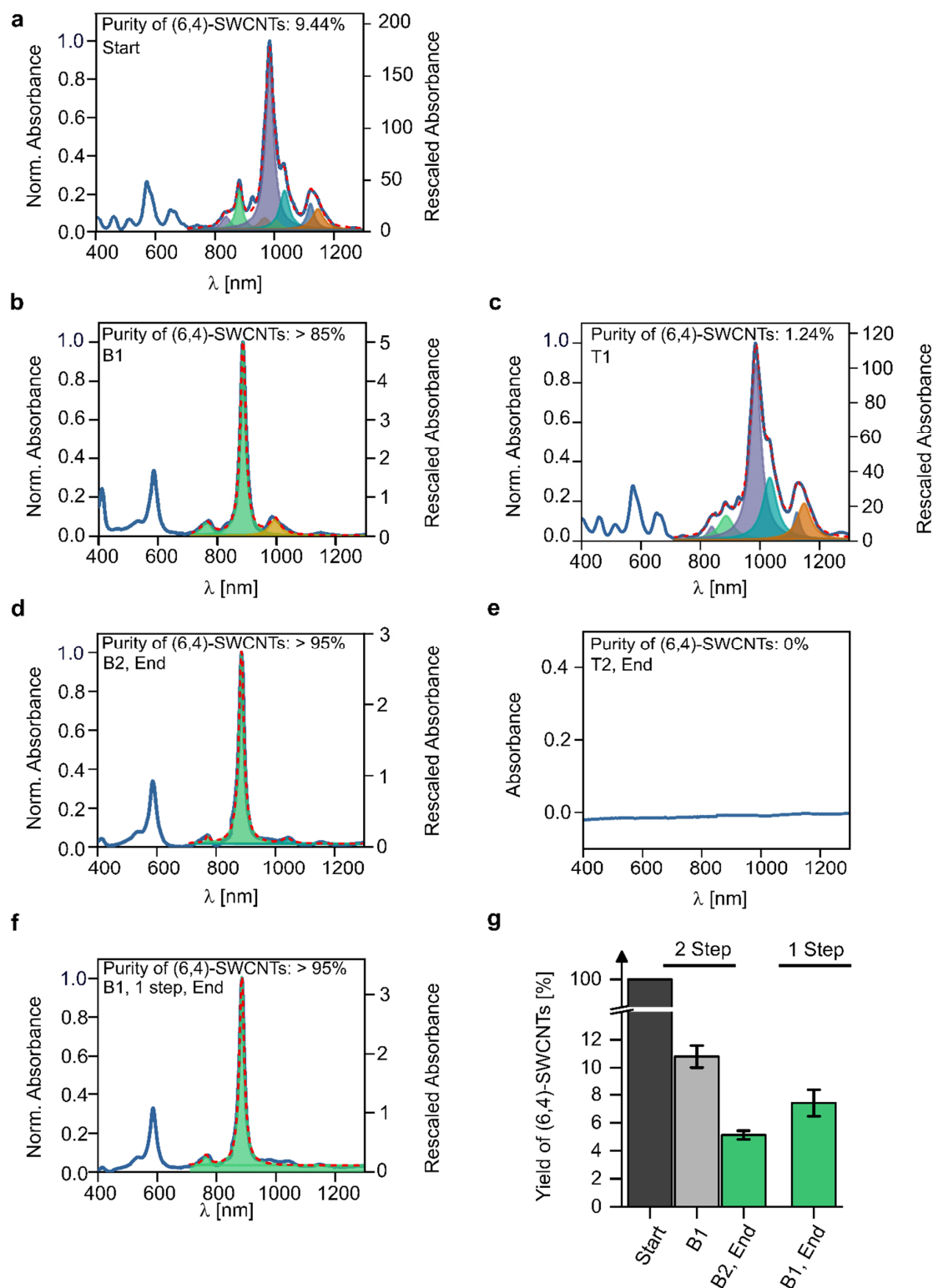
WILEY-VCH

Supporting Information

High sensitivity near-infrared imaging of fluorescent nanosensors

Julia Ackermann, Tim Smola, Eline Reger, Jan Stegemann, Sebastian Jung, Anne Schmitz, Svenja Herbertz, Luise Erpenbeck, Karsten Seidl, Sebastian Kruss*
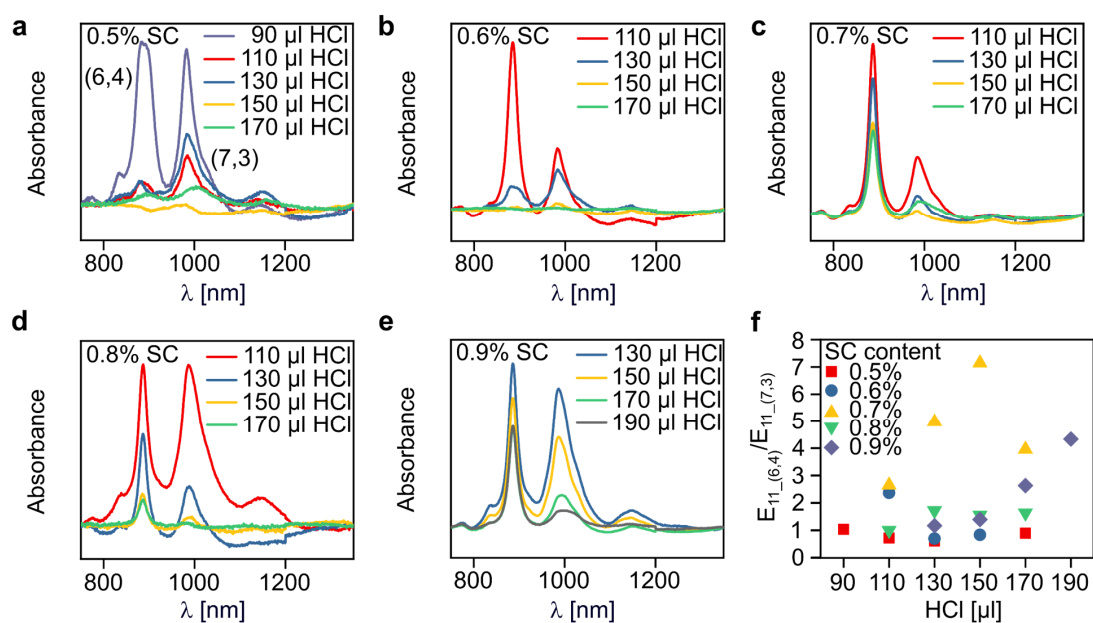
Figure S1. Parameter variation during ATPE. 8 ml batch with 0.025% DOC, 0.5% SDS and different concentration of SC (0.5% - 0.9% in 0.1% steps). a) – e) Absorbance spectra of the respective bottom phase showing the E_{11} transitions of the remaining SWCNT chiralities ((6,4) and (7,3)) for different additions of HCl for pH-driven SWCNT separation. f) The resulting $E_{11\_(6,4)}/E_{11\_(7,3)}$ peak ratio for the varied parameters shows an optimum for an SC concentration of 0.7% with an HCl addition of 150 µl.

WILEY-VCH

Figure S2. Yield and purity of (6,4)-SWCNTs during aqueous two-phase extraction (ATPE). Normalized and rescaled absorbance of a) the initial CoMoCAT-SWCNT solution

(start), b) the bottom phase (B1), and c) the top phase (T1) of ATPE after addition of HCl, leading to the separation of (6,4)-SWCNTs + metallic SWCNTs from the remaining SWCNTs, d) the bottom phase (B2) and e) the top phase (T2) after addition of NaClO, leading to the separation of (6,4)-SWCNTs from metallic SWCNTs, f) the bottom phase (B1, 1 step) after addition of HCl + NaClO directly within one step, leading to the same result compared to d) in one step. Rescaled absorbance means that the absolute absorbance has been recalculated to give equal weight to diluted samples and different volumes between the top and bottom phases. Purity is reported based on the area fraction of the (6,4)-SWCNT peak (green) relative to the fraction of the remaining E_{11} peaks (other colors). g) Comparison of the extraction yield of (6,4)-SWCNTs between 2- and 1-step separation (mean ± SD, $n \geq 4$).
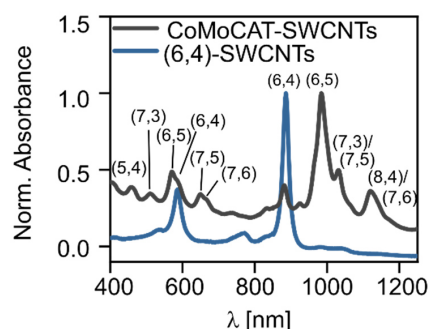
Figure S3. Normalized absorbance spectra with assigned chiralities before (CoMoCAT-SWCNTs) and after ((6,4)-SWCNTs) phase separation in 1% DOC.
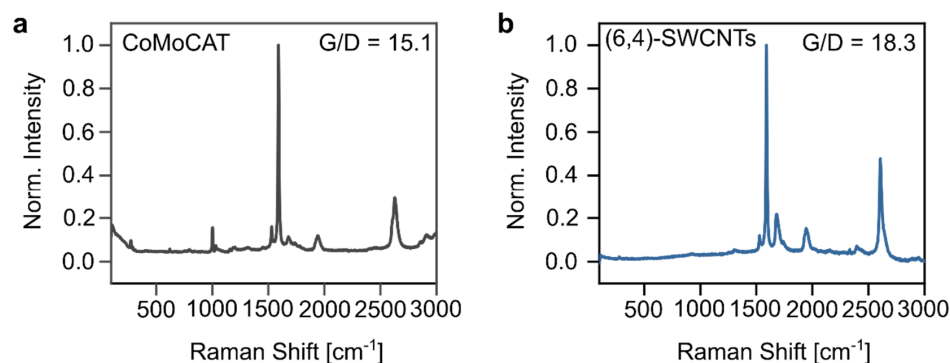
Figure S4. Raman spectra of parental CoMoCAT-SWCNTs and purified (6,4)-SWCNTs in 1% DOC (532 nm laser excitation wavelength). The G/D ratio as a measure of the defect number on the SWCNT surface indicates a lower defect ratio after SWCNT purification.

WILEY-VCH
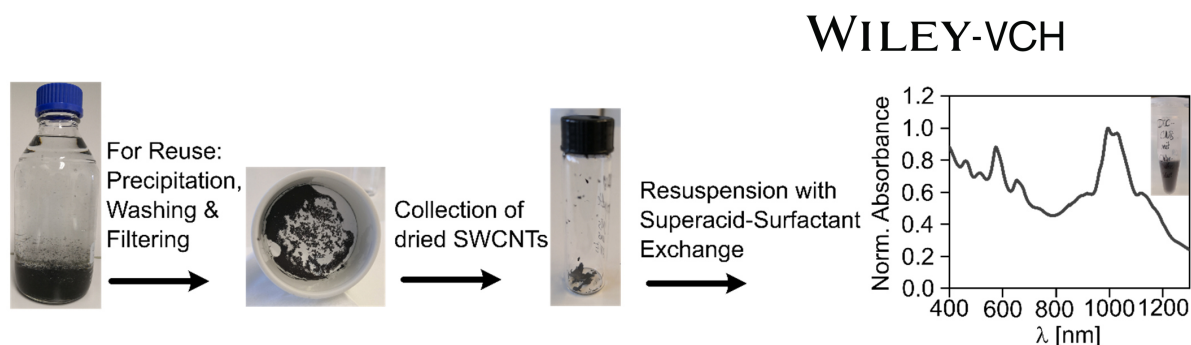
Figure S5. Reuse of remaining SWCNTs from the top phase of the aqueous two-phase extraction. SWCNTs are precipitated with methanol, washed with isopropanol and water, and filtered. After drying overnight (oven, 40 °C), SWCNTs are collected and serve as SWCNT material for further experiments. SWCNTs are resuspended in 1% DOC with superacid-surfactant exchange (based on previous literature) to avoid further SWCNT shorting by tip-sonication.

Simulation of the signal-to-background ratio (SBR):

A simulation of the SBR in imaging fluorophores acting like SWCNTs in a biological scenario (cells in PBS) for two typical camera systems (Si and InGaAs camera) was performed. The simulation was implemented in Python 3.9.7. For this, the respective signal and background were calculated based on the number of electrons generated by each detector per second. A conventional inverted microscope setup equipped with typical equipment served as the basis for the simulation.

For the excitation of the fluorophore (SWCNTs), a typical Gaussian spectrum of an LED was used with an irradiance of 250 mW·cm^{-2} in focus. The excitation wavelength was adjustable in wavelength by shifting the overall spectrum arbitrarily, considering a Stokes shift of 300 nm between excitation and emission. The excitation light passed through an excitation filter and a dichroic mirror, which both transmitted 98% of the signal (also adjustable in wavelength). The light then passed through a 10x objective (a typical aperture of $NA = 0.3$) to distribute the light over the focal plane (SWCNTs on a glass cover slide). The back reflection of photons due to the refractive index difference between air and glass is assumed to be 4%. SWCNTs located on a glass cover slide are excited. Parameters such as the typical quantum efficiency of SWCNTs, emission spectrum, lifetime, absorption cross-section, and concentration of SWCNTs are considered. In addition, interactions with other biological samples (endogenous fluorophores in cell cultures) in terms of scattering, absorption coefficient, and autofluorescence at defined concentrations are included. After second transmission of the optics (objective and long pass

WILEY-VCH

emission filter), the signal reaches the detector. Here, material properties, detector quantum efficiency, active sensor area, and noise are considered. The noise is composed of the excitation light, which is transmitted despite filtering, the autofluorescence of other samples, the dark current, at a typical temperature to which the sensor is cooled, and the black body radiation. Detailed assumptions for the respective parameters can be found in ***Table S1***.

Table S1. Parameters used for the simulation of the signal-to-background-ratio for two camera systems (Si and InGaAs camera).

Excitation LED	
Irradiance in Focus *I*	250 mW·cm^{-2}
Spectrum *I[λ]*	Gaussian curve with FWHM = 30 nm, adjustable in wavelength
Fluorophore (SWCNT)	
Spectrum *I[λ]*	Gaussian curve with FWHM = 30 nm, adjustable in wavelength
Quantum Yield *Φ[λ]*	1%
Absorption Cross Section *σ*	1.3·10^{-12} cm²
Concentration *c*	1 пм
Sample Volume *V*	200 µl
Stokes Shift	300 nm
Objective	
Numerical Aperture *NA*	0.3
Emission/Excitation Filter	
Transmission *T*	98%
Bandwidth *B*	50 nm
Optical Density *OD*	7
Dichroic Mirror	
Transmission *T*	98%
Optical Density *OD*	3
Si Camera	
Quantum Efficiency *Φ(λ)*	Hamamatsu ORCA Flash 4.0 V2
Material – Bandgap	Si – 1.12 eV
Pixel *Px*	2048 x 2048

WILEY-VCH

Pixel Size x	6.5 x 6.5 µm
Sensor Temperature T_{sensor}	-10 °C = 263.15 K
Dark Current I_{dark}	0.6 electrons·(s·pixel)$^{-1}$ at T_{sensor}

InGaAs Camera

Quantum Efficiency $\Phi[\lambda]$	Xeva 1.7 320 TE3 USB 100 Xenics
Material – Bandgap	InGaAs – 0.75 eV
Pixel Px	320 x 256
Pixel Size x	30 x 30 µm
Sensor Temperature T_{sensor}	-83.15 °C = 190 K
Dark Current I_{dark}	10,000 electrons·(s·pixel)$^{-1}$ at T_{sensor} = 223 K

Black Body Radiation

Ambient Temperature T_{amb}	23 °C

**Light Interaction with Sample**

|	
Scattering Soft Tissue μ_s	[1]
Absorption Water μ_a	[2]
Tissue Depth z	100 µm

Autofluorescence of biological samples

| Fluorophore	Maximum Excitation [nm]	Maximum Emission [nm]	Typical Cell Level [µM]	Molar Absorptivity [M^{-1} cm^{-1}]	Quantum Yield [%]
Phenylalanine	258[3]	280[3]	18[4]	195[5]	2.2[6]
Tryptophan	280[3]	300[3]	12[4]	5,579[5]	12[6]
Tyrosine	275[3]	300[3]	29[4]	1,405[5]	13[6]
Riboflavin	444[3]	558[3]	19[4]	33,000[7]	30[7]
NAD/NADH	355[3]	462[3]	83[4]	6,220[8]	60[9]

WILEY-VCH
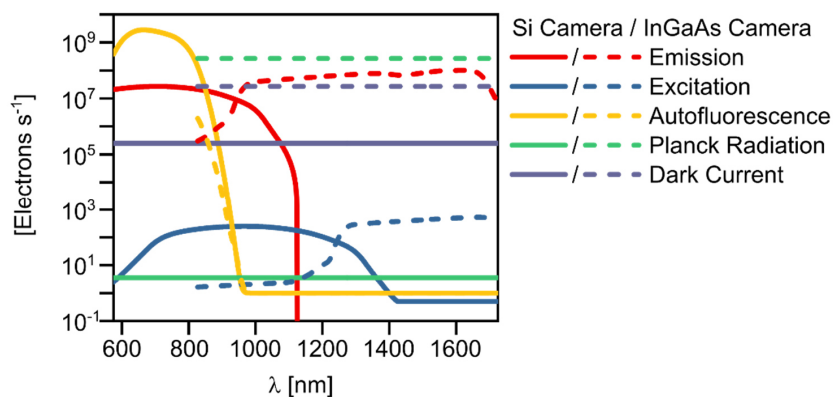
Figure S6. Parameters incorporated in the signal-to-background ratio simulation. Parameters of SWCNT emission, excitation light that is still detected by the cameras despite using filters, autofluorescence of soft tissue and typical fluorophores in cell cultures, dark current and plank radiation vary when using a Si and an InGaAs camera (dashed).
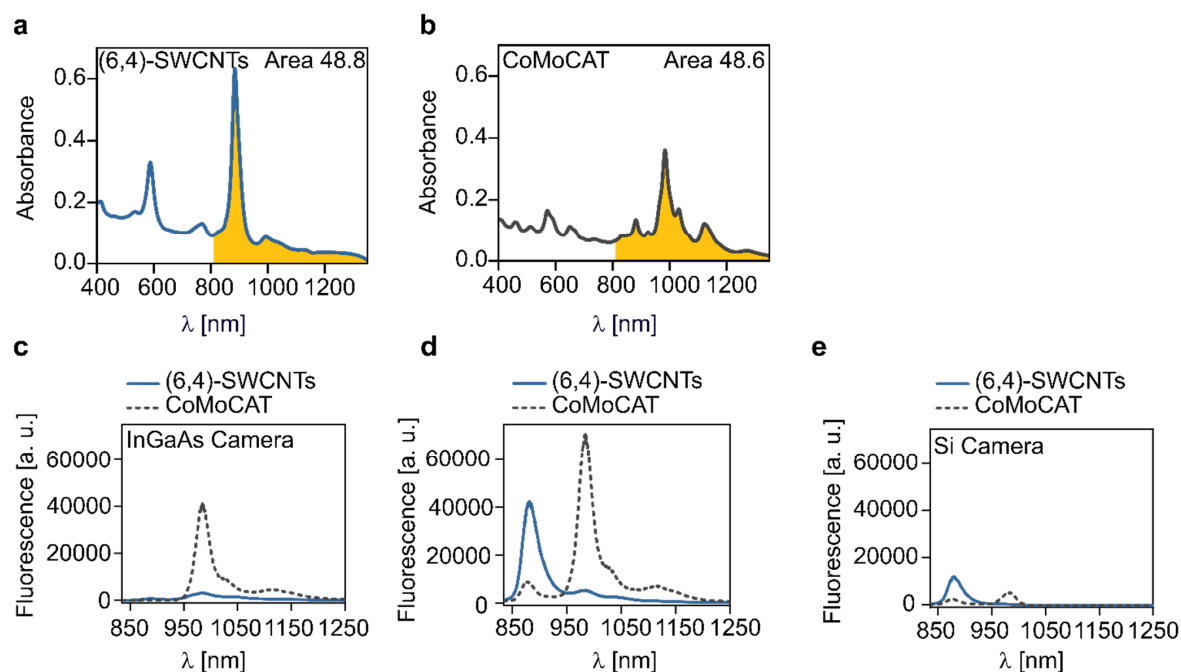
Figure S7. Sensitivity of (6,4)-SWCNTs. Absorbance spectra of a) (6,4)-SWCNTs and b) CoMoCAT-SWCNTs in 1% DOC. The carbon concentration of both samples was matched based on the area under the curve of the E_{11}-transitions in a range of $810 - 1350$ nm (highlighted in yellow). c) Fluorescence spectra of the samples in a) and b) collected with an InGaAs detector and converted with the quantum efficiency of a typical InGaAs camera. d) Fluorescence spectra of the data acquired in c), assuming a theoretical quantum efficiency of

WILEY-VCH

100% at each wavelength. e) Fluorescence spectra of the data acquired in c), converted with the quantum efficiency of a Si camera.
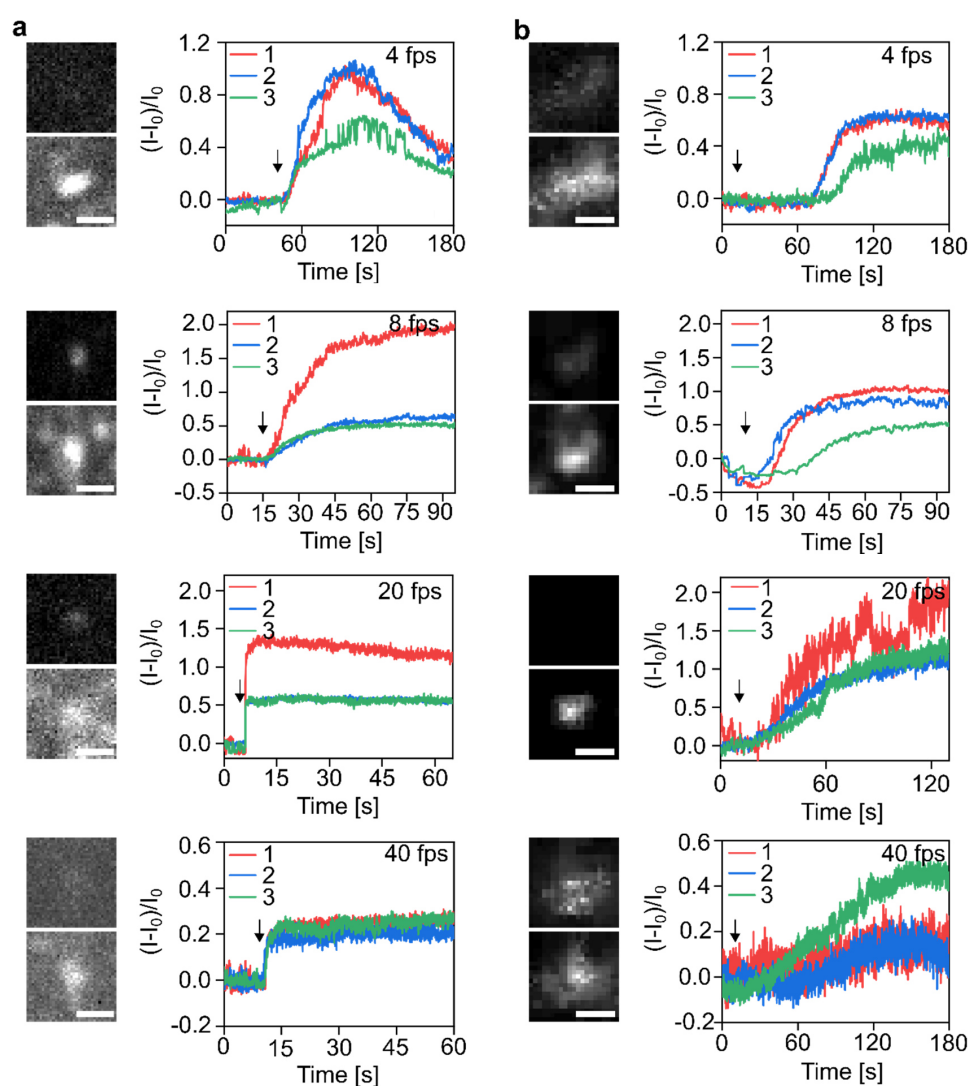
Figure S8. 10 µM dopamine detection with $(GT)_{10}$-(6,4)-SWCNTs using different microscopes and frame rates. Numbers 1 – 3 denote traces of different single SWCNTs, NIR images show exemplary one of these traces (top – before and bottom – after dopamine imaging), arrows mark dopamine addition. Scale bars represent 1 µm. a) Nikon microscope with white LED and 100x objective, b) Nikon microscope equipped with green LED and 60x objective.

Supplementary Movie M1

WILEY-VCH

A supplementary movie is available online. It shows the whole experiment described in ***Figure S8*** a) imaged with 20 fps. In short, $(GT)_{10}$-(6,4)-SWCNTs are immobilized onto a surface and 10 μM dopamine were added. The video is in original speed.

Simulation of the camera signal of two fluorescent point sources:

To simulate the optical resolution limit of two SWCNTs parallel to each other, they were considered simplified as point-like structures. The Rayleigh criterion states that two such points can just be distinguished from each other when the intensity maximum of the diffraction disk of the first point falls into the minimum of the diffraction disk of the second point.[10] For simplification, a Gaussian function was chosen for each point. The brightness of the darkest point between the two maxima is then 73.5% of the maxima and the distance between the two points is *d*. The resolution limit *d* depends here on the emission wavelength of the fluorophore and the *NA* of the objective (**Equation S1**).[10] Based on different pixel sizes (65 nm, 162 nm, and 444 nm), the generated intensity image was divided into different squares.

$$d = \frac{0.61 \cdot \lambda}{NA} \qquad (S1)$$
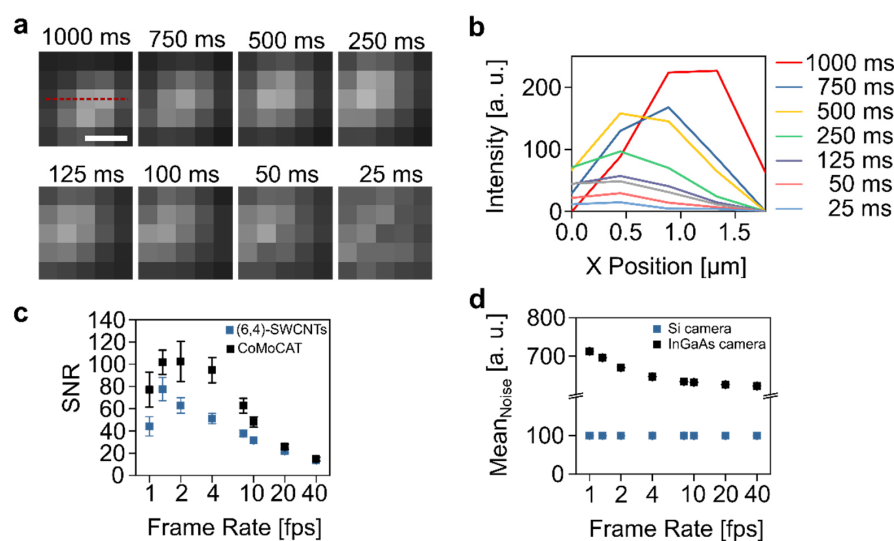
Figure S9. Single SWCNT imaging. a) Fluorescence images of $(GT)_{10}$-CoMoCAT-SWCNTs captured with an InGaAs camera at different frame rates. Scale bar represents 1 μm. b) Corresponding height traces of the images in a) and c) signal-to-noise ratios (SNR) in

comparison to the SNR of $(GT)_{10}$-$(6,4)$-SWCNTs captured with a Si camera (results from Figure 4 h, mean ± SE, $n = 6$). d) Comparison of the mean noise signal captured with the Si and InGaAs camera without illumination at different frame rates (mean ± SE, $n = 6$).
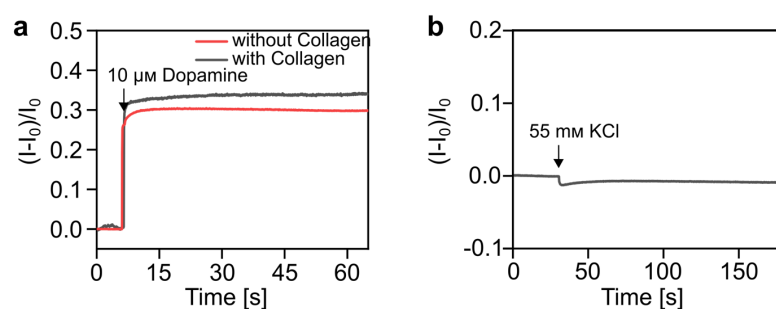
Figure S10. a) Coating $(GT)_{10}$-$(6,4)$-SWCNTs with collagen does not change the overall responsivity of these sensors when dopamine is added. b) Addition of 55 mM KCl does not change the intensity of $(GT)_{10}$-$(6,4)$-SWCNTs when no PC12 cells are cultured on top.

Supplementary Movie M2

A supplementary movie is available online. It shows the whole experiment described in *Figure 5* of the main manuscript. In short, $(GT)_{10}$-$(6,4)$-SWCNTs are immobilized onto a surface and dopamine-releasing PC12 cells were cultured on top. Dopamine release is stimulated by adding 55 mM KCl. The speed of the video was accelerated by 6 times.

References

[1]   S. L. Jacques, Phys. Med. Biol. 2013, 58, 5007.

[2]   D. J. Segelstein, Master Thesis, University of Missouri-Kansas City 1981.

[3]   A. B. Shrirao, R. S. Schloss, Z. Fritz, M. V. Shrirao, R. Rosen, M. L. Yarmush, Biotechnol. Bioeng. 2021, 118, 4550.

[4]   B. D. Bennett, E. H. Kimball, M. Gao, R. Osterhout, S. J. van Dien, J. D. Rabinowitz, Nat. Chem. Biol. 2009, 5, 593.

[5]   G. D. Fasman, Handbook of Biochemistry and Molecular Biology, CRC Press, Boca Raton 2019.

[6]   R. F. Chen, J. Res. Natl. Bur. Stand., Sect. A 1972, 76A, 593.

[7]   J. Koziol, Photochem. Photobiol. 1966, 5, 41.

[8]   R. M. C. Dawson, Data for biochemical research, Clarendon Press, Oxford 1986.

[9]   O. S. Vasyutinskiĭ, I. A. Gorbunova, M. K. Danilova, M. E. Sasin, V. P. Belik, D. P. Golyshev, (Preprint) SSRN Journal 2022.

WILEY-VCH

[10]   G. de Miguel, G. Vicidomini, B. Harke, A. Diaspro, in Micro and Nano Technologies,

Three-Dimensional Microfabrication Using Two-photon Polymerization (Ed.:

Tommaso   Baldacchini), William Andrew Publishing 2016, p. 190.

3.1.2 Publication Synopsis

Research Manuscript I presented an approach aimed at improving the sensitivity of fluorescent SWCNTs when detected using commonly used microscope equipment. The objective of the study was to shift the emission of SWCNTs closer to the visible wavelength region. Considering that (6,4)-SWCNTs represent the shortest NIR emitter among SWCNTs (emission at 880 nm), this specific chirality was chosen for the study (part 1). Another objective was to evaluate the detection efficiency with Si cameras (part 2) and to test it on a complex cellular system (part 3).

In the first part of the paper, an optimized separation protocol was developed for the extraction of (6,4)-SWCNTs. The inspiration for this protocol was derived from a previously published method that involved a two-step separation process based on ATPE [Li 19b]. By modifying specific parameters, the protocol was improved to achieve a one-step separation of (6,4)-SWCNTs. The purity of the extracted (6,4)-SWCNTs (> 95 %) was confirmed through absorption and 2D excitation-emission spectra. Absorbance measurements were employed to determine the initial concentration of the unpurified SWCNT suspension as well as the final concentration of (6,4)-SWCNTs after purification. These measurements were used to calculate the extraction yield. The results demonstrated that the transition from a two-step to a one-step separation increased the yield from 5.1 ± 0.3 % to 7.4 ± 1 %. Additionally, any remaining SWCNTs in the top polyethylene glycol (PEG) phase could be recycled. Raman spectra were utilized to compare the defect rate of (6,4)-SWCNTs after separation, which serves as a measure of the extent of covalent sidewall reactions, with that of the unpurified CoMoCAT-SWCNTs. The analysis revealed that (6,4)-SWCNTs exhibited a lower defect rate compared to CoMoCAT-SWCNTs (G/D ratio of 18.3 vs. 15.1). Overall, the development of the one-step (6,4)-SWCNT extraction protocol enables a simple, low-cost process in which different components can be easily mixed together and centrifuged for faster separation. The separation approach can be scaled up in volume so that larger amounts can be extracted and the time required is low.

After conducting the basic characterization of the extracted (6,4)-SWCNTs, the second part of the paper focused on comparing the detection efficiency of (6,4)-SWCNTs and CoMoCAT-SWCNTs, as well as comparing the performance of Si and InGaAs detectors. To assess the optimal emission wavelength for biological imaging, a simulation was designed to calculate the wavelength-dependent SBR during cell imaging in PBS using Si and InGaAs cameras. Here, the designation SBR was chosen instead of SNR because, as the name suggests, it is the ratio of the SWCNT signal to a background signal, which is not random like noise but can still infere in image processing. The simulation indicated that a wavelength of 908 nm provided the highest SBR when using a Si camera due to

its lower dark current. Consequently, (6,4)-SWCNTs emitting at around 880 nm were considered ideal for detection since they are closest to the emission wavelength of 908 nm among all available SWCNT chiralities.

The detection efficiency of (6,4)-SWCNTs and unpurified CoMoCAT-SWCNTs was then compared using Si and InGaAs detectors. It was observed that (6,4)-SWCNTs detected with a Si camera appeared approximately 1.7 times brighter than CoMoCAT-SWCNTs. Additionally, SWCNTs were rendered sensitive with $(GT)_{10}$-ssDNA to detect dopamine, and the imaging quality and sensitivity of single SWCNTs before and after dopamine addition were compared using both camera systems by immobilizing the SWCNTs on glass surfaces. The Si camera exhibited higher resolution and demonstrated a significant signal change of 51.3 % with $(GT)_{10}$-(6,4)-SWCNTs upon the addition of dopamine (10 µM), compared to a 6.7 % signal change with $(GT)_{10}$-CoMoCAT-SWCNTs using an InGaAs camera. This corresponds to a 7.5-fold increase in sensitivity. The image quality has improved due to the smaller pixel size of Si cameras. Thus, the spatial resolution of SWCNT imaging is no longer limited by the pixel size of InGaAs cameras (444 nm in this case) but by the optical resolution limit of microscopy of about 372 nm, which was illustrated in a second simulation.

Experiments were conducted to test the imaging acquisition speed, which was supported by calculated values of the SNR of the respective images. The results indicated that images with exposure times as short as 50 ms (20 fps) provided a sufficiently high SNR > 20. The highest SNR ratio was achieved at 500 ms exposure time (SNR of 75). Detection of dopamine at the single SWCNT level in two different standard microscope setups at such high frame rates was confirmed.

In the final part of the paper, the detection of dopamine using a Si camera in a real biological application, the cellular release of dopamine, was tested. SWCNT-coated glass bottom Petri dishes were coated with collagen for improved cell adhesion, which had no effect on sensor response, and dopamine-releasing neural progenitor cells were cultured on top. Immediately before starting the cell experiments, the cell medium was exchanged for PBS supplemented with $CaCl_2$, and exocytosis was induced by the addition of 55 mM KCl. The sensors exhibited a localized intensity increase of up to 10 % specifically within the area of the cell, while control experiments showed no signal change when KCl was added to the sensors without prior cell cultivation, indicating that the increase was due to dopamine release from the cells.

In conclusion, a rapid, cost-effective, and scalable method has been developed for the one-step separation of (6,4)-SWCNTs, providing convenient access to this specific SWCNT chirality. The imaging of (6,4)-SWCNTs is possible using standard microscopes, even at high

frame rates (> 20 fps). Both the spatial resolution and sensitivity of the dopamine sensors could be increased by using chirality-pure (6,4)-SWCNTs. This advancement makes the technology more accessible to a wider scientific community, eliminating the requirement for specialized and expensive equipment. Additionally, the interchangeable functionalization of SWCNTs opens up possibilities for diverse applications beyond the chemical mapping of cellular dopamine release.


In a Nutshell

✓ Easy access to (6,4)-SWCNTs (880 nm emission) due to development of a rapid, cost-effective, scalable, one-step separation

✓ Ideal for imaging cells in PBS according to a simulation on the SBR of SWCNTs

✓ 7.5-fold higher sensitivity for dopamine with $(GT)_{10}$-(6,4)-SWCNTs and Si cameras compared to CoMoCAT-SWCNTs with InGaAs cameras

✓ Successful detection of cellular dopamine release using Si cameras

✓ No need for special, expensive microscope equipment

✓ Broad spectrum of future applications due to modular surface chemistry of SWCNTs

---

3.2 Sensitive Neurotransmitter Detection with Homogeneous Sensor Coatings

The preceding Section 3.1 demonstrated that SWCNT-based sensor coatings have the potential to enable the chemical mapping of cell release processes using conventional microscopes. The technology has broader applications beyond understanding cell communication. It could serve as a general tool for gathering valuable information about cell cultures and assessing overall cellular health [Kie18]. Cell therapy could also benefit from this. It could be used to study cellular responses to environmental toxins or drugs, gaining insights into disease development processes. In addition, it could contribute to the development of new drugs by screening drug libraries and directly assessing cellular responses. However, a standardized method to integrate these sensors into labware to combine it with biological systems such as cells has been missing. For this purpose, it is crucial that sensor layers based on SWCNTs exhibit reliable and reproducible signal changes.

One common method employed thus so far is the coating of glass surfaces with a silane compound called (3-Aminopropyl)triethoxysilane (APTES). It enables the electrostatic interactions between the negative DNA backbone surrounding the SWCNT and the amine groups of the APTES molecules, which in turn are covalently bonded to the glass surface [Sta21, Syp22]. Subsequently, SWCNTs are immobilized by pipetting a dispersion of SWCNTs in PBS onto the coated surface. After immobilization (in the range between 5 min and overnight), non-immobilized SWCNT sensors are washed off, and the coated sample is then directly used for the planned sensor experiment [Kru17, Man17, Bey19]. However, this method has its drawbacks, such as the potential formation of aggregates and non-uniform coating. These differences in coating directly affect the overall signal change/sensitivity of the SWCNT sensors when an analyte is added (refer to Figure 3.1), as the differences in the coating are also directly visible when imaging at high magnifications (typically 60x - 100x objective to detect individual SWCNTs, used for cell experiments).
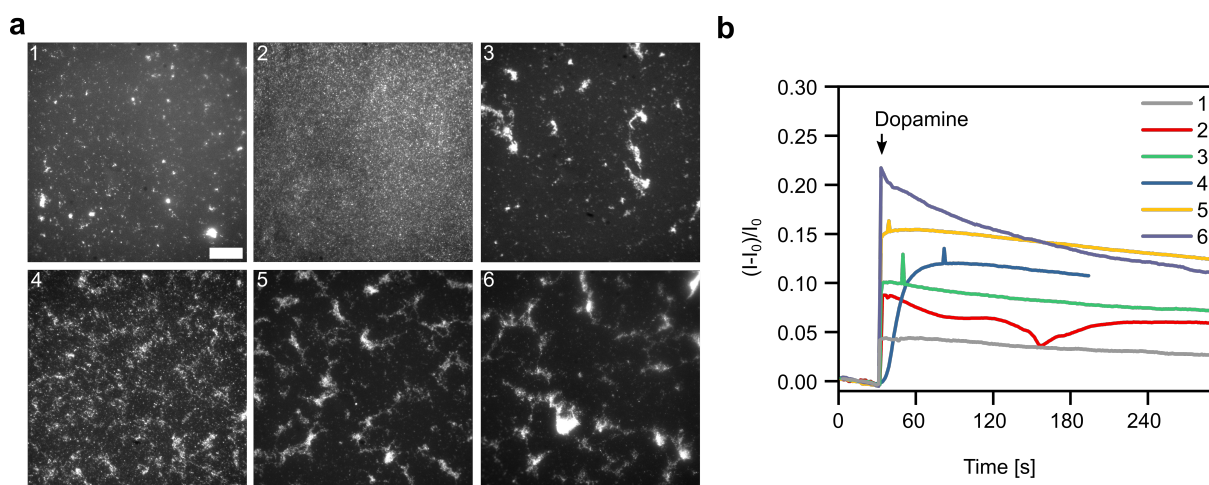
Figure 3.1: Manual SWCNT sensor coating leads to differences in SWCNT coating and resulting sensor responses to an analyte. a) NIR fluorescence images of six different $(GT)_{10}$-SWCNT sensor coatings imaged with a 100x objective. Scale bar = 20 µm. b) Resulting SWCNT fluorescence changes of these coatings in response to 100 µM dopamine.

The issue likely arises from the fact that the absolute signal change depends on the ratio between the number of SWCNT sensors/binding sites for an analyte and the number of analyte molecules present. In addition, reabsorption effects in densely populated areas can reduce fluorescence [Wei20]. This problem of a non-uniform sensor response has also been encountered, for example, by Elizarova *et al.* [Eli22]. To account for the differences in the sensor response, they, therefore, had to add 100 µM of dopamine at the end of each experiment for maximum activation of the sensor layer and then considered the

fluorescence increases due to cellular release signals as a proportion of the maximum value in each case. A uniform coating should thus help to make sensor responses more reliable, reproducible, and comparable, even between different coated samples and manufacturing batches.

Furthermore, there are uncertainties regarding the robustness of these sensors. From a commercialization perspective, SWCNT-based sensor coatings for cell culture monitoring need to be sterilizable as well as retain their functionality beyond several weeks of storage after SWCNT sensors have been immobilized and dried. Since the transfer step from science to commercialization has not yet taken place for fluorescent SWCNT sensors, such questions have not yet been resolved.

Moreover, it is important to showcase applications beyond the measurement of dopamine release. It is time to explore and demonstrate the versatility of SWCNT-based sensors by applying them to other relevant areas for research and industry. Driven by these ideas and questions, the concept of 'Smart Slides' emerged, which not only support cell adhesion but become 'smart' due to the integration of a functional sensor layer that can optically and non-invasively visualize biochemical cell responses in an optimized way.
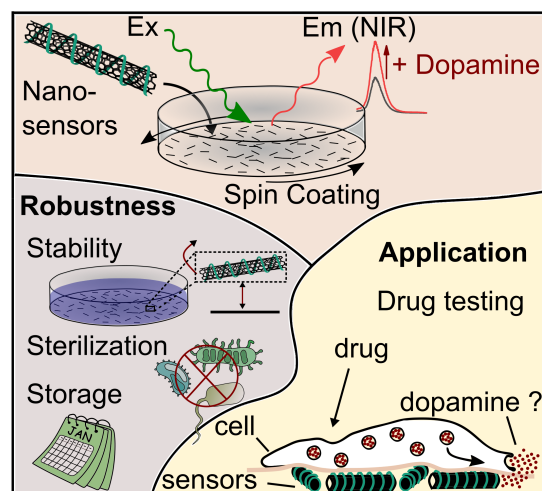
The Research Manuscript II reported in the upcoming Section 3.2.1 can therefore be viewed as a logical continuation of the research presented in Manuscript I (Section 3.1.1). Here, dopamine-sensitive SWCNT sensors were again used as a model system considering the significant role dopamine plays in neurological diseases. It addresses several key questions that emerged from the previous study and aims to further enhance the SWCNT-based sensor coatings for biomedical research. The following questions guided this research:

- Can the coating of glass surfaces with SWCNTs be improved to prevent aggregation and achieve homogeneous SWCNT coatings across different samples?

- What is the optimal coating density to enhance sensitivity?

- How robust are these sensor coatings? Can they be stored for several weeks without losing functionality? Can they be sterilized to enable contamination-free (cell) experiments?

- Can these optimizations make SWCNT-based sensor coatings a reliable tool for drug testing of psychotropic substances?

3.2.1 Smart Slides for Optical Monitoring of Cellular Processes (Research Manuscript II)

Graphical Abstract

SWCNTs exhibit fluorescence in the near-infrared (>880 nm) and can be effectively functionalized with DNA to serve as highly sensitive sensors. These versatile SWCNT sensors can be coated on diverse surfaces, forming smart functional sensor coatings. They enable real-time monitoring of cell responses to substances and drugs, offering valuable insights into cellular behavior.

Reference

Copyright Statement

Contributions

The research was designed and conceived by J.A. and S.K., with input from S.H. and K.S. J.A. and E.R. conducted the SWCNT coating of glass surfaces, analyte response measurements, and robustness tests of the sensors. S.J., with assistance from J.M., was responsible for cell cultivation and seeding of the cells on the sensors. Cell viability tests were performed by J.M., data analysis by J.A. Cell stimulation experiments, data analysis, and manuscript writing were performed by J.A. S.K. contributed to the final revision of the manuscript draft.

RESEARCH ARTICLE

Check for upd

Smart Slides for Optical Monitoring of Cellular Processes

Julia Ackermann, Eline Reger, Sebastian Jung, Jennifer Mohr, Svenja Herbertz, Karsten Seidl, and Sebastian Kruss*

The molecules released by cells are a fingerprint of their current state. Methods that measure them with high spatial and temporal resolution may provide valuable insights into cell physiology and diseases. Here, a nanosensor coating is developed that transforms standard cell culture materials/dishes into "Smart Slides" capable of optically monitoring biochemical efflux from cells. For this purpose, single wall carbon nanotubes (SWCNTs) that are fluorescent in the beneficial near-infrared (NIR, 850 – 1700 nm) window are used. They are chemically tailored to detect the neurotransmitter dopamine by a change in fluorescence intensity. These nanosensors are spin-coated on glass substrates and it is shown that such sensor layers can be sterilized by UV light and can be stored in dry condition or buffer for at least 6 weeks and have little influence on cell viability. The optimal sensor density to maximize sensitivity is also identified. Finally, these substrates are used to image dopamine release from neuronal cells cultivated on top in the presence of various psychotropic substances, which represents a system to test pharmaceuticals for neurological or neurodegenerative diseases. Therefore, Smart Slides are a powerful tool to monitor cellular processes in cell culture systems.

1. Introduction

Cells release molecules and the spatiotemporal concentration profile is a biochemical fingerprint of the biological state.[1,2] Real-time monitoring of these molecules is therefore important to gain insights into cell physiology and how cells respond to changes in their environment such as nutrient availability, environmental toxins, or drug exposure.[3,4]

Degeneration and death of neurons leading to a decline of cognitive and motor functions can be caused by a variety of factors, which is the reason why neurodegenerative disorders are currently incurable and represent a significant burden to society.[5,6] To understand such complex mechanisms and develop effective treatments, highly sensitive biosensors that detect temporarily- and spatially-resolved biomolecular changes at the cellular level are of great importance. For example, numerous methods have been developed to assess neurobiological processes by quantifying dopamine levels, which gives deeper insights into diseases such as Parkinson's, depression, and addiction. Such methods include electrochemical and fluorescence-based methods or imaging mass spectrometry, all of which have their own advantages and disadvantages.[7,8] However, to date a simple and ready-to-use tool for standardized in vitro cell culture to obtain dynamic information about the biological state of cells is missing.[4]

Biosensors based on nanomaterials have shown many advances in the past years.[9,10] One example is single wall carbon nanotubes (SWCNTs), which represent nanoscale building blocks with versatile surface chemistry.[11] Due to their fluorescence emission in the near-infrared (NIR, 850 – 1700 nm) biological transparency window, imaging and sensing applications benefit from reduced scattering and autofluorescence of biological samples and thus provide a high signal-to-noise ratio.[12,13] In addition, unlike many other fluorophores, they have excellent photostability and are suitable for long-term experiments.[14] Upon chemical surface functionalization they are able to detect different biomolecules with high sensitivity even at the single-molecule level.[15–17] For example, sensors have been developed for the detection of stress in plants,[18–20] proteins,[21,22] cancer markers,[23] bacteria,[24] or neurotransmitters.[25–27] Moreover, with stable SWCNT functionalization, these sensors exhibit very promising biocompatibility.[28,29] Neurotransmitter detection has been demonstrated with a high spatial and temporal

J. Ackermann, E. Reger, S. Herbertz, K. Seidl, S. Kruss
Fraunhofer Institute for Microelectronic Circuits and Systems
Finkenstrasse 61, 47057 Duisburg, Germany
E-mail: sebastian.kruss@rub.de
S. Jung
ZEMOS Center for Solvation Science
Ruhr-University Bochum
Universitätsstrasse 150, 44801 Bochum, Germany
J. Mohr, S. Kruss
Department of Chemistry
Ruhr-University Bochum
Universitätsstrasse 150, 44801 Bochum, Germany
K. Seidl
Department EBS
University Duisburg-Essen
Bismarkstrasse 81, 47057 Duisburg, Germany
K. Seidl, S. Kruss
Center for Nanointegration Duisburg-Essen (CENIDE)
Carl-Benz-Strasse 199, 47057 Duisburg, Germany

resolution for chemical mapping of cellular release processes of dopamine[17,30–32] and serotonin.[26] Recent developments also show that this technology can be tailored for common microscopy equipment[33] and that extracellular dopamine can be reported in 3D by combining time-correlated single photon counting and confocal fluorescence microscopy.[34] Moreover, SWCNT tracking can reveal the nanoscale extracellular space in brain tissue.[35]

However, to increase the accessibility of these SWCNT sensors and enable standardized biological experiments, it is crucial to integrate such sensors into common labware and microscopy settings. SWCNTs offer a distinct advantage in this regard, as they can form high-density sensor arrays. Stapleton et al. developed a SWCNT platform for studying nitric oxide by employing an avidin-biotin interaction as a SWCNT immobilization strategy.[36] This approach enabled them to immobilize higher concentrations of SWCNTs compared to the standard surface silanization with (3-aminopropyl)triethoxysilane (APTES), resulting in enhanced fluorescence signals. The main challenge is not to measure the fluorescence intensity itself but to ensure an even distribution of sensors on the sample. In general, prolonged physisorption times of sensors can lead to their aggregation, which complicates coating processes.

To address this issue, we present a method for converting glass substrates (glass bottom petri dishes) into "Smart Slides" by spin-coating SWCNT sensors on surfaces to achieve a homogeneous sensor coating (**Figure 1**a). The slides continue to support cell adhesion but also become "smart" by optically monitoring biochemical cell responses. We test the optimal conditions for analyte sensitivity and determine the functionality of the slides in terms of storage and sterilization conditions (Figure 1b). In addition, we demonstrate the potential for drug testing by studying dopamine release in a neuronal cell model. Overall, we aim to establish SWCNT-based fluorescent sensor coatings as powerful material/tool for the life sciences.

2. Results and Discussion

2.1. Optimization of Sensor Coating and Analyte Sensitivity

Dopamine plays an important role in various neurodegenerative and mental health diseases. Therefore, we aimed to develop and optimize a dopamine-sensitive coating for cell culture studies. For this purpose, SWCNTs were functionalized with single-stranded (ss)DNA $(GT)_{10}$ oligonucleotides, which noncovalently adsorb onto the SWCNT surface by $\pi-\pi$ stacking interactions.[37] Such $(GT)_{10}$-SWCNTs are known to exhibit a fluorescence increase in response to dopamine.[26,33,38] The prepared $(GT)_{10}$-SWCNTs showed individual and narrow peaks in the absorption spectra, which indicates that they are well-dispersed (Figure S1a, Supporting Information). Their fluorescence also increased after the addition of dopamine, confirming their sensitivity (**Figure 2**b).

To achieve a homogeneous coating of SWCNTs on glass slides or glass-bottom petri dishes, spin coating was performed. For this purpose, the substrates were first modified with amino silanes to increase the electrostatic interactions between the SWCNTs

and the glass surface. Subsequently, various parameters, such as SWCNT concentration (0.2 – 5 nM) and rotational speed (400 – 2000 rpm), were tested to optimize adsorption. To test the homogeneity and reproducibility of the coating, four samples were prepared under the same conditions, and seven images were taken on each sample (Figure S2a–c, Supporting Information). Both the intensity variation (Figure S2d, Supporting Information) and the fraction of SWCNT aggregation/clumping by area (Figure S2e,f, Supporting Information) were determined for these images and showed low variation for the different spin coating conditions, indicating homogeneous coating. The coating at the same SWCNT concentrations at different rotational speeds did not differ except for SWCNTs with a concentration of 5 nM. Consequently, we decided to use fixed spin coating parameters for all subsequent experiments with rotational speeds of 1600 rpm at which the distribution was homogeneous for all tested SWCNT concentrations and for which coating density could be adjusted by the SWCNT concentration (Figure 2a). In addition, $(GT)_{10}$-SWCNT coated surfaces exhibited a low defect ratio, as evidenced by the Raman G/D intensity ratio of 9.9 (Figure S3, Supporting Information).[39] Furthermore, we tested whether homogeneous coating is also possible for chirality-pure SWCNTs, which are more prone to aggregation.[40] For this purpose, $(GT)_{10}$-(6,4)-SWCNTs with a concentration of 0.1 nM (Figure S1b, Supporting Information) were spin-coated in a series of six consecutive coating cycles on the substrate. Again, a dense and homogenous coating could be achieved (Figure S4, Supporting Information), which shows that the approach is also possible for chirality pure samples. However, it is essential to centrifuge the SWCNT samples for a sufficiently long time to avoid aggregates during the coating procedure. We continued with the standard (6,5)-SWCNT enriched samples because they are more accessible to the broader community and available in larger quantities.

The samples with different densities of $(GT)_{10}$-SWCNT coatings were tested for dopamine sensitivity by recording the time course of fluorescence intensity. These samples with varying SWCNT concentrations (0.2 nM, 1 nM, and 5 nM) exhibited different intensity increases (Figure 2c) upon the addition of dopamine (100 μM). This suggests that the interaction between the dopamine molecules and the number of SWCNT sensors/binding sites on the SWCNTs plays a crucial role in maximizing fluorescence change.

The test series was extended to substrates with different SWCNT concentrations. Then the maximum intensity change after dopamine addition was plotted against the starting intensity I_0 of the SWCNT coating in PBS (Figure 2d), which showed a maximum response at medium (starting) intensities. The initial rise in signal change observed with increasing SWCNT concentration can be attributed to the increased likelihood of interactions between dopamine and the sensors. However, as the absolute SWCNT concentration continues to rise, excess binding sites accumulate. As a result, a larger number of binding sites remain unoccupied, combined with an increased likelihood of quenching/reabsorption due to the higher SWCNT density. This leads to an overall decrease in absolute signal change beyond a certain SWCNT concentration. Based on this picture, a model was developed, assuming a linear increase in the number of binding
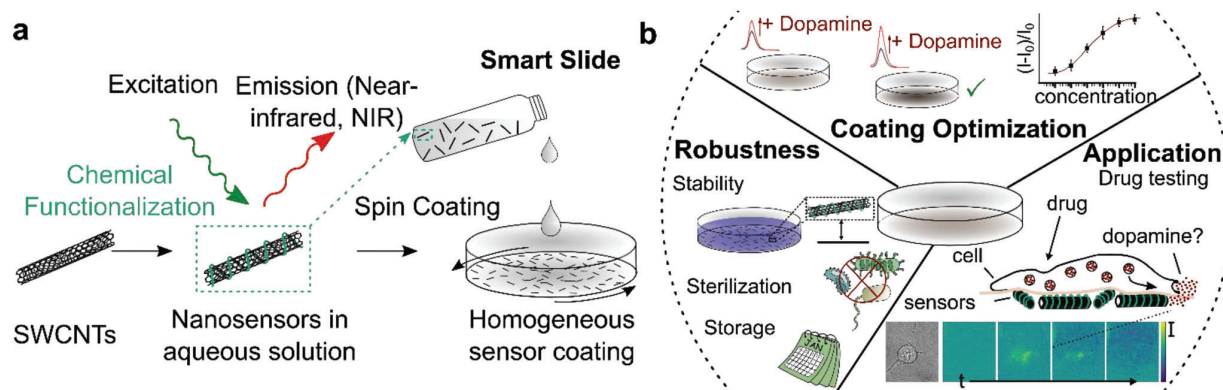
Figure 1. Smart Slides to image cellular responses by light. a) NIR fluorescent SWCNTs are rendered sensitive to the neurotransmitter dopamine by surface functionalization with specific ssDNA sequences. These nanosensors are coated on glass substrates (petri dishes) via spin coating. b) These sensor-coated substrates (Smart Slides) are optimized in terms of robustness for cell-based assays. They serve as versatile tools to assess the impact of pharmaceuticals on dopamine release by neurons.

sites of the SWCNT sensors with the starting intensity I_0 of the sensors:

$$\frac{I - I_0}{I_0} = \alpha I_0 + \gamma I_0^2 + B \tag{1}$$

Here, the signal change is first of all proportional to the starting intensity I_0, which is proportional (until a certain level) to the SWCNT concentration (see also Figure S5, Supporting Information). This can be explained by more occupied binding sites relative to the total number of binding sites. Beyond a turning point, the signal change decreases quadratically by γI_0^2 (with $\gamma < 0$), representing the fraction responsible for the density-dependent quenching/reabsorption and the oversupply of free binding sites with increasing SWCNT concentration. B accounts

for background signals. Despite the complexity of the underlying processes, this model fits the experimental data in Figure 2d (α α = 8.95E-4, with B = 0.20 and γ = −2.57E-6 ($R^2 > 0.95$)).

The most sensitive coating for dopamine detection, considering an upper concentration limit of 100 µm, can be achieved at a starting intensity I_0 of 175 a.u. with a maximum signal change of 46%, while the smallest signal change was 4% (11.5 times lower) at I_0 of 975 a.u. This illustrates the importance of optimizing the coating to maximize sensitivity. Since intensity values depend on the microscope and microscope settings I_0 was additionally plotted as a function of the SWCNT concentration used for spin coating which serves as a calibration curve for the desired fluorescence starting concentration (Figure S5, Supporting Information). The most sensitive coating was achieved at a concentration of 4.2 nM. The low standard deviations of I_0 as a function of the
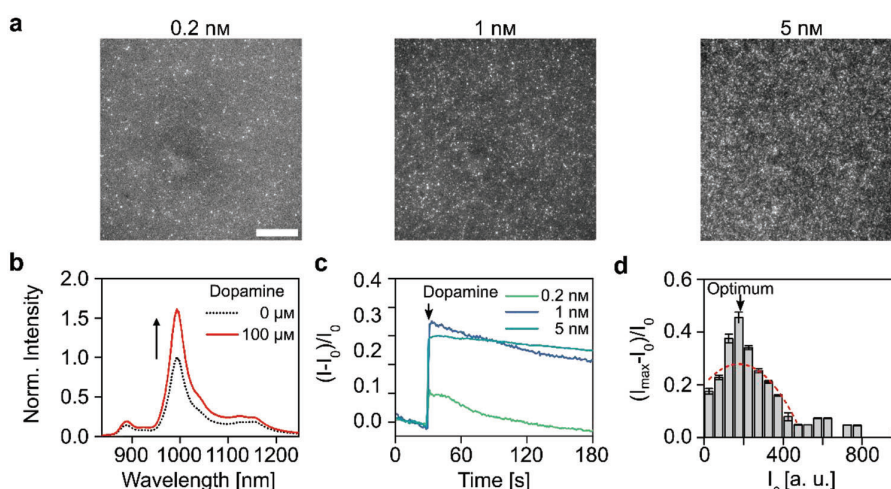
Figure 2. Optimal SWCNT density for Smart Slides. a) NIR fluorescence images of (GT)$_{10}$-SWCNTs spin-coated at 1600 rpm for different SWCNT suspension concentrations. Scale bar = 20 µm. b) Normalized NIR fluorescence spectra of (GT)$_{10}$-SWCNTs before and after addition of 100 µm dopamine in PBS. c) Real-time fluorescence changes of SWCNT coatings of different densities upon addition of 100 µm dopamine. d) Sensitivity of sensor coatings in response to 100 µm dopamine as a function of the initial SWCNT fluorescence intensity I_0 of (GT)$_{10}$-SWCNT coatings in PBS (mean ± SE, $n \geq 8$). The red curve represents a model that accounts for density-dependent photophysical effects (see formula (1), R^2 value of >0.95).

2309064 (3 of 10)
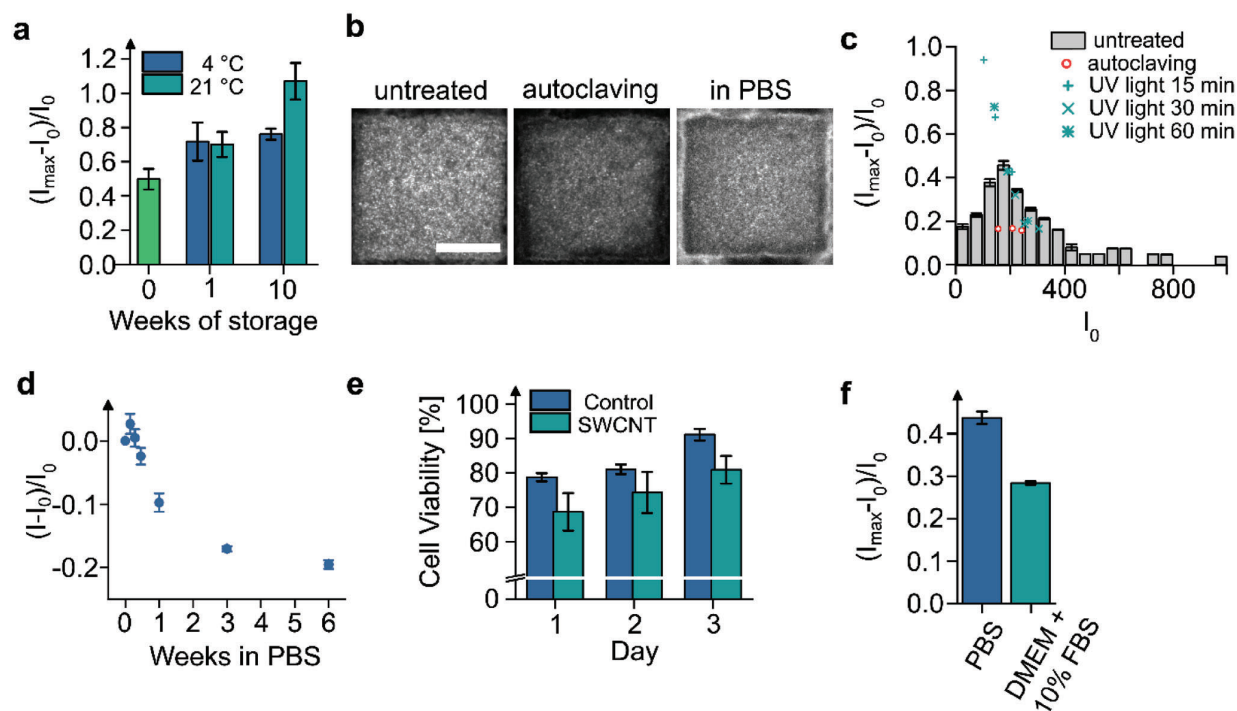
Figure 3. Robustness of $(GT)_{10}$-SWCNT-based sensor coatings. a) Long-term capability to detect dopamine (100 μM) of Smart Slides stored for several weeks in the refrigerator or at room temperature (mean ± SE, $n = 3$). b) NIR fluorescence images before (untreated) and after autoclaving (121 °C, 20 min) and in PBS (contrast adjusted as significantly darker). Scale bar = 20 μm. c) Individual sensor responses to dopamine (100 μM) after sterilization by autoclaving (red circles) and UV light (applied for 15, 30, or 60 min, blue crosses) compared to the averaged sensor responses of untreated sensor coatings (gray bars, results from Figure 2d, mean ± SE, $n \geq 8$) as a function of the initial SWCNT fluorescence intensity I_0 d) Change of $((GT)_{10}$-SWCNT coating) responses over the course of multiple weeks in PBS (mean ± SE, $n = 3$). e) Cell viability of Neuro-2a cells on glass without and with SWCNT coating (mean ±SE, $n = 3$). f) Functionality to detect dopamine (100 μM) in full cell culture medium on a Smart Slide compared to PBS (mean ± SE, $n = 3$).

spin-coated SWCNT concentrations again indicate a highly reproducible SWCNT coating. Note that manual coating of SWCNTs with a 5 nM SWCNT solution without spin coating (indicated by an asterisk in Figure S5, Supporting Information) resulted in both higher intensities I_0 and larger intensity variations. This suggests that spin coating leads to more consistent and reproducible results. It is also noticeable that the relationship between the initial intensity of the sensor coating I_0 and the SWCNT concentration does not increase linearly, but more sharply with increasing SWCNT concentration. This trend is interesting because normally a non-linear decrease in the fluorescence signal with increasing SWCNT concentration is observed due to reabsorption effects.[41] However, perhaps this effect is not as strong because the SWCNTs are immobilized and not in solution, which tends to result in greater spacing between individual SWCNTs. One possible explanation could be the preferential immobilization of long SWCNTs during the spin coating process. Due to the higher amount of long SWCNTs at higher SWCNT concentrations, longer SWCNTs may have a higher probability of being immobilized on the substrate. As longer SWCNTs have higher quantum yields compared to shorter SWCNTs,[42] this could account for the observed non-linear increase in SWCNT fluorescence with increasing SWCNT concentration. Another possibility is that at high concentrations physisorption of SWCNTs becomes faster, which could have an impact on the photophysical response.

2.2. Sensor material robustness

To ensure widespread use of a material such as Smart Slides, robustness under realistic experimental conditions has to be ensured. So far, such sensors have been used for experiments directly after preparation[17,30,38] and it was unknown whether they remain functional after drying. For this purpose, sensitivity was evaluated after storing the sensor coatings in dark conditions at room temperature and in the refrigerator (**Figure 3**a). When stored at room temperature, the sensors retained their functionality. However, after a period of 10 weeks, the intensity change observed after dopamine addition was twice as high as the immediate post-production values. If an accurate concentration determination is required when detecting a substance, this would require recalibration of the sensors to account for the increased intensity change. In contrast, the results for storage at 4 °C (refrigerator) showed high stability. After one week of storage, the sensors exhibited a slight signal increase upon dopamine addition, but the intensity change remained stable for storage durations exceeding two months. It should be noted that the responses for different

storage conditions could be partly due to the variance in addition of dopamine onto the Smart Slides and mixing/diffusion differences of individual experiments after a non-infinite time period. One possible reason for the altered intensity change during storage could be conformational changes in the single-stranded DNA (ssDNA) around the SWCNTs or exposure to oxygen.[43]

The more stable results observed at 4 °C storage align with general recommendations for storing ssDNA because refrigeration increases the stability of ssDNA by at least twice the time compared to storage at room temperature.[44] For SWCNT sensors based on other functionalization units such as proteins or peptides, the storage capability would still need to be evaluated. It is possible that the stability here is limited to a few days/weeks or that different conditions, such as salt concentrations, need to be tested.[45] However, many developed SWCNT sensors based on DNA exist,[11] and DNA-based aptamers are popular recognition units with a high affinity to their targets.[26,46,47]

To assess the functionality of the sensors after typical sterilization procedures autoclaving and UV light were used (Figure 3b,c). Autoclaving of the sensors involved a preliminary experiment to determine whether the SWCNT sensors in dispersion are resistant to heating. $(GT)_{10}$-SWCNTs, $(GT)_{40}$-SWCNTs, and locked nucleic acid (LNA) $(GT)_{15}$-SWCNTs are known for their lower flexibility and potentially higher thermal stability. They were subjected to heating at 60, 80, and 100 °C for 30 min to test if they were stable at these temperatures without aggregation (Figure S6a, Supporting Information). Both, $(GT)_{10}$- and LNA $(GT)_{15}$-SWCNTs precipitated when heated to 100 °C, while $(GT)_{40}$-SWCNTs showed increased stability and remained in solution. This is consistent with observations that SWCNTs with longer ssDNA sequences have higher thermal stability.[48] In contrast, dry $(GT)_{10}$-SWCNT coatings heated to 100 °C did not exhibit any limitations in functionality and responded with a fluorescence increase upon the addition of 100 μM dopamine (Figure S6b, Supporting Information). Thus, sensor coatings demonstrated superior stability compared to SWCNT dispersions, which suggests that autoclaving as a sterilization method could be possible.

To assess the adhesion of the sensor coating during autoclaving, the sensors were spin-coated onto glass substrates with an imprinted location grid. However, the grid did not allow homogeneous coating as on smooth glass substrates (Figure S7a, Supporting Information). After autoclaving, slight changes in the coating appeared on the surface. In some cases, there were fewer sensors and the surface appeared darker, while in others it appeared brighter. The addition of phosphate-buffered saline (PBS) quenched the fluorescence of the sensors, but also led to the detachment of SWCNTs, resulting in weaker responses to dopamine (Figure S7c, Supporting Information). To improve the adhesion of SWCNTs, an additional baking step (heating the silanized substrates at 120 °C for 2 h) was introduced after the amino silane and before the SWCNT coating process to remove physisorbed silane molecules, which does not affect covalently bonded silane molecules.[49] The SWCNT coating on the treated grids demonstrated significant improvements in homogeneity, adhesion after autoclaving, and sensitivity after dopamine addition (Figure 3b, Figure S7b,c, Supporting Information). Without the additional heating step of the APTES layer, the non-covalently bound APTES molecules most likely desorbed during autoclaving, and thus most SWCNTs detached after the addition of PBS.

A comparison of the starting intensities (Figure 3c) revealed that sensitivity was reduced by ≈50% compared to the non-autoclaved grids. Covalent functionalization methods[50] and/or immobilization via avidin-biotin interaction[36] could further improve the stability of the system.

Sterilization of the sensor coatings using UV light was performed with different exposure times (15, 30, and 60 min), followed by testing their functionality to detect dopamine. In most tests, the functionality of the sensors remained unaffected after UV exposure, regardless of the exposure duration, when compared to the untreated samples (Figure 3c). Only sensors with lower starting intensity I_0 showed larger signal changes than the untreated samples, although the reason for this observation remains unclear. The absorption of UV light can lead to the formation of pyrimidine dimers, primarily involving adjacent T-T and T-C sequences.[43] C-T and C-C sequences are less prone to photoreactivity. In rare cases, UV radiation can induce modifications in DNA purine bases, including adenine residues undergoing photocycloaddition reactions with adjacent adenine or thymine. The $(GT)_{10}$ sequences used in the sensor coatings are expected to be largely unaffected by UV radiation. It is possible that other DNA sequences could be more susceptible to the effects of UV radiation, as dimer formation can lead to changes in DNA conformation and a loss of sensitivity. However, in the specific coating region that was determined to be the most sensitive, the sensor responses remained unchanged for different exposure times. As a result, a 30 min UV exposure was chosen for subsequent cell experiments as a sterilization method. We refrained from testing other sterilization methods such as gamma radiation and ethylene oxide because glass discoloration occurs when sterilizing with gamma radiation[51] and autoclaving and UV irradiation are cheaper, faster, and easier sterilization options compared to ethylene oxide. In addition, there are uncertainties regarding the risk of toxicity from ethylene oxide residues.[52,53]

Next, the long-term adhesion of the sensors in liquid was studied, which is important for cell experiments requiring cell cultivation over several weeks. Signals decreased by ≈20% after 6 weeks (Figure 3d). Adhesion was compared in PBS and water, as well as in PBS after the aforementioned amino silane coating with an additional baking step (Figure S8, Supporting Information). Contrary to expectations, the last-mentioned variant exhibited lower long-term adhesion, with hardly any SWCNTs remaining after only 3 weeks. As mentioned earlier, the use of avidin-biotin interactions or covalent immobilization strategies could potentially enhance the stability of the sensors in liquid and improve long-term stability. However, for most cell experiments less than one week of cultivation is sufficient and the observed reduction in signal after 6 weeks should not pose a significant issue. Nevertheless, to test whether the SWCNT coating or the detachment of SWCNTs has an influence on the cells that are used for the following pharmaceutical testing a cell viability test via Trypan Blue staining was performed (Figure 3e). This showed slightly lower cell viability by glass-bottom petri dishes coated with SWCNTs compared to untreated dishes. This could be due to a direct effect by the SWCNTs on cell viability or an indirect effect due to altered adhesion on such a coated surface. Cell viability increased almost linearly with increasing cultivation time for both variants, suggesting that potentially detaching SWCNTs do not have a negative impact on cell growth. The general increase in cell viability

may be due to the increasing degree of coverage and the resulting reduced contact with the glass substrate (Figure S9, Supporting Information).

Finally, the sensitivity of the sensors was evaluated in a cell medium supplemented with 10% fetal bovine serum (FBS). Detection was possible in the cell medium but sensitivity was reduced by approximately one-third compared to the simple buffer environment (Figure 3f). The reduced sensitivity in the cell medium can be attributed to additional compounds in the cell medium that interact with the sensors and potentially interfere with the binding of dopamine, leading to a diminished fluorescence response. To improve the sensitivity of the sensors in protein-rich environments, a detailed understanding of the interaction between the nanosensors and their environment is required.[54] In addition, covalent linking of the SWCNTs to the surface could increase robustness by reducing desorption.[22] Alternatively, for the cell experiments, the cell medium could be replaced by simpler (low-serum) buffers.

2.3. Monitoring of Biochemical Cell Responses

Smart Slides are able to map dopaminergic release processes of neuronal cells, providing access to a better understanding of cellular communication. Furthermore, they have potential applications in drug development, allowing the measurement of the effects of different substances on dopamine release in the synaptic cleft. In this study, differentiated Neuro-2a cells, a standard dopaminergic cell model for neurodegenerative diseases, were directly seeded onto the sensors. After ≈18 h, the cells exhibited good adhesion without additional coating (Figure S10, Supporting Information). In order to evaluate the effectiveness of the Smart Slides, different dopaminergic substances, including levodopa (commonly used to increase dopamine levels in Parkinson's disease patients), nomifensine, and bupropion (both dopamine-norepinephrine reuptake inhibitors in antidepressant therapy), were added to the cell culture for 10 min. Since it is known that such sensors also respond to dopamine homologs such as epinephrine and norepinephrine,[25,38] it was tested whether $(GT)_{10}$-SWCNTs also elicit a sensor response by the added substances in solution (Figure S11, Supporting Information). Levodopa responds to $(GT)_{10}$-SWCNTs due to its chemically similar structure. However, the response is only half as strong compared to dopamine, while nomifensine and bupropion elicit slightly negative sensor responses. To ensure that the sensors were not biased during dopamine measurement, cells were washed twice with PBS before a third time PBS supplemented with calcium chloride was added to start the release experiments. Subsequently, spatial and temporal dopamine release from the cells was measured by stimulating exocytosis with potassium chloride (KCl).

Figure 4a–c illustrates the results of an untreated cell experiment where no substances were added. The bright field image shows a cell adhering to the sensor coating, while the color-coded image represents the NIR channel before and after the stimulus was added. Immediately after the stimulus, there is a localized increase in fluorescence intensity around the cell, which subsequently diminishes due to the diffusion of released dopamine. As

mentioned previously, other catecholamines may also interfere with the sensors used here, so the slides may also be affected by cellular release, e.g. of norepinephrine. However, the cells used here should release mainly dopamine due to the fact that they have been differentiated into dopaminergic neurons. For better comparison, the cell area was selected in each experiment to calculate the mean intensity changes over time (Figure 4c). Based on this analysis, there was an oscillating signal (red lines) caused by the InGaAs camera. For a clearer representation of the signal course, the spectra were smoothed (black lines, see data processing in the experimental section). Note that the replicates for each cell treatment condition are composed of the total number of all analyzed cells from at least $n \geq 6$ slides. Analysis of all individual experiments revealed some heterogeneity, wherein not all cells demonstrated dopamine release. This variability in response is consistent with other studies measuring cellular dopamine release.[31,55,56] Moreover, the sensors exhibited expected differences in signal change following treatment with dopaminergic substances. Selected measurements for the different conditions are provided for comparison in Figure S12 (Supporting Information). For instance, nomifensine and bupropion tended to show amplified and prolonged signal changes following stimulation, which can be attributed to their role as dopamine reuptake inhibitors, prolonging the presence of dopamine in the synaptic cleft.

To account for differences in cellular responses across experiments, the maximum intensity change I_{max} and the time required for the signal change to decrease from I_{max} to $I_{max}/2$ ($\tau_{Imax/2}$) were extracted and presented as a box plot based on the respective cell treatment conditions (Figure 4d,e). Additionally, a box blot was created to depict the time difference between stimulation and maximum signal change I_{max} (Figure S13, Supporting Information)

Note that the time- and spatially-resolved images and time traces contain even more information that could further be extracted. Additionally, determining the rate constants of the molecular sensors is useful to further interpret the kinetics of the chemical images, as the temporally and spatially resolved images are influenced by the rate constants/kinetics of the sensors.[57] The population means were found to be significantly different. Control experiments where KCl was added to the Smart Slides without cultured cells resulted in minimal or no fluorescence changes, which can be attributed to the local increase in ion concentration.[58] To address this issue, LNA nanosensors can increase stability to ion-induced perturbations[59] or optogenetic stimulation can be used for more specific and controlled stimulation.

The addition of levodopa to the cells resulted in an increase in dopamine release, as evidenced by a 193% increase in the median maximum signal change and a 152% increase in $\tau_{Imax/2}$ compared to untreated cells, indicating higher dopamine concentrations. The overall increase is consistent with previous studies, although the absolute values differ, which can be attributed to differences in the cellular system, concentration, and exposure time of levodopa.[55,60,61] The addition of nomifensine and bupropion increased the median maximum signal by 300%, with $\tau_{Imax/2}$ increasing from 11 s for untreated cells to longer-lasting presence times of dopamine in the synaptic cleft (288 s for nomifensine and 146 s for bupropion).
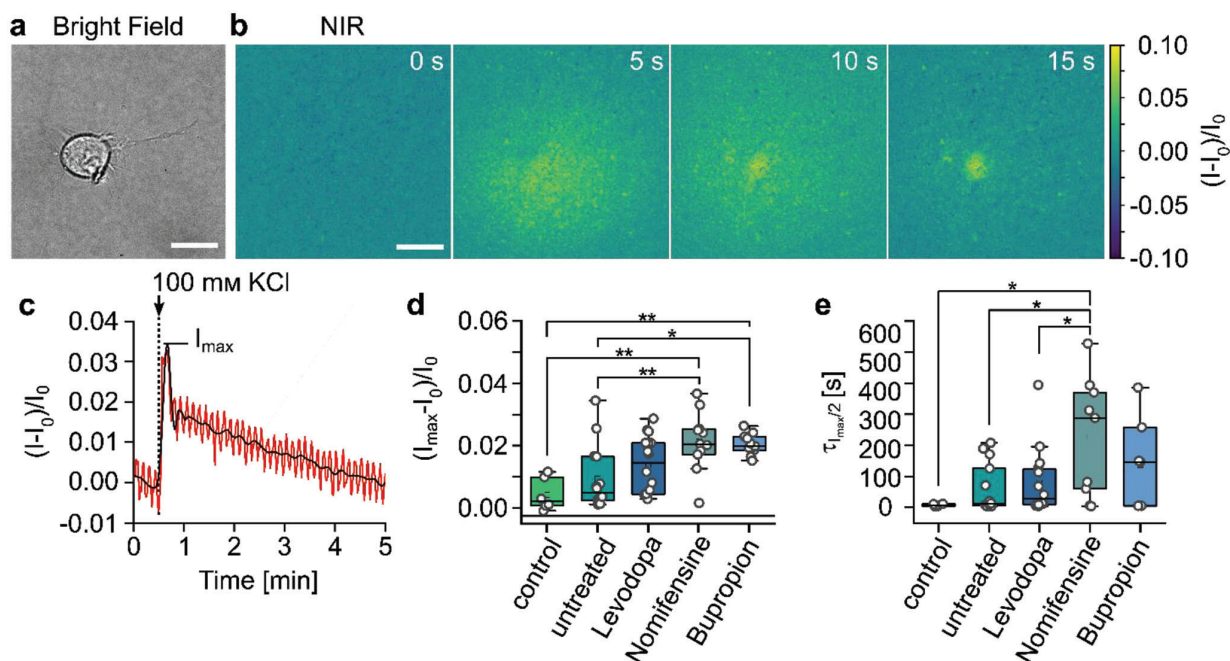
Figure 4. Smart Slides to monitor cell responses to drugs. a) Bright-field image of a Neuro-2a cell cultured on a $(GT)_{10}$-SWCNTs coated glass surface. b) Color-coded NIR intensity changes of $(GT)_{10}$-SWCNTs at different time points after stimulation of dopamine release with 100 mM KCl. Scale bars = 20 μm. c) Typical intensity change of the sensor layer under a single cell. d) Maximum intensity changes and e) decay time of the maximum intensity changes on $I_{max}/2$ of SWCNTs after KCl stimulation of controls (without cells), untreated cells, and cells treated with different drugs (5 μM for 10 min, $n = 6$ for control, $n \geq 11$ cells for the rest). Note that not for all experiments the value $\tau_{Imax/2}$ could be determined from the time traces, so that $n = 5$ for control, $n \geq 7$ cells for the rest. Statistically significant differences marked with * $p \leq 0.05$, ** $p \leq 0.01$, *** $p \leq 0.001$ (ANOVA and Tukey test). Not significant differences are not indicated.

For bupropion, the extracted values of $\tau_{Imax/2}$ are not significant compared to untreated cells, which is probably due to the fact that not all bupropion (and partially also nomifensine) cell experiments could be used to evaluate $I_{max}/2$, as the signal increase did not drop half of I_{max} within the 10-min experimental duration. In some cases, the maximum signal change was measured several minutes after stimulation (Figure S13, Supporting Information). Amperometric measurements in bovine chromaffin cells treated with 5 μM bupropion also showed significant increases in I_{max} level (≈151%).[62] However, no influence on the release kinetics was observed, as the half-width of an amperometric spike remained unchanged,[62] while nomifensine-treated PC12 cells exhibited prolonged times of dopamine presence in the synaptic cleft.[63]

Overall, these findings demonstrate the effectiveness of using Smart Slides to monitor cellular release processes and their modulation by the addition of neuropharmaceutical drugs. This approach can easily be extended to other targets/biological questions, such as coagulation disorders,[64] diabetes,[47,65] cancer,[66] hydrolytic enzyme activity,[67] or inflammatory markers.[68]

3. Conclusion

In summary, we tailored NIR fluorescent SWCNTs for dopamine detection and optimized the coating of these sensors on surfaces, resulting in functional and highly sensitive Smart Slides. These slides showed the necessary robustness in terms of their long-term stability during storage and in liquids for several weeks, as well as their compatibility with UV light sterilization and cell viability. Furthermore, we demonstrated their applicability in drug testing by directly measuring the effects of dopaminergic compounds on dopamine release. This approach is not limited to the detection of dopamine but can be extended to other targets and biological questions due to the easily customizable surface chemistry of the SWCNTs and the wide range of SWCNT sensors already developed. Overall, the development of these Smart Slides represents a significant advance in the field of cellular analysis by providing a simple tool that can access optically dynamic information about cellular communication and drug effects in a controlled and standardized manner.

4. Experimental Section

Materials: All materials were purchased from Sigma-Aldrich unless specified otherwise.

SWCNT Surface Modification: For surface modification of (6,5) chirality-enriched CoMoCAT-SWCNTs (Sigma-Aldrich, product no. 773 735) with ssDNA, a recently published protocol was used.[58] SWCNTs (100 μL, 2 mg mL^{-1} in PBS (Carl Roth)) were mixed with ssDNA (100 μL, 2 mg mL^{-1} in PBS), followed by tip sonication (ice bath, 10 min at 30% amplitude, Fisherbrand Model 120 Sonic Dismembrator) and centrifugation (2 × 30 min, 16 100 g, 4 °C, Hettich MIKRO 200R) to remove aggregates. The supernatant yielded homogenously dispersed $(GT)_{10}$-SWCNTs,

which were diluted in PBS to the desired SWCNT concentration after determination of SWCNT concentration via absorption measurements (see NIR Spectroscopy).

NIR Spectroscopy: Absorption spectra for the characterization of SWCNT samples were recorded using a JASCO V-780-ST spectrophotometer in the wavelength range of 400 – 1350 nm in 0.5 nm steps in quartz cuvettes (Hellma, 10 mm optical path). SWCNT concentration was calculated based on previous literature.[58,69–71]

Fluorescence spectra in the range between 835 – 1245 nm were recorded with 5 s integration time using a spectrometer (Shamrock 193i, Andor Technology Ltd.) connected to a microscope (IX73, Olympus) equipped with a 20x objective (plan achromat infrared objective LCPLN20XIR) and a 561 nm laser at 100 mW (Gem561, Laser Quantum) for excitation.

Raman Spectroscopy: Raman measurements were carried out using a confocal Raman microscope (inVia InSpect from Renishaw) equipped with a 100x objective and an excitation of 532 nm (25 mW laser power) with an integration time of 10 s.

SWCNT-Coated Surfaces: Glass bottom petri dishes (35 mm, ibidi) were treated with oxygen plasma (Atto B, Diener electronic, 0.6 mbar, 1 min). Directly after plasma cleaning, surfaces were coated with APTES solution (300 µL of 1 wt% APTES/H_2O in ethanol) and incubated for 1 h at room temperature. Subsequently, petri dishes were washed with ethanol, rinsed with H_2O, and then either dried directly with N_2 or baked at 120 °C for 2 h, followed by rinsing again with H_2O and drying with N_2. SWCNT coating was performed by spin coating (Laurell WS-650MZ-8NPP) at 1600 rpm for 60 s. 135 µL of diluted $(GT)_{10}$-SWCNT solution was added directly after starting the rotation. Parameter selection was guided by Card et al.[72] To remove non-immobilized SWCNTs, the surface was rinsed with H_2O and dried with N_2.

Imaging of Single SWCNT Sensor Coatings: For the characterization of SWCNT-coated surfaces and dopamine response measurements, an inverted microscope (Nikon Eclipse Ti2) equipped with a 100× oil immersion objective (CFI Plan Apochromat Lambda D 100× Oil/1.45/0.13) was used. A white LED (CoolLED pE300 Lite, 100% power) was used in combination with a 560 ± 40 nm bandpass filter (AHF analysentechnik F47-561) for the excitation of SWCNTs via the E_{22} transition. Excitation light was eliminated from emission via a dichroic mirror (transmission > 93% at 813.5 nm, AHF analysentechnik F38-801) and an 840 nm long-pass filter (AHF analysentechnik F47-841). Images were taken with a Si camera (Hamamatsu Orca Flash 4.0) with 2048 × 2048 pixels at 1 s integration time.

For dopamine response measurements, a freshly prepared dopamine solution (20 µL of dopamine hydrochloride in 1× PBS) was added to PBS/cell medium (2 mL) in the petri dish after a baseline I_0 was recorded for 30 s. The final dopamine concentration was 100 µM. For characterization of the resulting intensity change $(I-I_0)/I_0$ after dopamine addition, the initial (I_0) and final intensity after dopamine addition (I) were background-corrected (by images without SWCNT coating) and calculated by averaging the respective frames of the recorded video. Note that the SWCNT coating optimization was performed within this standard microscope with an LED and a Si camera for excitation and detection. In the later cell experiments, which were performed in a different setup with a laser and a NIR camera (see Cell Experiments), very low laser powers in the range of 55 and 120 mW were required, which means that the detection should also be possible with "standard" equipment using $(6,4)$-$(GT)_{10}$-SWCNTs for gaining even higher sensitivity.[33]

Homogeneity of SWCNT Coating: To determine the homogeneity of the SWCNT coating at different locations on the slides and for different samples, NIR fluorescence images were acquired at 100× magnification for four samples at seven different locations. The samples were each prepared with the same spin coating parameters. To determine the SWCNT distribution, the brightness of each image was determined and averaged over all images. To determine the areal fraction of clumping on the sample, the Particle Counting Tool from Fiji was used considering particles in a range of 300 – infinity pixel².

Robustness Tests: Storage of $(GT)_{10}$-SWCNT-coated petri dishes was performed after drying the dishes with N_2 either at room temperature in a

dark box or a refrigerator at 4 °C. To test sterilization capabilities, SWCNT-coated petri dishes were either autoclaved at 121 °C and 100% humidity (2 bar) for 20 min (Espec EHS-211 M) or irradiated with 254 nm UV light in a biosafety cabinet (HMC Europe BSC-700IIA2-G) for 15, 30 or 60 min. To test the stability of the SWCNT coating in liquid, SWCNTs were coated on an imaging dish with a glass bottom and an imprinted 50 µm grid (ibidi) to ensure easy imaging of the same SWCNT coated location on different days. Petri dishes were filled with 2 mL of the respective liquid. A lid and sealing with parafilm ensured that evaporation of the liquid was minimized. Cell viability was performed using a Trypan Blue exclusion test adapted from Strober.[73] In short, cultured Neuro-2a cells (for more information, see "Cell Culturing") were transferred to both untreated and SWCNT-coated, UV-sterilized glass-bottom petri dishes ($n = 3$) and were cultivated in Dulbeccos Modified Eagle Medium (DMEM) supplemented with dibutyryl cyclic adenosine monophosphate (dbcAMP, 1 mM) and 0.5% FBS. Cell viability was then determined at different time points (24, 48, and 72 h). For this purpose, the medium was pipetted off and carefully rinsed with PBS and the cells were incubated with PBS (600 µL) containing Trypan Blue (0.2%, Carl Roth) for ≈3 min. Based on brightfield images (Leica THUNDER Imager 3D Cell Culture, four images with 20x objective per dish), the unstained (viable) and stained (nonviable) cells were counted using the Cell Counting Tool from Fiji and the percentage of viable cells to the total number of all cells was calculated.

Cell Culturing: Neuro-2a cells were purchased from DSMZ German Collection of Microorganisms and Cell Cultures (ACC 148) and cultivated according to the supplier's protocol in a humidified 5% CO_2 atmosphere at 37 °C in T-75 flasks (Sarstedt) with a sub-cultivation ratio of 1:4 every 5–7 days. Cells were grown in DMEM (16 mL, Thermo Fisher Scientific) supplemented with FBS (10%), 1x non-essential amino acids, penicillin (100 units mL^{-1}), and streptomycin (100 µg mL^{-1}, Thermo Fisher Scientific). Differentiation of Neuro-2a cells was performed according to Tremblay et al.[74] Prior to experiments (96 h), cells were cultivated in DMEM supplemented with dbcAMP (1 mM) and 0.5% FBS. After three days cells were carefully rinsed with medium from the surface of cultivation flasks and a total number of 75 000 cells was transferred to SWCNT-coated glass surfaces, which had previously been sterilized with 30 min UV exposure, and allowed to adhere for 18 h.

Cell Experiments: The setup used to perform the cell experiments consisted of an inverted microscope (Olympus IX73) equipped with a 100× oil immersion objective (UPlanSApo/1.35/0.13-0.19). A 561 nm laser (Jive 500, Cobolt) at 55 or 120 mW was used for SWCNT excitation. Excitation light was eliminated from emission via a 900 nm long pass filter (Thorlabs FELH0900). The NIR fluorescence was imaged with a NIR camera (Xenics Cheetah-640-TE1 InGaAs camera) at 1 s exposure time. Bright-field images of cells were taken with a Si camera (pco.panda).

For dopamine release experiments, the cell medium was exchanged for PBS (1 mL) supplemented with $MgCl_2$ and $CaCl_2$. To stimulate dopamine release, a KCl solution (34 µL of 3 M) was added after recording a 30 s NIR fluorescence baseline, resulting in a final concentration of 100 mM KCl. Cells and PBS (Carl Roth) were kept at 37 °C before the experiment, assuming a temperature close to 37 °C during the cell experiments.

To assess the impact of dopaminergic substances on dopamine release, 10 min before the start of the cell experiment, the specific substance of interest (levodopa, nomifensine maleate salt (Medchem Express, Fisher Scientific), bupropion hydrochloride (Enzo Life Sciences, Fisher Scientific) diluted in PBS was added to the cell medium (20 µL to 600 µL cell medium), resulting in a concentration of 5 µM. After 10 min of exposure, the cell medium was carefully aspirated and the cells were rinsed twice with PBS. Subsequently, PBS (1 mL) was added to perform the imaging and stimulation with KCl. In control experiments, KCl (100 mM) was added to the Smart Slides containing PBS (1 mL) without cultured cells.

Data Processing and Statistical Analysis: Fiji was used for image data processing and OriginPro for statistical analysis. To determine the intensity changes of SWCNT fluorescence after dopamine addition or in the cell experiments after KCl addition, the average intensity of the whole image/the cell area was selected for analysis in each case. The first 30 frames, which served to record the baseline I_0, were averaged and the resulting time-dependent signal change $(I-I_0)/I_0$ was calculated. When averaging

multiple experiments, sample size and type of error bar could be taken from the corresponding figure caption in each case. In the cell experiments the signal change was smoothed (OriginPro, Wavelet DB6). From these spectra, the maximum signal change I_{max}, the decay time $\tau_{Imax/2}$, and the time difference between stimulation and maximum signal change $\tau_{\Delta I\_max}$ were extracted. A one-way analysis of variance (ANOVA) was conducted to examine statistically significant differences among the various treated cell groups, using a significance level of 0.05. Post-hoc comparisons of mean values were performed using the Tukey test.

Supporting Information

Supporting Information is available from the Wiley Online Library or from the author.

Acknowledgements

Conflict of Interest

The authors declare no conflicts of interest.

Data Availability Statement

The data that support the findings of this study are available from the corresponding author upon reasonable request.

Keywords

[1] M. Schieber, N. S. Chandel, *Curr. Biol.* **2014**, *24*, R453.
[2] T. B. Kornberg, S. Roy, *Trends Cell Biol.* **2014**, *24*, 370.
[3] W. Wong, *Sci Signal* **2009**, *2*, eg14.
[4] J. Kieninger, A. Weltin, H. Flamm, G. A. Urban, *Lab Chip* **2018**, *18*, 1274.
[5] R. I. Teleanu, A. G. Niculescu, E. Roza, O. Vlâdâcenco, A. M. Grumezescu, D. M. Teleanu, *Int. J. Mol. Sci.* **2022**, *23*, 5954.
[6] M. Conrad, S. M. Lorenz, B. Proneth, *Trends Mol. Med.* **2021**, *27*, 113.
[7] L. Yu, L. Feng, Z. Wei, S. Wang, Y. Feng, J. Shen, J. Cai, J. Wu, Y. Xiao, *Adv. Funct. Mater.* **2023**, *33*, 2300309.
[8] B. Si, E. Song, *Chemosensors* **2018**, *6*, 1.
[9] C. Cheng, S. Li, A. Thomas, N. A. Kotov, R. Haag, *Chem. Rev.* **2017**, *117*, 1826.

[10] R. M. Williams, S. Chen, R. E. Langenbacher, T. V. Galassi, J. D. Harvey, P. V. Jena, J. Budhathoki-Uprety, M. Luo, D. A. Heller, *Nat. Chem. Biol.* **2021**, *17*, 129.
[11] J. Ackermann, J. T. Metternich, S. Herbertz, S. Kruss, *Angew Chem Int Ed Engl* **2022**, *61*, e202112372.
[12] M. J. O'Connell, S. M. Bachilo, C. B. Huffman, V. C. Moore, M. S. Strano, E. H. Haroz, K. L. Rialon, P. J. Boul, W. H. Noon, C. Kittrell, J. Ma, R. H. Hauge, R. B. Weisman, R. E. Smalley, *Science* **2002**, *297*, 593.
[13] G. Hong, A. L. Antaris, H. Dai, *Nat. Biomed. Eng.* **2017**, *1*, 0010.
[14] L. Dai, Y. Xue, L. Qu, H. J. Choi, J. B. Baek, *Chem. Rev.* **2015**, *115*, 4823.
[15] L. Cognet, D. A. Tsyboulski, J.-D. R. Rocha, C. D. Doyle, J. M. Tour, R. B. Weisman, *Science* **2007**, *316*, 1465.
[16] J. Zhang, A. A. Boghossian, P. W. Barone, A. Rwei, J.-H.o Kim, D. Lin, D. A. Heller, A. J. Hilmer, N. Nair, N. F. Reuel, M. S. Strano, *J. Am. Chem. Soc.* **2011**, *133*, 567.
[17] S. Kruss, D. P. Salem, L. Vukovic, B. Lima, E. Vander Ende, E. S. Boyden, M. S. Strano, *Proc Natl Acad Sci U S A* **2017**, *114*, 1789.
[18] H. Wu, R. Nißler, V. Morris, N. Herrmann, P. Hu, S.-J.i Jeon, S. Kruss, J. P. Giraldo, *Nano Lett.* **2020**, *20*, 2432.
[19] T. T. S. Lew, V. B. Koman, K. S. Silmore, J. S. Seo, P. Gordiichuk, S. Y. Kwak, M. Park, M. C.-Y.i Ang, D. T. Khong, M. A. Lee, M. B. Chan-Park, N. H. Chua, M. S. Strano, *Nat Plants* **2020**, *6*, 404.
[20] R. Nißler, A. T. Müller, F. Dohrman, L. Kurth, H. Li, E. G. Cosio, B. S. Flavel, J. P. Giraldo, A. Mithöfer, S. Kruss, *Angew Chem Int Ed. Engl* **2022**, *61*, e202108373.
[21] G. Bisker, J. Dong, H. D. Park, N. M. Iverson, J. Ahn, J. T. Nelson, M. P. Landry, S. Kruss, M. S. Strano, *Nat. Commun.* **2016**, *7*, 10241.
[22] J. T. Metternich, J. A. C. Wartmann, L. Sistemich, R. Nißler, S. Herbertz, S. Kruss, *J. Am. Chem. Soc.* **2023**, *145*, 14776.
[23] M. Kim, C. Chen, P. Wang, J. J. Mulvey, Y. Yang, C. Wun, M. Antman-Passig, H. B. Luo, S. Cho, K. Long-Roche, L. V. Ramanathan, A. Jagota, M. Zheng, Y. Wang, D. A. Heller, *Nat. Biomed. Eng.* **2022**, *6*, 267.
[24] R. Nißler, O. Bader, M. Dohmen, S. G. Walter, C. Noll, G. Selvaggio, U. Groß, S. Kruss, *Nat. Commun.* **2020**, *11*, 5995.
[25] S. Kruss, M. P. Landry, E. Vander Ende, B. M. A. Lima, N. F. Reuel, J. Zhang, J. Nelson, B. Mu, A. Hilmer, M. Strano, *J. Am. Chem. Soc.* **2014**, *136*, 713.
[26] M. Dinarvand, E. Neubert, D. Meyer, G. Selvaggio, F. A. Mann, L. Erpenbeck, S. Kruss, *Nano Lett.* **2019**, *19*, 6604.
[27] S. Jeong, D. Yang, A. G. Beyene, J. T. Del Bonis-O'donnell, A. M. M. Gest, N. Navarro, X. Sun, M. P. Landry, *Sci. Adv.* **2019**, *5*, eaay3771.
[28] K. Huth, M. Glaeske, K. Achazi, G. Gordeev, S. Kumar, R. Arenal, S. K. Sharma, M. Adeli, A. Setaro, S. Reich, R. Haag, *Small* **2018**, *14*, 1800796.
[29] A. Nadeem, A. Kindopp, I. Wyllie, L. Hubert, J. Joubert, S. Lucente, E. Randall, P. V. Jena, D. Roxbury, *Nano Lett.* **2023**, *23*, 6588.
[30] A. G. Beyene, K. Delevich, J. T. Del Bonis-O'donnell, D. J. Piekarski, W. C. Lin, A. W. Thomas, S. J. Yang, P. Kosillo, D. Yang, G. S. Prounis, L. Wilbrecht, M. P. Landry, *Sci. Adv.* **2019**, *5*, eaaw3108.
[31] S. Elizarova, A. A. Chouaib, A. Shaib, B. Hill, F. Mann, N. Brose, S. Kruss, J. A. Daniel, *Proc Natl Acad Sci U S A* **2022**, *119*, 2202842119.
[32] C. Bulumulla, A. T. Krasley, B. Cristofori-Armstrong, W. C. Valinsky, D. Walpita, D. Ackerman, D. E. Clapham, A. G. Beyene, *elife* **2022**, *11*, e78773.
[33] J. Ackermann, J. Stegemann, T. Smola, E. Reger, S. Jung, A. Schmitz, S. Herbertz, L. Erpenbeck, K. Seidl, S. Kruss, *Small* **2023**, *19*, e2206856.
[34] L. Sistemich, P. Galonska, J. Stegemann, J. Ackermann, S. Kruss, *Angew Chem Int Ed Engl* **2023**, *62*, e202300682.
[35] C. Paviolo, J. S. Ferreira, A. Lee, D. Hunter, I. Calaresu, S. Nandi, L. Groc, L. Cognet, *Nano Lett.* **2022**, *22*, 6849.

**ADVANCED
SCIENCE NEWS**

**ADVANCED
FUNCTIONAL
MATERIALS**

[36] J. A. Stapleton, E. M. Hofferber, J. Meier, I. A. Ramirez, N. M. Iverson, *ACS Appl. Nano Mater.* **2021**, *4*, 33.

[37] M. Zheng, A. Jagota, E. D. Semke, B. A. Diner, R. S. Mclean, S. R. Lustig, R. E. Richardson, N. G. Tassi, *Nat. Mater.* **2003**, *2*, 338.

[38] F. Mann, N. Herrmann, D. Meyer, S. Kruss, *Sensors* **2017**, *17*, 1521.

[39] M. S. Dresselhaus, G. Dresselhaus, R. Saito, A. Jorio, *Phys Rep* **2005**, *409*, 47.

[40] R. Nißler, L. Kurth, H. Li, A. Spreinat, I. Kuhlemann, B. S. Flavel, S. Kruss, *Anal. Chem.* **2021**, *93*, 6446.

[41] X. Wei, T. Tanaka, S. Li, M. Tsuzuki, G. Wang, Z. Yao, L. Li, Y. Yomogida, A. Hirano, H. Liu, H. Kataura, *Nano Lett.* **2020**, *20*, 410.

[42] A. V. Naumov, D. A. Tsyboulski, S. M. Bachilo, R. B. Weisman, *Chem. Phys.* **2013**, *422*, 255.

[43] R. P. Rastogi, Richa, A. Kumar, M. B. Tyagi, R. P. Sinha, *J. Nucleic Acids* **2010**, *2010*, 592980.

[44] Sigma-Aldrich, Oligonucleotide Handling & Stability, https://www.sigmaaldrich.com/DE/en/technical-documents/protocol/genomics/dna-and-rna-purification/oligonucleotide-handling-and-stability, (accessed: October 2023).

[45] V. Caratelli, S. Fillo, N. D'amore, O. Rossetto, M. Pirazzini, M. Moccia, C. Avitabile, D. Moscone, F. Lista, F. Arduini, *Biosens. Bioelectron.* **2021**, *183*, 113210.

[46] M. R. Dunn, R. M. Jimenez, J. C. Chaput, *Nat Rev Chem* **2017**, *1*, 76.

[47] R. Ehrlich, A. Hendler-Neumark, V. Wulf, D. Amir, G. Bisker, *Small* **2021**, *17*, e2101660.

[48] F. Albertorio, M. E. Hughes, J. A. Golovchenko, D. Branton, *Nanotechnol* **2009**, *20*, 395101.

[49] M. Sypabekova, A. Hagemann, D. Rho, S. Kim, *Biosensors* **2022**, *13*, 36.

[50] P. Galonska, J. M. Mohr, C. A. Schrage, L. Schnitzler, S. Kruss, *J. Phys. Chem. Lett.* **2023**, *14*, 3483.

[51] S. Yang, Z. Xu, S. Xue, P. Kandlakunta, L. Cao, J. Huang, *Adv. Mater.* **2019**, *31*, 1805547.

[52] U. S. EPA, *Evaluation of the Inhalation Carcinogenicity of Ethylene Oxide (Final Report)*, U.S. Environmental Protection Agency, Washington, DC, EPA/635/R-16/350F **2016**.

[53] H. N. Lynch, J. S. Kozal, A. J. Russell, W. J. Thompson, H. R. Divis, R. D. Freid, E. J. Calabrese, K. A. Mundt, *Chem Biol Interact* **2022**, *364*, 110031.

[54] R. L. Pinals, D. Yang, D. J. Rosenberg, T. Chaudhary, A. R. Crothers, A. T. Iavarone, M. Hammel, M. P. Landry, *Angew Chem Int Ed Engl* **2020**, *59*, 23668.

[55] K. A. White, B. N. Kim, *Nat. Commun.* **2021**, *12*, 431.

[56] R. H. S. Westerink, A. De Groot, H. P. M. Vijverberg, *Biochem. Biophys. Res. Commun.* **2000**, *270*, 625.

[57] D. Meyer, A. Hagemann, S. Kruss, *ACS Nano* **2017**, *11*, 4017.

[58] G. Chaturvedi, A. Kaur, S. K. Kansal, *J. Phys. Chem. C* **2019**, *123*, 16857.

[59] A. J. Gillen, J. Kupis-Rozmyslowicz, C. Gigli, N. Schuergers, A. A. Boghossian, *J. Phys. Chem. Lett.* **2018**, *9*, 4336.

[60] E. Pothos, M. Desmond, D. Sulzer, *J. Neurochem.* **1996**, *66*, 629.

[61] K. D. Kozminski, D. A. Gutman, V. Davila, D. Sulzer, A. G. Ewing, *Anal. Chem.* **1998**, *70*, 3123.

[62] M. Huang, S. S. Rathore, M. Lindau, *J. Neurochem.* **2019**, *151*, 38.

[63] H. F. Cui, J. S. Ye, Y.u Chen, S. C. Chong, F. S. Sheu, *Anal. Chem.* **2006**, *78*, 6347.

[64] E. Gerstman, A. Hendler-Neumark, V. Wulf, G. Bisker, *ACS Appl. Mater. Interfaces* **2023**, *15*, 21866.

[65] V. Zubkovs, H. Wang, N. Schuergers, A. Weninger, A. Glieder, S. Cattaneo, A. A. Boghossian, *Nanoscale Adv* **2022**, *4*, 2420.

[66] R. M. Williams, C. Lee, D. A. Heller, *ACS Sens.* **2018**, *3*, 1838.

[67] N. E. Kallmyer, M. S. Abdennadher, S. Agarwal, R. Baldwin-Kordick, R. L. Khor, A. S. Kooistra, E. Peterson, M. D. Mcdaniel, N. F. Reuel, *Anal. Chem.* **2021**, *93*, 4800.

[68] P. Gaikwad, N. Rahman, R. Parikh, J. Crespo, Z. Cohen, R. Williams, *Optical Nanosensor Passivation Enables Highly Sensitive Detection of the Inflammatory Cytokine Il-6*, bioRxiv **2023**.

[69] S. R. Sanchez, S. M. Bachilo, Y. Kadria-Vili, C. W. Lin, R. B. Weisman, *Nano Lett.* **2016**, *16*, 6903.

[70] F. Schöppler, C. Mann, T. C. Hain, F. M. Neubauer, G. Privitera, F. Bonaccorso, D. Chu, A. C. Ferrari, T. Hertel, *J. Phys. Chem. C* **2011**, *115*, 14682.

[71] J. K. Streit, S. M. Bachilo, S. Ghosh, C. W. Lin, R. B. Weisman, *Nano Lett.* **2014**, *14*, 1530.

[72] M. Card, M. Gravely, S. Z. M. Madani, D. Roxbury, *ACS Appl. Mater. Interfaces* **2021**, *13*, 31986.

[73] W. Strober, *Curr. Protoc. Immunol.* **2015**, *111*, A3.B.1.

[74] R. G. Tremblay, M. Sikorska, J. K. Sandhu, P. Lanthier, M. Ribecco-Lutkiewicz, M. Bani-Yaghoub, *J Neurosci Methods* **2010**, *186*, 60.

**ADVANCED
FUNCTIONAL
MATERIALS**

Supporting Information

Smart Slides for Optical Monitoring of Cellular Processes

Julia Ackermann, Eline Reger, Sebastian Jung, Jennifer Mohr, Svenja Herbertz, Karsten Seidl and Sebastian Kruss*

Supporting Information

Smart Slides for Optical Monitoring of Cellular Processes

Julia Ackermann, Eline Reger, Sebastian Jung, Jennifer Mohr, Svenja Herbertz, Karsten Seidl, Sebastian Kruss*
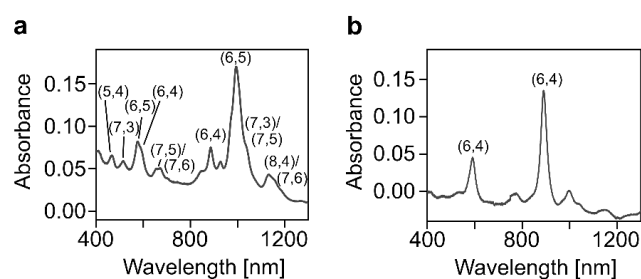
Figure S1. Absorbance spectra of SWCNTs. *a) (GT)$_{10}$-CoMoCAT-SWCNTs, b) (GT)$_{10}$-(6,4)-SWCNTs with assigned chiralities.*
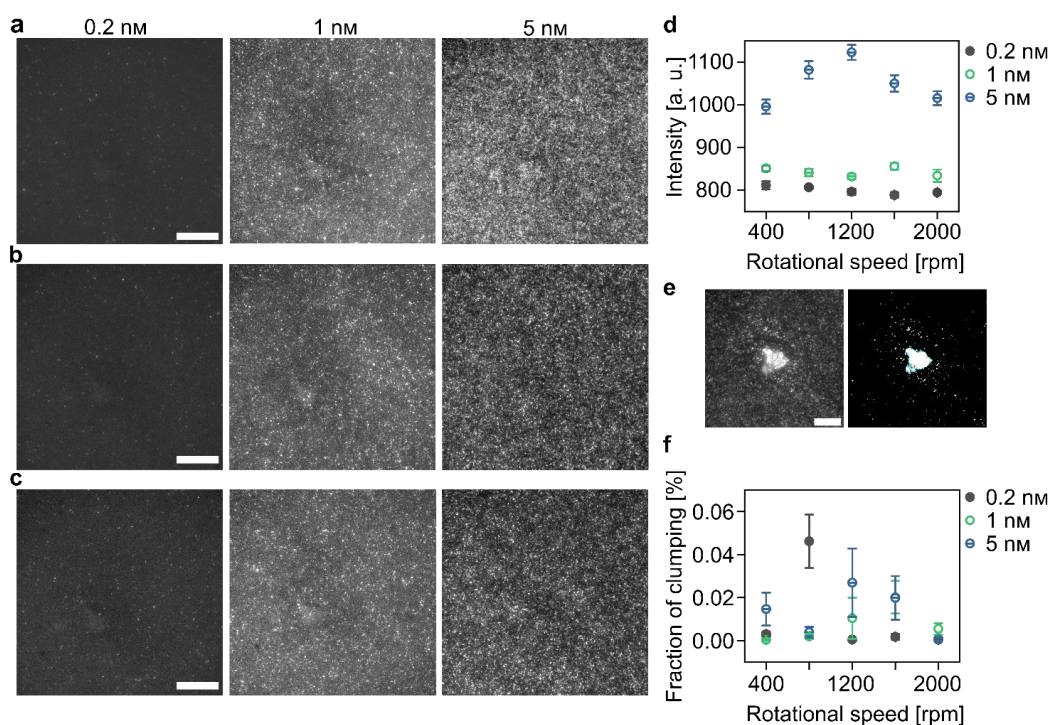
Figure S2. NIR fluorescence images of (GT)$_{10}$-SWCNT coatings. *Prepared by spin coating at a) 400 rpm, b) 1200 rpm and c) 2000 rpm with different SWCNT suspension concentrations. Scale bars = 20 µm. d) SWCNT fluorescence intensity of (GT)$_{10}$-SWCNT coatings of different concentrations as a function of the rotational speed used for spin coating (mean ± SE, n=28). e) Example of clumping determination using NIR fluorescence images of SWCNT coating following by thresholding and particle counting. Scale bar = 10 µm. f) Area*

fraction of clumping of the SWCNT coating in relation to the total coated area as a function of the rotational speed of spin coating (mean ± SE, n=28).
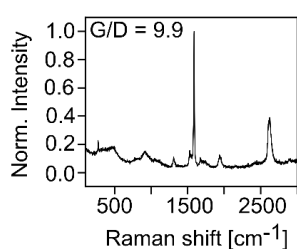
Figure S3. Raman spectrum of a (GT)_{10}-SWCNT coated surface. *The G/D ratio indicates a low defect level in the SWCNTs.*
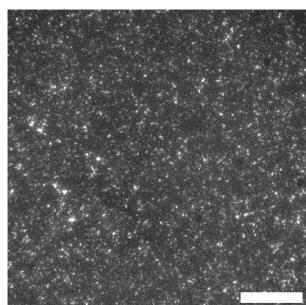
Figure S4. NIR image of spin coated (GT)_{10}-(6,4)-SWCNTs. *135 µl of a 0.1 nM SWCNT solution was spin coated six times in succession at 1600 rpm to obtain a dense coating. Scale bar = 20 µm.*
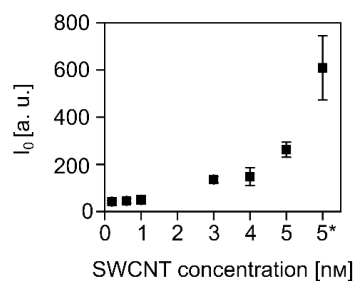
Figure S5. Intensity calibration curve. *Initial SWCNT fluorescence intensity I_0 of (GT)_{10}-SWCNT coatings in PBS as a function of the SWCNT concentration used for spin coating. Note 5* represents manual coating of 5 нм SWCNTs without spin coating (mean ± SD, n>30).*
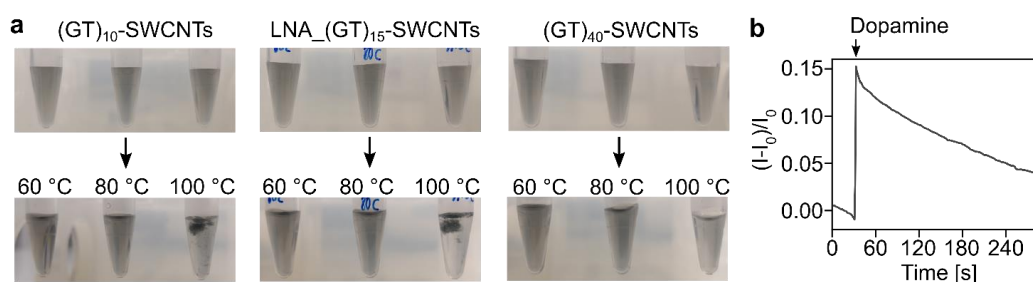
Figure S6. Heating of ssDNA-SWCNTs. *a) Images of different ssDNA-SWCNT suspensions ((GT)$_{10}$-, locked nucleic acid (LNA) (GT)$_{15}$- and (GT)$_{40}$-SWCNTs) before and after heating (60°C, 80°C, 100°C for 30 min). With the exception of (GT)$_{40}$-SWCNTs, ssDNA-SWCNTs precipitate when heated to 100°C. b) Immobilized (GT)$_{10}$-SWCNTs remain functional to detect 100 μM dopamine after heating to 100°C for 30 min.*
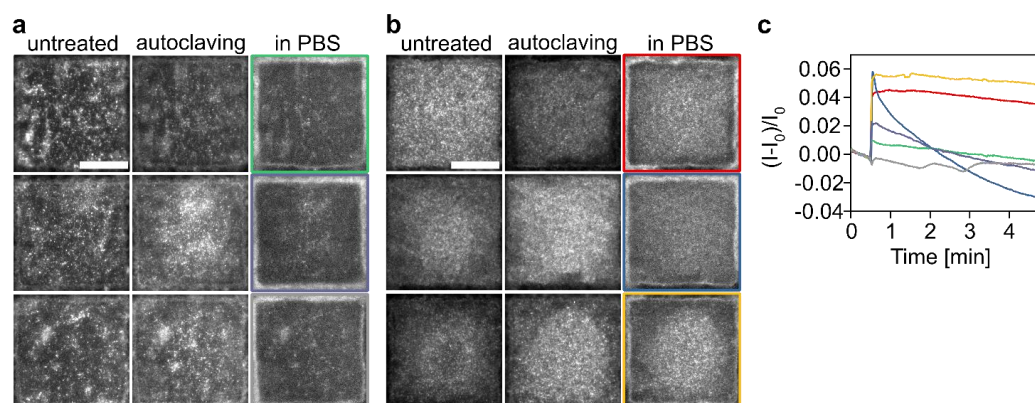
Figure S7. Autoclaving of immobilized ssDNA-SWCNTs. *Images of immobilized (GT)$_{10}$-SWCNTs before (untreated) and after autoclaving (121°C, 20 min) and in PBS. APTES coated surface a) rinsed with ethanol and water, b) additionally heated for 2 h at 120 °C before SWCNTs coating. c) 100 μM dopamine detection with these SWCNT coatings (assignment via respective colors). Scale bars = 20 μm.*
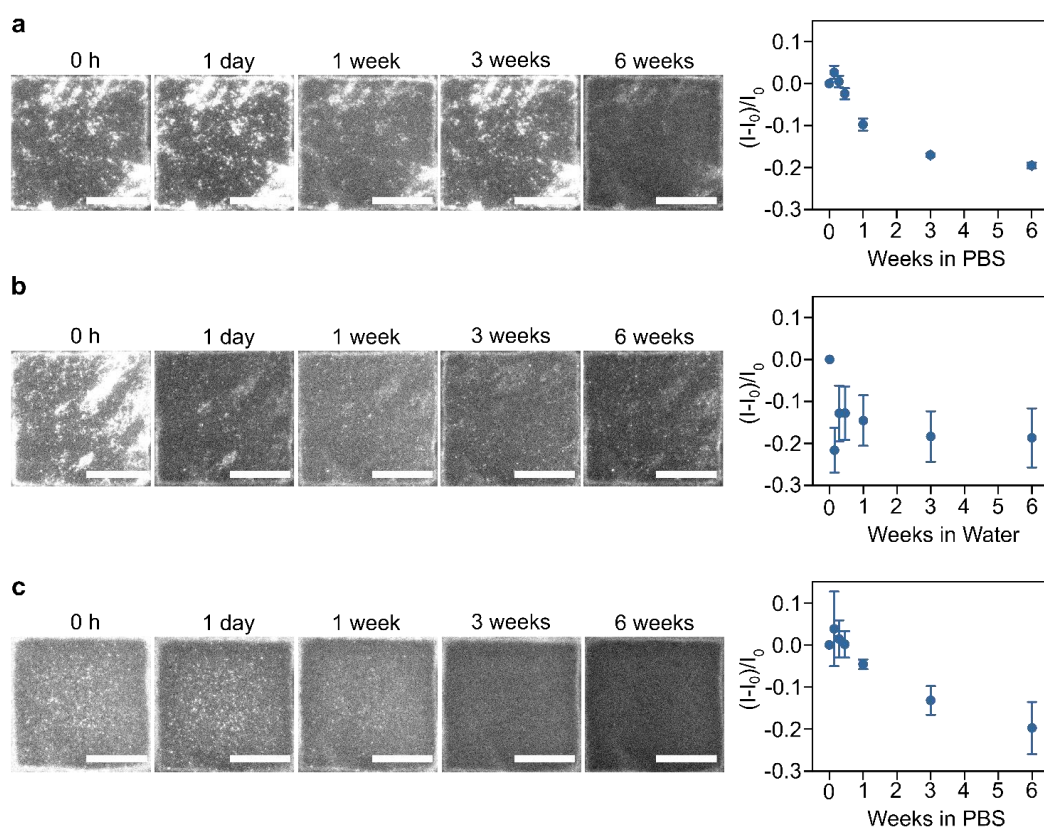
Figure S8. Stability of immobilized ssDNA-SWCNTs in liquid. *NIR Images and intensity changes of the same position on 1% APTES-treated glass surfaces at different time points. a) In PBS, b) in water, c) in PBS with APTES-treated glass surfaces preheated for 2 h at 120°C (mean ± SE, n = 3). All scale bars = 20 μm.*
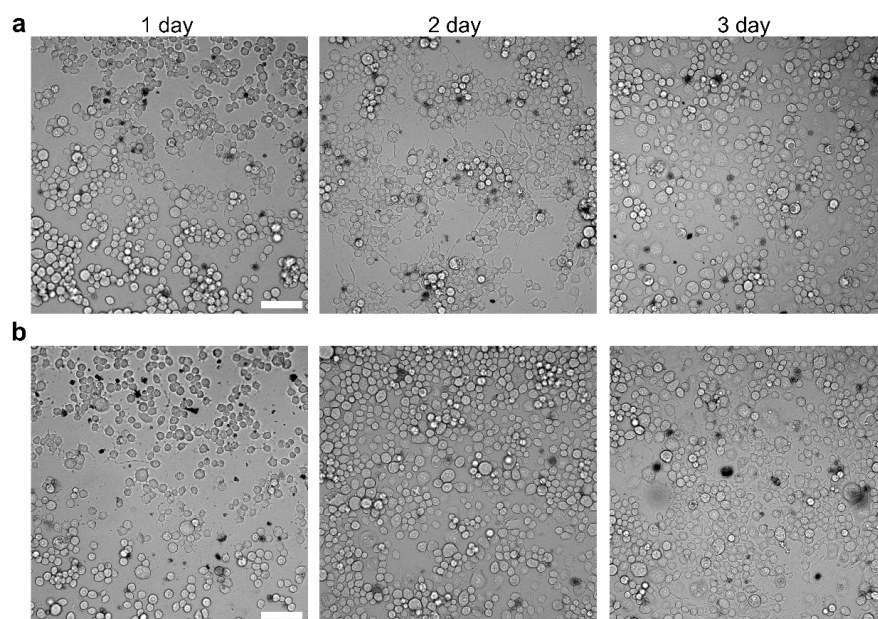
Figure S9. Bright field image of Neuro2a cells in differentiation medium at different time points after Trypan Blue staining a) on untreated glass, b) on SWCNT coating. *Scale bars = 100 µm.*
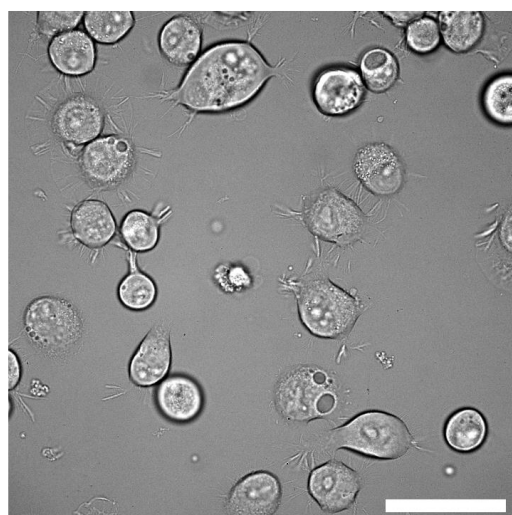
Figure S10. Bright field image of differentiated Neuro2a cells adhering to the (GT)$_{10}$-SWCNT sensor coating shortly before performing the dopamine-release experiments. *Scale bar = 50 µm.*
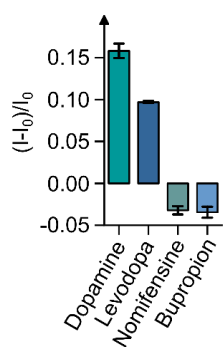
Figure S11. Sensor response of (GT)$_{10}$-SWCNTs in solution. *After addition of 5 μм dopamine in comparison to the tested dopaminergic substances (levodopa, nomifensine, and bupropion, mean ± SE, n=3).*
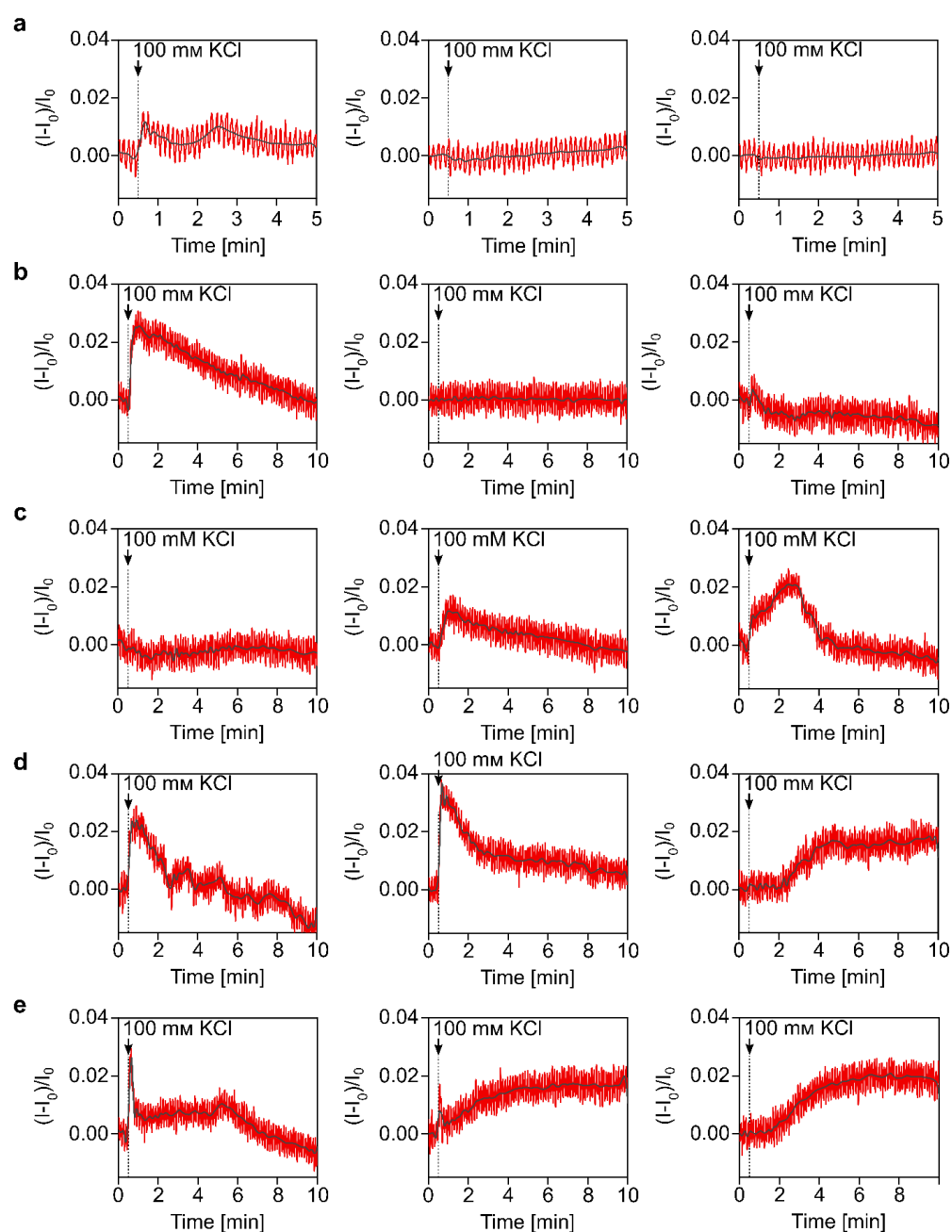
Figure S12. Mean SWCNT intensity change of different experiments. *During addition of 100 mм KCl a) without cells (control), b) with untreated cells and c) after addition of 5 μм levodopa, d) nomifensine, and e) bupropion.*
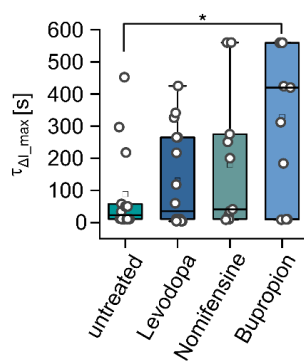
Figure S13. *Box plot of the time difference between stimulation and maximum signal change I_{max} of untreated cells and cells treated with different drugs (5 µм for 10 min, n=5 for control, n≥11 cells for the rest. Statistically significant differences marked with * p≤0.05 (ANOVA and Tukey test). Not significant differences are not indicated.*

3.2.2 Publication Synopsis

Research Manuscript II presented the development of Smart Slides for the improved optical monitoring of biochemical cell responses. The objectives of the study were to integrate fluorescent SWCNT sensors into cell culture materials, optimize their coating for homogeneity and sensitivity (part 1), characterize their robustness (part 2), and demonstrate their usability in measuring altered dopaminergic cell responses after the addition of different psychotropic substances (part 3).

In the first part, dopamine-sensitive SWCNT sensors were fabricated by functionalizing CoMoCAT-SWCNTs with $(GT)_{10}$-ssDNA. The coating of glass substrates was optimized using spin coating at varying parameters. The most homogeneous results were obtained at 1600 rpm for all SWCNT concentrations tested. Additionally, it was tested whether chirality-pure $(GT)_{10}$-(6,4)-SWCNTs, which show stronger tendencies to aggregate due to their purity, also allow homogeneous coatings. Due to a low concentration of 0.1 nM, these SWCNT were coated in six consecutive cycles, which also produced good results. $(GT)_{10}$-CoMoCAT-SWCNT coatings were optimized in terms of sensitivity for dopamine detection due to their higher concentration and faster processing. However, the process should also be transferable to $(GT)_{10}$-(6,4)-SWCNTs. For sensitivity determination, different dense coatings were produced and their maximum signal response after dopamine addition was determined. The signal response was plotted against the starting intensity I_0 of the sensor coating before dopamine addition, which showed a Gaussian-like behavior with an optimum response at an intensity I_0 of 175 a.u. A simple model was set up to describe this behavior, which assumes that the sensor response firstly linearly increases with increasing SWCNT concentration (I_0), due to the increasing probability of interaction between dopamine and the SWCNT sensors. A further increase in SWCNT concentration (I_0) leads to a decrease in sensor response after a certain point due to an increasing number of unoccupied SWCNT binding sites. A calibration curve was established to relate fluorescence start intensity to SWCNT concentration, indicating reproducibility even among differently prepared samples due to low error bars of different coated samples.

After optimization of the coating, the second part of the paper focused on the robustness of the Smart Slides. The sensor coatings remained functional after 10 weeks of storage in the refrigerator, with a slight increase in sensor response over time. As a pre-test for autoclaving, both SWCNT sensors in solution and immobilized on a surface were heated to temperatures up to 100 °C. SWCNT sensors in solution were unstable and precipitated, except for sensors functionalized with a long ssDNA sequence ($(GT)_{40}$-SWCNTs). In contrast, immobilized sensors retained their sensitivity for dopamine detection. Sterilization tests using UV light (254 nm) or autoclaving were conducted, with autoclaving resulting in

detachment of SWCNTs most likely due to desorption of noncovalently attached APTES molecules. To enhance adhesion, a baking step was introduced after APTES coating, leading to improved stability against autoclaving. Functionality for dopamine detection was preserved with about 50 % reduced sensitivity. UV light sterilization had minimal impact on sensor functionality. Stability tests in liquid showed a signal reduction of about 20 % after 6 weeks in PBS. The sensitivity of the sensors for dopamine detection in cell medium showed a reduced sensitivity by about one-third, which can be prevented by the exchange of medium to PBS shortly before the start of the cell experiments.

In the third part, the Smart Slides were applied to measure altered dopaminergic cell responses after the addition of different psychotropic substances using Neuro-2a cells. Tested substances were L-DOPA, which is the precursor of dopamine and is commonly used in Parkinson's disease patients to increase dopamine levels, and nomifensine and bupropion, which are dopamine-norepinephrine-reuptake inhibitors and are typically used in antidepression therapy. Dopamine release experiments were conducted by stimulating cells with 100 mM KCl, and spatial and temporal changes in SWCNT fluorescence were measured. Analysis of cell responses revealed significant differences between untreated cells and those treated with L-DOPA, nomifensine, and bupropion. Compared with untreated cells, cells with L-DOPA showed increased signal changes on average, whereas experiments with nomifensine and bupropion showed both increased and prolonged signaling, each within expectations. The experiments demonstrated the effectiveness of Smart Slides for monitoring cellular processes and drug effectiveness testing.

In conclusion, an optimized sensor coating in terms of homogeneity and sensitivity has been developed. The Smart Slides showed the necessary robustness required for cellular assays and demonstrated their use for life science applications such as drug development. Due to the modular surface chemistry of SWCNTs, the dopamine-sensitive coating can easily be extended to other targets. Overall, Smart Slides offer a simple, non-invasive, and ready-to-use tool for obtaining dynamic optical information about cells.

In a Nutshell

✓ Smart Slides support cell adhesion and optically report biochemical changes

✓ Optimized sensor density for reproducible and sensitive measurements

✓ High robustness necessary for wide-spread use in labware and biological assays

✓ Measurement of altered dopaminergic cell reactions in drug testing

✓ Extension to other targets of interest possible

Chapter 4

Discussion and Outlook

This chapter places the major findings of the two research manuscripts in Chapters 3.1.1 and 3.2.1 in the context of the current state of the literature and describes their implications for new research opportunities. Possible solutions to overcome existing challenges are addressed. Finally, a short summary and outlook will be provided.

4.1 Implications of Research Manuscript I and Existing Challenges

4.1.1 (6,4)-SWCNT Extraction and Conversion to Sensors

The optimized separation protocol for the extraction of (6,4)-SWCNTs in Research Manuscript I enables for the first time a very fast, simple, and inexpensive extraction of this SWCNT chirality at high purity (> 95 %), which requires minimal equipment (ultrasonic instrument and centrifuge). Previous approaches for (6,4)-SWCNT separation relied on expensive/elaborate chromatography (with purities in the range of 46 % - 76 %) [Liu11, Liu13, Yom20] and DGU (99 % purity) [Ant15] as well as on two-step ATPE (purity not determined) [Li 19b]. By reducing the ATPE to a single step, the protocol in this work is even less prone to execution errors and thus reproducible and highly scalable (limited by admissible centrifuge volume or time). It enables other research groups easy access to this chirality, and moreover, to a variety of possible experimental studies in which they can use their standard optical equipment to measure the NIR fluorescence of these SWCNTs or sensors. The interest in one-step methods is also demonstrated by the existence of other recently published one-step ATPE methods for (6,5)-SWCNTs [Pod20], but also for (6,4)-SWCNTs [Pod23]. The latter appeared after the publication of Research Manuscript I and emphasizes the great interest in this particular SWCNT chirality.

In Research Manuscript I, the yield of extracted (6,4)-SWCNTs was increased from 5.1 % to 7.4 % by reducing the separation from a two-step to a one-step procedure. This yield may seem low; however, only low amounts are required for optical SWCNT sensors. Further progress in SWCNT synthesis will also yield commercially available syntheses with enriched (6,4)-SWCNTs, where current research results allow a preferential enrichment of 57 % [Xu 17]. This will then also increase the absolute extracted amount of SWCNTs in ATPE. In addition, little is known in the literature about yields of other phase separations. The recently published alternative protocol for the extraction of (6,4)-SWCNTs uses non-ionic surfactants in addition to the anionic surfactants that were also used in Research Manuscript I, but did not provide information on extraction yields or defined purity [Pod23]. A comparison of the two methods would therefore be useful. In the procedure developed here, the 7.4 % chirality-pure SWCNTs were in the lower dextran phase. The substantial remaining (6,4)-SWCNT portion was in the upper PEG phase along with the remaining SWCNT chiralities and in an intermediate layer between the phases (known as interfacial trapping), and thus not accessible for extraction. It is known that additional separation steps lead to stronger interfacial trapping, making the reduction of separation steps beneficial [Sub14, Li 19b]. However, further parameter tuning as well as a detailed understanding of the interfacial losses would be beneficial for further increases in the extraction yield. The ATPE is a very sensitive technique driven by the competitive interactions of the various surfactants and other modulators between the two phases, and even slight variations can alter the experimental outcome. For example, previous studies on ATPE have demonstrated that adjusting the molecular weights of the polymers PEG and dextran, responsible for forming the immiscible phases, can influence interfacial trapping, so a closer investigation in this direction could be targeted [Lyu19, Sim22].

Research Manuscript I reports for the first time a sensor application using monochiral (6,4)-SWCNTs. Why this has not been shown before could be due to the fact that a straightforward protocol for extracting this SWCNT chirality, but also a simple functionalization exchange process for arbitrary design of SWCNT-based sensing has long been lacking. Indeed, separation processes such as DGU or ATPE are based on the need to functionalize the SWCNTs first to make them water soluble, so the functionalization is already predetermined. Surfactants are not very suitable for a specific sensor design due to the dense micelle-like coating of SWCNTs, but there are also some ATPE protocols based on SWCNTs functionalized with ssDNA [Lyu19, Pod21]. However, this then also limits the sensor application, and parameter adjustment of the ATPE for another ssDNA sequence is laborious. Furthermore, this ATPE method is based on a high ssDNA consumption, since also all unwanted, sorted-out SWCNTs are functionalized with this ssDNA sequence. However, there are now established exchange procedures that allow the

functionalization of surfactants to any ssDNA sequences to be exchanged by dialysis or a methanol-assisted method [Str17]. Thus, with the addition of the simple protocol for the separation of surfactant-dispersed (6,4)-SWCNTs, the process chain for the variable fabrication of (6,4)-SWCNT-based sensors accessible with normal microscopes is now complete.

Nevertheless, there were two issues observed during the process steps after the separation of (6,4)-SWCNTs to ssDNA-SWCNTs that were not discussed in Research Manuscript I. First, (6,4)-SWCNTs partially precipitated during dialysis in the surfactant 1 % sodium deoxycholate (DOC), the purpose of which was to remove polymer residues and other surfactants surrounding the (6,4)-SWCNTs from the ATPE. The precipitation of the SWCNTs indicates instability of the (6,4)-SWCNTs and thus insufficient micelle formation of DOC molecules around the SWCNTs. Secondly, the exchange yield of DOC-(6,4)-SWCNTs subsequently functionalized with ssDNA was low as well as these monochiral ssDNA-SWCNTs showed a high tendency to aggregate after ssDNA functionalization.

In the ATPE protocol according to Research Manuscript I, sodium hypochlorite (NaClO), which acts as an oxidant for SWCNTs, is used to separate the (6,4)-SWCNTs from metallic SWCNTs. Redox reactions cause electron transfer between the SWCNTs and exogenous redox molecules, which can induce a reorganization of the surfactant shell surrounding the SWCNTs and thus affect the binding affinity of the SWCNTs with the surfactant [Gui15]. According to the observations of Gui *et al.*, less stable dispersions are possible under oxidative conditions, so the addition of a reducing agent such as sodium borohydride (NaBH$_4$) after the ATPE of the (6,4)-SWCNTs and before dialysis for exchange to 1 % DOC-(6,4)-SWCNTs could potentially increase the stability of the SWCNT dispersion [Gui15].

Regarding the subsequent exchange of DOC-(6,4)-SWCNTs to ssDNA-SWCNTs, optimizations could also still take place, since the high exchange rates of over 90 % reported in the literature [Str17] are partly sequence-specific and in practice lower yields occur with monochiral SWCNTs presumably due to the strong tendency towards aggregation [Nis21]. This is presumably due to stronger hydrophobic interactions between monochiral SWCNTs due to the absence of impurities such as catalyst residues from synthesis as well as amorphous carbon [Nis21]. In addition to the specific ssDNA sequence used, the kinetics with which the desorption of the first functionalization and the adsorption of the second functionalization takes place plays a crucial role in the effectiveness of the exchange process [Yan20b]. The use of polymer matrices as crowding agents for the reduction of aggregation can aim to enhance the exchange yields within these processes [Str17].

The other challenge is the low stability of monochiral SWCNTs after functionalization in solution. In Research Manuscript I, this issue was bypassed by immobilizing SWCNTs directly onto surfaces. However, for easier handling and for sensor applications where immobilization is not necessary or desired, addressing this stability issue in solution is important for sensor advancements in this field. As mentioned before for the exchange process, the specific ssDNA sequence has been shown to influence the (long-term) stability of chirality-pure SWCNTs, which exhibit a stronger tendency to aggregate compared to CoMoCAT-SWCNTs in solution [Nis21]. Pretreatment of ATPE-derived (6,4)-SWCNTs with reducing agents [Gui15], non-covalent functionalizations with LNA sequences [Gil18], covalent functionalization strategies [Gal23], or the use of crowding agents [Chr13, Str17] could offer potential solutions to enhance the stability of monochiral SWCNTs in solution.

4.1.2 Detection Efficiency with Standard Microscopes

Research Manuscript I demonstrated in a simulation that the optimal wavelength for imaging cells in a buffer environment using Si cameras is 908 nm. This value may vary slightly due to the slightly varying quantum efficiencies of different Si cameras but can be taken as a guide. This simulation is tailored to a specific biological scenario but can be extended for other applications by integrating autofluorescence, scattering, and absorption data from diverse biological samples. Imaging in deeper tissue will certainly require fluorophores with wavelengths exceeding 1000 nm. These NIR-II fluorophores (1000 - 1700 nm) offer the potential for enhanced imaging depth at higher SNR due to the even further reduced scattering and autofluorescence of biological samples [Che23]. However, this also means that NIR cameras are inevitably needed for these longer wavelengths, and while their performance has improved over the years, Si-based cameras maintain a technological advantage and remain the best developed [Hon17]. This highlights that simulation is important to estimate what is the ideal fluorophore for a specific application in combination with the detector system. (6,4)-SWCNTs represent the sweet spot between the detector efficiency of standard cameras and the advantages of NIR for imaging in thin tissue-like environments, owing to their emission wavelength of 880 nm. The simulation is designed for imaging SWCNTs in solution at a fixed concentration. However, it could be extended to include immobilized SWCNTs as well as concentration and density-dependent physical effects such as quenching and reabsorption, providing an even more accurate estimation of ideal imaging quality.

The use of (6,4)-SWCNT sensors opened the possibility for highly sensitive detection of dopamine with standard Si cameras. Specifically, these monochiral sensors showed 7.5-fold greater sensitivity compared to the detection of dopamine with multichiral sensors using

InGaAs cameras. The greater sensitivity may be due to an interplay of several factors. For example, the pixel size of the camera devices may influence the analysis of intensity changes, since the detection is based on individual SWCNTs that appear as luminous dots due to the optical resolution limit. InGaAs cameras degrade this resolution limit due to their pixel size, therefore they might face challenges in detecting such weak signals due to the higher background noise, resulting in smaller absolute signal changes. In addition, the higher sensitivity could also be attributed to the absence of fluorescence overlap between individual SWCNT chirality emission peaks, leading to a lower fluorescence background. Furthermore, these monochiral SWCNTs exhibit 1.7-fold higher fluorescence brightnesses. This is probably due to the elimination of quenching sites through the removal of impurities such as amorphous carbon and catalyst residues during synthesis [Nis21], as well as due to the fact that the compared CoMoCAT- and (6,4)-SWCNT sensors were functionalized with the ssDNA sequence $(GT)_{10}$ in different ways (tip sonication vs. exchange *via* dialysis). This can lead to different wrappings around the SWCNTs and thus varying sensor responses [Yan20b]. The elimination of impurities also impacts the biocompatibility of SWCNTs. For example, purification by ATPE recently showed to increase the residence time of monochiral ssDNA-SWCNTs in cells while improving optical performance and stability [Nad23]. The promising prospects for the use of fluorescent monochiral SWCNT-based biosensors have also been outlined in a Perspective Article, which summarizes the so far few but promising uses of monochiral SWCNT sensors for biosensor applications, their advantages and also challenges in fabrication [Nis22], to which I actively contributed as a second author, but which is not part of this dissertation.

By imaging (6,4)-SWCNTs close to the sweet spot of Si cameras it was possible to resolve individual SWCNTs with high temporal resolution (50 ms) without limitations of standard equipment (LED, standard Si camera). The high spatial and temporal resolution possible with this technology and now also with standard equipment is thus almost unrivaled compared to current methods for the analysis of fast-release processes (refer to Section 2.3 for comparison). As a final application, Research Manuscript I showed the detection of cellular dopamine release by $(GT)_{10}$-(6,4)-SWCNT sensors for the first time using Si cameras. However, it should be mentioned that because of cross-selectivity to chemically similar neurotransmitters, signal changes due to release by norepinephrine are also measured, since the PC12 cells used in Research Manuscript I also have norepinephrine-containing vesicles. However, the norepinephrine concentration is lower, so the signal change, although superimposed, closely corresponds to that induced by dopamine [Gre76, Byr86, Kru17].

Considering the variable surface chemistry of SWCNTs, it is possible to extend this example to other targets of cellular release processes and beyond. Si cameras are widely

available in laboratory microscopes and also in smartphones. Although currently NIR blocking filters prevent the detection of (6,4)-SWCNT emission, it is technologically possible and would allow access to point-of-care testing with optical SWCNT sensor technology [Gha17].

4.2 Implications of Research Manuscript II and Existing Challenges

Research Manuscript II built on the findings of Research Manuscript I and aimed to make the technology accessible as a simple ready-to-use tool. During the investigation in Research Manuscript I, it was observed that the sensor coating exhibited inhomogeneities between different samples, and sometimes even within the same sample. Because this had a direct impact on the imaging quality and comparison between different sensing experiments, Research Manuscript II aimed at optimizing the immobilization of SWCNT sensors. For this purpose, spin coating was chosen as a coating technique and reproducible, homogeneous, and density-controllable SWCNT coatings could be obtained. Although these coating optimizations were primarily performed for CoMoCAT-SWCNTs due to their higher concentration and faster processing, it could also be shown that homogeneous coating with (6,4)-SWCNT sensors is possible, so the concept is also transferable. Spray coating could also be established in the future to coat substrates on a larger scale [Maj10].

Sensitivity analysis revealed a strong dependence on the coating density of the sensors, which was optimized to achieve the highest sensitivity. A physical model was established to describe the density-dependent sensitivity, indicating that the sensor response is influenced by the number of analyte molecules relative to the number of SWCNT sensors/available binding sites. Density-dependent physical effects, such as quenching and reabsorption, also played a role due to the increasing proximity of SWCNT sensors at higher densities. The sensor response, as a function of sensor density, exhibited variations between 4 % at starting intensities of 975 a.u. to 46 % at 175 a.u. (11.5 times higher). Therefore, optimization of the coating to achieve the highest sensitivity is thus important and should also be considered for other SWCNT sensor-analyte systems depending on typical analyte concentrations. Despite the use of CoMoCAT-SWCNTs, the optimization of the sensing response was performed using a standard microscope (LED and Si camera). The subsequent cell experiments were performed in a microscope equipped with a laser and a NIR camera. Optimization of the coating thereby allowed the use of very low laser powers (55 to 120 mW), so that normal LEDs and Si cameras with (6,4)-SWCNTs could also be used in the future.

Furthermore, Research Manuscript II demonstrated that the SWCNT coating supported cell adhesion of Neuro-2a cells throughout the 18-hour experiment duration. In Research Manuscript I, PC12 cells were also incubated on the sensors for 4 – 7 days, but here additional coating with collagen was necessary for adhesion mediation due to the different cell type. A detailed study of cell viability on SWCNT-coated surfaces compared to uncoated surfaces over a certain time period and for different cell types would therefore be useful. However, studies for other SWCNT-based sensors are already available [Gal20, Sta21, Had21].

The characterization of various robustness parameters presented in Research Manuscript II is important for the widespread application of SWCNT-based sensors in biomedical research and so far such investigations have not been performed on this scale before. UV light sterilization of the SWCNT coatings exhibited promising results while autoclaving led to the partial desorption of SWCNT sensors. These stability issues were optimized by the introduction of an additional baking step of the APTES layer to remove non-covalently bound APTES molecules before SWCNT coating, but the sensors still showed a reduced signal response by about 50 %. For UV sterilization, the study should still be extended to other ssDNA sequences/functionalizations, as dimer formation can occur, especially with other nucleotide sequences [Ras10]. With the development of more stable coatings [Gal23], signal response after autoclaving could be increased, provided that the sensor design does not consist of hybridized/double-stranded DNA, in which the hydrogen bonds between the complementary bases would break due to denaturation and thus change the DNA conformation and sensor response. Furthermore, compatibility with common sterilization methods such as gamma radiation and ethylene oxide remains unexplored. Gamma radiation is especially popular for sterilizing medical devices as it can penetrate sealed packages and quickly sterilize them. However, glass discoloration occurs during sterilization due to gamma radiation [Gam10, Yan19] and sterilization by autoclaving and UV exposure are cheaper, faster, and easier sterilization options compared to ethylene oxide. Moreover, ethylene oxide poses potential risks of toxicity from residue exposure, leading to regulatory concerns from the Occupational Safety and Health Administration (OSHA) [Occ23] and the Environmental Protection Agency (EPA) [Uni16].

The stability of the sensor coating in liquid showed a stability of at least 6 weeks, albeit with fluorescence losses of about 20 %. In the studies of Research Manuscripts I and II, such long cultivations on the sensors were not necessary. The cells were cultured beforehand and then transferred. Especially for the Neuro2a cells in Research Manuscript II, 4 – 18 h were sufficient for cell adhesion, whereas the PC12 cells in Research Manuscript I generally showed low adhesion and were therefore cultured on the dishes for up to one week. However, primary dopaminergic neurons have to be differentiated in culture over

several weeks [Eli22] and if information about the state of cells is to be recorded directly in cell culture, stability must also be ensured over a longer period. If the sensor coating changes continuously due to the desorption of SWCNT sensors, comparison over several weeks is difficult. To solve this problem, such sensitivity curves depending on the starting concentration for different analyte concentrations could serve as calibration, or only sensor coatings under the same cultivation time should be compared in each case. However, the ideal approach would be to further optimize the coating stability for longer-term applications without any SWCNT losses.

The established immobilization strategy using APTES, which mediates electrostatic interactions between the substrate and the SWCNTs, was not changed within this thesis. While the covalent bond of APTES molecules to the glass substrate should be stable over time, it is not surprising that SWCNTs, which are only adsorbed, can detach over time. In general, not much has been changed in recent years in this research area for immobilization of SWCNT-based sensors, and deposition methods for ssDNA-SWCNTs are almost exclusively limited to nonspecific or electrostatic interactions [Sta21, Kru17, Man17, Bey19]. To the current knowledge, there are only two examples where immobilization was achieved by means of an avidin/neutravidin-biotin interaction, where SWCNTs were either non-covalently functionalized with biotinylated ssDNA [Sta21] or covalently bound to biotin [Chi20], maintaining their functionality as sensors. However, the fluorescence signal decreased by 23 % over 9 days, and data over a longer period are not shown [Sta21]. The studies showed that non-biotinylated SWCNTs also adhered to the avidin-coated surface presumably due to electrostatic effects between the cationic protein avidin and the SWCNTs [Sta21]. It is possible that the interaction could thus prove to be more stable over a period of > 6 weeks compared with the APTES–SWCNT interaction when all electrostatically adherent SWCNTs are desorbed because the avidin-biotin bond is one of the strongest binding partners occurring in nature [Liu16]. Nonetheless, it is essential to explore covalent strategies as well. Covalent functionalization approaches have been successful in binding ssDNA to glass [Per22], and it may be possible to covalently bind ssDNA-SWCNTs to the glass surface using an anchor sequence without compromising sensor functionality.

The long-lasting sensor functionality over several weeks is promising. In general, the study should be extended over even longer periods and also for other ssDNA sequences. This would be important to ensure whether sensor responses of different batches with different storage durations can be compared or whether the sensor response shifts with a fixed factor around which sensor responses of different storage durations could be corrected.

In Research Manuscript II, a comparison between sensor sensitivity for dopamine detection in PBS and cell medium revealed a one-third reduction in sensitivity in cell medium.

This lower sensitivity can be attributed to the potential interference of compounds in the cell medium. Consequently, to improve the sensitivity of the sensors in protein-rich environments, a detailed understanding of the interaction between the SWCNTs and their environment is required [Pin20]. Addressing reduced sensitivity in complex media and potential cross-sensitivities to chemically similar molecules will be a significant challenge in the future. Covalent functionalizations have shown a higher sensitivity in complex media compared to non-covalent functionalizations [Met23]. One other possible solution is to perform functionalized SWCNT screenings that identify dopamine-sensitive functionalization directly in the application medium, enabling the discovery of more specific functionalizations.

By exchanging the cell medium with PBS, functional SWCNT-based sensor coatings were used for the first time to report the efficacy of various dopaminergic drugs. For this purpose, time recordings of the mean SWCNT fluorescence changes in the cell area were extracted from the recorded videos for easier data processing, and various parameters were extracted from these time recordings (maximum signal change I_{max}, time $\tau_{I_{max}/2}$ that elapses until the signal has fallen from I_{max} to $I_{max}/2$, and time $\tau_{\Delta I_{max}}$ between stimulation and reaching I_{max}). Significant differences between the tested substances were found, which were also in line with expectations. For example, L-DOPA as a precursor of dopamine showed increased dopamine release, whereas nomifensine and bupropion as reuptake inhibitors showed increased $\tau_{I_{max}/2}$ values, indicating a higher residence time of dopamine molecules in the synaptic cleft due to inhibited uptake of dopamine by presynaptic cells. Such similar parameters are also used in amperometric measurements to evaluate different dopaminergic compounds [Hua19, Whi21], but even much more information could be extracted based on the spatiotemporal recordings. As also mentioned in Chapter 2.4, in the future, the kinetics of the dopamine release could be better interpreted by knowing the rate constants of the SWCNT sensors since the visual temporal representation of dopamine release depends on these in particular [Mey17]. In addition, the use of SWCNT sensors functionalized with LNA could help increase stability against higher ionic fluctuations (e.g., when KCl is added for dopamine stimulation) [Gil18]. This could lead to even more sensitive measurements when testing and comparing different dopaminergic compounds because, in contrast to the measurements in Research Manuscript I, Research Manuscript II found small increases in sensor response after addition of higher KCl concentrations (100 mM instead of 55 mM).

These Smart Slides could find applications in various biomedical research fields. For instance, they could be used for drug library screening and direct assessment of cellular responses that could replace animal testing. Furthermore, SWCNT-coated sensor technology could also be of interest for novel incubator imaging systems for cell research, allowing

automated real-time monitoring of cell cultures in the visible range. By incorporating functional SWCNT coatings into labware, researchers can obtain additional information about cell culture beyond the visible range in a non-invasive manner. As mentioned in the Research Manuscript II, this approach can be easily expanded to other analytes relevant to different biological issues, such as coagulation disorders [Ger23], diabetes [Ehr21, Zub22], or cancer [Wil18b].

4.3 Concluding Summary and Outlook

Both research manuscripts have contributed to making SWCNT-based sensing more accessible to other research groups and beyond. The simpler separation protocol for the extraction of (6,4)-SWCNTs demonstrated that no special equipment for SWCNT-based optical sensors is needed for the detection of even rapid biological release processes. The integration of SWCNT-based sensor technology into standard cell culture dishes has resulted in the development of a simple, ready-to-use tool. Using the summary tables created from the Review Manuscript (Section 2.4.1 *Appendix*), SWCNTs can also be easily made selective for other targets through the variety of other sensors already available.

Other excitation and readout modes of the SWCNTs-based sensors could also be considered, depending on the necessary advantages in a specific application. In a separate research manuscript, which arose during the time as a Ph.D. student, the change in SWCNT sensor lifetime in response to dopamine was measured instead of change in intensity [Sis23]. The $(GT)_{10}$-(6,4)-SWCNT sensors developed in Research Manuscript I were used for this purpose, among others. Lifetime readout is a more robust metric compared to intensity changes due to its reduced susceptibility to fluctuations in external intensity and differing concentrations of the sensor. Consequently, it benefits from an inherent internal calibration mechanism. However, SWCNT sensor lifetimes are in the order of hundreds of picoseconds [Har16, Ber21], so measurement is also challenging. Using time-correlated single photon counting in combination with confocal fluorescence microscopy, it has been possible to report the extracellular dopamine release from cells in 3D [Sis23]. This approach could be used to conduct a more realistic analysis that better mimics the *in vivo* environment, cell-cell interaction, or drug testing [Kie18, Bol19]. Furthermore, the electrical and optical signal transduction of the $(GT)_{10}$-SWCNT sensors to different small molecules, including dopamine, was compared in collaboration and it was found that an increase in fluorescence intensity correlates with a decrease in SWCNT electrical current, indicating that the sensing mechanism for the dopamine sensors correlates [Cle22]. The use of electrical or luminescence-based SWCNT sensors could open up further diagnostic

applications in the life science field, which would require, for example, a compact, integrated readout chip. While this would not be relevant for the rapid release of biomolecules such as neurotransmitters, it could be interesting for smart readout devices to monitor neurotransmitter balance in urine [Mar11] or as a wearable to support continuous drug monitoring in real time [Bia21].

Looking at the main pain points of SWCNT-based sensing for neurotransmitter detection from Section 2.4.2, the equipment cost could be reduced by approximately 29,000 € by eliminating the need for a NIR camera and laser. This leaves only the standard fluorescence emission detection equipment, a high-resolution objective, and a suitable NIR filter set, that are already available to many research groups (except for the specific NIR filters). Cell viability studies for compatibility with SWCNT-based sensors should be acquired with regard to the specific surface functionalization. However, the current trend in the literature favors the use of monochiral SWCNTs with appropriate surface functionalization for improved results. Sensitivity enhancements of dopamine-sensitive SWCNT sensors have been achieved by using both (6,4)-SWCNTs and SWCNT coating optimizations and should be combined in the future to achieve maximum sensitivity using Si cameras. Improvements in selectivity for the detection of dopamine versus dopamine homologs and other interference factors will further advance sensor technology. Furthermore, with the availability of different emitting SWCNT chiralities or by arranging different SWCNT sensors into an array, the multiplexing of a variety of different biological release processes could be studied in parallel and could thus provide even more detailed insights into complex biological processes.

Chapter 5

Conclusion

In this thesis, a decisive step has been taken toward the easier use of SWCNT-based sensors for the high-resolution detection of the important neurotransmitter dopamine, aimed at increasing the sensitivity and reproducibility of these sensors (Figure 5.1).

The Review Manuscript aimed to give a comprehensive overview of the developments of fluorescent SWCNTs in recent years ranging from photophysical properties to surface functionalization approaches, biocompatibility, existing SWCNT-based sensors, sensor mechanisms, considerations of imaging and kinetics as well as measurement approaches such as ratiometric and hyperspectral imaging. Compared to the state-of-the-art for neurotransmitter detection, SWCNTs outperform other technologies in terms of high spatial and temporal resolution. However, expensive equipment was required for detection.

Research Manuscript I aimed to make fluorescent SWCNT technology accessible to standard equipment (Si camera, LED) instead of relying on specialized InGaAs cameras and lasers. The key challenge was to extract monochiral (6,4)-SWCNTs (emitting around 880 nm) from the synthesis-related multichiral CoMoCAT-SWCNT mix (with emission between 850 - 1200 nm). This shifted the overall wavelength emission of the SWCNTs closer to the visible range, while still remaining in the biological transparency window. Herein, for the first time, a simple one-step ATPE procedure for the extraction of (6,4)-SWCNTs was developed. The improvement from an original two-step to a one-step process increased the extraction yield from 5.1 ± 0.3 % to 7.4 ± 1 % and Raman spectra demonstrated a lower defect rate on the (6,4)-SWCNT surface compared to the parental CoMoCAT-SWCNTs, due to the sorting out of impurities. The one-step extraction makes the separation even less prone to errors and enables easy access to this chirality in an inexpensive, fast, and highly scalable way.

Simulation of the SBR confirmed that (6,4)-SWCNTs, combined with Si cameras, are the optimal choice for achieving the highest contrast when imaging cells in a buffer environment and are superior to CoMoCAT-SWCNTs with InGaAs cameras mainly be-

cause of the high dark current due to the small direct band gap of InGaAs. Additionally, the (6,4)-SWCNTs were successfully converted into highly sensitive dopamine sensors by functionalization with $(GT)_{10}$-ssDNA, demonstrating a 7.5-fold higher sensitivity in direct comparison to $(GT)_{10}$-CoMoCAT-SWCNTs detected with an InGaAs camera. This advancement enabled the imaging of single SWCNTs with 50x higher resolution by changing to a standard microscope at frame rates exceeding 20 fps. Moreover, the ability to detect dopamine at such high frame rates was confirmed independently in three microscope setups. Finally, the sensors were used to demonstrate dopaminergic release processes in a neurological cell model for the first time using Si cameras. Research Manuscript I thus serves as a prime example that even fast-moving dynamic biological processes can be imaged with standard available laboratory equipment using SWCNT sensors by combining the best of two worlds, namely Si technology and the advantages of the NIR.

Research Manuscript II aimed to make SWCNT optical sensors even more user-friendly by developing a simple ready-to-use tool (Smart Slides), for the analysis of various biological questions. The key improvements involved optimizing the previously inhomogeneous sensor coating using spin coating and fine-tuning the sensor density to achieve the highest sensitivity for dopamine detection. A physical model was developed to describe the sensor density-dependent behavior of sensitivity, which fits the experimental results. The importance of the coating optimization was shown by a sensitivity enhancement factor of up to 11.5 between the most insensitive and most sensitive SWCNT coating density.

Characterizations of the robustness of the sensor coatings for broad use in diverse biomedical applications showed the necessary stability in both dry and buffer environments for at least 6 weeks, retaining their functionality even after sterilization using UV light. These Smart Slides supported cell adhesion and were used for the first time for drug testing of dopaminergic substances. The fluorescence change of the SWCNT sensors, recorded over time, provided information about the released dopamine concentration from a neurodegenerative cell model, which showed the expected responses after addition of the respective substances. Research Manuscript II showcased that SWCNT-based sensing has the potential for various applications, such as drug library screening for new drug evaluation.

The combination of Manuscript I and II results in a strong synergy, offering not only easy access to high-sensitivity SWCNT-based sensing for monitoring dopaminergic release processes but also extending its applicability beyond. As the field of SWCNT-based sensor technology rapidly expands, the diverse range of developed SWCNT sensors, coupled with the availability of various SWCNT chiralities, holds immense potential for shedding light on complex biological questions. SWCNT-based sensing could thus open exciting possibilities for simultaneous sensing of multiple targets and a make a significant contribution to biomedical research and future applications.
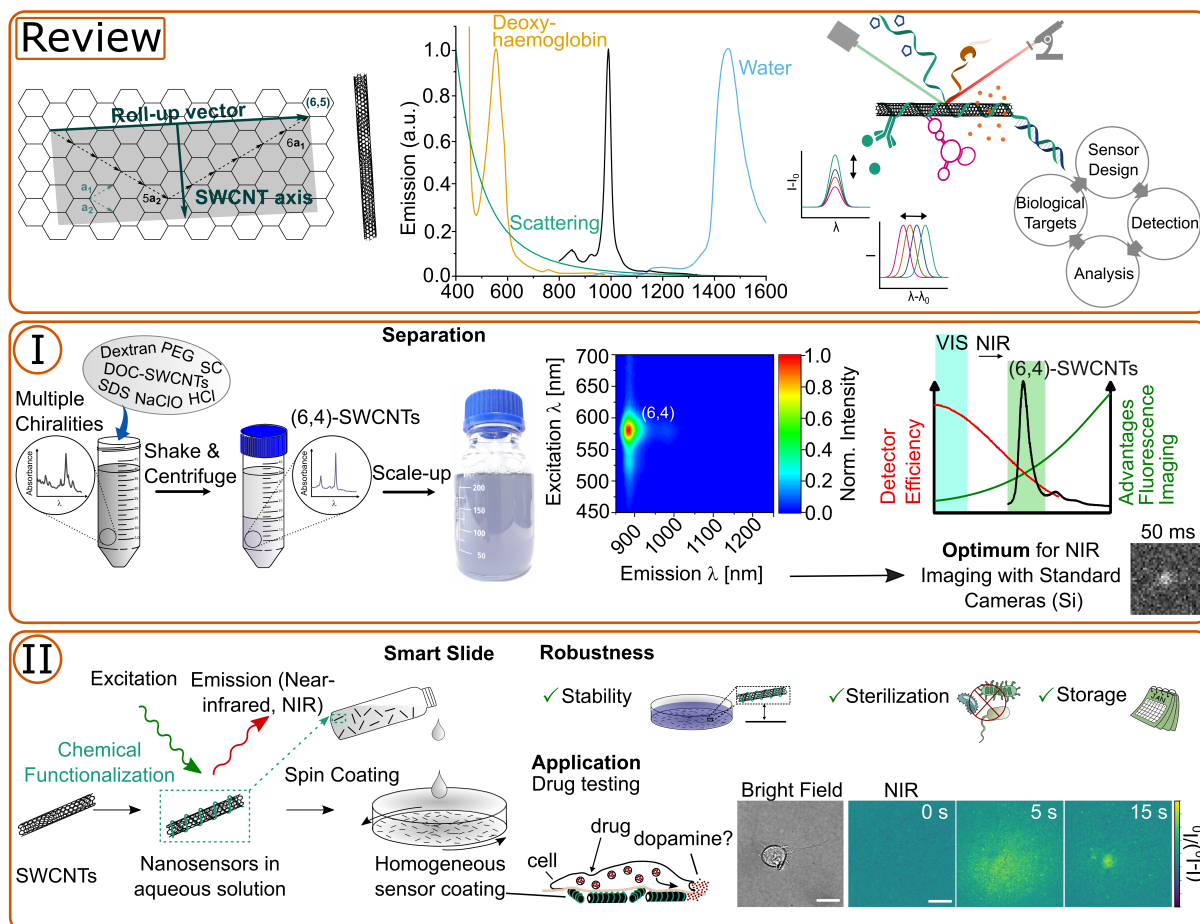
Figure 5.1: Overview of topics described in this dissertation. This work focussed on making SWCNT sensor technology readily accessible. The Research Manuscript covers the various advantages and developments of SWCNT topics in recent years. Adapted with permission from [Ack22]. Copyright 2022 Angew. Chem. Int. Ed. published by Wiley-VCH GmbH. Manuscript I covers the development of a one-step (6,4)-SWCNT separation that enables high-resolution imaging and sensing with conventional Si cameras. Adapted with permission from [Ack23b]. Copyright 2023 Small published by Wiley-VCH GmbH. Manuscript II covers the development of Smart Slides by optimizing sensor coating, determining robustness parameters, and measuring altered dopaminergic cell reactions in drug testing [Ack23a].

Bibliography

[Ack22]   ACKERMANN, J.; METTERNICH, J. T.; HERBERTZ, S. AND KRUSS, S.:
           Biosensing with Fluorescent Carbon Nanotubes. Angew. Chem. Int. Ed.,
           61(18):e202112372, 2022.

[Ack23a]   ACKERMANN, J.; REGER, E.; JUNG, S.; MOHR, J.; HERBERTZ, S.; SEIDL,
           K. AND KRUSS, S.: *Smart Slides for Optical Monitoring of Cellular Processes.*
           BioRxiv, 2023.

[Ack23b]   ACKERMANN, J.; STEGEMANN, J.; SMOLA, T.; REGER, E.; JUNG, S.;
           SCHMITZ, A.; HERBERTZ, S.; ERPENBECK, L.; SEIDL, K. AND KRUSS, S.:
           High Sensitivity Near-Infrared Imaging of Fluorescent Nanosensors. Small,
           19(14):e2206856, 2023.

[Aga22]   AGARWAL, S.; KALLMYER, N. E.; VANG, D. X.; RAMIREZ, A. V.; ISLAM,
           M. M.; HILLIER, A. C.; HALVERSON, L. J. AND REUEL, N. F.: *Single-
           Walled Carbon Nanotube Probes for the Characterization of Biofilm-Degrading
           Enzymes Demonstrated against Pseudomonas aeruginosa Extracellular Matri-
           ces.* Anal. Chem., 94(2):856–865, 2022.

[Ant15]   ANTARIS, A. L.; YAGHI, O. K.; HONG, G.; DIAO, S.; ZHANG, B.; YANG,
           J.; CHEW, L. AND DAI, H.: *Single Chirality (6,4) Single-Walled Carbon Nan-
           otubes for Fluorescence Imaging with Silicon Detectors.* Small, 11(47):6325–
           6330, 2015.

[Ant17]   ANTONUCCI, A.; KUPIS-ROZMYSŁOWICZ, J. AND BOGHOSSIAN, A. A.: *Non-
           covalent Protein and Peptide Functionalization of Single-Walled Carbon Nan-
           otubes for Biodelivery and Optical Sensing Applications.* ACS Appl. Mater.
           Interfaces, 9(13):11321–11331, 2017.

[Arn06]   ARNOLD, M. S.; GREEN, A. A.; HULVAT, J. F.; STUPP, S. I. AND HER-
           SAM, M. C.: *Sorting carbon nanotubes by electronic structure using density
           differentiation.* Nat. Nanotechnol., 1(1):60–65, 2006.

[Bac02]   BACHILO, S. M.; STRANO, M. S.; KITTRELL, C.; HAUGE, R. H.; SMALLEY,
           R. E. AND WEISMAN, R. B.: *Structure-assigned optical spectra of single-walled*

carbon nanotubes. Science, 298(5602):2361–2366, 2002.

[Bau02]   BAUGHMAN, R. H.; ZAKHIDOV, A. A. AND DE HEER, W. A.: *Carbon nanotubes–the route toward applications.* Science, 297(5582):787–792, 2002.

[Ben15]   BENES, F. M.: *The Development of the Prefrontal Cortex: The Maturation of Neurotransmitter Systems and Their Interactions*, chapter 5, pages 216–258. John Wiley & Sons, Ltd, 2015.

[Ber21]   BERGER, F. J.; DE SOUSA, J. A.; ZHAO, S.; ZORN, N. F.; EL YUMIN, A. A.; QUINTANA GARCÍA, A.; SETTELE, S.; HÖGELE, A.; CRIVILLERS, N. AND ZAUMSEIL, J.: *Interaction of Luminescent Defects in Carbon Nanotubes with Covalently Attached Stable Organic Radicals.* ACS Nano, 15(3):5147–5157, 2021.

[Bey19]   BEYENE, A. G.; DELEVICH, K.; DEL BONIS-O'DONNELL, J. T.; PIEKARSKI, D. J.; LIN, W. C.; THOMAS, A. W.; YANG, S. J.; KOSILLO, P.; YANG, D.; PROUNIS, G. S.; WILBRECHT, L. AND LANDRY, M. P.: *Imaging striatal dopamine release using a nongenetically encoded near infrared fluorescent catecholamine nanosensor.* Sci. Adv., 5(7):eaaw3108, 2019.

[Bia21]   BIAN, S; ZHU, B.; RONG, G. AND SAWAN, M.: *Towards wearable and implantable continuous drug monitoring: A review.* J. Pharm. Anal., 11(1):1–14, 2021.

[Bis16]   BISKER, G.; DONG, J.; PARK, H. D.; IVERSON, N. M.; AHN, J.; NELSON, J. T.; LANDRY, M. P.; KRUSS, S. AND STRANO, M. S.: *Protein-targeted corona phase molecular recognition.* Nat. Commun., 7:10241, 2016.

[Bol19]   BOLOGNIN, S.; FOSSEPRE, M.; QING, X.; JARAZO, J.; SCANCAR, J.; MORENO, E. L.; NICKELS, S. L.; WASNER, K.; OUZREN, N.; WALTER, J.; GRÜNEWALD, A.; GLAAB, E.; SALAMANCA, L.; FLEMING, R. M. T.; ANTONY, P. M. A. AND SCHWAMBORN, J. C.: *3D Cultures of Parkinson's Disease-Specific Dopaminergic Neurons for High Content Phenotyping and Drug Testing.* Adv. Sci, 6(1):1800927, 2019.

[Buc15]   BUCHER, E. S. AND WIGHTMAN, R. M.: *Electrochemical Analysis of Neurotransmitters.* Annu. Rev. Anal. Chem., 8:239–261, 2015.

[Byr86]   BYRD, J. C. AND HADJICONSTANTINOU, M. AND CAVALLA, D.: *Epinephrine synthesis in the PC12 pheochromocytoma cell line.* Eur. J. Pharmacol., 127(1-2):139–142, 1986.

[Cec12]   CECCARINI, J.; VRIEZE, E.; KOOLE, M.; MUYLLE, T.; BORMANS, G.;

CLAES, S. AND VAN LAERE, K.: *Optimized in vivo detection of dopamine release using 18F-fallypride PET.* J. Nucl. Med., 53(10):1565–1572, 2012.

[Che08] CHEN, Y.; GUO, C.; LIM, L.; CHEONG, S.; ZHANG, Q.; TANG, K. AND REBOUD, J.: *Compact microelectrode array system: tool for in situ monitoring of drug effects on neurotransmitter release from neural cells.* Anal. Chem., 80(4):1133–1140, 2008.

[Che17] CHENG, C.; LI, S.; THOMAS, A.; KOTOV, N. A. AND HAAG, R.: *Functional Graphene Nanomaterials Based Architectures: Biointeractions, Fabrications, and Emerging Biological Applications.* Chem. Rev., 117(3):1826–1914, 2017.

[Che21] CHENG, Y.-J.; LIN, C.-H. AND LANE, H.-Y.: *Involvement of Cholinergic, Adrenergic, and Glutamatergic Network Modulation with Cognitive Dysfunction in Alzheimer's Disease.* Int. J. Mol. Sci., 22(5), 2021.

[Che23] CHEN, Y.; WANG, S. AND ZHANG, F.: *Near-infrared luminescence high-contrast in vivo biomedical imaging.* Nat. Rev. Bioeng., 1(1):60–78, 2023.

[Chi20] CHIO, L.; PINALS, R. L.; MURALI, A.; GOH, N. S. AND LANDRY, M. P.: *Covalent Surface Modification Effects on Single–Walled Carbon Nanotubes for Targeted Sensing and Optical Imaging.* Adv. Funct. Mater., 30(17):1910556, 2020.

[Chr13] CHRISTIANSEN, A., WANG, Q., CHEUNG, M. S. AND WITTUNG-STAFSHEDE, P.: *Effects of macromolecular crowding agents on protein folding in vitro and in silico.* Biophys. Rev., 5(2):137–145, 2013.

[Cle22] CLEMENT, P.; ACKERMANN, J.; SAHIN-SOLMAZ, N.; HERBERTZ, S.; BOERO, G.; KRUSS, S. AND BRUGGER, J.: *Comparison of electrical and optical transduction modes of DNA-wrapped SWCNT nanosensors for the reversible detection of neurotransmitters.* Biosens. Bioelectron., 216:114642, 2022.

[Cog07] COGNET, L.; TSYBOULSKI, D. A.; ROCHA, J.-D. R.; DOYLE, C. D.; TOUR, J. M. AND WEISMAN, R. B.: *Stepwise quenching of exciton fluorescence in carbon nanotubes by single-molecule reactions.* Science, 316(5830):1465–1468, 2007.

[Dal20] DALGLEISH, T.; BLACK, M.; JOHNSTON, D. AND BEVAN, A.: *Transdiagnostic approaches to mental health problems: Current status and future directions.* J. Consult. Clin. Psychol., 88(3):179–195, 2020.

[DeP21] DEPALMA, A. BIOCOMPARE: *Guide to HPLC System Selection.*

https://www.biocompare.com/Editorial-Articles/580407-Guide-to-HPL
C-System-Selection/#:~:text=%E2%80%9CAnalytical%20scientists%20con
sider%20a%20number,K%20to%20%24120K%20range., 2021.   Viewed on
30.08.2023.

[Din19]   DINARVAND, M.; NEUBERT, E.; MEYER, D.; SELVAGGIO, G.; MANN, F. A.;
ERPENBECK, L. AND KRUSS, S.: *Near-Infrared Imaging of Serotonin Release
from Cells with Fluorescent Nanosensors.* Nano Lett., 19(9):6604–6611, 2019.

[Dol20]   DOLPHIN, A. C. AND LEE, A.: *Presynaptic calcium channels: specialized con-
trol of synaptic neurotransmitter release.* Nat. Rev. Neurosci., 21(4):213–229,
2020.

[Dun17]   DUNN, M. R.; JIMENEZ, R. M. AND CHAPUT, J. C.: *Analysis of aptamer
discovery and technology.* Nat. Rev. Chem., 1(10):0076, 2017.

[Ehr21]   EHRLICH, R.; HENDLER-NEUMARK, A.; WULF, V.; AMIR, D. AND BISKER,
G.: *Optical Nanosensors for Real-Time Feedback on Insulin Secretion by β-
Cells.* Small, 17(30):2101660, 2021.

[Eli22]   ELIZAROVA, S.; CHOUAIB, A. A.; SHAIB, A.; HILL, B.; MANN, F.; BROSE,
N.; KRUSS, S. AND DANIEL, J. A.: *A fluorescent nanosensor paint detects
dopamine release at axonal varicosities with high spatiotemporal resolution.*
Proc. Natl. Acad. Sci. U.S.A., 119(22):e2202842119, 2022.

[Emm21]   EMMANUEL, N.; NAIR, R. B.; ABRAHAM, B.; YOOSAF, K.: *Fabricating a
Low-Cost Raman Spectrometer to Introduce Students to Spectroscopy Basics
and Applied Instrument Design.* J. Chem. Educ., 98(6):2109–2116, 2021.

[Far17]   FARRERA, C.; TORRES ANDÓN, F. AND FELIU, N.: *Carbon Nanotubes as
Optical Sensors in Biomedicine.* ACS Nano, 11(11):10637–10643, 2017.

[Fei20]   FEIGIN, V. L.; VOS, T.; NICHOLS, E.; OWOLABI, M. O.; CARROLL, W.
M.; DICHGANS, M.; DEUSCHL, G.; PARMAR, P.; BRAININ, M. AND MUR-
RAY, C.: *The growing burden of neurological disorders in low-income and
middle-income countries: priorities for policy making.* The Lancet. Neurology,
19(3):200–202, 2020.

[Fig20]   FIGUEIREDO, M. L. B.; MARTIN, C. S.; FURINI, L. N.; RUBIRA, R. J. G.;
BATAGIN-NETO, A.; ALESSIO, P. AND CONSTANTINO, C. J. L.: *Surface-
enhanced Raman scattering for dopamine in Ag colloid: Adsorption mechanism
and detection in the presence of interfering species.* Appl. Surf. Sci, 522:146466,
2020.

[Fla13]   FLAVEL, B. S.; KAPPES, M. M.; KRUPKE, R. AND HENNRICH, F.: *Separation of single-walled carbon nanotubes by 1-dodecanol-mediated size-exclusion chromatography.* ACS Nano, 7(4):3557–3564, 2013.

[For08]   FORNELL, D.: *SPECT Scanner vs. PET, Which is Best?* https://www.dicardiology.com/article/spect-scanner-vs-pet-which-best, 2008. Viewed on 30.08.2023.

[Fos14]   FOSTER, J.: *Design of a Portable Fast Scan Cyclic Voltammetry System for Measuring Neurotransmitter Levels.* Master Thesis, Grand Valley State University, Michigan, 2014.

[Fuj15]   FUJIGAYA, T. AND NAKASHIMA, N.: *Non-covalent polymer wrapping of carbon nanotubes and the role of wrapped polymers as functional dispersants.* Sci. Technol. Adv. Mater., 16:024802, 2015.

[Gal20]   GALASSI, T. V.; ANTMAN-PASSIG, M.; YAARI, Z.; JESSURUN, J.; SCHWARTZ, R. E. AND HELLER, D. A.: *Long-term in vivo biocompatibility of single-walled carbon nanotubes.* PLoS One, 15(5):e0226791, 2020.

[Gal23]   GALONSKA, P.; MOHR, J. M.; SCHRAGE, C. A.; SCHNITZLER, L. AND KRUSS, S.: *Guanine Quantum Defects in Carbon Nanotubes for Biosensing.* J. Phys. Chem. Lett., 14(14):3483–3490, 2023.

[Gam10]   *Gamma Irradiation in the Pharmaceutical Manufacturing Environment.* Pharm. Technol., 2010 Supplement(1), 2010.

[Gan23]   GANDY, M.: *The role of psychologists in managing mental health comorbidities in adults with neurological disorders.* Aust. Psychol., 58(3):161–168, 2023.

[Gao17]   GAO, Z.; DANNÉ, N.; GODIN, A. G.; LOUNIS, B. AND COGNET, L.: *Evaluation of Different Single-Walled Carbon Nanotube Surface Coatings for Single-Particle Tracking Applications in Biological Environments.* Nanomater., 7(11):393, 2017.

[Ger23]   GERSTMAN, E.; HENDLER-NEUMARK, A.; WULF, V. AND BISKER, G.: *Monitoring the Formation of Fibrin Clots as Part of the Coagulation Cascade Using Fluorescent Single-Walled Carbon Nanotubes.* ACS Appl. Mater. Interfaces, 15(18):21866–21876, 2023.

[Gha17]   GHASSEMI, P.; WANG, B.; WANG, J.; WANG, Q.; CHEN, Y. AND PFEFER, J. T.: *Evaluation of Mobile Phone Performance for Near-Infrared Fluorescence Imaging.* IEEE Trans. Biomed. Eng., 64(7):1650–1653, 2017.

[Gho10]   GHOSH, S.; BACHILO, S. M. AND WEISMAN, R. B.: *Advanced sorting of*

single-walled carbon nanotubes by nonlinear density-gradient ultracentrifugation. Nat. Nanotechnol., 5(6):443–450, 2010.

[Gho22]   GHOSH, K. K.; PADMANABHAN, P.; YANG, C.-T.; NG, D. C. E.; PALANIVEL, M.; MISHRA, S.; HALLDIN, C. AND GULYÁS, B.: *Positron emission tomographic imaging in drug discovery.* Drug Discov. Today, 27(1):280–291, 2022.

[Gil18]   GILLEN, A. J.; KUPIS-ROZMYSŁOWICZ, J.; GIGLI, C.; SCHUERGERS, N. AND BOGHOSSIAN, A. A.: *Xeno Nucleic Acid Nanosensors for Enhanced Stability Against Ion-Induced Perturbations.* J. Phys. Chem. Lett., 9(15):4336–4343, 2018.

[Gil21]   GILLEN, A. J.; ANTONUCCI, A.; REGGENTE, M.; MORALES, D. AND BOGHOSSIAN, A. A.: *Distinguishing dopamine and calcium responses using XNA-nanotube sensors for improved neurochemical sensing.* bioRxiv, 2021.

[God18]   GODOY-REYES, T. M.; LLOPIS-LORENTE, A.; COSTERO, A. M.; SANCENÓN, F.; GAVIÑA, P. AND MARTÍNEZ-MÁÑEZ, R.: *Selective and sensitive colorimetric detection of the neurotransmitter serotonin based on the aggregation of bifunctionalised gold nanoparticles.* Sens. Actuators B Chem., 258:829–835, 2018.

[Gon22]   GONG, X.; RENEGAR, N.; LEVI, R.; STRANO, M. S.: *Machine learning for the discovery of molecular recognition based on single-walled carbon nanotube corona-phases.* npj Comput. Mater., 8(1):135, 2022.

[Gre76]   GREENE, L. A. AND TISCHLER, A. S.: *Establishment of a noradrenergic clonal line of rat adrenal pheochromocytoma cells which respond to nerve growth factor.* Proc. Natl. Acad. Sci. U. S. A., 73(7):2424–2428, 1976.

[Gru04]   GRUNWALD, B. AND HOLST, G.: *Fibre optic refractive index microsensor based on white-light SPR excitation.* Sens. Actuator A Phys., 113(2):174–180, 2004.

[Gub09]   GUBERNATOR, N. G.; ZHANG, H.; STAAL, R. G. W.; MOSHAROV, E. V.; PEREIRA, D. B.; YUE, M.; BALSANEK, V.; VADOLA, P. A.; MUKHERJEE, B.; EDWARDS, R. H.; SULZER, D.; SAMES, D.: *Fluorescent false neurotransmitters visualize dopamine release from individual presynaptic terminals.* Science, 324(5933):1441–1444, 2009.

[Gui15]   GUI, H.; STREIT, J. K.; FAGAN, J. A.; HIGHT WALKER, A. R.; ZHOU, C. AND ZHENG, M.: *Redox sorting of carbon nanotubes.* Nano Lett., 15(3):1642–1646, 2015.

[Had21] HADIDI, N.; SHAHBAHRAMI MOGHADAM, N.; PAZUKI, G.; PARVIN, P. AND
         SHAHI, F.: *In Vitro Evaluation of DSPE-PEG (5000) Amine SWCNT Toxicity
         and Efficacy as a Novel Nanovector Candidate in Photothermal Therapy by
         Response Surface Methodology (RSM)*. Cells, 10(11):2874, 2021.

[Hai18] HAINES, D. E. AND MIHAILOFF, G. A.: *Fundamental Neuroscience for Basic
         and Clinical Applications*. Elsevier, 5 edition, 2018.

[Ham23] HAMAMATSU PHOTONICS: *ORCA-Flash4.0 LT3 Digital CMOS camera
         C11440-42U40*. https://www.hamamatsu.com/us/en/product/cameras/cmo
         s-cameras/C11440-42U40.html, 2023. Viewed on 30.08.2023.

[Har16] HARTMANN, N. F.; VELIZHANIN, K. A.; HAROZ, E. H.; KIM, M.; MA, X.;
         WANG, Y.; HTOON, H. AND DOORN, S. K.: *Photoluminescence Dynamics
         of Aryl sp(3) Defect States in Single-Walled Carbon Nanotubes*. ACS nano,
         10(9):8355–8365, 2016.

[Har19] HARVEY, J. D.; WILLIAMS, R. M.; TULLY, K. M.; BAKER, H. A.; SHAMAY,
         Y. AND HELLER, D. A.: *An in Vivo Nanosensor Measures Compartmental
         Doxorubicin Exposure*. Nano Lett., 19(7):4343–4354, 2019.

[Hen17] HENGARTNER, M. P.: *Methodological Flaws, Conflicts of Interest, and Scien-
         tific Fallacies: Implications for the Evaluation of Antidepressants' Efficacy and
         Harm*. Front. Psychiatry, 8:275, 2017.

[Her05] HERZOG, H. AND RÖSCH, F.: *Chemie und Physik der Bildgebung. PET- und
         SPECT-Technik*. Pharm Unserer Zeit, 34(6):468–473, 2005.

[Hon15] HONG, G.; DIAO, S.; ANTARIS, A. L. AND DAI, H.: *Carbon Nanoma-
         terials for Biological Imaging and Nanomedicinal Therapy*. Chem. Rev.,
         115(19):10816–10906, 2015.

[Hon17] HONG, G.; ANTARIS, A. L.; AND DAI, H.: *Near-infrared fluorophores for
         biomedical imaging*. Nat. Biomed. Eng., 1(1):1–22, 2017.

[How14] HOWES, P. D.; CHANDRAWATI, R.; STEVENS, M. M.: *Bionanotech-
         nology. Colloidal nanoparticles as advanced biological sensors*. Science,
         346(6205):1247390, 2014.

[Hu 18] HU , W.; HUANG, Y.; CHEN, C.; LIU, Y.; GUO, T. AND GUAN, B.-O.:
         *Highly sensitive detection of dopamine using a graphene functionalized plas-
         monic fiber-optic sensor with aptamer conformational amplification*. Sens. Ac-
         tuators B Chem., 264:440–447, 2018.

[Hua19] HUANG, M.; RATHORE, S. S. AND LINDAU, M.: *Drug testing complementary*

metal-oxide-semiconductor chip reveals drug modulation of transmitter release for potential therapeutic applications. Journal of Neurochemistry, 151(1):38–49, 2019.

[Iij91] IIJIMA, S.: *Helical microtubules of graphitic carbon.* Nature, 354(6348):56–58, 1991.

[Jaf17] JAFARINEJAD, S.; GHAZI-KHANSARI, M.; GHASEMI, F.; SASANPOUR, P. AND HORMOZI-NEZHAD, M. R.: *Colorimetric Fingerprints of Gold Nanorods for Discriminating Catecholamine Neurotransmitters in Urine Samples.* Sci. Rep., 7(1):8266, 2017.

[Jeo19] JEONG, S.; YANG, D.; BEYENE, A. G.; DEL BONIS-O'DONNELL, J. T.; GEST, A. M. M.; NAVARRO, N.; SUN, X. AND LANDRY, M. P.: *High-throughput evolution of near-infrared serotonin nanosensors.* Sci. Adv., 5(12):eaay3771, 2019.

[Jin10] JIN, H.; HELLER, D. A.; KALBACOVA, M.; KIM, J.-H.; ZHANG, J.; BOGHOSSIAN, A. A.; MAHESHRI, N. AND STRANO, M. S.: *Detection of single-molecule H2O2 signalling from epidermal growth factor receptor using fluorescent single-walled carbon nanotubes.* Nat. Nanotechnol., 5(4):302–309, 2010.

[Kag22] KAGAN, B.; HENDLER-NEUMARK, A.; WULF, V.; KAMBER, D.; EHRLICH, R. AND BISKER, G.: *Super–Resolution Near–Infrared Fluorescence Microscopy of Single–Walled Carbon Nanotubes Using Deep Learning.* Adv. Photonics Res., 3(11):2200244, 2022.

[Kel22] KELICH, P.; JEONG, S.; NAVARRO, N.; ADAMS, J.; SUN, X.; ZHAO, H.; LANDRY, M. P. AND VUKOVIĆ, L.: *Discovery of DNA-Carbon Nanotube Sensors for Serotonin with Machine Learning and Near-infrared Fluorescence Spectroscopy.* ACS Nano, 16(1):736–745, 2022.

[Kie18] KIENINGER, J.; WELTIN, A.; FLAMM, H. AND URBAN, G. A.: *Microsensor systems for cell metabolism - from 2D culture to organ-on-chip.* Lab on a Chip, 18(9):1274–1291, 2018.

[Kle19] KLEIN, M. O.; BATTAGELLO, D. S.; CARDOSO, A. R.; HAUSER, D. N.; BITTENCOURT, J. C.; CORREA, R. G.: *Dopamine: Functions, Signaling, and Association with Neurological Diseases.* Cell. Mol. Neurobiol., 39(1):31–59, 2019.

[Kru14] KRUSS, S.; LANDRY, M. P.; VANDER ENDE, E.; LIMA, B. M. A.; REUEL, N. F.; ZHANG, J.; NELSON, J.; MU, B.; HILMER, A. AND STRANO, M.:

Neurotransmitter detection using corona phase molecular recognition on fluorescent single-walled carbon nanotube sensors. J. Am. Chem. Soc., 136(2):713–724, 2014.

[Kru17]   KRUSS, S.; SALEM, D. P.; VUKOVIĆ, L.; LIMA, B.; VANDER ENDE, E.; BOYDEN, E. S. AND STRANO, M. S.: *High-resolution imaging of cellular dopamine efflux using a fluorescent nanosensor array.* Proc. Natl. Acad. Sci. U.S.A., 114(8):1789–1794, 2017.

[Lan19]   LAN, Y.; YUAN, F.; FEREJA, T. H.; WANG, C.; LOU, B.; LI, J. AND XU, G.: *Chemiluminescence of Lucigenin/Riboflavin and Its Application for Selective and Sensitive Dopamine Detection.* Anal.Chem., 91(3):2135–2139, 2019.

[Lee21]   LEE, W.; KANG, B.-H.; YANG, H.; PARK, M.; KWAK, J. H.; CHUNG, T.; JEONG, Y.; KIM, B. K. AND JEONG, K.-H.: *Spread spectrum SERS allows label-free detection of attomolar neurotransmitters.* Nat. Commun., 12(1):159, 2021.

[Leo19]   LEOPOLD, A. V.; SHCHERBAKOVA, D. M. AND VERKHUSHA, V. V.: *Fluorescent Biosensors for Neurotransmission and Neuromodulation: Engineering and Applications.* Front. Cell. Neurosci., 13:474, 2019.

[Li 19a] LI , F.; LIU, J.; GUO, L.; WANG, J.; ZHANG, K.; HE, J. AND CUI, H.: *High-resolution temporally resolved chemiluminescence based on double-layered 3D microfluidic paper-based device for multiplexed analysis.* Biosens. Bioelectron., 141:111472, 2019.

[Li 19b] LI , H.; GORDEEV, G.; GARRITY, O.; REICH, S. AND FLAVEL, B. S.: *Separation of Small-Diameter Single-Walled Carbon Nanotubes in One to Three Steps with Aqueous Two-Phase Extraction.* ACS Nano, 13(2):2567–2578, 2019.

[Li 20]   LI , F.; GUO, L.; LI, Z.; HE, J.; CUI, H.: *Temporal-Spatial-Color Multiresolved Chemiluminescence Imaging for Multiplex Immunoassays Using a Smartphone Coupled with Microfluidic Chip.* Anal. Chem., 92(10):6827–6831, 2020.

[Lin09]   LIN, E. AND ALESSIO, A.: *What are the basic concepts of temporal, contrast, and spatial resolution in cardiac CT?* J. Cardiovasc. Comput. Tomogr., 3(6):403–408, 2009.

[Liu11]   LIU, H.; NISHIDE, D.; TANAKA, T. AND KATAURA, H.: *Large-scale single-chirality separation of single-wall carbon nanotubes by simple gel chromatography.* Nat. Commun., 2:309, 2011.

[Liu13]   LIU, H.; TANAKA, T.; URABE, Y. AND KATAURA, H.: *High-efficiency single-chirality separation of carbon nanotubes using temperature-controlled gel chromatography.* Nano Lett., 13(5):1996–2003, 2013.

[Liu14]   LIU, L.; ZHANG, X.; LOU, Y.; RAO, Y. AND ZHANG, X.: *Cerebral microdialysis in glioma studies, from theory to application.* J. Pharm. Biomed. Anal., 96:77–89, 2014.

[Liu16]   LIU, F.; ZHANG, J. Z. H. AND MEI, Y.: *The origin of the cooperativity in the streptavidin-biotin system: A computational investigation through molecular dynamics simulations.* Sci. Rep., 6:27190, 2016.

[Liu21]   LIU, X. AND LIU, J.: *Biosensors and sensors for dopamine detection.* View, 2(1):20200102, 2021.

[Loe21]   LOEWI, O.: *Über humorale Übertragbarkeit der Herznervenwirkung.* Pflugers Archiv : European journal of physiology, 189(1):239–242, 1921.

[Lyu19]   LYU, M.; MEANY, B.; YANG, J.; LI, Y.; ZHENG, M.: *Toward Complete Resolution of DNA/Carbon Nanotube Hybrids by Aqueous Two-Phase Systems.* J. Am. Chem. Soc., 141(51):20177–20186, 2019.

[Ma 20]   MA , L.; ZHAO, T.; ZHANG, P.; LIU, M.; SHI, H. AND KANG, W.: *Determination of monoamine neurotransmitters and metabolites by high-performance liquid chromatography based on Ag(III) complex chemiluminescence detection.* Anal. Biochem., 593:113594, 2020.

[Maj10]   MAJUMDER, M.; RENDALL, C.; LI, M.; BEHABTU, N.; EUKEL, J. A.; HAUGE, R. H.; SCHMIDT, H. K. AND PASQUALI, M.: *Insights into the physics of spray coating of SWNT films.* Chem. Eng. Sci., 65(6):2000–2008, 2010.

[Mal13]   MALAPANIS, A.; PEREBEINOS, V.; SINHA, D. P.; COMFORT, E. AND LEE, J. U.: *Quantum efficiency and capture cross section of first and second excitonic transitions of single-walled carbon nanotubes measured through photoconductivity.* Nano Lett., 13(8):3531–3538, 2013.

[Man17]   MANN, F. A.; HERRMANN, N.; MEYER, D. AND KRUSS, S.: *Tuning Selectivity of Fluorescent Carbon Nanotube-Based Neurotransmitter Sensors.* Sensors, 17(7):1521, 2017.

[Man19]   MANN, F. A.; LV, Z.; GROSSHANS, J.; OPAZO, F. AND KRUSS, S.: *Nanobody-Conjugated Nanotubes for Targeted Near-Infrared In Vivo Imaging and Sensing.* Angew. Chem. Int. Ed., 58(33):11469–11473, 2019.

[Mar11]   MARC, D. T.; AILTS, J. W.; AILTS CAMPEAU, D. C.; BULL, M. J. AND

OLSON, K. L.: *Neurotransmitters excreted in the urine as biomarkers of nervous system activity: validity and clinical applicability.* Neurosci Biobehav Rev, 35(3):635–644, 2011.

[Met23] METTERNICH, J. T.; WARTMANN, J. A. C.; SISTEMICH, L.; NISSLER, R.; HERBERTZ, S. and KRUSS, S.: *Near-Infrared Fluorescent Biosensors Based on Covalent DNA Anchors.* J. Am. Chem. Soc., 145(27):14776–14783, 2023.

[Mey17] MEYER, D.; HAGEMANN, A. and KRUSS, S.: *Kinetic Requirements for Spatiotemporal Chemical Imaging with Fluorescent Nanosensors.* ACS Nano, 11(4):4017–4027, 2017.

[Nad23] NADEEM, A.; KINDOPP, A.; WYLLIE, I.; HUBERT, L.; JOUBERT, J.; LUCENTE, S.; RANDALL, E.; JENA, P. V. and ROXBURY, D.: *Enhancing Intracellular Optical Performance and Stability of Engineered Nanomaterials via Aqueous Two-Phase Purification.* Nano Lett., 23(14):6588—-6595, 2023.

[Nan22] NANDI, S.; CAICEDO, K.; COGNET, L.: *When Super-Resolution Localization Microscopy Meets Carbon Nanotubes.* Nanomater., 12(9):1433, 2022.

[Nis19] NISSLER, R.; MANN, F. A.; CHATURVEDI, P.; HORLEBEIN, J.; MEYER, D.; VUKOVIĆ, L. and KRUSS, S.: *Quantification of the Number of Adsorbed DNA Molecules on Single-Walled Carbon Nanotubes.* J. Phys. Chem. C, 123(8):4837–4847, 2019.

[Nis20] NISSLER, R.; BADER, O.; DOHMEN, M.; WALTER, S. G.; NOLL, C.; SELVAGGIO, G.; GROSS, U. and KRUSS, S.: *Remote near infrared identification of pathogens with multiplexed nanosensors.* Nat. Commun., 11(1):5995, 2020.

[Nis21] NISSLER, R.; KURTH, L.; LI, H.; SPREINAT, A.; KUHLEMANN, I.; FLAVEL, B. S. and KRUSS, S.: *Sensing with Chirality-Pure Near-Infrared Fluorescent Carbon Nanotubes.* Anal.l Chem., 93(16):6446–6455, 2021.

[Nis22] NISSLER, R. and ACKERMANN, J. and MA, C. and KRUSS, S.: *Prospects of Fluorescent Single-Chirality Carbon Nanotube-Based Biosensors.* Anal. Chem., 94(28):9941–9951, 2022.

[Niy19] NIYONAMBAZA, S. D.; KUMAR, P.;XING, P.; MATHAULT, J.; DE KONINCK, P.; BOISSELIER, E.; BOUKADOUM, M. and MILED, A.: *A Review of Neurotransmitters Sensing Methods for Neuro-Engineering Research.* Appl. Sci., 9(21):4719, 2019.

[O'C02] O'CONNELL, M. J.; BACHILO, S. M.; HUFFMAN, C. B.; MOORE, V. C.; STRANO, M. S.; HAROZ, E. H.; RIALON, K. L.; BOUL, P. J.; NOON, W.

H.; Kittrell, C.; Ma, J.; Hauge, R. H.; Weisman, R. B. and Smalley, R. E.: *Band gap fluorescence from individual single-walled carbon nanotubes.* Science, 297(5581):593–596, 2002.

[Occ23]   Occupational Safety and Health Administration: *Ethylene Oxide.* https://www.osha.gov/ethylene-oxide, 2023. Viewed on 30.08.2023.

[Opt23]   Opto Engine LLC: *561NM DPSS LASER SYSTEMS.* http://www.oemlasersystems.com/product-catalog/continuous-wave-laser-systems/501nm-600nm-laser-systems/561nm-dpss-laser-systems.html, 2023. Viewed on 30.08.2023.

[Ou 19]   Ou , Y.; Buchanan, A. M.; Witt, C. E.; Hashemi, P.: *Frontiers in Electrochemical Sensors for Neurotransmitter Detection: Towards Measuring Neurotransmitters as Chemical Diagnostics for Brain Disorders.* Anal. Methods, 11(21):2738–2755, 2019.

[Pan18]   Pan, J.-X.; Xia, J.-J.; Deng, F.-L.; Liang, W.-W.; Wu, J.; Yin, B.-M.; Dong, M.-X.; Chen, J.-J.; Ye, F.; Wang, H.-Y.; Zheng, P. and Xie, P.: *Diagnosis of major depressive disorder based on changes in multiple plasma neurotransmitters: a targeted metabolomics study.* Transl. Psychiatry, 8(1):130, 2018.

[Pao19]   Paoletti, P. F.; Tambasco, N. and Parnetti, L.: *Levodopa treatment in Parkinson's disease: earlier or later?* Ann. Transl. Med., 7(Suppl 6):S189, 2019.

[Per16]   Perez-Lloret, S. and Barrantes, F. J.: *Deficits in cholinergic neurotransmission and their clinical correlates in Parkinson's disease.* NPJ Parkinsons. Dis., 2:16001, 2016.

[Per22]   Perets, E. A.; Olesen, K. B. and Yan, E. C. Y.: *Chiral Sum Frequency Generation Spectroscopy Detects Double-Helix DNA at Interfaces.* Langmuir, 38(18):5765–5778, 2022.

[Pfa22]   Pfaff, D. W.; Volkow, N. D. and Rubenstein, J. L.: *Neuroscience in the 21st Century.* Springer International Publishing, Cham, 2022.

[Pin20]   Pinals, R. L.; Yang, D.; Rosenberg, D. J.; Chaudhary, T.; Crothers, A. R.; Iavarone, A. T.; Hammel, M. and Landry, M. P.: *Quantitative Protein Corona Composition and Dynamics on Carbon Nanotubes in Biological Environments.* Angew. Chem. Int. Ed., 59(52):23668–23677, 2020.

[Plo21]   Plou, J.; Charconnet, M.; García, I.; Calvo, J. and Liz-Marzán, L.

M.: *Preventing Memory Effects in Surface-Enhanced Raman Scattering Substrates by Polymer Coating and Laser-Activated Deprotection.* ACS Nano, 15(5):8984–8995, 2021.

[Pod20] PODLESNY, B.; SHIRAKI, T. AND JANAS, D.: *One-step sorting of single-walled carbon nanotubes using aqueous two-phase extraction in the presence of basic salts.* Sci. Rep., 10(1):9250, 2020.

[Pod21] PODLESNY, B.; OLSZEWSKA, B.; YAARI, Z.; JENA, P. V.; GHAHRAMANI, G.; FEINER, R.; HELLER, D. A. AND JANAS, D.: *En route to single-step, two-phase purification of carbon nanotubes facilitated by high-throughput spectroscopy.* Sci. Rep., 11(1):10618, 2021.

[Pod23] PODLESNY, B.; HINKLE, K. R.; HAYASHI, K.; NIIDOME, Y.; SHIRAKI, T. AND JANAS, D.: *Highly-Selective Harvesting of (6,4) SWCNTs Using the Aqueous Two-Phase Extraction Method and Nonionic Surfactants.* Adv. Sci., 10(14):e2207218, 2023.

[Put20] PUTHONGKHAM, P. AND VENTON, B. J.: *Recent advances in fast-scan cyclic voltammetry.* Analyst, 145(4):1087–1102, 2020.

[Rag00] RAGAB, G. H.; NOHTA, H. AND ZAITSU, K.: *Chemiluminescence determination of catecholamines in human blood plasma using 1,2-bis(3-chlorophenyl)ethylenediamine as pre-column derivatizing reagent for liquid chromatography.* Anal. Chim. Acta., 403(1-2):155–160, 2000.

[Ras10] RASTOGI, R. P.; RICHA; KUMAR, A.; TYAGI, M. B. AND SINHA, R. P.: *Molecular mechanisms of ultraviolet radiation-induced DNA damage and repair.* J. Nucleic Acids, 2010:592980, 2010.

[Sal17] SALEM, D. P.; GONG, X.; LIU, A. T.; KOMAN, V. B.; DONG, J. AND STRANO, M. S.: *Ionic Strength-Mediated Phase Transitions of Surface-Adsorbed DNA on Single-Walled Carbon Nanotubes.* J. Am. Chem. Soc., 139(46):16791–16802, 2017.

[San21] SANGUBOTLA, R. AND KIM, J.: *Fiber-optic biosensor based on the laccase immobilization on silica-functionalized fluorescent carbon dots for the detection of dopamine and multi-color imaging applications in neuroblastoma cells.* Mater. Sci. Eng. C., 122:111916, 2021.

[Sch13] SCHMIDT, A. C.; WANG, X.; ZHU, Y. AND SOMBERS, L. A.: *Carbon nanotube yarn electrodes for enhanced detection of neurotransmitter dynamics in live brain tissue.* ACS Nano, 7(9):7864–7873, 2013.

[Sch14] SCHLÜCKER, S.: *Surface-enhanced Raman spectroscopy: concepts and chemical applications.* Angew. Chem. Int. Ed., 53(19):4756–4795, 2014.

[Sch19] SCHROEDER, V.; SAVAGATRUP, S.; HE, M.; LIN, S. AND SWAGER, T. M.: *Carbon Nanotube Chemical Sensors.* Chem. Rev., 119(1):599–663, 2019.

[Sci23] SCIENTIFIC SUPPORT: *Dionex PAD-2 Pulsed Amperometric Detector.* http://www.sci-support.com/items/Dionex-PAD-2-Pulsed-Amperometric-D etector-1727.htm, 2023. Viewed on 30.08.2023.

[Si 18] SI , B. AND SONG, E.: *Recent Advances in the Detection of Neurotransmitters.* Chemosensors, 6(1):1, 2018.

[Sim22] SIMS, C. M. AND FAGAN, J. A.: *Surfactant Chemistry and Polymer Choice Affect Single-Wall Carbon Nanotube Extraction Conditions in Aqueous Two-Polymer Phase Extraction.* Carbon, 191:215–226, 2022.

[Sis23] SISTEMICH, L.; GALONSKA, P.; STEGEMANN, J.; ACKERMANN, J. AND KRUSS, S.: *Near-Infrared Fluorescence Lifetime Imaging of Biomolecules with Carbon Nanotubes.* Angew. Chem. Int. Ed., 62(24):e202300682, 2023.

[Smi09] SMITH, A. M.; MANCINI, M. C. AND NIE, S.: *Bioimaging: second window for in vivo imaging.* Nat. Nanotechnol., 4(11):710–711, 2009.

[Sta21] STAPLETON, J. A.; HOFFERBER, E. M.; MEIER, J.; RAMIREZ, I. A. AND IVERSON, N. M.: *Single-Walled Carbon Nanotube Sensor Platform for the Study of Extracellular Analytes.* ACS Appl. Nano Mater., 4(1):33–42, 2021.

[Str17] STREIT, J. K.; FAGAN, J. A. AND ZHENG, M.: *A Low Energy Route to DNA-Wrapped Carbon Nanotubes via Replacement of Bile Salt Surfactants.* Anal. Chem., 89(19):10496–10503, 2017.

[Sub14] SUBBAIYAN, N. K.; CAMBRÉ, S.; PARRA-VASQUEZ, A. N. G.; HÁROZ, E. H.; DOORN, S. K. AND DUQUE, J. G.: *Role of surfactants and salt in aqueous two-phase separation of carbon nanotubes toward simple chirality isolation.* ACS Nano, 8(2):1619–1628, 2014.

[Swa18] SWAGER, T. M.: *Sensor Technologies Empowered by Materials and Molecular Innovations.* Angew. Chem. Int. Ed., 57(16):4248–4257, 2018.

[Syp22] SYPABEKOVA, M.; HAGEMANN, A.; RHO, D. AND KIM, S.: *Review: 3-Aminopropyltriethoxysilane (APTES) Deposition Methods on Oxide Surfaces in Solution and Vapor Phases for Biosensing Applications.* Biosensors, 13(1):36, 2022.

[Tan15] TANG, L.; LI, S.; HAN, F.; LIU, L.; XU, L.; MA, W.; KUANG, H.; LI, A.;

Wang, L. and Xu, C.: *SERS-active Au@Ag nanorod dimers for ultrasensitive dopamine detection.* Biosens. Bioelectron., 71:7–12, 2015.

[Tan19] Tang, Z.; Jiang, K.; Sun, S.; Qian, S.; Wang, Y.; Lin, H.: *A conjugated carbon-dot-tyrosinase bioprobe for highly selective and sensitive detection of dopamine.* The Analyst, 144(2):468–473, 2019.

[Tav19] Tavakolian-Ardakani, Z.; Hosu, O.; Cristea, C.; Mazloum-Ardakani, M. and Marrazza, G.: *Latest Trends in Electrochemical Sensors for Neurotransmitters: A Review.* Sensors, 19(9):2037, 2019.

[Ten22] Teniou, A.; Rhouati, A.; and Catanante, G.: *A Simple Fluorescent Aptasensing Platform Based on Graphene Oxide for Dopamine Determination.* Appl. Biochem. Biotechnol., 194(5):1925–1937, 2022.

[Tog16] TogoTV: *DBCLS TogoTV, CC-BY-4.0.* https://creativecommons.org/licenses/by/4.0/, 2016.

[Tye17] Tyebji, S. and Hannan, A. J.: *Synaptopathic mechanisms of neurodegeneration and dementia: Insights from Huntington's disease.* Prog. Neurobiol., 153:18–45, 2017.

[Tyn12] Tynan, C. J.; Clarke, D. T.; Coles, B. C.; Rolfe, D. J.; Martin-Fernandez, M. L. and Webb, S. E. D.: *Multicolour single molecule imaging in cells with near infra-red dyes.* PLoS One, 7(4):e36265, 2012.

[Uni16] United States Environmental Protection Agency: *Evaluation of the Inhalation Carcinogenicity of Ethylene Oxide (Final Report). U.S. Environmental Protection Agency, Washington, DC, EPA/635/R-16/350F.* https://cfpub.epa.gov/ncea/iris_drafts/recordisplay.cfm?deid=329730, 2016. Viewed on 30.08.2023.

[Uni19] Universitätsmedizin Mainz: *PET/CT-Methodik.* https://www.unimedizin-mainz.de/nuklearmedizin/patienten/petct/petct-methodik.html, 2019. Viewed on 30.08.2023.

[Wan03] Wang, S.; Humphreys, E. S.; Chung, S.-Y.; Delduco, D. F.; Lustig, S. R.; Wang, H.; Parker, K. N.; Rizzo, N. W.; Subramoney, S.; Chiang, Y.-M. and Jagota, A.: *Peptides with selective affinity for carbon nanotubes.* Nat. Mater., 2(3):196–200, 2003.

[Wan15] Wang, H.-B.; Zhang, H.-D.; Chen, Y.; Huang, K.-J.; Liu, Y.-M.: *A label-free and ultrasensitive fluorescent sensor for dopamine detection based on double-stranded DNA templated copper nanoparticles.* Sens. Actuators B

Chem., 220:146–153, 2015.

[Wan19]   WANG, G.: *High Temporal-Resolution Dynamic PET Image Reconstruction Using a New Spatiotemporal Kernel Method.* IEEE Trans. Med. Imaging, 38(3):664–674, 2019.

[Wei20]   WEI, X.; TANAKA, T.; LI, S.; TSUZUKI, M.; WANG, G.; YAO, Z.; LI, L.; YOMOGIDA, Y.; HIRANO, A.; LIU, H. AND KATAURA, H.: *Photoluminescence Quantum Yield of Single-Wall Carbon Nanotubes Corrected for the Photon Reabsorption Effect.* Nano Lett., 20(1):410–417, 2020.

[Whi21]   WHITE, K. A. AND KIM, B. N.: *Quantifying neurotransmitter secretion at single-vesicle resolution using high-density complementary metal-oxide-semiconductor electrode array.* Nat. Commun., 12(1):431, 2021.

[WHO22]   WHO - WORLD HEALTH ORGANIZATION: *World mental health report: Transforming mental health for all.* https://apps.who.int/iris/rest/bitstream s/1433523/retrieve, 2022.

[Wil18a] WILLIAMS, R. M.; LEE, C. AND HELLER, D. A.: *A Fluorescent Carbon Nanotube Sensor Detects the Metastatic Prostate Cancer Biomarker uPA.* ACS Sens., 3(9):1838–1845, 2018.

[Wil18b] WILLIAMS, R. M.; LEE, C.; GALASSI, T. V.; HARVEY, J. D.; LEICHER, R.; SIRENKO, M.; DORSO, M. A.; SHAH, J.; OLVERA, N.; DAO, F.; LEVINE, D. A.; HELLER, D. A.: *Noninvasive ovarian cancer biomarker detection via an optical nanosensor implant.* Sci. Adv., 4(4):eaaq1090, 2018.

[Won17]   WONG, M. H.; GIRALDO, J. P.; KWAK, S.-Y.; KOMAN, V. B.; SINCLAIR, R.; LEW, T. T. S.; BISKER, G.; LIU, P.; STRANO, M. S.: *Nitroaromatic detection and infrared communication from wild-type plants using plant nanobionics.* Nat. Mater., 16(2):264–272, 2017.

[Wu 16]   WU , D.; XIE, H.; LU, H.; LI, W. AND ZHANG, Q.: *Sensitive determination of norepinephrine, epinephrine, dopamine and 5-hydroxytryptamine by coupling HPLC with Ag(HIO6)2 (5-) -luminol chemiluminescence detection.* Biomed. Chromatogr., 30(9):1458–1466, 2016.

[Xen]   XENICS: *Xeva 320 Series.* https://www.xenics.com/short-wave-infrared-ima gers/xeva-320-series/. Viewed on 30.08.2023.

[Xu 17]   XU , B.; KANEKO, T.; SHIBUTA, Y. AND KATO, T.: *Preferential synthesis of (6,4) single-walled carbon nanotubes by controlling oxidation degree of Co catalyst.* Sci. Rep., 7(1):11149, 2017.

[Xu 22]   XU , H. AND YANG, F.: *The interplay of dopamine metabolism abnormalities and mitochondrial defects in the pathogenesis of schizophrenia.* Transl. Psychiatry, 12(1):464, 2022.

[Yan19]   YANG, S.; XU, Z.; XUE, S.; KANDLAKUNTA, P.; CAO, L. AND HUANG, J.: *Organohalide Lead Perovskites: More Stable than Glass under Gamma-Ray Radiation.* Adv. Mater., 31(4):e1805547, 2019.

[Yan20a] YANG, F.; WANG, M.; ZHANG, D.; YANG, J.; ZHENG, M. AND LI, Y.: *Chirality Pure Carbon Nanotubes: Growth, Sorting, and Characterization.* Chem. Rev., 120(5):2693–2758, 2020.

[Yan20b] YANG, Y.; SHARMA, A.; NOETINGER, G.; ZHENG, M. AND JAGOTA, A.: *Pathway-Dependent Structures of DNA-Wrapped Carbon Nanotubes: Direct Sonication vs Surfactant/DNA Exchange.* J. Phys. Chem. C, 124(16):9045–9055, 2020.

[Yan21]   YANG, S. J.; DEL BONIS-O'DONNELL, J. T.; BEYENE, A. G. AND LANDRY, M. P.: *Near-infrared catecholamine nanosensors for high spatiotemporal dopamine imaging.* Nat. Protoc., 16(6):3026–3048, 2021.

[Yom20]   YOMOGIDA, Y.; TANAKA, T.; TSUZUKI, M.; WEI, X.; KATAURA, H.: *Automatic Sorting of Single-Chirality Single-Wall Carbon Nanotubes Using Hydrophobic Cholates: Implications for Multicolor Near-Infrared Optical Technologies.* ACS Appl. Nano Mater., 3(11):11289–11297, 2020.

[Yoo20]   YOON, J.; SHIN, M.; LEE, T. AND CHOI, J.-W.: *Highly Sensitive Biosensors Based on Biomolecules and Functional Nanomaterials Depending on the Types of Nanomaterials: A Perspective Review.* Mater., 13(2), 2020.

[Yu 22]   YU , Z. AND TANG, D.: *Artificial Neural Network-Assisted Wearable Flexible Sweat Patch for Drug Management in Parkinson's Patients Based on Vacancy-Engineered Processing of g-C3N4.* Analytical Chemistry, 94(51):18000–18008, 2022.

[Yum12]   YUM, K.; AHN, J.-H.; MCNICHOLAS, T. P.; BARONE, P. W.; MU, B.; KIM, J.-H.; JAIN, R. M. AND STRANO, M. S.: *Boronic acid library for selective, reversible near-infrared fluorescence quenching of surfactant suspended single-walled carbon nanotubes in response to glucose.* ACS Nano, 6(1):819–830, 2012.

[Zes17]   ZESTOS, A. G. AND KENNEDY, R. T.: *Microdialysis Coupled with LC-MS/MS for In Vivo Neurochemical Monitoring.* AAPS J., 19(5):1284–1293, 2017.

[Zha11] ZHANG, J.; BOGHOSSIAN, A. A.; BARONE, P. W.; RWEI, A.; KIM, J.-H.; LIN, D.; HELLER, D. A.; HILMER, A. J.; NAIR, N.; REUEL, N. F.; STRANO, M. S.: *Single molecule detection of nitric oxide enabled by d(AT)15 DNA adsorbed to near infrared fluorescent single-walled carbon nanotubes.* J. Am. Chem. Soc., 133(3):567–581, 2011.

[Zha13] ZHANG, J.; LANDRY, M. P.; BARONE, P. W.; KIM, J.-H.; LIN, S.; ULISSI, Z. W.; LIN, D.; MU, B.; BOGHOSSIAN, A. A.; HILMER, A. J.; RWEI, A.; HINCKLEY, A. C.; KRUSS, S.; SHANDELL, M. A.; NAIR, N.; BLAKE, S.; ŞEN, F.; ŞEN, S.; CROY, R. G.; LI, D.; YUM, K.; AHN, J.-H.; JIN, H.; HELLER, D. A.; ESSIGMANN, J. M.; BLANKSCHTEIN, D. AND STRANO, M. S.: *Molecular recognition using corona phase complexes made of synthetic polymers adsorbed on carbon nanotubes.* Nat. Nanotechnol., 8(12):959–968, 2013.

[Zha14] ZHANG, J.; KRUSS, S.; HILMER, A. J.; SHIMIZU, S.; SCHMOIS, Z.; DE LA CRUZ, F.; BARONE, P. W.; REUEL, N. F. ; HELLER, D. A. AND STRANO, M. S.: *A rapid, direct, quantitative, and label-free detector of cardiac biomarker troponin T using near-infrared fluorescent single-walled carbon nanotube sensors.* Adv. Healthc. Mater., 3(3):412–423, 2014.

[Zha22] ZHANG, Y.; DING, L.; ZHANG, H.; WANG, P. AND LI, H.: *A new optical fiber biosensor for acetylcholine detection based on pH sensitive fluorescent carbon quantum dots.* Sens. Actuators B Chem., 369:132268, 2022.

[Zhe03] ZHENG, M.; JAGOTA, A.; SEMKE, E. D.; DINER, B. A.; MCLEAN, R. S.; LUSTIG, S. R.; RICHARDSON, R. E. AND TASSI, N. G.: *DNA-assisted dispersion and separation of carbon nanotubes.* Nat. Mater., 2(5):338–342, 2003.

[Zib16] ZIBAII, M. I.; LATIFI, H.; ASADOLLAHI, A.; BAYAT, A. H.; DARGAHI, L. AND HAGHPARAST, A.: *Label Free Fiber Optic Apta-Biosensor for In-Vitro Detection of Dopamine.* J. Light. Technol., 34(19):4516–4524, 2016.

[Zub22] ZUBKOVS, V.; WANG, H.; SCHUERGERS, N.; WENINGER, A.; GLIEDER, A.; CATTANEO, S. AND BOGHOSSIAN, A. A.: *Bioengineering a glucose oxidase nanosensor for near-infrared continuous glucose monitoring.* Nanoscale Adv., 4(11):2420–2427, 2022.

A Publications

First-Author Publications

1. *Smart Slides for Optical Monitoring of Cellular Processes*
   <u>J. Ackermann</u>, E. Reger, S. Jung, J. Mohr, S. Herbertz, K. Seidl, S. Kruss, *Adv. Funct. Mater.* **2024**, 34(6), 2309064, doi.org/10.1002/adfm.202309064

2. *High Sensitivity Near-Infrared Imaging of Fluorescent Nanosensors*
   <u>J. Ackermann</u>, J. Stegemann, T. Smola, E. Reger, S. Jung, A. Schmitz, S. Herbertz, L. Erpenbeck, K. Seidl, S. Kruss, *Small* **2023**, 19(14), 2206856, doi.org/10.1002/smll.202206856

3. *Biosensing with Fluorescent Carbon Nanotubes*
   <u>J. Ackermann</u>, J. T. Metternich, S. Herbertz, S. Kruss, *Angew. Chem. Int. Ed.* **2022**, 61(18), e202112372, doi.org/10.1002/anie.202112372

Co-Authored Publications

1. *Molekulare Architektur: Nanosensoren mit DNA-Ankern*
   J. T. Metternich, <u>J. Ackermann</u>, S. Kruss, *Biospektrum* **2024**, 30, 165, doi.org/10.1007/s12268-024-2130-0

2. *Near-Infrared Lifetime Imaging of Biomolecules with Carbon Nanotubes*
   L. Sistemich, P. Galonska, J. Stegemann, <u>J. Ackermann</u>, S. Kruss, *Angew. Chem. Int. Ed.* **2023**, 62(24), e202300682, doi.org/10.1002/anie.202300682

3. *Comparison of electrical and optical transduction modes of DNA-wrapped SWCNT nanosensors for the reversible detection of neurotransmitters*
   P. Clément, <u>J. Ackermann</u>, N. Sahin-Solmaz, S. Herbertz, G. Boero, S. Kruss, J. Brugger, *Biosens. Bioelectron.* **2022**, 216, 114642, doi.org/10.1016/j.bios.2022.114642

4. *Prospects of Fluorescent Single-Chirality Carbon Nanotube-Based Biosensors*
   R. Nißler, <u>J. Ackermann</u>, C. Ma, S. Kruss, *Anal. Chem.* **2022**, 94(28), 9941, doi.o
   rg/10.1021/acs.analchem.2c01321

Oral Talks

1. *Carbon nanotubes as powerful platform for optical biosensing*
   <u>J. Ackermann</u>, J. Metternich, J. Stegemann, S. Herbertz, K. Seidl, S. Kruss, German
   Society of Biomedical Engineering (BMT Annual Meeting) in Duisburg, Germany,
   2023

2. *Carbon nanotubes as powerful platform for optical biosensing*
   <u>J. Ackermann</u>, J. Metternich, J. Stegemann, S. Herbertz, S. Kruss, 10th NRW Nano
   Conference in Dortmund, Germany, **2023**

3. *Neurotransmitter detection based on near-infrared fluorescent carbon nanotubes*
   <u>J. Ackermann</u>, S. Herbertz, K. Seidl, S. Kruss, Annual Meeting of the German So-
   ciety for Biomaterials in Essen, Germany, **2022**

Supervised Theses

1. *Prozessoptimierung der lösungsbasierten Separation von Kohlenstoffnanoröhren*
   D. Sorokin, Bachelor Thesis, Universität Duisburg-Essen, **2023**

2. *Entwicklung von fluoreszenten Nanosensor-Hydrogel-Arrays zur Detektion von
   Biomolekülen*
   M. Blawat, Bachelor Thesis, Universität Duisburg-Essen, **2023**

3. *Entwicklung eines optischen Nanobiosensor-Arrays auf Papier*
   E. Reger, Bachelor Thesis, Universität Duisburg-Essen, **2022**

4. *Entwicklung eines kompakten automatisierten Messaufbaus für das Screening von
   fluoreszenten Biosensoren*
   J. Stegemann, Master Thesis, FH Münster, **2021**

5. *Entwicklung von optischen Biosensoren auf Basis von fluoreszierenden Kohlenstoff-
   nanoröhren*
   M. Blawat, D. Sorokin, T. Weber, Project Work, Universität Duisburg-Essen, **2021**

B Danksagung

Ich möchte diese Gelegenheit nutzen, um von Herzen meinen aufrichtigen Dank auszusprechen. Eure Unterstützung auf meinem Weg zur Erstellung meiner Doktorarbeit war von unschätzbarem Wert und hat mir geholfen, diesen Meilenstein zu erreichen. Ich möchte mich insbesondere bei folgenden Personen bedanken:

Prof. Sebastian Kruss danke ich dafür, dass er mir die Möglichkeit gegeben hat in der Biomedical Nanosensor Gruppe zu promovieren. Als einer der ersten Mitarbeiter hat es mir Spaß gemacht diese Gruppe mit aufzubauen und an spannenden Forschungsthemen mitzuwirken. Deine stete Unterstützung hat meine Arbeit bereichert.

Prof. Karsten Seidl, meinem Doktorvater, danke ich für die fachliche Unterstützung in unseren regelmäßigen Gesprächen, die mich stets motiviert haben, weiterzumachen.

Prof. Sebastian Schlücker möchte ich für die Bereitschaft zur Übernahme des Zweitgutachtens und für seine Zeit danken, die er sich für die Prüfung dieser Arbeit genommen hat.

Ein herzliches Dankeschön geht auch an die gesamte *Biomedical Nanosensor Gruppe* und die *AG Kruss*. Die produktiven Diskussionen während unserer Gruppenmeetings, die entspannte Atmosphäre und eure hilfreichen Ratschläge während der Status Reports haben mir geholfen, meinen Fokus zu behalten. Für die technische Unterstützung danke ich vor allem *Robert Nißler* für die allererste Einführung zur Herstellung von SWCNT-Sensoren sowie *Lena Schnitzler* und *Juliana Gretz* für die Einführungen zu den optischen Setups. Mein Dank gilt aber vor allem auch allen *Koautoren*, ohne die meine Publikationen nicht möglich gewesen wären. Besonders möchte ich *Sebastian Jung* hervorheben, der die Zellen kultiviert und ihr Überleben bis zum Beginn der Experimente gesichert hat, aber auch *Jennifer Mohr*, die immer mal wieder eingesprungen ist, um die Zellexperimente durchführen zu können. *Justus Metternich* danke ich für das verlässliche 'Kurier spielen' für den Probenautsausch zwischen Bochum und Duisburg und für die gute Zusammenarbeit beim Schreiben des Review Manuskripts. *Srenja Herbertz* danke ich für unseren regelmäßigen Austausch, Ihre wertvollen Ratschläge, Ihr Interesse an meiner Arbeit und für das aufmerksame Korrekturlesen. *Christina Derichsweiler* danke ich für ihr Interesse

am Fortschritt beim Verfassen dieser Arbeit, ihre fröhliche Art und der kleinen Pausen zwischendurch.

Ein besonderer Dank gilt meinen Studenten, die ich im Laufe dieser Arbeit betreut habe, insbesondere *Eline Reger* und *Tim Smola*, die durch ihre Praktika und Hiwi-Tätigkeiten meine Forschungsarbeiten vorangebracht haben. Aber auch *Daniela Sorokin*, *Marcel Blawat*, *Tom Weber* und *Jan Stegemann* danke ich für ihre Mitarbeit an den spannenden Nebenprojekten. Inbesondere freue ich mich, dass durch Jans Interesse an den Forschungsthemen nach Anschluss seiner Masterarbeit unsere Gruppe noch weiter interdiziplinär gewachsen ist. Auch für seine Simulation beim (6,4)-SWCNT Paper danke ich ihm für diesen wichtigen Beitrag der die Gesamtstory dieses Papers komplettiert hat.

Zu guter Letzt geht mein Dank an meine *Familie und Freunde*, eure Geduld und euer Verständnis während der letzten Wochen und Monate bedeuten mir unendlich viel. Eure ständige Unterstützung und motivierenden Worte haben mich auf der Zielgeraden begleitet und mich angetrieben. Auch meine lieben *Fellnasen* verdienen Dank für ihren Einsatz als Fliegenfänger und ihre haarige Unterstützung während der Schreibphase im Home-Office. Besonders Otto danke ich für seine Ratschläge zur Textgestaltung, auch wenn ich sie leider nicht annehmen konnte.

Ich danke *Lars* für seine unendliche Geduld, die Blümchen, die für die Verschönerung meiner Schreibkulisse in der Endphase, aber auch zum Ausbruch der Florfliegenlarven-Attake auf meine Wände und mich gesorgt haben, die All-Inklusive Essensversorgung und dafür, dass er einfach immer an meiner Seite steht. Du hast mich in jeder Hinsicht unterstützt und all die kleinen Gesten haben den Weg zur Fertigstellung meiner Doktorarbeit erleichtert.

Nochmals vielen herzlichen Dank an euch alle. Ohne eure Unterstützung wäre dieser Erfolg nicht möglich gewesen.

Julia

DuEPublico

Duisburg-Essen Publications online